

Universidad Autónoma de Madrid

Departamento de Bioquímica

**Activation Mechanisms of the Innate Immune System:
Structure-Function Studies of Interactions Between
Death Domains of MyD88 and IRAK Proteins**

PhD Thesis

Elena de Mendoza Barberá

Madrid, 2012

Departamento de Bioquímica
Facultad de Medicina
Universidad Autónoma de Madrid

**Activation Mechanisms of the Innate Immune System:
Structure-Function Studies of Interactions Between
Death Domains of MyD88 and IRAK Proteins**

PhD Thesis

Elena de Mendoza Barberá

BSc Biology

Directors:

Dr. Pablo Fuentes Prior

Institut de Reserca, Hospital de la Santa Creu i Sant Pau

Dr. Eduardo López-Collazo

Unidad de Investigación, Hospital Universitario La Paz

Agradecimientos (Acknowledgments)

Durante el desarrollo de esta tesis sois muchos los que me habéis ayudado, tanto a nivel científico como a nivel personal. Me gustaría expresaros mi más profundo agradecimiento.

En primer lugar, agradezco especialmente la ayuda y el apoyo que me brindó el Dr. Fernando Hernández, del Hospital La Paz, en mis primeros comienzos. Él me proporcionó, además de los medios económicos, toda su ayuda y disponibilidad, y siempre con esa amabilidad y encanto que a él tanto le caracterizaba. Gracias, Fernando.

Estoy también muy agradecida al Ministerio de Ciencia e Innovación por haber podido disfrutar de una beca FPI durante el desarrollo de este trabajo, y al Dr. Jaume Kulisevsky, director del IIB Sant Pau, por las ayudas que me ha otorgado cuando lo he necesitado.

Quiero agradecer especialmente la ayuda inestimable de mis directores de tesis, el Dr. Pablo Fuentes Prior y el Dr. Eduardo López-Collazo. Gracias por aceptarme en vuestros laboratorios, y por motivarme a crecer profesional y personalmente. Esta tesis no hubiera sido posible sin vosotros y sin vuestra meticulosa revisión de los datos. Mi más sincero agradecimiento.

Al equipo de Xavi Gomis-Rüth, del CID-CSIC de Barcelona, gracias por dejarme utilizar vuestras instalaciones, y por ayudarme siempre que lo he necesitado. Gracias Tibi, por las horas que me has dedicado, siempre con una sonrisa en la cara.

Al Dr. Josep Julve, por ayudarme con los experimentos de filtración en gel. Gràcies, Josep, pel teu ajut, disponibilitat i paciència.

A la Dra. Lina Badimón, del CSIC-ICCC, le agradezco la posibilidad que me otorgó de realizar mucha parte de esta tesis en el centro que ella dirige, y la disposición de los medios materiales que me permitieron realizar gran parte del trabajo.

El tiempo que pasé en el ICCC me permitió conocer a mi pequeña familia de científicos que, sin duda, ha sido la mejor parte de esta tesis. Gracias a Marta Miguel, Blanca, Rodri, Roberta, Maurizio, Marta Cinta, Roi, María Borrell, Jordi Farré, Juli, Montse, Marta Vilalta., Javi F., Anna, Javi Crespo, Silvia, Mari, Pablo Catalina, Montse, Xevi, Javi Crespo, Laura Casaní., Maísa y Pepelu, por todos los momentos que hemos compartido juntos. Gracias, Rosa, por compartir el laboratorio conmigo y aguantarme, a pesar de mis invasiones de poyata. Gracias, Judith, por acogerme tan bien desde el principio (siempre serás mi rubita!). Gracias, Marta (pelorrojo), por tu alegría y tu risa contagiosa (el viaje a Boston fue inolvidable!). Gracias, Vanessa, por tener esa personalidad tan auténtica y tan bonita. Gracias, Jose, por estar siempre ahí, dispuesto a todo. Gracias, Carlota, por todo tu cariño y dulzura. Gracias, Laura (Nasarre), por los momentos vividos y por tu buen humor. Gracias, María (de Burgos), por tantas y tantas conversaciones, risas y demás, que hemos compartido. Gracias a todos por estar a mi lado en todo momento... Vuelvo a formar parte del núcleo duro! :)

Estoy muy agradecida a toda la gente que conocí durante mi estancia en el IBS de Grenoble, por hacerme la vida allí mucho más fácil y agradable. Gracias, Asun, por dedicarme tu tiempo a pesar de todo tu trabajo, por ayudarme con el FPLC, y por compartir conmigo algunas cervecitas. Merci, Mylene, pour ton sourire et ta bonne humeur! Merci, Eva et Aline, pour votre aide avec l'AUC et tout le reste. Merci, Gael, pour les conversations et les cafés qu'on a pris

ensemble. Merci, Florent, pour le voyage à Montpellier et pour la course finale vers le train! Merci, Eugénie, pour ta sympathie. Merci, Julien, pour ta visite agréable à Barcelone. Merci, Romain, pour tes leçons sur la crystallo et ta gentillesse. Merci, Jacques, pour ton amitié, pour le temps qu'on a partagé à Grenoble et aussi à Barcelone, pour toutes les conversations, et pour les rires qu'on a fait ensemble... Il nous reste beaucoup de cafés / bières en attente!

Je voudrais offrir des remerciements spéciaux au Dr. Frederic Vellieux, pour m'avoir accueilli si gentiment à l'IBS. Merci, Fred, pour partager avec moi tes connaissances scientifiques et pour ton hospitalité.

Je suis aussi très reconnaissante au Dr. Dominique Madern, pour son aide et sa contribution à ma carrière scientifique, ainsi qu'à la Dr. Nicole Thielens, pour tout le temps qu'elle m'a dédié pendant les expériences de Biacore.

L'aide du Dr. Bruno Franzetti a été toujours impayable. Merci Bruno, pour partager avec moi les moments de joie et de tristesse, et pour ton aide au labo et dehors... Rachel et Maxime, merci pour partager votre maison avec moi et pour m'aider à améliorer mon français en regardant Astérix et Obélix, et pour tous les bons moments qu'on a partagé.

Agradezco la ayuda de toda la gente de la unidad de investigación del Hospital La Paz, con quienes compartí los comienzos de este trabajo y con quienes tan buenos momentos he pasado. Gracias, Carlos, por tu paciencia y por enseñarme tantas cosas durante los primeros meses. Vane y Ale, gracias por haber estado siempre ahí, por todas vuestras risas y la alegría que desprendéis. Vane, te agradezco especialmente la ayuda que me has dado en estos últimos momentos... sin ti no lo hubiera conseguido!

Gracias a Fabián y a Eva, por las horas de laboratorio compartidas durante los últimos tiempos, y a la gente de Blanes, por aguantarme mientras escribía esta tesis. Gracias especialmente a María Elena, Roser, Uri, Eduard y Agnès, por ser tan simpáticos y acogerme de una manera tan agradable.

Quiero expresar mi más profundo agradecimiento a todos aquellos que habéis estado a mi lado en todo momento. Nunca olvidaré todo lo que hemos vivido juntos.

A mi querida amiga María, con la que tantas cosas he compartido en el laboratorio y fuera de él. Es tanto lo que tengo que agradecer que no sería posible escribirlo todo en este texto. Sin embargo, no quiero desaprovechar la ocasión para agradecer todo el apoyo profesional y personal que me has brindado durante todos estos años. Gracias por ayudarme en los momentos más difíciles y por seguir haciéndolo aún en la distancia. Gracias por irradiar alegría allá donde vas. Además de ser divertida, inteligente, y tener un gran sentido del humor, tienes una bondad y sensibilidad admirables. Gracias por convertirme en mejor persona, y por compartir tu felicidad y alegría conmigo. En el mundo debería haber más gente como tú. Para mi eres un ejemplo a seguir, y no sabes cuánto me alegro de haberte conocido. Te quiero, pequeña!

A Erick, porque tu llegada al laboratorio fue una bocanada de aire fresco. Gracias por traer esa paz y tranquilidad al laboratorio, que tan bien nos ha venido a todos. Nunca olvidaré los momentos que hemos vivido juntos, las risas, las conversaciones sobre la vida, y las muchas horas de poyata a tu lado. Gracias también por los viajes a Grenoble, por los desayunos en el Sant Pau, y por acogerme en tu casa siempre que lo he necesitado. Gracias por tu apoyo y ayuda...no sabes cuánto lo valoro.

A Mariola, Paula, Alberto, Marta, y Vicky, gracias por hacer siempre de la casa un hogar. Gracias por ser tan divertidos, organizados, respetuosos, comprensivos, tan buenos compañeros y mejores amigos. Nunca olvidaré el tiempo compartido con vosotros. A Mariola, por ser tan divertida y cuidar de todos nosotros, por darle tanta alegría a la casa, y por sacarle tanto provecho a la terraza! A Paula, por ser como eres, tan increíble, divertida, positiva, lista y resolutiva. Si alguna vez vuelvo a ir contigo al trabajo, bien temprano y con prisas, no me olvidaré de ponerle una tapa al café! A Alberto, porque le diste una chispa al piso muy especial, por tu felicidad y sentido del humor. A Marta, por todos los momentos compartidos, y por la manera tan simpática en que nos conocimos. Gracias por tu sonrisa y tu disponibilidad incondicional. Gracias, Vicky, por estar ahí en los primeros momentos de esta tesis, y por compartir tu día a día conmigo durante una etapa que recordaré siempre con mucha alegría.

A Ferran y César, con quienes también compartí piso, y sobre todo felicidad. Gràcies, Ferran, per la teva companyia, per tots els bons moments, per les rialles i els debats que hem compartit. La teva presència donava vida a la casa. Gràcies per la teva simpatia i alegria ... i pels bolets de Berga! Gracias, César, por tu gran personalidad, por tu carácter feliz y divertido que se contagia, por hacerme reír tanto y tantas veces... y por tus teriyaki con nata!

A Carol R., Carol M., Lara, Odette, Zaira y Paloma, por estar siempre ahí. Lara, eres la persona más eficiente que conozco, y nunca olvidaré todo el apoyo y ayuda que me has dado en esta última etapa. Gracias!

A toda la familia Savirón: Luis, Carmen, Javier, Nando, Pedro y Ana (especialmente a ti, Ana, por tantas y tantas cosas vividas, y que empezaron ya mucho tiempo atrás por los pasillos de la UAM...). No sabéis lo mucho que agradezco el apoyo y la ayuda que me habéis dado en todo momento. Vuestra casa siempre ha sido un hogar para mí, en todos los sentidos... Sois mi segunda familia. Gracias!

A mis hermanos, Pablo, Willie y Ana. Gracias por estar siempre ahí. Gracias por vuestra compañía, comprensión e inteligencia. He aprendido tanto de cada uno de vosotros... Gracias por vuestro sentido del humor, y por los momentos tan divertidos que me hacéis vivir. Gracias, Willie, por dejar que hiciera de tu sofá mi mesa de trabajo... Os quiero con locura.

Tess, thanks for all the support I've always received from you, and also for all the laughs and good times we have spent together. I'm back on the field now! :)

A tí, Víctor, por el amor que me das cada día. Por tu personalidad calmada y tranquila, que tanto necesito. Por la comprensión y apoyo que siempre me has dado. Por cuidarme, mimarme y consentirme. Por tu inteligencia e inestimable ayuda durante esta tesis. No puedo expresar en estas líneas todo lo que me gustaría decirte... Gracias por hacerme feliz.

A mis padres. Son tantas cosas las que os debo que necesitaría un capítulo entero sólo para vosotros. Desde lo más profundo de mi corazón os agradezco todas las oportunidades que siempre me habéis dado. Gracias por vuestro amor, vuestro apoyo, y vuestro ejemplo. Papá, gracias por la diversión, compañía, y seriedad que me has brindado durante tanto tiempo. Por tu gran visión científica y pragmática de las cosas. Por lo mucho que me has ayudado no sólo en esta tesis sino durante toda mi vida. Te quiero. Gracias, mamá, por ser la mejor madre que haya podido tener. Por tu sabiduría, tu saber estar, tu amor incondicional, y el cariño que me ofreces y trasmites cada día. Por ser tan buena médico y mejor madre. Porque te lo mereces todo, porque me enorgullece ser tu hija, y porque te quiero.

Summary

Toll-like receptors (TLRs) mediate evolutionary conserved immune responses against invading microorganisms by recognizing specific pathogen-associated molecules. Major inflammatory pathways elicited upon engagement of TLRs and interleukin-1 receptor (IL-1R) proceed through the bipartite adaptor, MyD88. The adaptor is comprised of an N-terminal death domain (DD, residues Thr¹⁷ to Gln¹²⁰ in the human protein) and a C-terminal Toll-IL-1R (TIR) domain (Glu¹⁵⁹ to Pro²⁹⁶), connected by a long, unstructured linker. TLR•MyD88 and IL-1R•MyD88 complexes bind protein kinases IRAK-1 and 4 to trigger a phosphorylation cascade that eventually culminates with NF- κ B activation and downstream transcription of pro- and anti-inflammatory genes. This inflammatory response, in turn, is down-regulated by the catalytically disabled member of the family, IRAK-M, although the mechanisms underlying this process are currently unknown. In addition, although it is known that formation of MyD88•IRAK complexes depends upon homotypic interactions of their death domains, the architecture of these complexes also remains in dispute. A truncated splice variant of the adaptor, MyD88s, which lacks residues Glu¹¹⁰ to Leu¹⁵⁴, cannot recruit IRAK-4 and fails to elicit inflammatory responses.

In the present work, with the aim of elucidating the interactions between MyD88 and IRAK proteins in the TLR/IL-1R signaling pathway, we have cloned, overexpressed, purified and characterized recombinant proteins comprising the death domains of MyD88, IRAK-1, IRAK-M and IRAK-4, both alone and extended by the linker to C-terminal TIR or kinase domains, respectively. Using these recombinant fragments, we have shown that the DDs of MyD88 and IRAK proteins form large aggregates in solution. In addition, we have demonstrated that the death domain of the adaptor is able to interact with similar domains from IRAK-M and IRAK-4. Of particular note, both forms of recombinant MyD88 are able to bind to the linker-extended variant of IRAK-4 death domain and pull down native, full-length IRAK-4 from monocyte extracts. Specifically, we show that residues Glu¹¹⁰-Gln¹²⁰ including the C-terminal helix α 7 of MyD88, but not the irregular DD-TIR linker, are required for IRAK-4 recruitment, while residues up to Lys¹¹⁵ in the DD-kinase linker of IRAK-4, and not beyond, are needed for strong interactions with the adaptor. Further, we demonstrate that residues beyond Glu¹⁴³ in the MyD88 DD-TIR linker, at least, are dispensable for IRAK-M binding to MyD88. Altogether, the current findings can be integrated in a model for sequential assembly of membrane-proximal MyD88 complexes, as we propose, and provide a straightforward explanation for the negative regulation of innate immune responses mediated by MyD88s.

Resumen

Los receptores tipo Toll (TLR) median las respuestas inmunes evolutivamente conservadas contra microorganismos invasores, reconociendo moléculas específicas asociadas a patógenos. Los mecanismos inflamatorios más importantes que se activan tras la unión de los TLR y el receptor de interleukina-1 (IL-1R) proceden a través del adaptador bipartito, MyD88. Este adaptador se compone de un dominio globular DD, (residuos N-terminales Thr¹⁷-Gln¹²⁰ en la proteína humana), y un dominio C-terminal Toll-IL-1R (TIR) (Glu¹⁵⁹-Pro²⁹⁶), unidos entre sí por un conector largo y carente de estructura secundaria. Los complejos TLR•MyD88 e IL-1R•MyD88 se unen a las proteínas quinasas IRAK-1 y 4 para desencadenar una cascada de fosforilación que culmina eventualmente con la activación de NF-κB y la transcripción de genes pro- y anti-inflamatorios. Esta respuesta inflamatoria, a su vez, está regulada negativamente por el miembro catalíticamente inactivo de la familia, IRAK-M, aunque los mecanismos que subyacen a este proceso se desconocen actualmente. Asimismo, aunque es sabido que la formación de los complejos MyD88•IRAK se basa en las interacciones homotípicas entre sus dominios DD, la arquitectura de estos complejos también permanece en disputa. Una variante truncada del adaptador, MyD88s, carente de los residuos Glu¹¹⁰-Leu¹⁵⁴, no puede reclutar IRAK-4 y es incapaz de producir respuestas inflamatorias.

En el presente trabajo, con el objetivo de elucidar las interacciones entre MyD88 y las proteínas IRAK en la ruta de señalización de TLR/IL-1R, hemos clonado, sobreexpresado, purificado y caracterizado proteínas recombinantes que comprenden los dominios DD de MyD88, IRAK-1, IRAK-M e IRAK-4, tanto solos como extendidos por el conector entre los dominios DD y los dominios C-terminales TIR o quinasa, respectivamente. Utilizando estos fragmentos recombinantes, hemos demostrado que los dominios DD de las proteínas MyD88 e IRAK forman grandes agregados en disolución. Además, hemos demostrado que el dominio DD del adaptador es capaz de interactuar con dominios similares de IRAK-M e IRAK-4. De especial relevancia es que ambas formas recombinantes del DD de MyD88 son capaces de unirse a la variante de IRAK-4 extendida por el conector, y reclutar proteína IRAK-4 nativa y completa, procedente de extractos de monocitos. Específicamente, hemos demostrado que los residuos Glu¹¹⁰-Gln¹²⁰, que incluyen la hélice C-terminal α7 pero no el conector irregular DD-TIR, son necesarios para el reclutamiento de IRAK-4, mientras que los residuos hasta Lys¹¹⁵ en el conector DD-TIR de IRAK-4, y no más allá, son necesarios para establecer interacciones fuertes con el adaptador. Además, hemos demostrado que los residuos del conector DD-TIR de MyD88, como mínimo a partir de Glu¹⁴³, son prescindibles para la unión del adaptador con IRAK-M. En conjunto, los resultados aquí presentados pueden integrarse en un modelo de ensamblaje secuencial de complejos de MyD88 próximos a la membrana, como proponemos, y proporcionan una explicación directa a la regulación negativa de la respuesta inmune innata mediada por MyD88s.

Table of Contents

List of Figures	21
List of Tables	25
Abbreviations	27
1. Introduction	29
1.1 The Innate Immune System	31
1.1.1 Overview of the Innate Immune System	31
1.1.2 Cell Surface Receptors of the Innate Immune System	31
1.2 Toll-Like Receptors	32
1.2.1 General Aspects of TLRs	32
1.2.2 TLR Classification	32
1.3 TLR Signaling Pathway	33
1.3.1 MyD88-Independent Signaling Pathway	33
1.3.2 MyD88-Dependent Signaling Pathway	34
1.4 The DD Superfamily	36
1.5 DD-Containing Proteins in the TLR/MyD88/IRAK System	38
1.5.1 Protein Adaptor MyD88	38
1.5.2 IL-1 Receptor Associated Kinase Family	39
1.6 Negative Regulation of the TLR/MyD88/IRAK Pathway	42
1.7 Known Three-Dimensional Structures in the Toll/TLR Signaling Pathway:	
MyD88 and IRAK-4	44
1.7.1 Structure of Individual Domains of MyD88/IRAKs	44
1.7.2 Multimeric Structures	46
1.8 Involvement of the TLR/MyD88/IRAK System in Disease	49
2. Objectives	51

3. Materials and Methods	55
3.1 Recombinant Protein Expression	57
3.1.1 Sequence Alignments and Secondary Structure Prediction	57
3.1.2 Cloning of Death Domains	57
3.2 Site-Directed Mutagenesis	58
3.2.1 Primer Design	58
3.2.2 PCR Conditions	60
3.2.3 DNA Extraction and Sequencing	61
3.3 Heterologous Expression of MyD88, IRAK-1, IRAK-4 and IRAK-M Variants	62
3.3.1 <i>Escherichia coli</i> Strains	62
3.3.2 Transformation of Competent Cells	62
3.3.3 Preparation of Starter Cultures	63
3.3.4 Preparation of Glycerol Stocks	63
3.3.5 Preparation of Larger Cultures	63
3.4 Extraction and Renaturation of Recombinant Fragments	64
3.4.1 Extraction of MyD88 and IRAK Recombinant Fragments	64
3.4.2 Renaturation of Recombinant Proteins	64
3.5 Purification of Recombinant Fragments of MyD88 and IRAK Proteins	65
3.5.1 Purification of MyD88 and its Complexes by Affinity Chromatography	65
3.5.2 Ion-Exchange Chromatography of IRAK Proteins	67
3.5.3 Size-Exclusion Chromatography	67
3.6 Ultrafiltration of Protein Solutions and Determination of Protein Concentration	68
3.6.1 Determination of Protein Concentration from the Absorbance at 280 nm	68
3.6.2 Ultrafiltration of Protein Solutions	69
3.7 Protein Detection	71
3.7.1 Protein Separation by SDS-PAGE	71
3.7.2 Protein Gel Staining	72
3.7.3 Protein Immunodetection by Western Blot	73
3.8 Monocyte Isolation and Culture	75

3.9 Heterocomplex Formation of MyD88 and IRAK Proteins in Solution	76
3.9.1 Binding Assays Performed with Soluble MyD88/IRAK-4 Recombinant Fragments	76
3.9.2 Demonstration of Recombinant MyD88 Interaction with Natural Full-Lenght IRAK-4 Kinase	77
3.9.3 Detergent Screening to Enhance MyD88(L)-IRAK-4(L) Complex Formation	77
3.9.4 Co-renaturation of MyD88 and IRAK Recombinant Domains	77
3.10 Protein Characterization	78
3.10.1 Dynamic Light Scattering	78
3.10.2 Limited Proteolysis	78
3.10.3 Surface Plasmon Resonance Studies	80
3.10.4 Analytical Ultracentrifugation	81
3.11 Crystallization of MyD88 DD Recombinant Fragments and Their Complexes with IRAK-4(L)	82
3.11.1 Protein and Complex Preparation for Crystallization	82
3.11.2 Finding Optimal Crystallization Conditions for Crystal Growth	82
3.11.3 Crystal-quality Optimization Methods	83
3.11.4 Crystal Harvesting and Cryopreservation	86
3.11.5 X-Ray Diffraction Data Collection	86
3.11.6 Diffraction Data Processing: Integration and Data Reduction	88
3.11.7 Crystal Structure Determination	89
3.12 Three-Dimensional Modeling of MyD88 and IRAK-4 Death Domains	90
2. Results	91
4.1 Preliminary Studies on MyD88 and IRAK Recombinant Proteins	93
4.1.1 Sequence Comparisons Indicate the Presence of a Seventh C- Terminal Helix in the Death Domain of MyD88, in Addition to the Conserved Six-Helix Bundle	93
4.1.2 Expression and Characterization of MyD88 and IRAK Death Domains	94

4.1.3 Purified Death Domains of MyD88 and IRAK-4 Form Large Aggregates in the Absence of Detergents	97
4.2 Interactions Between MyD88 and IRAK-4 Recombinant Variants	99
4.2.1 The Isolated Death Domains of MyD88 and IRAK-4 Form a Stable Complex in Solution	99
4.2.2 The Death-Domains of MyD88 and IRAK-4 Can Be Co-renatured to Form a Stoichiometric Complex	101
4.2.3 The Unstructured Death Domain-TIR Linker of MyD88 Is Not Required for IRAK-4 Recruitment	103
4.2.3.1 The Isolated Death-Domain of MyD88 Interacts with Native IRAK-4	104
4.2.3.2 SPR Analysis of DD-Mediated MyD88–IRAK-4 Interactions	105
4.2.4 Residues up to Ser ¹¹⁴ in IRAK-4 DD-Kinase Linker Are Required for MyD88 Binding	106
4.2.5 MyD88•IRAK-4 Complexes Form Large Aggregates in Solution	108
4.2.6 Recombinant Death Domain-Only Variants of MyD88 Can Be Crystallized	112
4.3 Interactions Between MyD88 and IRAK-M Recombinant Variants	115
4.3.1 The Linker-Extended Versions of MyD88 and IRAK-M Form a Stable Complex in Solution	115
4.3.2 Residues Beyond Glu143 in the DD-TIR Linker of MyD88 Are Not Required for IRAK-M Recruitment	117
5. Discussion	119
5.1 Overexpression and Characterization of Death Domains of MyD88 and IRAK Proteins	121
5.2 Death Domain Interactions Between MyD88 and IRAK Proteins	126
5.3 A Proposed Mechanism for MyD88•IRAK-4 Complex Assembly	129

6. Conclusions	135
6.1 Conclusions	137
6.2 Conclusiones	139
7. Appendices	141
Appendix I: Structure and Classification of Amino Acids	143
Appendix II: Structure-Based Sequence Alignment of Death Domains from MyD88 and IRAK-4	145
Appendix III: Putative protein-protein interaction sites in MyD88 death domain	147
Appendix IV: Putative protein-protein interaction sites in IRAK-4 death domain	149
Appendix V: pET-3a Restriction Map	151
Appendix VI: DNA Sequences of MyD88 and IRAK Recombinant Fragments	153
Appendix VII: Buffers and Solutions	155
Appendix VIII: FoldIt Screen	161
Appendix IX: Detergent Screen 1 Formulation	163
Appendix X: Crystallization Conditions	165
Appendix XI: Supplemental Figures	173
Appendix XII: Articles Published During the PhD Period	177
8. References	179

List of Figures

Figure 1.1 Schematic representation of TLR/MyD88-dependent signaling pathways	35
Figure 1.2 Ribbon diagrams of selected modules of each subfamily within the DD superfamily	37
Figure 1.3 Schematic representation of human MyD88 structural organization	38
Figure 1.4 Domains of the human receptor-associated kinases (IRAKs)	40
Figure 1.5 Negative regulation of TLR signaling	44
Figure 1.6 NMR solution structure of human MyD88 TIR domain	45
Figure 1.7 Schematic representation of IRAK-4 DD	46
Figure 1.8 Conservation and divergence of TLR-mediated innate immune response in insects and mammals	47
Figure 1.9 Three-dimensional crystal structure of <i>Drosophila</i> Tube DD•Pelle DD complex	48
Figure 1.20 Structure of the ternary Myddosome complex	49
Figure 3.1 Generated mutations over the MyD88(L) and IRAK-4(L) nucleotide sequences	59
Figure 3.2 Schematic representation of the interaction between neighboring residues in the 6xHis tag and the Ni-NTA matrix	66
Figure 3.3 Ultrafiltration devices used for protein concentration and dialysis	70
Figure 3.4 Schematic representation of the “sandwich” assembly for transferring proteins to a synthetic membrane	74
Figure 3.5 Ni ²⁺ -NTA interaction with polyhistidine-tagged ligands	80
Figure 3.6 Hanging- and sitting-drop vapor diffusion crystallization methods	83
Figure 3.7 Schematic illustration of a protein solubility phase diagram	84
Figure 3.8 Micro-seeding technique for growing protein crystals	85
Figure 3.9 Typical X-ray diffraction unit	87
Figure 4.1 Schematic representation of domain organization in human MyD88 and IRAK proteins	93
Figure 4.2 Overexpression of human death domains from MyD88 and IRAK proteins	95

Figure 4.3 Preferential cleavage of interdomain linkers in recombinant proteins suggests correct folding of MyD88 and IRAK variants	96
Figure 4.4 Human MyD88 and IRAK-4 death domains have a strong tendency to form aggregates	97
Figure 4.5 DLS analysis of purified recombinant proteins	98
Figure 4.6 Gel filtration analysis of recombinant MyD88(L) samples	99
Figure 4.7 Formation of MyD88(L)•IRAK-4(L) heterodimer in solution	100
Figure 4.8 Several non-ionic detergents support formation of stoichiometric MyD88(L)•IRAK-4(L) complex	101
Figure 4.9 MyD88(L) and IRAK-4(L) co-renaturation trial by rapid dilution in refolding solutions	102
Figure 4.10 The isolated death domains of MyD88(L) and IRAK-4(L) form a stable complex in solution	102
Figure 4.11 The death domain-TIR linker of MyD88 is not required for kinase recruitment, but the DD-kinase linker of IRAK-4 is important for heterodimer formation	103
Figure 4.12 The death domain of MyD88 pulls down natural IRAK-4 from monocyte extracts	104
Figure 4.13 Surface plasmon resonance studies of MyD88(S)–IRAK-4(L) interactions	105
Figure 4.14 Residues up to Glu ¹¹⁶ in IRAK-4 linker are protected from proteolytic attack in the complex with MyD88	107
Figure 4.15 Similar kinetics of chymotrypsin cleavage of free and complexed IRAK-4(L)	107
Figure 4.16 Residues beyond Ser ¹¹⁴ in IRAK-4 linker do not contribute to complex formation with MyD88	108
Figure 4.17 AUC analysis of MyD88 and IRAK-4 recombinant fragments and their complexes	109
Figure 4.18 FPLC analysis on MyD88(L)•IRAK-4(L) and MyD88 E143X•IRAK-4(L) complexes	111
Figure 4.19 Orthogonal images of diffraction patterns obtained from MyD88 E143X crystals	113

Figure 4.20 Formation of MyD88(L)•IRAK-M(L) heterodimer in solution	115
Figure 4.21 MyD88 and IRAK-M(L) co-renaturation trials by rapid dilution in refolding solutions	116
Figure 4.22 The linker-extended variants of MyD88 and IRAK-M form a stable complex	116
Figure 4.23 Residues beyond Glu ¹⁴³ in the DD-TIR linker of MyD88 are not required for IRAK-M recruitment	117
Figure 5.1 Overexpressed MyD88 is localized in the cytoplasm as large condensed forms	123
Figure 5.2 Aggregation is a common feature of members of the DD superfamily	125
Figure 5.3 Partial sequence comparison between human IRAK-4 and IRAK-M	127
Figure 5.4 Hypothetical model of death domain-mediated heterocomplex formation between MyD88 and IRAK-4	131
Figure 5.5 Different arrangements of death domain heterodimers	133
Supplemental Figure 1 Overexpression of MyD88 E143X and IRAK-4 K115X truncated variants	173
Supplemental Figure 2 Gel filtration analysis of MyD88 E143X variant	173
Supplemental Figure 3 Electrophoretic analysis of MyD88(L)•IRAK-4(L) and MyD88(L)•IRAK-4 K115X complexes under native conditions	174
Supplemental Figure 4 Formation of MyD88 E143X•IRAK-4(L) complex in solution	174
Supplemental Figure 5 Orthogonal images of diffraction patterns obtained for MyD88(L) and MyD88 E143X crystals	175

List of Tables

Table 1.1 Some of the proposed ligands for the different TLRs identified	33
Table 3.1 Designed MyD88 and IRAK-4 primer sequences for site-directed mutagenesis	60
Table 3.2 Main characteristics of the ESRF beamlines used for X-ray diffraction analysis of protein crystals	87
Table 4.1 Summary of expression, renaturation and purification conditions for MyD88 and IRAK recombinant fragments generated in the current investigation	94
Table 4.2 Major physicochemical parameters of recombinant proteins generated for the current study	95
Table 4.3 Summary of experimental set-up and solutions used for SPR analysis of MyD88(S)–IRAK-4(L) interactions	106
Table 4.4 Main characteristics of samples and buffers used for AUC analysis	110
Table 4.5 Summary of crystallization conditions used on MyD88 recombinant fragments	112
Table 4.6 Summary of used and calculated parameters during data collection of MyD88 E143X crystals	114

Abbreviations

- Akt (also known as PKB):** Protein kinase B
- AP-1:** Activating protein-1
- Apaf-1:** Apoptotic protease activating factor-1
- APC:** Antigen presenting cell
- CARD:** Caspase recruitment domain
- CD:** Cluster of differentiation
- DD:** Death domain
- DED:** Death effector domain
- DISC:** Death-inducing signaling complex
- ERK:** Extracellular signal-regulated kinase
- FADD:** Fas-associated protein with death domain
- HSP:** Heat shock protein
- IB:** Inclusion body
- IKK:** Inhibitor of NF- κ B kinase
- IL-1R:** Interleukin-1 receptor
- IPTG:** Isopropyl β -D-1-thiogalactopyranoside
- IRAK:** Interleukin-1 receptor-associated kinase
- IRF:** Interferon regulatory factor
- LB medium:** Luria Bertani medium
- LBP:** Lipopolysaccharide binding protein
- LRR:** Leucine-rich-repeat
- Mal:** MyD88-adaptor-like
- MyD88:** Myeloid differentiation factor 88
- NF- κ B:** Nuclear factor kappa B
- NK:** Natural killer
- NTA:** Nitrilotriacetic acid
- PAMPs:** Pathogen-associated molecular patterns
- PI3K:** Phosphatidylinositol 3- kinase
- PIDD:** p53-induced protein with a death domain
- PYD:** Pyrin domain
- RAIDD:** RIP-associated ICH-1/CED-3 homologous protein with a death domain

SIGIRR: Single immunoglobulin IL-1R-related protein

SOB medium: Super optimal broth medium

SOC medium: SOB medium with catabolite repression

SOCS: Suppressor of cytokine signaling

TIR: Toll-IL-1R

TLR: Toll-like receptors

TNF- α : Tumor necrosis factor α

TOLLIP: Toll interacting protein

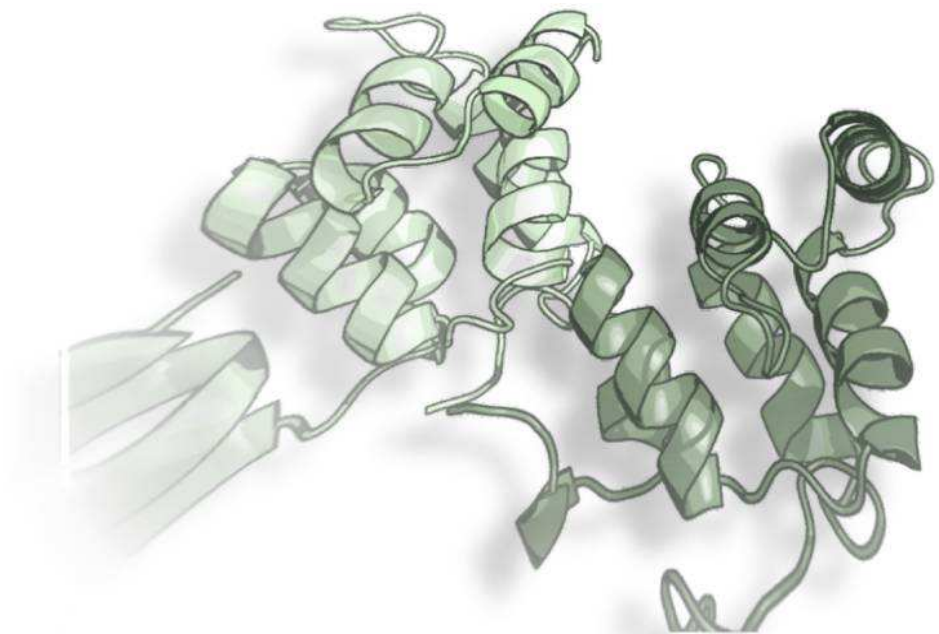
TRAF6: TNF receptor-associated factor 6

TRAM: TRIF-related adaptor molecule

TRIF: TIR domain-containing adapter inducing IFN- β

β -OG: n-octyl- β -D-glucopyranoside

1. Introduction



1.1 The Innate Immune System

1.1.1 Overview of the Innate Immune System

Although we are constantly in contact with potentially pathogenic microorganisms, we rarely become ill. This is because the microorganisms that penetrate the epithelial surface of the body are initially recognized and attacked by defense mechanisms that do not require a prolonged period of exposure, as they do not depend on the clonal expansion of lymphocytes in response to certain antigens. These defense mechanisms act immediately after infection and are part of the innate immune response. Moreover, the innate immune system plays a critical role in controlling infections during this first period, because there is a delay of four to seven days before the initial adaptive immune response takes place [1]. Until recently, it was thought that the innate immune system was not specific [2]. The specificity of the innate immune system was shown, however, with the initial description in *Drosophila melanogaster* of the *Toll* gene product, involved in both antifungal defense and dorsoventral development in insects [3-8]. The innate immune system is activated not only in the presence of microorganisms but also as a result of external damage such as burns, contusions, bone fractures and wounds [9], as well as internal changes that accompany tumor formation [10]. This defense mechanism is present in all multicellular organisms and is phylogenetically conserved [11].

The main cells involved in the innate immune response are those of the myeloid lineage, among them Antigen Presenting Cells (APCs) such as monocytes (macrophages precursors), dendritic cells and neutrophils; although the latter lack antigen presenting ability, they possess phagocytic activity. Natural killer (NK) cells, of lymphoid origin, appear also to be involved in innate immune defense against intracellular pathogens. Macrophages and neutrophils, besides being the first line of defense against many common microorganisms, are crucial in initiation and subsequent direction of the adaptive immune system, and also in removing pathogens captured by this type of response [1].

To initiate an inflammatory immune response, macrophages and neutrophils count on cell surface receptors able to recognize and bind to common elements of many different pathogens. These receptors are crucial for antigen recognition and, therefore, are essential at the initial stages of the immune response.

1.1.2 Cell Surface Receptors of the Innate Immune System

A number of cell surface receptors can specifically recognize molecular structures collectively referred to as pathogen-associated molecular patterns (PAMPs) [1]. Among these receptors, it is worth mentioning the macrophage mannose receptor, exclusive to these cells; the

scavenger receptors, which bind to many charged ligands; CD14 and LBP (lipopolysaccharide-binding protein), which are found mainly in monocytes and macrophages [1]; and the Toll-like receptors (TLRs), expressed in monocytes, dendritic cells, and other mucosal and endothelial cells. TLRs have been identified in plants and mammals as proteins homologous to the *Drosophila* Toll protein [8], and major inflammatory responses that take place after infection evolve through these receptors [12].

1.2 Toll-Like Receptors

1.2.1 General Aspects of TLRs

Toll-like receptors are transmembrane proteins of the Interleukin-1 (IL-1) Receptor (IL-1R) family. This family of receptors belongs, in turn, to a superfamily that includes receptors of the proinflammatory cytokines IL-1 and IL-18, and their co-receptors [3-8]. TLRs have an N-terminal, ligand-binding, extracellular domain with several LRR (Leucine-Rich-Repeat) motifs, a transmembrane domain, and a well-conserved intracellular, C-terminal domain through which they interact with signal transduction proteins. This TLR cytoplasmic domain is homologous to the cytoplasmic domains of e.g. human IL-1R and *Drosophila* Toll, and it is thus termed TIR (Toll-IL-1 Receptor) domain [5, 11, 13-15].

1.2.2 TLR Classification

In humans, at least ten TLRs of known function are present, all of them with the ability to recognize specific ligands and activate an inflammatory immune response [16]. These receptors are expressed in a wide range of cell types, including macrophages, dendritic cells, B-cells, some T-cell types, and even in non-immune cells such as fibroblasts and epithelial cells [11, 14]. These receptors, either as monomers or as homo/heterodimers, are specialized in the recognition of different PAMPs [17]. TLRs can be both intra and extracellularly expressed, depending on the ligands they recognize. In this manner, TLRs responsible for detection of bacterial products and endogenous ligands (TLRs 1, 2, 4, 5 and 6) are expressed on the cell surface, while those able to detect viral components (TLRs 3, 7, 8 and 9) are located at the endosome membranes (Table 1.1) [14, 18]. Noteworthy, some TLRs can recognize ligands that are neither structurally nor functionally related with each other. TLR4, for example, recognizes a number of exogenous ligands such as bacterial lipopolysaccharides (LPS) and respiratory syncytial virus fusion protein, but also self-proteins such as fibronectin and heat shock proteins [14] (Table 1.1).

Table 1.1 Some of the proposed ligands for the different TLRs identified. The ligand for TLR10 remains unknown up to date. ND, Not determined. HSP, Heat Shock Protein.

TLR	Bacterial Ligand	Endogenous Ligands
TLR1/2	Triacylated lipoproteins [19]	ND
TLR2	Lipoteichoic acid [20], Peptidoglycan [21]	HSP-60 [22], -70 [23-25], -90 [26]
TLR2/6	Diacylated lipoproteins [19], Zymosan [27, 28]	ND
TLR4	Lipopolysaccharide [15, 29-34]	Fibronectin [35], HSP-22 [36], HSP-60 [22, 37, 38], HSP-70 [23-25], HSP-90 [26]
TLR5	Flagellin [39]	ND
TLR9	CpG motifs [40, 41]	DNA [42, 43]
TLR	Viral Ligands	Endogenous Ligands
TLR2	Hemagglutinin [44]	ND
TLR4	F-protein (respiratory syncytial virus) [45]	ND
TLR3	dsRNA [46]	mRNA [47]
TLR7/8	ssRNA [48-50]	ssRNA [51, 52]
TLR9	CpG motifs [53-56]	DNA [57, 58]

TLR activation can lead, through transcription Nuclear Factor kappa B (NF- κ B) to production of inflammatory cytokines or even of costimulatory molecules, which activate the adaptive immune system [59, 60]. The mechanisms through which these molecules are produced downstream of TLR ligand recognition are known as the TLR signaling pathway, which is briefly explained below.

1.3 TLR Signaling Pathway

Engagement of TLRs allows activation of different signaling cascades, which are crucial for the innate immune response to work properly [59]. Activation of almost all TLRs, with the exception of TLR3 [61], stimulates an intracellular signaling pathway that involves the initial recruitment of the adaptor protein Myeloid Differentiation Factor 88 (MyD88). There are also alternative, MyD88-independent pathways, but these are specific for TLR3 and TLR4 receptors [62, 63]. Both MyD88-dependent and independent signaling pathways culminate with the induction of proinflammatory cytokines and interferons [64].

1.3.1 MyD88-Independent Signaling Pathway

The MyD88-independent signaling pathway, specific for TLR3 and TLR4, relies on protein adaptors other than MyD88, such as TRIF (TIR domain-containing adapter inducing IFN- β) and TRAM (TRIF-related adaptor molecule), as well as the interferon regulatory factors (IRF) 3 and 7, which induce type I IFN expression and costimulatory molecules [55, 65]. This signaling

pathway is involved in the late phase of NF- κ B and mitogen-activated protein kinase (MAPK) activation [66, 67], as well as in the transcription of target genes such as type I interferons [68, 69], which are critical for proper anti-viral and anti-bacterial responses [70, 71].

1.3.2 MyD88-Dependent Signaling Pathway

The MyD88-dependent signaling pathway is characterized by the recruitment of the bipartite adaptor MyD88, upon TLR interaction with its corresponding ligand and subsequent receptor multimerization [72-74]. This adaptor features a C-terminal TIR domain that interacts with the membrane proximal TIR domain of the TLR, and an N-terminal death domain (DD), responsible for the recruitment of Interleukin (IL)-1 receptor-associated kinases (IRAK) 1 and 4, via homotypic DD interactions [75]. High protein concentrations due to the formation of MyD88•IRAK-4•IRAK-1 multimers trigger a complex cascade of phosphorylation reactions, conceptually similar to the induced proximity mechanism of caspase activation (reviewed in [76, 77]). As a result of this cascade, hyperphosphorylation of IRAK-1 occurs at several positions of the DD-Kinase linker [78]. MyD88 plays a crucial role in this pathway, because it mediates a close interaction of the two related IRAK molecules, which is essential to allow IRAK-4 to phosphorylate IRAK-1 [79]. This probably triggers IRAK-1's own kinase activity, resulting in multiple autophosphorylation events [80]. Conformational changes induced thereupon eventually allow IRAK-1 to bind to the signal transducer TRAF6 (*Tumor Necrosis Factor* (TNF) Receptor-Associated Factor 6) [62, 81], and to dissociate from its membrane-proximal complex with MyD88 [82]. The IRAK-1/TRAF6 complex can then activate downstream targets [82, 83], through three different signaling pathways that regulate the balance between cellular viability and inflammation [14, 84]. These pathways are the IKK (inhibitor of NF- κ B kinase) pathway, the MAPK pathway, and the PI3K (Phosphatidylinositol 3- Kinase)/Akt (also known as Protein Kinase B) pathway [85, 86]. These signaling pathways culminate in the nuclear localization of NF- κ B/AP-1 (Activating Protein-1) and the transcription of several genes that regulate pro- and anti-inflammatory responses [81, 87] (Figure 1.1). It is important to emphasize that IRAK-1 is not only phosphorylated but also degraded upon IL-1 stimulation [88, 89]. IRAK-1 degradation leads to a shutdown of the IL-1 response, initiating a negative feedback loop in this signaling pathway [88, 90].

a) IKK signaling pathway

IKK proteins initiate a kinase activation cascade in which two kinases, IKK- α e IKK- β , which form the IKK dimer, are activated and phosphorylate an inhibitory protein known as inhibitor of NF- κ B (I κ B)- α . Under normal conditions, I κ B- α binds to NF- κ B to form a cytosolic complex that inhibits NF- κ B nuclear translocation. Phosphorylation of I κ B- α causes its

degradation, upon which NF- κ B is released and translocated to the nucleus of the cell, where it activates transcription of several genes responsible for the expression of proinflammatory cytokines such as TNF- α , IL-1 β , IL-6, and IL-12 [14, 84] (Figure 1.1).

b) MAPK signaling pathway

The MAPK pathway is initiated with the activation of MAPKKK (MAPK Kinase Kinase) proteins. These proteins phosphorylate MEK 1/2 (mitogen-activated or extracellular signal-regulated protein kinase kinase -MAPKK-) which, in turn, activates ERK 1/2 (extracellular signal-regulated kinase 1/2). This signaling pathway culminates with AP-1 nuclear translocation. Although the response of this pathway to LPS through the TLR4 receptor is not well characterized yet [91], it is known that AP-1 activation requires TRAF6 activation in endothelial cells [92], while it requires a serine/threonine kinase termed TLP-2 (Tumor Progression Locus-2) in macrophages [93]. TLP-2 acts as a MAPKKK ultimately inducing ERK 1/2 activation and the subsequent AP-1 nuclear translocation, thus modulating the expression of proinflammatory genes [91] (Figure 1.1).

c) PI3K signaling pathway

PI3Ks constitute a family of kinases classified in three subfamilies according to their structure and specific substrates. The most thoroughly studied of these subfamilies is the one known as class I PI3Ks, which are activated by cellular receptors and mediate phosphoinositide phosphorylation [94]. The phosphorylated lipidic products act as a second messenger that activates a wide variety of mediators including Akt, which is responsible for I κ B- α phosphorylation and subsequent NF- κ B activation (Figure 1.1).

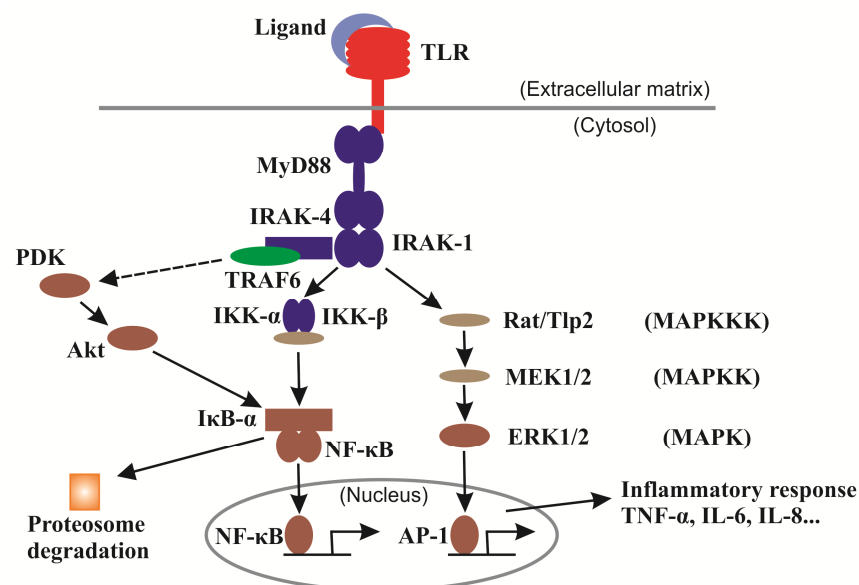


Figure 1.1 Schematic representation of TLR/MyD88-dependent signaling pathways. The illustration covers the IKK, MAPK and PI3K signaling pathways, which initiate with the recruitment of MyD88 to TLR and culminate in the nuclear localization of NF- κ B/AP-1 (see text for more details). (Based on [85]).

The axis of the MyD88-dependent signaling pathway, as it has been discussed, is the TLR/MyD88/IRAK system, common to almost all TLRs. This pathway plays a critical role in the regulation of inflammation, antiviral response and subsequent activation of the adaptive immune response, but has also been implicated in autoimmune diseases. Downstream signaling in this pathway strongly relies on protein-protein interactions through their different domains, TIRs and DDs. The latter motifs are among the most important domains involved in protein-protein interactions, and pertain to a larger superfamily of structurally related domains, termed the DD superfamily.

1.4 The DD Superfamily

The DD superfamily is one of the largest and most studied domain superfamilies [95], and comprises four subfamilies: the death effector domain (DED) [96], the caspase recruitment domain (CARD) [97, 98], the pyrin domain (PYD) [98, 99], and the death domain (DD) subfamilies [98]. All these domains share a six-helical bundle fold, as revealed by X-ray diffraction and/or NMR structural studies of at least one member of each subfamily. Representative structures of each subfamily are given in Figure 1.2: the FADD DED [100] (Fig. 1.2a), the RAIDD CARD [101] (Fig. 1.2b), the NALP1 PYD [102] (Fig. 1.2c) and the Fas DD [103] (Fig. 1.2d). Although this six-helical bundle fold is evolutionarily conserved in many multicellular organisms from insects to mammals, individual subfamilies also exhibit distinct structural and sequence characteristics. While some proteins are composed only of motifs from the same DD superfamily (e.g. FADD), most often DD superfamily domains are found within the protein combined with other adapter motifs (e.g. MyD88), or domains with catalytic activity (e.g. caspase 8, IRAK-1) [104].

Proteins that belong to the DD superfamily usually play critical roles in the assembly of molecular complexes and subsequent “proximity induced activation”. Indeed, formation of these complexes drives quite different physiological processes such as apoptosis via caspase activation [76], or innate immune responses through trans-phosphorylation of IRAK proteins. Interactions between DD superfamily members are usually homotypic, i.e. only domains within the same subfamily interact with each other [104]. The main structural features of each subfamily are described below.

a) DED subfamily

DEDs have two conserved surface features that distinguish them from other members of the DD superfamily. The first one is a conserved, hydrogen-bonded charge triad involving Arg and Asp residues in helix H6 and its preceding loop [105], and a negatively charged residue in helix H2 [106]. These hydrogen bonds are likely involved in maintaining the organization of the

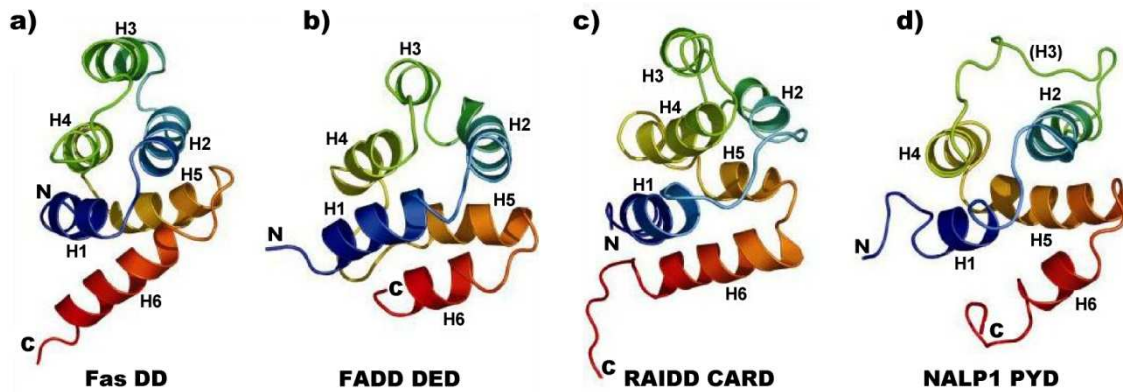


Figure 1.2 Ribbon diagrams of selected modules of each subfamily within the DD superfamily. The DED domain of FADD (a), the CARD domain of RAIDD (b), the PYD domain of NALP1 (c) and the DD domain of Fas (d) are represented in approximately the same orientation. (Modified from [104]).

side chains, which may be functionally important. It is also possible that they play a local structural role in maintaining the conformation of this DED region. The second conserved feature is a hydrophobic patch formed mostly by residues on helix H2, used extensively in DED–DED interactions [104].

b) CARD subfamily

CARD domains are unique because the helix H1 tends to be either bent or broken into two separated helices. The orientation and length of several helices may be somewhat different among the different CARDS, but one important feature is that the surfaces of CARDS are polarized with both basic and acidic surfaces, which may be used for protein-protein interactions. Unlike other DD subfamilies, it is possible that CARDS, at least those that form the prodomains of some caspases, do not possess the ability for stable self-association but are rather mostly involved in interactions with other CARDS [104].

c) PYD subfamily

PYD domains, although possessing also the classical six-helical bundle fold, are special in that they have an altered helix H3. This helix can be completely or partially replaced by a flexible, elongated loop, as in the PYD domain of NALP1 (Fig. 1.2c). Since helix H3 seems to play a critical role in protein-protein interactions in the DD superfamily [107, 108], PYD–PYD interactions could significantly differ from classical modes of interaction in the DD superfamily.

d) DD subfamily

DD domains are involved in protein-protein interactions and have a strong tendency to aggregate. This is why many so far available structures of isolated DDs were determined under non-physiological conditions such as extreme pH and/or with “disaggregating” mutations. The

NMR structures of Fas DD [103, 109] and FADD DD [109, 110], as well as the crystal structures of IRAK-4 DD [111] and RAIDD DD [112] are some examples available. While they all exhibit the six-helical bundle fold, there are some variations in the lengths and relative orientations of the helices. Moreover, because of the low sequence similarity among DDs, the surface features of these DD structures are entirely different, and this may be responsible for their specificity in protein-protein interactions [104].

The adaptor MyD88 and the kinases of the IRAK family, crucial in the downstream signaling of the TLR/MyD88/IRAK system and the main subject of the work presented here, belong to this DD subfamily.

1.5 DD-Containing Proteins in the TLR/MyD88/IRAK System

1.5.1 Protein Adaptor MyD88

MyD88 was discovered during studies addressing the differentiation of mouse myeloid cells in response to growth inhibitory stimuli [113]. Although the role of MyD88 as a signal transducer was first shown in the pathways triggered by the engagement of IL-1R [74, 114] and TLR4 [30], further studies showed that all TLRs, with the sole exception of TLR3, utilize this adaptor protein to initiate their signaling pathway [115].

Structurally, MyD88 possesses a C-terminal TIR domain (comprising residues from Glu¹⁵⁹ to Pro²⁹⁶ in humans) that interacts with other TIR domain-containing molecules such as TLRs, and an N-terminal death domain (residues from Thr¹⁷ to Gln¹²⁰) that binds other death domain-containing molecules, such as members of the IRAK family [11] (see also section 1.5.2). These domains are connected through a long polypeptide with no regular 3D-structure, sometimes termed “intermediate domain” (ID) (Figure 1.3a).

It is known that MyD88 is an essential adaptor for mediating the phosphorylation of IRAK-1 by IRAK-4 [79]. The functional importance of this adaptor in innate immune defenses

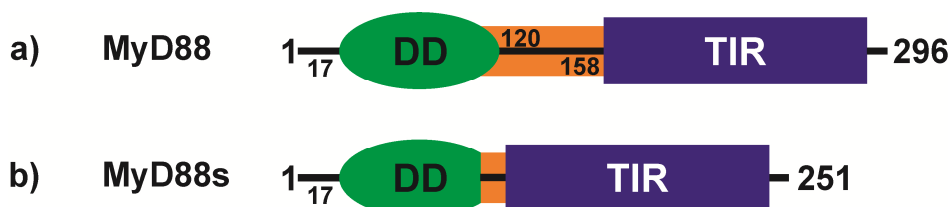


Figure 1.3 Schematic representation of human MyD88 structural organization. a) WT human MyD88 comprises a DD (residues from Thr¹⁷ to Gln¹²⁰), a long linker sometimes termed “intermediate domain”, ID (residues from Gln¹²⁰ to Glu¹⁵⁹, both excluded), and a TIR domain (residues from Glu¹⁵⁹ to Pro²⁹⁶). b) MyD88s, a splice variant of MyD88, lacks residues from Glu¹¹⁰ to Leu¹⁵⁴, both included.

was recently illustrated by rare *MyD88* point mutations identified in individuals that are highly susceptible to infection with pyogenic bacteria [116]. Although it is generally accepted that MyD88 acts by recruiting kinases IRAK-1 and 4 through interactions between their respective DDs, the specific residues involved in such interactions have been only partially characterized. Remarkably, an alternatively spliced variant of MyD88 (MyD88s), lacking residues Glu¹¹⁰ to Leu¹⁵⁴ (Figure 1.3b), failed to interact with IRAK-4, suggesting that residues located in both the DD and ID of MyD88 are crucially involved in kinase recruitment [79]. On the other hand, studies based on site-directed mutagenesis of MyD88 provided strong evidence that MyD88 DD residues 27 to 72 are required for the recruitment of IRAK-1 [117]. These data are indirectly supported by the fact that two naturally occurring mutations in the MyD88 DD (S34Y and R98C) have recently been shown to be dysfunctional in downstream signaling [118].

Most studies on the subcellular localization of MyD88 have shown that the protein is present as condensed forms in the cytoplasm, such as discrete foci, fibrillar aggregates, and inclusion bodies [119-122]. It has been also found that aggregated structures of MyD88 have irregular morphologies and do not reside in known particular organelles. Furthermore, some authors report that both DD and ID regions are required to form these structures [121]. However, because overexpressed MyD88 automatically induces death domain-dependent activation of downstream signaling pathways [30, 121, 123, 124], it is still not known whether such condensed distributions are artifacts due to the high protein concentrations achieved during overexpression.

1.5.2 IL-1 Receptor Associated Kinase Family

As explained above, TLR-bound MyD88 rapidly recruits some serine/threonine kinases of the Pelle subfamily, termed IRAKs [125-132], in close proximity to the membrane. The term IRAK originally referred to a serine/threonine-specific kinase, currently known as IRAK-1, which could be coprecipitated in an IL-1-inducible manner with the IL-1R [133, 134]. Four different mammalian IRAK proteins have been identified, with a crucial role in the signaling pathways initiated by members of the TLR/IL-1R family [74, 75, 135, 136]. These four IRAKs are termed IRAK-1 [80], IRAK-2 [74], IRAK-M (also known as IRAK-3) [137] and IRAK-4 [75, 138]. Human IRAK-1, IRAK-2 and IRAK-4 are ubiquitously expressed, whereas human IRAK-M is only detectable in monocytes and macrophages in an inducible manner [80, 139].

Structurally, IRAK family members share a similar organization (Figure 1.4). They contain an N-terminal DD followed by a long linker, a conserved kinase domain, and a C-terminal stretch that contains binding sites for TRAF6 (except for IRAK-4) [78, 140]. IRAK-1 contains three TRAF6 interaction motifs, whereas IRAK-2 is reported to have two, and IRAK-M contains only one TRAF6 interaction motif [141]. IRAK-4 lacks this C-terminal sequence and it is therefore unclear whether it could interact with TRAF6. The DD is vital for signaling since it

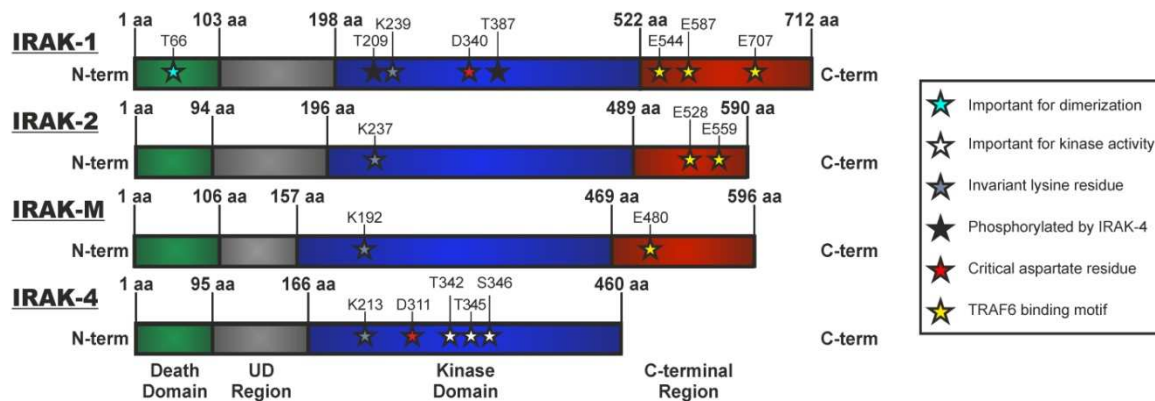


Figure 1.4 Domains of the human receptor-associated kinases (IRAKs). Each member has a death domain, a long DD-kinase linker, a conserved kinase domain, and a C-terminal region, with the exception of IRAK-4 which lacks the C-terminal region. (Modified from [142]).

interacts with MyD88 [74], further discussed in sections 1.7.2b and c. The DD-kinase linker, of lower similarity, is rich in serines, prolines and threonines. The IRAK-1 linker, which has been reported to be hyperphosphorylated [78], contains two potential PEST sequences that may facilitate its degradation. By contrast, IRAK-2, which does not display these sequences, is not degraded [143]. The kinase domain in all IRAK molecules possesses a functional ATP binding pocket with an invariant lysine residue, critical for the catalytic activity [144]. In addition, they have a tyrosine residue at the centre of the ATP binding site, called the gatekeeper residue, which controls access to a pre-existing internal hydrophobic pocket at the back of the ATP-binding site [145]. This feature is exclusive to the IRAK family of kinases [146]. Whereas IRAK-1 and IRAK-4 contain a functional catalytic site with a critical aspartate residue (D340 in human IRAK-1 and D311 in human IRAK-4, Figure 1.4), this residue is changed into an asparagine in IRAK-M, which renders this kinase inactive [137, 147]. Since this critical aspartate residue is also changed into a serine in IRAK-2, it was first believed that this kinase was also inactive [137]. However, a recent study demonstrated that IRAK-2 is enzymatically active [148].

a) IRAK-1

IRAK-1 was the first member of the IRAK family to be discovered, and shown to play a role in IL-1 signaling [80]. This kinase, a protein of 712 amino acids in length and a molecular mass of ~85 kDa, is ubiquitously expressed in humans, and has been shown to undergo phosphorylation upon TLR stimulation. Phosphorylation of IRAK-1 is essential for downstream signaling [82, 114], and some residues appear to be of critical importance in this regard (Figure 1.4). Phosphorylation of IRAK-1 takes place in a series of steps. It has been shown, *in vitro*, that IRAK-1 is initially phosphorylated at Thr²⁰⁹, a functionally critical residue as its mutation completely disrupts kinase activity. Phosphorylation of Thr²⁰⁹ results in a conformational change in the kinase domain of IRAK-1 that allows subsequent phosphorylations including Thr³⁸⁷, a critical residue that has been suggested to be a potential target for phosphorylation by IRAK-4 (Figure 1.4) [78].

b) IRAK-2

In 1997, a 65-kDa protein of 590 amino acids sharing sequence and functional similarity to IRAK-1 was discovered and named IRAK-2 (Figure 1.4). Initial reports showed that overexpressed IRAK-2 activated NF- κ B, and that IRAK-2 DD was required for this activity, since a truncated IRAK-2 variant lacking the whole DD failed to activate NF- κ B [74]. Further evidence that IRAK-2 played a role in the TLR pathway emerged when it was shown that IRAK-2 interacts with MyD88, TRAF6 and TIRAP (TIR domain-containing adaptor protein)/Mal (MyD88-adaptor-like), a critical adaptor protein acting as a linker between MyD88 and TLR2/4 [74, 149-151].

It has long been thought that IRAK-1 and IRAK-4 were the only active members of the IRAK family. However, some studies revealed the importance of IRAK-2 in TLR-induced NF- κ B activation. Ten years after its discovery, studies with vaccinia virus showed that A52, an important protein for virus virulence [152], interacts with IRAK-2 and TRAF6, but not with IRAK-1, inhibiting TLR-mediated NF- κ B signaling [153]. Recently, it has been proposed that the active-site lysine residue in the protein kinase subdomain, common to all IRAKs, is sufficient for IRAK-2 to act as an active enzyme, since an *in vitro* kinase assay showed that IRAK-2 is phosphorylated upon stimulation with a TLR2 ligand [148]. These findings thus revealed a potential crucial role for the IRAK-2 kinase activity in TLR-mediated NF- κ B activation, although its mechanism of action remains uncertain.

c) IRAK-M

IRAK-M is a protein of 596 amino acids with a molecular mass of 68 kDa (Figure 1.4), whose expression is limited to monocytes and macrophages [137]. While the other members of the IRAK family share many structural features, IRAK-M is unique, as it is the only member of this family that lacks kinase activity, working as a negative regulator of TLR signaling [136]. Initial reports on IRAK-M showed that, upon overexpression, it was able to activate NF- κ B and to restore NF- κ B activation when expressed in cells lacking IRAK-1 [137]. It was therefore assumed that IRAK-M was a positive regulator of TLR-mediated NF- κ B signaling. However, macrophages derived from IRAK-M knockout mice display enhanced activation of IL-1/TLR signaling [136, 154], thus suggesting a negative role for this family member.

Additionally, it has been shown that IRAK-M is involved in different processes, such as osteoclastogenesis control [131, 147] and monocytes/macrophages tolerance to endotoxins [126, 132] in patients with acute coronary syndrome [127]. IRAK-M has been also described as an essential element for cancer tolerance shown by tumor infiltrated monocytes/macrophages [125]. In terms of its regulation, our group showed that TNF- α plays an important role in this process [129].

d) IRAK-4

Human IRAK-4, the most recently discovered member of the IRAK family, is a 460 amino acids protein with a molecular weight of 52 kDa [138]. It is the closest human homologue of the *Drosophila* Pelle protein, a kinase involved in signaling downstream of the Toll pathway during embryonic development and also essential for insect immunity [80, 155]. The key role of IRAK-4 in TLR signaling was revealed through studies with knockout mice. Indeed, *Irak4(-/-)* animals were shown to be fully resistant to LPS-induced septic shock, and lacked a cytokine response when challenged with various TLR ligands. Furthermore, IL-1-induced NF- κ B was severely defective in cells lacking IRAK-4, and LPS-induced NF- κ B activation was delayed [75].

IRAK-4 plays a critical role in mediating NF- κ B activation through initially interacting with MyD88 [79] (see sections 1.7.2b and c). Activated IRAK-4 presumably phosphorylates IRAK-1, leading to the autophosphorylation and activation of IRAK-1 itself. It has been shown that IRAK-4 also induces degradation of IRAK-1 [156], which indicates that IRAK-4 acts in a negative feedback loop to regulate the MyD88-dependent pathway. It is also noteworthy that, to date, IRAK-4 is one of the few IL-1/TLR signaling proteins to be implicated in human disease, as a group of patients with recurrent infections and a poor inflammatory response were found to have an inherited *IRAK4* deficiency [157-160].

1.6 Negative Regulation of the TLR/MyD88/IRAK Pathway

As discussed above, stimulation of TLRs by microbial components results in the upregulation of specific proinflammatory cytokines and chemokines, which ultimately leads to pathogen control and clearance. However, when these molecules are produced in excess they induce serious systemic disorders leading to severe complications and even death. Bacterial sepsis, autoimmune disorders, and chronic inflammatory diseases are examples of hyperimmune conditions arising from excessive, dysregulated activity of the innate and adaptive immune systems [161]. It is therefore not surprising that mechanisms have evolved for modulating TLR-mediated responses. Some well-characterized negative regulators of TLR signaling are briefly described below (Figure 1.5).

a) IRAK-M

As discussed above, IRAK-M is expressed only in monocytes and macrophages, and is upregulated upon stimulation with TLR agonists [137]. A direct relationship between IRAK-M protein levels and induction of a tolerance state to cancer cells in human tumor-infiltrating monocytes has been established [125]. Although the inhibitory mechanism of IRAK-M is unclear, it appears to block formation of the IRAK-1/TRAF6 complex, but not recruitment of IRAK-1 to MyD88 [136]. Therefore, IRAK-M can inhibit dissociation of IRAK-1 and IRAK-4 from TLRs

by either blocking their phosphorylation or by stabilizing the TLR/MyD88/IRAK-4 complex, so TRAF6 is excluded and signaling to NF- κ B and/or MAPKs cannot proceed. However, a novel role for IRAK-M as a specific negative regulator of TLR2-induced p38 activation has recently been shown [162]. Regardless of the mechanism of action, IRAK-M mediated inhibition is stronger in human monocytes previously exposed to TLR ligands or tumor cells [125, 132].

b) SOCS-1

SOCS-1 is a member of the SOCS (Suppressor Of Cytokine Signaling) family of proteins induced by cytokines, which negatively regulates TLR signaling pathways by an up to date unknown mechanism [163]. SOCS-1 might function by blocking IRAK-1 activation, but recent data suggest that it negatively regulates signaling via TLR2 and TLR4 through degradation of TIRAP [164]. Alternatively, two recent studies indicate that SOCS-1-dependent inhibition of TLR signaling is indirect and occurs by blocking or decreasing type I IFN autocrine/paracrine signaling after TLR-mediated IFN- α/β secretion [165, 166].

c) TOLLIP

Toll interacting protein (TOLLIP) is an adaptor protein that interacts with the cytoplasmic TIR domain of several TLRs, including TLR2 and TLR4, blocking their ability to induce NF- κ B activation [167, 168]. Overexpression of TOLLIP results in formation of a complex with IRAK-1, consequently inhibiting IL-1-induced signaling by blocking IRAK-1 phosphorylation [168].

d) MyD88s

MyD88s, an alternatively spliced variant of MyD88 that lacks residues from Glu¹¹⁰ to Leu¹⁵⁴, both included (Figure 1.3b), is overexpressed in monocytes upon stimulation with LPS or proinflammatory cytokines [169]. This variant is unable to recruit IRAK-4 and therefore inhibits IRAK-4-mediated IRAK-1 phosphorylation. This impairs LPS-induced NF- κ B activation, and decreases the inflammatory response to several stimuli [79].

e) SIGIRR/TIR8 and ST2/T1

In addition to cytoplasmic molecules, membrane-bound proteins such as SIGIRR/TIR8 and ST2/T1 may also play a role in modulating TLR signaling. The single immunoglobulin IL-1R-related protein (SIGIRR) is an orphan receptor that does not induce NF- κ B activation, as it possesses an intracellular TIR domain that lacks two amino acids essential for signaling by IL-1R [170, 171]. SIGIRR is expressed in different cell types ranging from epithelial cells to immature dendritic cells, but it is not expressed in macrophages, fibroblasts, or endothelial cells. Although the exact mechanism by which SIGIRR functions is unclear, it appears to be recruited by TLR4 to block signaling by sequestering IRAK-1 and TRAF6 [171, 172]. In a similar manner, ST2/T1, a

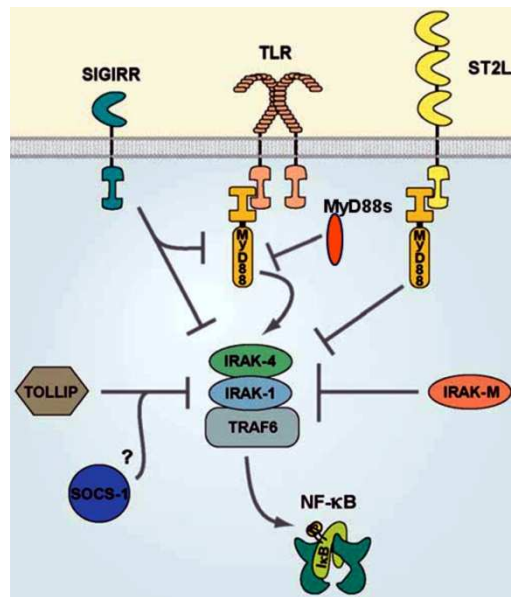


Figure 1.5 Negative regulation of TLR signaling. IRAK-M has been postulated to inhibit dissociation of the IRAK-1•IRAK-4 complex from the receptor. MyD88s blocks association of IRAK-4 with MyD88. SOCS-1 is likely to associate with IRAK-1 and inhibit its activity. TOLLIP inhibits autophosphorylation of IRAK-1. Transmembrane receptors, such as SIGIRR and ST2L, also downregulate TLR signaling by blocking MyD88/IRAK-1/4 activation or sequestering MyD88, respectively. (Modified from [11]).

membrane-bound member of the IL-1 receptor family, may inhibit IL-1R- and TLR4-mediated signaling, but not TLR3 signaling, by sequestering the TIR-containing adaptors MyD88 and TIRAP [173].

1.7 Known Three-Dimensional Structures in the Toll/TLR Signaling Pathway: MyD88 and IRAK-4

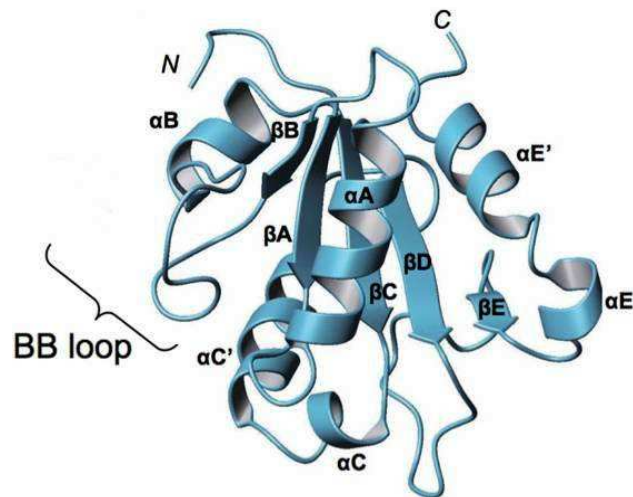
The TLR/MyD88/IRAK system has been thoroughly studied in recent years. Despite the biological importance of DDs, the crystal structure of the monomeric Pelle DD•Tube DD complex in the *Drosophila* Toll pathway was the only structure available from this system [174]. In addition, the NMR solution structure of MyD88 TIR domain [175, 176], and the crystal structures of IRAK-4 kinase domain [145, 146] and DD [111] have also been determined. However, studies on MyD88–IRAK-4 interactions came out only very recently (2009) [177], and the crystal structure of the MyD88•IRAK-4•IRAK-2 complex was just released in 2010 [178]. The main features of these structures are discussed in some detail below.

1.7.1 Structure of Individual Domains of MyD88/IRAKs

a) Solution structure of MyD88 TIR domain

To date, out of the MyD88 domains, only the C-terminal TIR domain has been structurally characterized in isolation. The two most recently reported structures of this module,

Figure 1.6 NMR solution structure of human MyD88 TIR domain. Ribbon drawing of the NMR structure of human MyD88 TIR domain, residues 157-296. The notation of the secondary structures (β A- β E, α A- α C, and α E) is based on that of TLR TIR domains [179-181]. (From [175]).



released in 2009, were determined in solution by NMR spectroscopy [175, 176]. Although these structures were solved under different experimental conditions, their overall folding is essentially identical. It should be noted that the isolated MyD88-TIR domain exists as a monomer in solution, while some TIR domains have been reported to form dimers when crystallized [179, 180]. In this regard, although full-length MyD88 is known to form aggregates (see above), aggregation seems to be mediated via homotypic interactions between death domains [73, 182].

The MyD88 TIR domain structure comprises a central 5-stranded parallel β -sheet (β A- β E) surrounded by 4 α -helices (α A- α C and α E) (Figure 1.6). The global fold is similar to that previously observed in the crystal structures of TIR domains of receptors TLR1, TLR2, TLR10, and IL-1RAPL [179-181] (PDB codes: 1FYV, 1FYW, 2J67, and 1T3G, respectively); MyD88 TIR domain exhibits the highest sequence similarity to TLR2 [175]. Previous studies have indicated that three short sequence motifs, termed boxes 1-3, are conserved between the TIR domains [183]. Of these, the box 2 motif, which resides in the so-called BB loop region (Ser¹⁹⁴-Ala²⁰⁸ of the human MyD88 TIR domain) (Figure 1.6), has been suggested to be important for specific TIR-TIR interactions [33, 181].

b) Crystal structure of IRAK-4 kinase domain

The crystal structure of the kinase domain of IRAK-4 has been recently reported by two separate groups both as the non-liganded, active form and complexed with different inhibitors [145, 146]. These structures reveal structural features typical of both Ser/Thr and tyrosine kinases. The structural analysis revealed extra ordered residues extending from the N-terminus of the kinase domain, found to be important for protein expression as well as for kinase activity, and demonstrate that the ATP-binding site in IRAK-4 has not a deep pocket in the back, but does have a prominent front pocket [145]. As predicted from sequence analysis, the gatekeeper residue at the ATP-binding site is a tyrosine, a unique feature of the IRAK family.



Figure 1.7 Schematic representation of IRAK-4 DD. The hexahelical bundle structure is shown with colored-coded helices, and the tail regions and interconnecting loops denoted in gray. N- and C-termini are represented by the letters N and C, respectively. (From [111]).

c) Crystal structure of IRAK-4 DD

The crystal structure of mouse IRAK-4 DD, solved in 2005, reveals a compact, hexahelical domain (helices α 1-6, Figure 1.7) [111], similar to other previously characterized members of the family such as the FADD DD [109].

Several features of the protein are noteworthy. There is a highly structured N-terminal tail preceding helix α 1, which engages in several hydrogen bonds with the loop connecting helices α 4 and α 5. A rigid tail is also observed at the C-terminus, potentially required for orienting the C-terminal kinase domain so that proper molecular recognition can take place [111]. Furthermore, the structure shows an ordered loop between two of the major α -helices (α 2 and α 3), apparently unique to IRAK-4 [111], which could preclude interactions of IRAK-4 similar to those seen in *Drosophila* Tube•Pelle complex (see section 1.7.2a).

1.7.2 Multimeric Structures

a) Crystal structure of Tube DD•Pelle DD

The *Drosophila* Toll pathway is conceptually similar to the mammalian TLR/IL-1R system (Figure 1.8). In *Drosophila*, a heterotrimeric complex of MyD88, Tube and Pelle mediates the orthologous Toll pathway [184], which is important for immune responses against fungal infection [7], as well as for dorsoventral patterning [185]. While Pelle is the functional orthologue of IRAK, Tube is an adaptor protein that has no counterpart in mammals. MyD88, Tube and Pelle all contain a DD, and assemble via DD-mediated interactions.

In 1999, the crystal structure of the binary complex between DDs of the *Drosophila* kinase Pelle and its adaptor Tube [174] provided the first structural information about homotypic DD-mediated complex formation (Figure 1.9). Previously, genetic experiments had demonstrated that Tube functions upstream of Pelle [186], suggesting that Tube is the link between the receptor and the kinase. Tube acts as a bridge between MyD88, which interacts directly with Toll, and Pelle, which signals downstream for the nuclear translocation and activation of the NF- κ B

orthologue Dorsal, the key event in dorsoventral patterning. On the other hand, sequence comparisons indicate that Pelle is most closely related to IRAK-4 among the members of the IRAK family [138]. Moreover, it has been proposed that signal-induced Pelle activation leads to the phosphorylation of Toll, Tube, and Pelle itself, allowing the dissociation of the Toll•Tube•Pelle membrane proximal complex that forms immediately upon receptor activation. Dissociation of the receptor complex would allow Pelle, and likely Tube, to disengage from the transmembrane receptor after activation, and to move into the cytoplasm where they are required to mediate signal transduction [187].

The crystal structure of Tube DD•Pelle DD shows that both components of the complex exhibit the six-helix bundles characteristic of the DD superfamily (helices $\alpha 1$ - $\alpha 6$, Figure 1.9) [174]. Regardless of the details of the interaction, the most remarkable aspect is perhaps its asymmetry, considering what might have been expected for homotypic interactions. The first interface involves the $\alpha 4$ helix and the following loop of Pelle, which contact the helix $\alpha 6$ and the loops $\alpha 1$ - $\alpha 2$ and $\alpha 5$ - $\alpha 6$ in Tube. Most strikingly, the C-terminal tail of Tube sits in a narrow groove formed by a cavity between the Pelle $\alpha 4$ - $\alpha 5$ and $\alpha 2$ - $\alpha 3$ loops to form a second interface that contributes significantly to strengthen the interaction [174]. Both loops are rather small and lack secondary structure or polar contact pairs within them. However, in this second interface, three Tube residues with bulky hydrophobic side chains (Ile¹⁶⁹, Leu¹⁷¹, and Leu¹⁷³) are involved in the interaction (Figure 1.9b). Interestingly, it has been shown that Pelle, which lacks

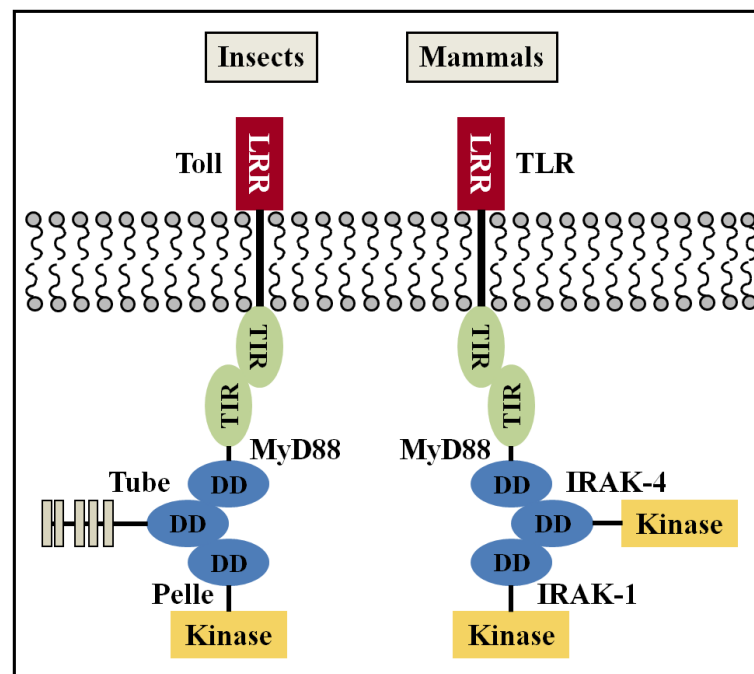


Figure 1.8 Conservation and divergence of TLR-mediated innate immune response in insects and mammals. Schematic representation of complex formation following ligand binding to transmembrane receptors Toll (insects, left) or TLR (mammals, right). A second non-enzymatic adaptor in insects, Tube, seems to be replaced by IRAK-4 in mammals.

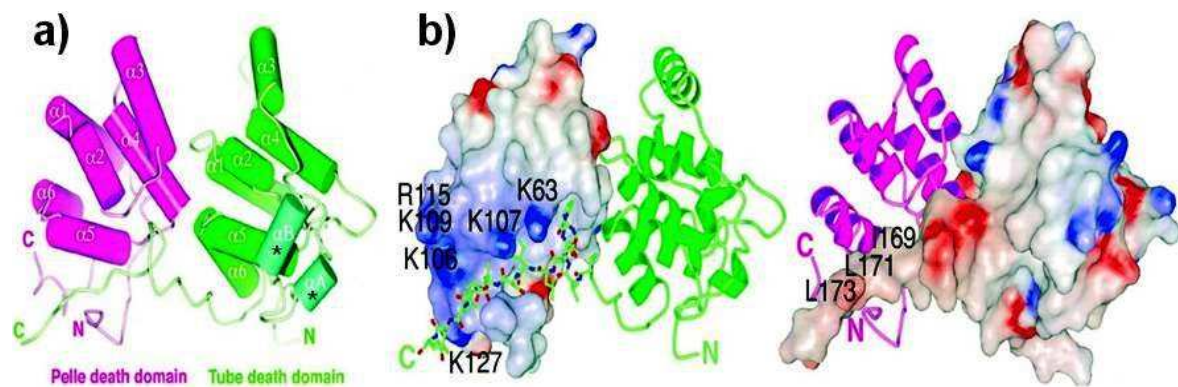


Figure 1.9 Three-dimensional crystal structure of *Drosophila* Tube DD•Pelle DD complex. a) The six-helix bundle fold of both components of the complex is shown with Pelle in magenta and Tube in green. Inserted helices αA and αB of Tube-DD are marked with *. b) Electrostatic surface representation of the Tube•Pelle dimer. Pelle is displayed with its electrostatic surface potential (left) and a magenta ribbon (right), and Tube is represented as a green ribbon (left) or its electrostatic surface potential (right). Notice that the C-terminal tail of Tube-DD contributes significantly to the interaction interface. Hydrophobic residues of this carboxy-terminal end that are in contact with Pelle, as well as charged residues of Pelle surrounding the above region, are labeled on the respective surfaces. (Modified from [174]).

the C-terminal sequence of the kinase domain as IRAK-4 does in mammals, seems to interact with *Drosophila* TRAF1 through its DD [188].

b) Stoichiometry of the MyD88•IRAK-4 complex

Although the Toll-MyD88-Tube-Pelle cascade is functionally equivalent to that of TLRs-MyD88-IRAKs (Figure 1.8) [184, 189], there are major differences between mammalian and insect immune responses. Most relevant, mammals lack a Tube orthologue, whose role appears to be assumed by IRAK-4 [79, 138, 184, 190-192]. Indeed, it has recently been reported that DDs of IRAK-4 and MyD88 form a large oligomeric structure termed the Myddosome [177]. The results of analytical ultracentrifugation, mass spectrometry, and small angle X-ray scattering studies suggest that the DDs of human MyD88 and IRAK-4 assemble into defined structures having 7:4 or 8:4 stoichiometries, in a two-layer structure with a ring of seven or eight MyD88 subunits and a second layer of four IRAK-4 subunits, although resolution was too low to determine the arrangement of the subunits in the complex.

c) Crystal structure of the MyD88 DD•IRAK-4 DD•IRAK-2 DD ternary complex

The recently reported crystal structure of the MyD88•IRAK-4•IRAK-2 DD complex [178] represents a milestone in structural immunobiology, and elucidated in particular some of the questions regarding the architecture and stoichiometry of this complex. The structure, determined at 3.4 Å resolution, revealed a single stranded, left-handed helix of DDs with a tower-shaped arrangement of four layers (Figure 1.10). The nature of this helical assembly therefore dictates

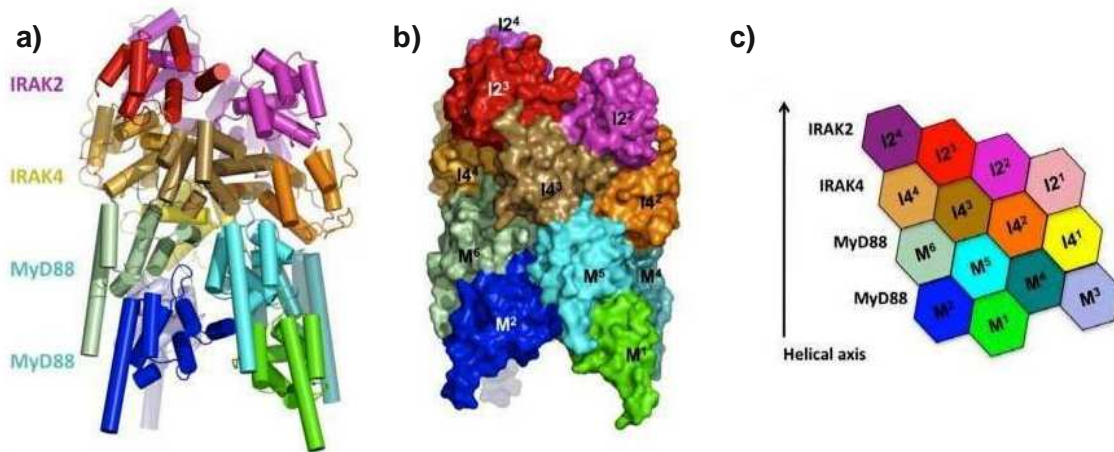


Figure 1.30 Structure of the ternary Myddosome complex. **a)** Ribbon diagram of the structure, with the six MyD88 molecules in cold colors, the four IRAK-4 molecules in earth-tone colors and the four IRAK-2 molecules in warm colors. **b)** Surface diagram of the complex with each subunit labeled using the same color coding as in **(a)**. M, MyD88; I4, IRAK-4; I2, IRAK-2. **c)** Planar arrangement of the complex. (From [178]).

that molecules at both ends of the helix are less ordered or perhaps exhibit less occupancy than the central molecules.

The crystal structure of the MyD88•IRAK-4•IRAK-2 DD complex reveals that Myddosome assembly is nucleated by oligomerization of six MyD88 DDs, which form the “bottom” two layers of the structure (M1-6). Through an unknown mechanism, four IRAK-4 DDs are subsequently incorporated into the complex, forming the middle layer (I41-4), and this forms a docking site for four IRAK-2 DDs (I21-4) to shape the top layer (Figure 1.10). The hierarchical assembly of this “signaling tower” seems to bring the kinase domains of IRAKs into close proximity for trans-phosphorylation and activation. This study also showed that the affinity of the MyD88 DD oligomer for IRAK-4 DDs exceeds that for IRAK-2 DDs, apparently due to a better charge complementarity.

As a conclusion, it can be stated that *Drosophila* and mammals use a similar three layer system with different stoichiometries in Toll or TLR/IL-1R signaling: unlike the oligomeric MyD88•IRAK-4•IRAK-2 complex, the MyD88•Tube•Pelle ternary complex in solution possesses a 1:1:1 stoichiometry [193].

1.8 Involvement of the TLR/MyD88/IRAK System in Disease

Several lines of evidence indicate that TLR-mediated pathways are implicated in inflammatory and immune disorders. Production of proinflammatory cytokines such as IL-1 β , IL-6, TNF- α and IL-12 is a major process stimulated upon TLR activation [194]. Secreted cytokines, however, induce a positive feedback in the immune system, which could cause severe

immunopathology if uncontrolled. We conclude this introduction with a brief outline of some of the conditions in which MyD88 or IRAK proteins are involved.

Several diseases have been associated to MyD88. For example, development of atherosclerosis observed in apolipoprotein E-deficient mice is rescued by introduction of MyD88 deficiency, indicating that the TLR-mediated pathway is responsible for the development of atherosclerosis [195, 196]. Also, the MyD88-dependent pathway has been implicated in allograft rejection [197], and MyD88-deficiency is shown to increase the risk of diabetes in mice [198]. Finally, it has been reported that children with *MyD88* mutations that affect either the DD or the TIR domain of the protein present recurrent pyogenic infections [116].

IRAK family members have also been related to various inflammatory and infectious diseases [199]. For example, IRAK-M overexpression has been shown to be involved in several conditions such as in sepsis [132], acute coronary syndrome [127, 200], cancer [125, 201], and osteoporosis [147].

Since aberrant regulation of TLR/MyD88/IRAK pathway is relevant for several inflammatory and autoimmune diseases [202, 203], it is likely that specific inhibitors of this pathway would constitute valuable tools for novel therapeutic approaches [204, 205]. Given the essential and universal role of IRAK family members as signaling molecules in TLR/IL-1R responses, interference with IRAK activity is appealing as a therapeutic strategy. For instance, synthetic peptides, corresponding to the binding site between IRAK-1 and TRAF6, have been successfully used to block NF- κ B activation [141]. Moreover, drugs/inhibitors targeting individual IRAKs could be used for certain IL-1/TLR pathways in specific contexts, while not affecting the entire IL-1/TLR system.

Therefore, a deep understanding of the structural organization of the complexes formed by components of the TLR/MyD88/IRAK system is essential to develop therapeutic drugs in the future, which could up- or downregulate this pathway whenever needed.

2. Objectives

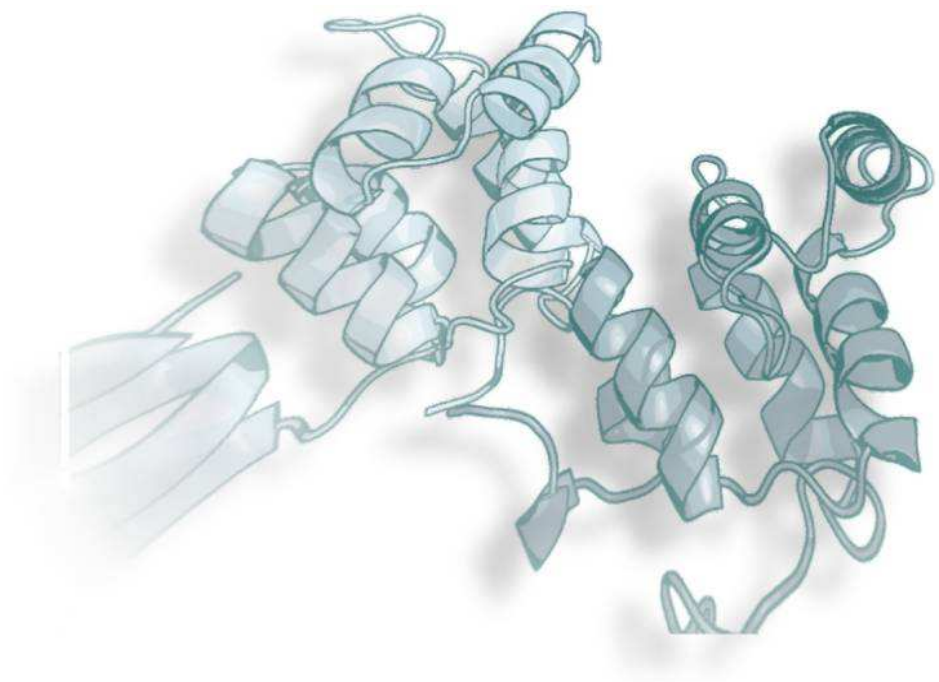


2 Objectives

The main goal of this work is to elucidate the molecular bases of the TLR-MyD88-IRAK signaling pathway, as part of the immune system. In particular, we set the following objectives:

- 1) Establishment of expression and purification protocols for the different functional domains of the adaptor MyD88 and the kinases IRAK-1 and IRAK-4, as well as of the negative regulator IRAK-M.
- 2) Setting up protocols for obtaining purified complexes between the death domains of MyD88 and the different IRAK recombinant variants.
- 3) Determination of the regions (globular domain vs linker) necessary for the formation of stable complexes between MyD88 and IRAK proteins.
- 4) Determination of the mechanisms by which IRAK-M plays an inhibitory role in immune responses: competition with IRAK-4 for MyD88 binding vs. MyD88•IRAK-1 complex stabilization.
- 5) Crystallization and structure resolution of the MyD88 and IRAK isolated DDs, as well as of their complexes.

3. Materials and Methods



3.1 Recombinant Protein Expression

To design and produce the MyD88 and IRAK recombinant fragments of interest, several aspects needed to be considered such as the length, amino acid composition, presence of hydrophobic stretches, and secondary structure of the polypeptides. These factors influence the correct assembly, solubility properties and purification possibilities of each peptide, and are the main focus of this section.

3.1.1 Sequence Alignments and Secondary Structure Prediction

Before deciding the synthesis of selected recombinant fragments we performed a thorough analysis of the amino acid sequences of MyD88, IRAK-1, IRAK-M, IRAK-4, which were also compared to the *Drosophila melanogaster* Tube and Pelle proteins. These sequences were retrieved using the sequence retrieval system (SRS) from the Swiss-Prot database [206], with the following accession numbers: Q99836 (human MyD88), P51617 (human IRAK-1), Q9Y616 (human IRAK-M), Q9NWZ3 (human IRAK-4), Q8R4K2 (mouse IRAK-4), P22812 (*Drosophila melanogaster* Tube) and Q05652 (*D. melanogaster* Pelle). The propensity to form globular domains (order/disorder) was analyzed with GlobPlot [207], DISOPRED [208] and IUPred [209]. Next, to determine the boundaries of globular domains, amino acid sequences of MyD88 and IRAK-4 from various species, together with those of *Drosophila* Tube and Pelle, were aligned according to the structural information available at the moment [111, 174], using ClustalW [210]. Finally, to disfavor gaps or insertions within the secondary structure elements, the secondary structure was predicted with the programs JPred [211] and PSIPRED [212]. The results of these combined analyses are summarized in Appendix II. Putative interactions sites in MyD88 and IRAK-4 death domains, predicted with PPI-Pred, are given in Appendices III and IV, respectively.

3.1.2 Cloning of Death Domains

Synthetic genes coding for the fragments of interest were designed to maximize the odds of heterologous expression in *Escherichia coli*, and all sequences were optimized in terms of codon usage and mRNA secondary structure. Selected fragments included six to eight amino acid residues N-terminally from the start of the first predicted α -helix of each death domain, and C-terminally from the end of the last helix. They were termed MyD88(S)¹, IRAK-1(S), IRAK-M(S) and IRAK-4(S), respectively (see Table 4.2 in Results). In addition, similar constructs coding for both the globular death domains and the DD-TIR (MyD88) or DD-kinase linkers (IRAK proteins)

¹ The C-terminus of MyD88(S) differs from the previously reported natural form, MyD88s, which lacks residues 110 to 157.

were generated. These fragments were termed MyD88(L), IRAK-1(L), IRAK-M(L), and IRAK-4(L), respectively. To help protein detection and purification, N-terminal 6xHis, c-MYC (EQKLISEED) and FLAG® M2 (DYKDDDDK) tags were included in MyD88, IRAK-M and IRAK-4 variants, respectively. The main physico-chemical parameters of the resulting recombinant fragments are summarized in Table 4.2 (Results).

All eight synthetic genes coding for the different variants of death domains were generated via oligonucleotide assembly. The resulting fragments were digested with restriction enzymes *Nde* I and *Bam*H I, and ligated into the corresponding sites of the T7 promoter region of the expression plasmid pET-3a (Novagen, Schwalbach, Germany). This plasmid contains a *bla* coding sequence, which confers resistance to ampicillin (see Appendix V for the full pET-3a restriction map). Oligonucleotide synthesis and assembly, as well as cloning in the expression vector, were performed at Entelechon GmbH (Heidelberg, Germany). The DNA sequences of these artificial genes are shown in Appendix VI.

3.2 Site-Directed Mutagenesis

Site-directed mutagenesis is a technique for generating changes over a double-stranded nucleotide sequence. The methods used in this investigation basically involve a polymerase chain reaction (PCR) using a supercoiled plasmid vector as template and two synthetic oligonucleotide primers containing the desired mutation. During PCR, thousands to millions of copies of the mutated DNA sequence are generated. The template (wild-type) plasmid, which is methylated in almost all *E. coli* strains, is then removed by digestion with *Dpn* I, a DNase specific for methylated DNA. The new (mutant) DNA is not methylated and remains intact in the reaction.

3.2.1 Primer Design

Mis- or nonsense mutants were designed based on the nucleotide sequences of expression plasmids coding for either MyD88(L) or IRAK-4(L), and according to the codons most frequently used by *E. coli*. The mutants generated are given in Figure 3.1, and they were termed MyD88 R81E, MyD88 I109X, MyD88 Y116C, MyD88 E143X, IRAK-4 E92R, IRAK-4 V105X, IRAK-4 N110X, and IRAK-4 K115X (see Table 4.2 in Results for the main physicochemical parameters of these constructs).

The mutagenic oligonucleotides were designed considering that both mutagenic primers (sense and antisense) must contain the desired mutation and anneal to the same sequence on opposite strands of the plasmid (sequences shown in Table 3.1). In addition, we had to consider that primers should be between 25 and 45 bases long, since shorter primers could bind DNA

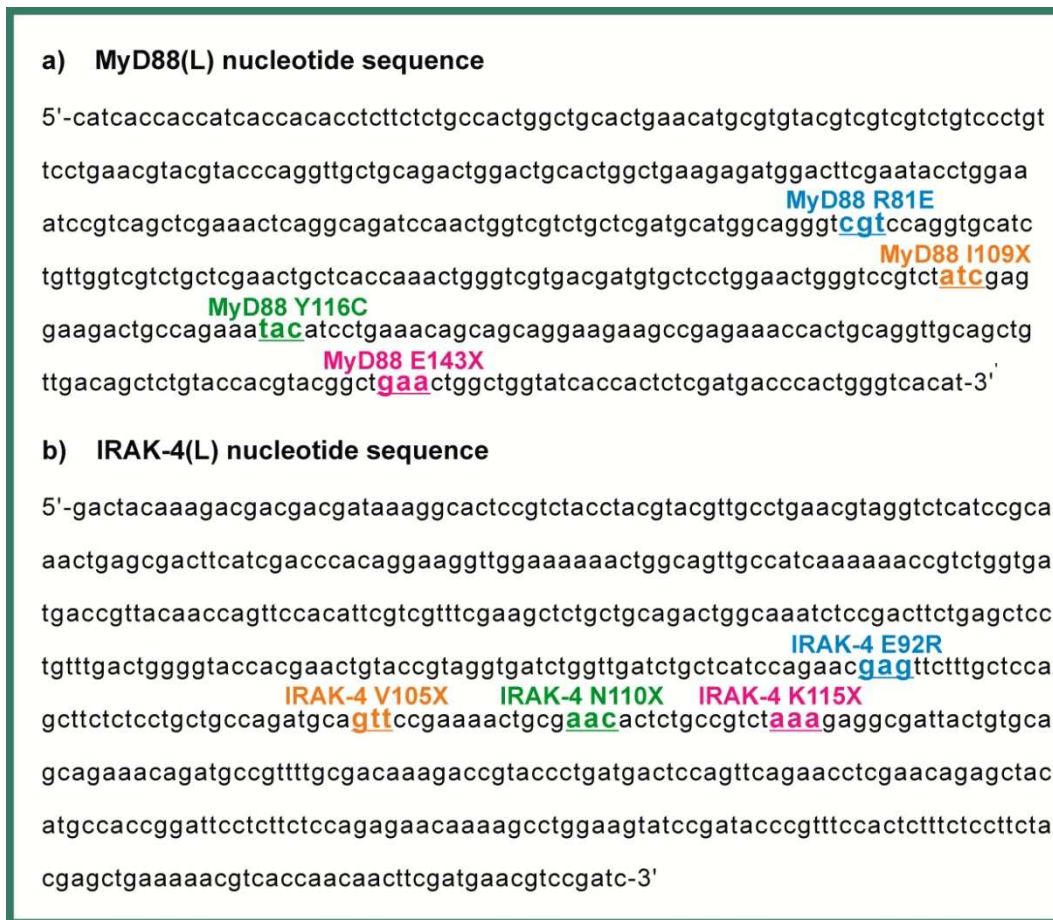


Figure 3.1 Generated mutations over the MyD88(L) and IRAK-4(L) nucleotide sequences. **a)** Nucleotide sequence of MyD88(L) highlighting generated mutations. Triplets modified by site-directed mutagenesis (corresponding to Arg⁸¹, Ile¹⁰⁹, Tyr¹¹⁶ and Glu¹⁴³) are colored as the mutants generated from their replacement, shown next to them. **b)** Nucleotide sequence of IRAK-4(L) highlighting generated mutations. Triplets modified by site-directed mutagenesis (corresponding to Glu⁹², Val¹⁰⁵, Asn¹¹⁰ and Lys¹¹⁵) are colored as the mutants generated from their replacement, shown next to them.

nonspecifically, and longer primers increase the likelihood of secondary structure formation, lowering the efficiency of the mutagenesis reaction. Secondly, the desired mutation should be in the middle of the primer with ~10-15 bases of correct sequence on both sides, and should preferably end in one or more C or G bases. Finally, the primer melting temperature (T_m) should be $\geq 78^\circ\text{C}$. The value of T_m , the temperature at which 50% of the DNA duplex dissociates into single-stranded, can be estimated by Equation 3.1, where N is the primer length in bases, %GC is the number of G's and C's in the primer as a percentage of the total number of bases (optimally $\geq 40\%$), and % mismatch is the number of bases in the primer that do not match the dsDNA template as a percentage of the total number of bases.

$$T_m = 81.5 + 0.41(\%GC) - \frac{675}{N} - \% \text{ mismatch} \quad \text{Equation 3.1}$$

Table 3.1 Designed MyD88 and IRAK-4 primer sequences for site-directed mutagenesis. Mutated triplets are shown in capital letters and underlined. The specific nucleotides replaced within the codons are shown in bold and underlined. (The original sequences of MyD88(L) and IRAK-4(L) are given in Figure 3.1).

Mutation	Primer	Sequence	T _m (°C)
MyD88 R81E	Sense	5'-cgatgcatggcagggt <u>GAA</u> ccagggtgcatctgttgg-3'	78.33
	Antisense	3'-gctacgtaccgtccca <u>CTT</u> gggccacgtagacaacc-5'	
MyD88 I109X	Sense	5'-cctggaactgggtccgtct <u>TAA</u> taggaagactgccag-3'	78.40
	Antisense	3'-ggaccttgaccaggcaga <u>ATT</u> atccttctgacggtc-5'	
MyD88 Y116C	Sense	5'-ggaagactgccagaaa <u>TG</u> Catcctgaaacagcag-3'	79.20
	Antisense	3'-ccttctgacggcttt <u>AC</u> Gtaggactttgtcgtc-5'	
MyD88 E143X	Sense	5'-ctgtaccacgtacggct <u>TAA</u> ctggctggtatcacc-3'	81.60
	Antisense	3'-gacatggtgcatgccga <u>ATT</u> gaccgaccatagtg-5'	
IRAK-4 E92R	Sense	5'-ctgctcatccagaac <u>CGT</u> ttctttgctccagcttctctcc-3'	78.65
	Antisense	3'-gacgagtaggtcttg <u>GCA</u> aagaaacgaggtcgaagagagg-5'	
IRAK-4 V105X	Sense	5'-ctcctgctgccagatgca <u>TAA</u> ccgaaaactgcaaacactc-3'	78.65
	Antisense	3'-gaggacgacggctctacgt <u>ATT</u> ggctttgacgcttgtgag-5'	
IRAK-4 N110X	Sense	5'-gcagtccgaaaactgcg <u>TAA</u> actctgccgtctaaagag-3'	79.00
	Antisense	3'-cgtcaagcctttgacgc <u>ATT</u> tgagacggcagatttctc-5'	
IRAK-4 K115X	Sense	5'-cgaacactctgccgtct <u>TAA</u> gaggcgattactgtg-3'	80.44
	Antisense	3'-gcttgtgagacggcaga <u>ATT</u> Tctccgctaatgacac-5'	

Primers (50 nmol each, purified by HPLC) were synthesized at Invitrogen (www.invitrogen.com). The resulting lyophilized product was dissolved in bidistilled water to a final concentration of 200 ng/μL, from which working dilutions at 100 ng/μL were prepared.

3.2.2 PCR Conditions

PCR site-directed mutagenesis was performed using the QuikChange™ II Site-directed Mutagenesis kit (Stratagene), following manufacturer's instructions. Two reactions were prepared for each mutant, using from 10 to 50 ng of template DNA. The volumes and reagents used for the mutagenesis of 50 ng of DNA template were as follows:

- 5 μL 10X reaction buffer (supplied by the manufacturer)
- 5 μL (50 ng) dsDNA template (*pMyD88(L)* or *pIRAK-4(L)*)
- 6.25 μL (125 ng) *sense* primer (20 ng/μL)
- 6.25 μL (125 ng) *antisense* primer (20 ng/μL)
- 1 μL dNTP mix
- ddH₂O to a final volume of 50 μL
- 1 μL *PfuUltra* HF DNA polymerase (2.5 U/μL) (added just before the start of the PCR reaction)

PCR reactions were carried out using the GeneAmp® PCR System 9700 (Applied Biosystems) or the MultiGene Mini (Labnet) thermal cycler, with the following parameters:

Segment	# of cycles	T (°C)	Time
1	1	95	30 s
		95	30 s
2	16	55	1 min
		68	5 min
3	-	4	∞

To digest the parental (non-mutated) supercoiled dsDNA, each amplification reaction was mixed thoroughly with 1 µL of the *Dpn* I restriction enzyme (10 U/µL), and incubated at 37°C for 1 h.

The reaction products were then transformed into XL1-Blue supercompetent cells (Stratagene) according to the transformation protocol detailed in section 3.3.2, with some modifications: 5 µL of *Dpn* I-treated DNA were used for transformation, and transformed cells were spread onto an LB/agar plate (see Appendix VII for composition) with 100 µg/mL ampicillin, 80 µg/mL X-gal and 20 mM IPTG, in order to perform the blue-white color screening test. This color screening for recombinant plasmids is available when transforming host cells containing the *lacIqZDM15* gene on the F' episome (such as the XL1-Blue strain) with a plasmid providing α -complementation (such as the pET-3a plasmid used here). When *lacZ* expression is induced by IPTG in the presence of the chromogenic substrate X-gal, colonies without the desired insert are stained blue while those containing plasmids with the insert of interest remain white.

3.2.3 DNA Extraction and Sequencing

To verify the mutant DNA sequence, single white colonies from the transformed XL1-blue cells plate (see section 3.2.2) are inoculated into 5 mL LB (see Appendix VII for composition) containing 100 µg/mL ampicillin. The culture was grown overnight at 37°C, and cells were collected by centrifugation at 3,000g for 10 min. The mutated DNA was then extracted with the *Wizard® Plus SV Minipreps* purification kit (Promega), following the manufacturer's protocol.

Mutated DNA sequences were verified using a T7 primer compatible with the T7 promoter of pET-3a (see Appendix V) (reactions performed by Dr. Mercè Miquel, DNA Sequencing platform of the CID-CSIC, Barcelona, Spain).

3.3 Heterologous Expression of MyD88, IRAK-1, IRAK-4 and IRAK-M Variants

3.3.1 *Escherichia coli* Strains

Heterologous expression of the recombinant proteins was performed in different strains of One Shot® *E. coli* competent cells, from Invitrogen: BL21(DE3), BL21(DE3)pLysS and BL21 Star™(DE3)pLysS. These *E. coli* strains contain a λ prophage (DE3), carrying the T7 RNA polymerase gene and the T7lac promoter. In the transformed pET vector constructs, the cloned genes are under control of the T7lac promoter and expression is repressed until IPTG induction of T7 RNA polymerase from the lac promoter. The pLysS plasmid codes for T7 lysozyme, a natural inhibitor of the T7 polymerase, which is constitutively expressed. Therefore, the *E. coli* BL21(DE3)pLysS and BL21Star™(DE3)pLysS strains are used to minimize low-level expression of potentially toxic gene products before IPTG induction. The BL21Star™(DE3)pLysS strain also carries a mutated *rne* gene (*rne131*), which encodes a truncated RNase E variant. This modified enzyme lacks the ability to degrade mRNA, resulting in an increase in mRNA stability.

In terms of antibiotic resistance, all these *E. coli* strains are resistant to ampicillin. BL21(DE3)pLysS and BL21 Star™(DE3)pLysS strains are also resistant to chloramphenicol, since they contain a Cam^R marker.

3.3.2 Transformation of Competent Cells

Transformation of competent cells was performed using the heat shock method, as follows:

1. Competent cells were allowed to thaw on ice.
2. Ten ng of plasmid DNA were added to the cells in a laminar-flow hood or on a cleaned bench surface next to a Bunsen burner, and mixed gently.
3. The tubes were incubated on ice for 30 min, then heat-shocked at 42°C for 45 seconds, and incubated on ice for at least 2 additional min.
4. Two hundred and fifty μ l SOC medium (see Appendix VII for composition) were warmed to 37°C and then added to the cells.
5. The cells were incubated at 37°C for 1 h with constant agitation at 225 rpm.
6. Afterwards, the samples were centrifuged at 3500 rpm for 1 min, the supernatant was discarded, and the pellet was slowly resuspended in 50 μ l SOC medium.
7. The entire transformation was spread onto a pre-warmed LB/agar plate with the appropriate antibiotics, which was incubated overnight, upside down, at 37°C.

The antibiotic concentrations used in all media throughout this work were 100 µg/mL ampicillin (for all strains) and 34 µg/mL chloramphenicol (additionally, for BL21(DE3)pLysS and BL21 Star™(DE3)pLysS strains).

3.3.3 Preparation of Starter Cultures

Bacterial starter cultures for protein overexpression were prepared as follows:

1. A single colony was picked from a freshly grown transformation plate with a sterile pipet tip, and inoculated into 50 mL LB medium containing the appropriate antibiotics.
2. The culture was grown overnight at 20°C with constant agitation at 225 rpm.
3. Next morning, either larger cultures or glycerol stocks were prepared as explained in the following sections.

3.3.4 Preparation of Glycerol Stocks

E. coli strains can be stored for years at -80°C in a medium containing 15% glycerol. These glycerol stocks of bacterial cells containing the plasmid of interest were generally prepared as follows:

1. Five-hundred-microliter aliquots were taken from the starter culture (section 3.2.3) and added to 0.5 mL of a 30% glycerol solution in LB, previously sterilized.
2. The tubes were gently mixed, quickly frozen in liquid nitrogen, and stored at -80°C until needed.
3. To prepare a starter culture from a glycerol stock, a glycerol stock vial was allowed to thaw and inoculated into 50 mL LB medium (previously autoclaved), with the appropriate antibiotics. The culture was then treated as explained in section 3.2.3, for preparing starting cultures.

3.3.5 Preparation of Larger Cultures

After preparing a starter culture either by inoculating a single colony or from a glycerol stock preparation, larger cultures were obtained by the following procedure:

1. The starter culture was diluted into 500 mL LB medium with the appropriate antibiotics, in a 2-L flask.
2. The culture was grown at 37°C with constant shaking at 225 rpm until the optical density at 600 nm (A_{600}) was 0.4-0.8 (indicating the beginning of the exponential growth phase). LB medium was used as a blank for all A_{600} measurements.

3. Protein expression was then induced by adding 0.8 mM IPTG. The culture was incubated at 20°C for 6 h with constant agitation at 225 rpm, to ensure sufficient aeration.
4. Cells were harvested by centrifugation at 4,500g for 15 min at 4°C. The supernatant was removed and cell pellets were either stored at -80°C or lysed as explained in section 3.4.1.

3.4 Extraction and Renaturation of Recombinant Fragments

Proteins overexpressed in *E. coli* were always extracted by chemical cell lysis, and unfolded proteins were then renatured using different solutions, as explained below.

3.4.1 Extraction of MyD88 and IRAK Recombinant Fragments

Both MyD88 and IRAK proteins were extracted by cell lysis. Cell membranes were disrupted with detergents, as follows:

1. Frozen cell pellets were resuspended in B-PER® reagent (Thermo Scientific) supplemented with 10 mM MgCl₂, 20 mM 2-mercaptoethanol (2-ME), 1 mM EDTA, 200 mM NaCl and 10 mM imidazole. From now on, B-PER® reagent with these additives will be referred to as B-PER (see Appendix VII, approximately 100 µL B-PER were used per 1 mL culture).
2. Once resuspended, 1 unit/mL DNase I was added to the mixture, which was incubated at room temperature for 30 min under agitation.
3. Mixtures were then centrifuged at 13,000g for 15 min at 4°C, the supernatant extracted, and the resulting pellet resuspended again in the same volume of B-PER as in step 2.
4. The pellet from the 2nd B-PER extraction was then resuspended in extraction buffer (see Appendix VII), supplemented with increasing quantities of urea (from 2 to 8 M). Samples were taken after each extraction step for further analysis by gel electrophoresis. See Table 4.1 (Results) for the expression and extraction conditions used for each protein.

3.4.2 Renaturation of Recombinant Proteins

In many cases, expression of recombinant proteins in *E. coli* leads to formation of insoluble inclusion bodies (IBs). In general, folding insoluble proteins into a biologically native conformation, although technically challenging, has the advantage of working with large quantities of essentially pure protein. To refold insoluble proteins, some features regarding the tested renaturing solutions must be taken into account. The folding solution should favor

formation of the native state while minimizing aggregation of folding intermediates. Polar additives such as arginine, osmolytes, detergents, and chaotropes can minimize aggregation and increase the yield of biologically active material [213]. Other factors affecting formation and stability of the folded state are pH, redox environment, ionic strength, protein concentration, and the presence or absence of specific ligands.

Here, in order to search for the proper folding conditions, 50 μL of recombinant proteins fully unfolded in an 8-M urea solution were added to 950 μL of each of the 16 unique folding solutions of the fractional factorial protein-folding screen prepared in house essentially following the work of N. Armstrong and co-workers [214] with minor modifications, such as the use of lauryldimethylamine-*N*-oxide (LDAO) as detergent, at a concentration of 1.4 mM, instead of lauryl maltoside. The final protein concentration in these solutions was of 0.1 mg/mL (see Appendix VIII for the formulation of these buffers). Mixtures were incubated overnight at 4°C on a rocker, then centrifuged at 13000 rpm for 10 min to remove precipitated material, and supernatants were analyzed by SDS-PAGE. Suitable FoldIt conditions were noted and renatured proteins were buffer-exchanged and purified by either affinity or ion-exchange chromatography (sections 3.5.1 and 3.5.2, respectively). Once the most significant factors had been identified, the folding conditions were optimized for larger scale renaturation experiments. These were performed essentially as for the initial screens but protein solutions were added drop-wise to the most suitable FoldIt solution(s) under continuous stirring. IRAK-4(S) was alternatively renatured by overnight dialysis against 20 mM Tris-HCl, pH 8.0, 100 mM NaCl, 5 mM 2-ME, 1 mM LDAO. The specific renaturing conditions used in each case are shown in Table 4.1 (Results).

3.5 Purification of Recombinant Fragments of MyD88 and IRAK Proteins

Recombinant fragments of MyD88 and IRAK proteins were purified by a combination of one or several of the following purification techniques: metal affinity chromatography in batch or by HPLC using prepacked columns (MyD88 variants and its complexes), ion-exchange chromatography (for IRAK proteins), and size-exclusion chromatography (to separate MyD88 aggregates from non-aggregated forms and the MyD88•IRAK-4 complex(es) from its components).

3.5.1 Purification of MyD88 and its Complexes by Affinity Chromatography

This purification step is based on the interaction of nickel ions, bound to a specific resin, with the 6xHis tags present at the NH₂-terminal ends of MyD88 recombinant fragments. The matrix used in this investigation was Ni-NTA agarose, from Qiagen. Nitrilotriacetic acid (NTA) is a tetradentate chelating agent that occupies four of the six ligand binding sites in the coordination

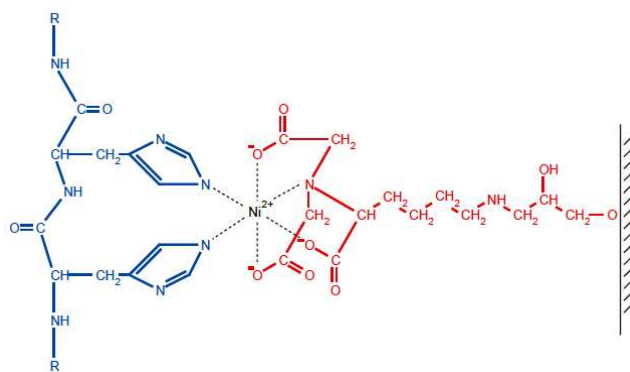


Figure 3.2 Schematic representation of the interaction between neighboring residues in the 6xHis tag and the Ni-NTA matrix. Nitrilotriacetic acid (NTA) is a tetradentate chelating adsorbent that occupies four of the six ligand binding sites in the coordination sphere of the nickel ion, leaving two sites free to interact with the 6xHis tag. (From [215]).

sphere of the nickel ion, leaving two sites free to interact with the 6xHis tag of the recombinant MyD88 variants (Figure 3.2). The matrix is then washed and bound proteins are eluted with increasing concentrations of imidazole, which can bind to Ni^{2+} and therefore disrupt protein to matrix interactions. Affinity chromatography was performed either in batch or by FPLC using prepacked columns mounted on an ÄKTA Explorer System (GE Healthcare).

Purification procedure with Ni-NTA agarose

The batch procedure entails binding the protein to the Ni-NTA resin in solution. This strategy is fast and promotes efficient binding of the 6xHis-tagged protein, especially when the 6xHis tag is not fully accessible or when the protein in the lysate is present at a very low concentration. The batch purification procedure used for MyD88 purification is described below (see Appendix VII for buffers compositions):

1. The extracted protein mixture (section 3.4) was diluted in binding buffer to a final concentration of 0.2 mg/mL and added to the Ni-NTA agarose matrix, previously equilibrated with binding buffer, and gently mixed by shaking (200 rpm on a rotary shaker) for 3-4 h, at 4°C. 1 mL of Ni-NTA agarose was used for every 5 mg protein, corresponding to 25 mL of the initial bacterial culture.
 - For Ni-NTA agarose matrix equilibration, 2 mL of the Ni-NTA agarose slurry (for every mL of Ni-NTA agarose matrix to be used) were pipetted into an empty Eppendorf tube and centrifuged at 800g for 2 min. The supernatant was removed and binding buffer was added to the matrix. The mixture was gently mixed by inverting, centrifuged, and the supernatant discarded.
2. The protein mixture was centrifuged at 800g for 2 min, and the supernatant was collected (non-bound fraction).
3. The matrix was washed with 10 volumes of wash buffer, centrifuged for 2 min at 800g, and the supernatant collected (wash fraction).

4. Specifically bound proteins were finally eluted from the affinity matrix with 5 volumes of elution buffer (containing 500 mM imidazole). The mixture was centrifuged for 2 min at 800g and the supernatant was collected in different fractions (elution fractions).

Samples were taken after each extraction step for further analysis by gel electrophoresis.

Alternatively, the Ni-NTA matrix was first settled at the bottom of an empty PD-10 column, and the procedure continued as described above.

3.5.2 Ion-Exchange Chromatography of IRAK Proteins

Ion chromatography is based on the ionic (Coulombic) interactions of analyte ions with a stationary phase displaying oppositely charged functional groups. Retention of the analyte is related to its affinity to the ion exchanger inside the column. Cation exchange matrices retain positively charged cations using a negatively charged stationary phase, while anion exchange resins hold anions using a positively charged stationary one. Usually, samples are loaded under low ionic strength conditions and bound proteins are then eluted using a buffer with higher ionic strength.

In this work, IRAK-4(S), IRAK-1(S) and IRAK-M(S) proteins were purified, when necessary, by anion exchange chromatography on Q (quaternary ammonium)-Sephacryl™ Fast Flow matrix (GE Healthcare). The followed procedure was similar as for batch and column purification on Ni-NTA agarose (section 3.5.1), but with the following specificities (see Appendix VII for buffers compositions):

1. The Q-Sephacryl matrix was equilibrated with equilibration buffer. One mL of Q-Sephacryl matrix was used for every 5 mg protein to be purified.
2. The protein fraction to be purified was diluted to ~0.2 mg/mL in equilibration buffer.
3. The matrix was washed and proteins eluted with equilibration buffer, supplemented with increasing concentrations of NaCl (from 100 to 500 mM).

Samples were taken after each extraction step for further analysis by gel electrophoresis.

3.5.3 Size-Exclusion Chromatography

Size-exclusion chromatography is a purification method in which particles of different sizes pass through a stationary phase at different rates. As a result, particles of a solution are separated by size rather than by molecular weight. As the solution travels down a column filled with a porous matrix, small particles enter into the pores, while larger particles cannot. Consequently, larger molecules elute faster from the column than smaller particles. Typically,

when an aqueous solution is used to transport the sample through the column, the technique is known as gel filtration chromatography.

In this work, gel filtration chromatography was used to separate MyD88(L) and MyD88 E143X monomers from other multimeric forms, as well as MyD88(L)•IRAK-4(L) and MyD88 E143X•IRAK-4(L) complexes from non-complexed forms. Gel filtration chromatography was performed using a HiPrep 16/60 Sephacryl S-200 High Resolution column (GE Healthcare) connected to an FPLC system. The column was always washed first with distilled water, and then equilibrated with gel filtration buffer (see Appendix VII for composition) before use. The column was calibrated with six standard samples of known molecular weight: Blue Dextran (to determine the void volume (V_o) of the column; M_r 2000 kDa), β -amylase (M_r 200 kDa), alcohol dehydrogenase (M_r 150 kDa), albumin (M_r 66 kDa), carbonic anhydrase (M_r 29 kDa) and cytochrome C (M_r 12.4 kDa).

The quotients between elution volumes of standard proteins (V_e) and V_o were plotted against the logarithm of the molecular weights of standard proteins. All samples (standards and newly characterized MyD88/IRAK fragments and complexes thereof) were dissolved in gel filtration buffer. In this manner, the M_r of the different eluted fractions of a sample could be calculated with the calibration curve created for this buffer, as a reference. The initial sample volume to be injected into the column was kept to 1-2 mL at an initial concentration of 1-3 mg/mL, and gel filtration was performed at a constant flow of 0.5-2 mL/min. Samples were examined by absorbance readings at 280 nm throughout the process, and elution fractions were collected manually.

3.6 Ultrafiltration of Protein Solutions and Determination of Protein Concentration

Knowledge of the protein concentration is important for most biochemical and biophysical studies. In this work, protein concentrations were either determined with the BCATM protein assay kit (Pierce) following manufacturer's instructions, or in most cases, by the absorbance of aqueous protein solutions at 280 nm (A_{280}), a faster and cleaner technique. When a higher concentration of a protein was needed, ultrafiltration devices were used to reduce sample volumes by separating larger solutes from other molecules of lower molecular weight. These ultrafiltration devices were used not only for protein concentration but also for protein dialysis and separation. These techniques constitute the main topic of this section.

3.6.1 Determination of Protein Concentration from the Absorbance at 280 nm

Absorbance assays are fast and convenient, since no additional reagents or incubations are required, and no protein standard needs to be prepared. This method is mostly used to monitor

fractions from pure proteins, since any non-protein component of the solution that absorbs ultraviolet (UV) radiation will interfere with the assay. Proteins in solution absorb UV radiation with absorbance maxima at about 280 and 200 nm. Peptide bonds are primarily responsible for the peak at around 200 nm, and amino acids with aromatic rings are the primary reason for the absorbance peak at about 280 nm. The relationship of absorbance to protein concentration is linear over a large concentration range, and is determined by Lambert-Beer's Law (given in Equation 3.2), where A is the absorbance, at a given wavelength of light, c is the molar concentration of solute in the solution being measured, ϵ is the molar extinction coefficient, expressed in $M^{-1}cm^{-1}$, and l is the path length of the sample (distance that light travels through the sample contained in an analytical cell), expressed in cm.

$$A = \epsilon cl \quad \text{Equation 3.2}$$

Absorbance was measured at 280 nm with either the UV-Vis Cary 100 Bio dual beam spectrophotometer (Varian), using 100- μ L quartz micro cuvettes with a 1-cm path length (Hellma), or the Nanodrop ND-1000 spectrophotometer (Thermo). As blank buffer we used the one in which the protein to be measured was dissolved. From the A_{280} value obtained, protein concentration was calculated using the theoretical absorption coefficients and molecular weights given in Tables 3.1 and 3.2, and applying Equation 3.2. Although protein concentration can be monitored by collecting data at a single wavelength (usually 280 nm), a complete UV spectrum (e.g. in the range of 240-320 nm) was usually recorded so that information about protein quality could be gathered, and distortions due to the presence of contaminating substances absorbing at close wavelengths (for example, DNA or RNA, absorbing at 260 nm) could be excluded.

3.6.2 Ultrafiltration of Protein Solutions

Protein solutions are often required to be concentrated and/or buffer-exchanged for further use. This can be done by ultrafiltration, which is far gentler to labile macromolecules than other techniques such as precipitation. This technique is very efficient because it can simultaneously be used for protein buffer-exchange, desalting, concentration, or removal of materials of low molecular weight from a solution of macromolecules. When using commercially available ultrafiltration devices, a centrifugal force is applied to force the passage of small molecules through a membrane that contains pores of a definite size. Retention and product recovery are a function of a variety of other factors, including the molecular shape and size of the molecule, electrical characteristics, sample concentration and composition, operating conditions, and device or system configuration. Nevertheless, the nominal molecular weight limit of a membrane has proven to be an effective general indicator of membrane performance for globular

proteins. This limit indicates that most dissolved molecules with lower molecular weights will pass through the membrane while proteins of higher molecular weight will be retained.

Here, in order to separate MyD88 and IRAK proteins (or their complexes) from other buffer components, three different ultrafiltration devices were used:

1. Centricon devices (Millipore): for initial protein solution volumes of up to 2 mL and desired final volumes of 40 μ L or higher (Figure 3.3a).
2. Amicon Ultra-15 devices (Millipore): for initial volumes of up to 15 mL and final recovery volumes of 200 μ L or higher (Figure 3.3b).
3. Microcon devices (Millipore): for initial protein solution volumes of up to 500 μ L and final recovery volumes of 10 μ L or higher (Figure 3.3c).

The above mentioned devices contain a low-adhesion cellulose membrane with a specific nominal weight limit according to its pore size. Depending on the protein or complex to be retained, the most frequently used membranes had nominal molecular weight limits of 3, 10 or 30 kDa. For safety margin, the cut-off of the selected membrane was usually well below the molecular weight of the macromolecule to be concentrated/desalted. Since these membranes contain trace amounts of glycerin, they were always pre-rinsed with distilled water prior to use. Ultrafiltration was always performed at 4°C following manufacturer's instructions.

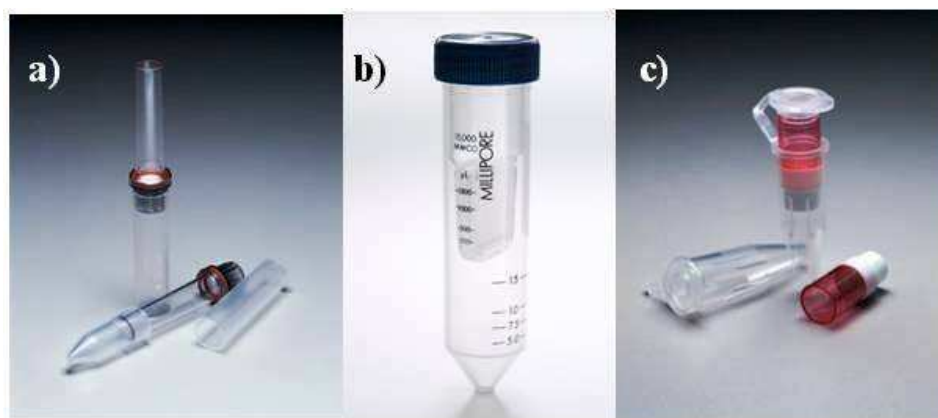


Figure 3.3 Ultrafiltration devices used for protein concentration and dialysis. Ultrafiltration of protein solutions was performed with devices containing a low adhesion cellulose membrane with a specific pore size. The protein solution to be concentrated or buffer-exchanged is loaded into the upper part of the device. When centrifuged, macromolecules larger than the membrane pore size will be retained on top of the device, while smaller molecules will pass through the membrane to the bottom part of the device. Depending on the initial volume of protein solution and on the final concentration desired, three different devices were used (all from Millipore): **a)** Centricon devices, for initial protein solution volumes of up to 2 mL and desired final volumes of 40 μ L or higher; **b)** Amicon devices, for initial volumes of up to 15 mL and final recovery volumes of 200 μ L or higher; or **c)** Microcon devices, for initial protein solution volumes of up to 500 μ L and final recovery volumes of 10 μ L or higher. (Modified from [216]).

3.7 Protein Detection

3.7.1 Protein Separation by SDS-PAGE

Sodium dodecyl sulfate-polyacrylamide gel electrophoresis (SDS-PAGE) is a common technique used to separate proteins according to their electrophoretic mobility, which is a function of molecular mass if they are previously denatured and homogeneously charged using the detergent sodium dodecyl sulfate (SDS), a strong ionic detergent. Thus, this relatively simple technique allows for the estimation of the molecular mass of a protein and/or its domains. Further, SDS-PAGE is routinely used to assess the purity of protein samples and the progress of a fractionation or purification procedure. In this study, SDS-PAGE was performed as follows (see Appendix VII for buffers compositions):

Proteins to be analyzed were previously denatured and evenly negatively charged so they could be separated primarily by mass. This was accomplished by treating the proteins with sample buffer (which contains 2% (w/v) SDS) and heating them at 95°C for 10 min in a heating block. The sample buffer includes the bromophenol blue dye as well, which facilitates supervision of the electrophoresis process. In some cases, the sample buffer additionally contained a reducing agent, usually 200 mM DTT, in order to reduce disulfide bonds and ensure disruption of tertiary and quaternary protein structures.

To obtain optimal resolution, the gels were prepared with a “stacking” gel cast over the top of the “separating” gel. The separating gel, responsible for the separation of polypeptides by size, was approximately 5 cm in length. The stacking is prepared with a lower concentration of acrylamide, lower pH and different ionic content than the separating gel. It included the sample wells, and allowed the loaded protein samples to be concentrated into a thin layer before they reached the separating gel. Gels were mounted on a Mini Protean 3 electrophoresis system (BioRad), and electrophoresis was performed with adequate buffers. (Please note that different buffers are used as cathode and anode in Tris-Tricine systems). Generally, 5-10 µg protein were loaded in each well, with equal sample volumes typically of 30 µL. Novex Sharp (Invitrogen) molecular weight marker was loaded in one well, in order to determine the molecular weight of the proteins being analyzed. Once samples were loaded into the wells, the proteins were forced to move through the gel matrix by applying a difference potential (80 V at first, and 100-120 V once the front end had reached the separating gel). Electrophoresis was usually performed until the front end reached the end of the gel (2 h approximately).

In some occasions, in particular to verify complex formation, samples were run under native conditions, using the gel, buffer and sample compositions specified in Appendix VII.

Once separated by electrophoresis, proteins were either detected directly in the gel using Coomassie blue or Silver staining methods, or transferred to nitrocellulose or PVDF membranes for analysis by Western blotting. These detection methods are described in the following sections.

3.7.2 Protein Gel Staining

To visualize protein bands in a gel, two different protein staining techniques were used, depending on the sensitivity needed: Coomassie blue staining, usually sensitive enough for regular purposes; and silver staining, of higher sensitivity.

a) Coomassie Blue Staining

Coomassie dye is the most popular reagent for staining protein bands after gel electrophoresis. In acidic solutions, Coomassie dye binds to basic and hydrophobic residues of proteins being able to detect, for most proteins, as few as 50-100 ng per band in a mini-gel [217]. Coomassie blue staining was performed as follows (see Appendix VII for the composition of solutions used):

1. The polyacrylamide gel was rinsed once with ddH₂O in a suitable container, not much larger than the gel itself.
2. Enough Coomassie stain solution was added to cover the gel, which was incubated on a rocking table for 30-60 min at room temperature.
3. After discarding the Coomassie stain solution, the gel was rinsed twice with ddH₂O and incubated in destaining solution I on a rocking table. The incubation took place for 30 min, at room temperature, and the solution was then discarded. This step was repeated twice.
4. Destaining solution I was then removed and replaced with destaining solution II. The gel was incubated in this solution at room temperature, on a rocking table, until the blue protein bands stood out against a clear background. The solution was changed as many times as necessary.

b) Silver Staining

Silver staining is a highly sensitive method for detecting proteins in polyacrylamide gels. With this technique, metallic silver is deposited onto the surface of a gel at the location of the protein bands. Proteins bind silver ions and, when these are reduced under appropriate conditions, a visible image of protein bands is achieved. This method is 100-fold more sensitive than Coomassie blue staining [218], although it requires a considerably more tedious procedure, described below (see Appendix VII for the composition of solutions used):

1. The polyacrylamide gel was rinsed once with ddH₂O in a suitable container, not much larger than the gel itself.
2. The proteins were fixed in the gel by incubating in fixative solution for at least 1 h.
3. After this time, the fixative solution was discarded and the gel was washed three times in 30% (v/v) ethanol (about 20 min each).
4. The gel was then reduced by incubation in a 0.02% (w/v) sodium thiosulfate (Na₂S₂O₃) solution for 1 min.
5. The Na₂S₂O₃ solution was discarded and the gel was washed three times with ddH₂O (about 1 min each).
6. The gel was then incubated with silver staining solution for 1 h.
7. After this time, the staining solution was removed and the gel was washed three times with ddH₂O (about 1 min each).
8. The gel was then incubated in developer solution until the protein bands became visible and, at this point, the reaction was stopped with fixative solution.

3.7.3 Protein Immunodetection by Western Blot

The Western blot (WB) is a technique used to detect specific proteins after separation by gel electrophoresis. After SDS-PAGE, proteins are electrophoretically transferred to an appropriate nitrocellulose or PVDF membrane, and probed with an antibody specific to the target protein (the primary antibody). The membrane is then incubated with another antibody (secondary antibody), directed at a species-specific portion of the primary antibody. The secondary antibody is usually linked to a reporter enzyme such as horseradish peroxidase (HRP), which in turn reacts with a chemiluminescent agent, and the reaction product produces luminescence in proportion to the amount of protein. An image of the antibodies bound to the blot can then be created by chemiluminescent detection methods.

In this work, mouse anti-His monoclonal antibody (GE Healthcare) was used for the detection of recombinant MyD88 fragments, which contain an N-terminal 6xHis tag. IRAK-4 fragments, containing an N-terminal FLAG® M2 tag (DYKDDDDK), were detected with mouse anti-FLAG® M2 monoclonal antibody (Sigma-Aldrich). Natural IRAK-4 from monocyte extracts (see section 3.8) was detected with anti-human IRAK-4 polyclonal antibody (R&D Systems). Lastly, mouse anti-MYC monoclonal antibody (Sigma-Aldrich) was used for detecting IRAK-M proteins, which have an N-terminal c-MYC (EQKLISEED) tag. Rabbit HRP-linked anti-mouse polyclonal antibody (Dako) was used, in all cases, as the secondary antibody. Protein immunodetection was performed following the procedure described below (see Appendix VII for the composition of used buffers):

1. Proteins were separated by SDS-PAGE (section 3.7.1).
2. When using a PVDF membrane, this was soaked in 100% methanol for a few seconds until its appearance changed from opaque to semi-transparent.
3. A transfer “sandwich” was prepared using the Mini Trans-blot cell system (BioRad):
 - For each gel to be transferred, four pieces of Whatman paper (about the size of the gel), one piece of nitrocellulose or PVDF membrane and two sponges were pre-wet in transfer buffer.
 - The gel and pre-wet materials were stacked as shown in Figure 3.4 and air bubbles were removed by carefully rolling a clean glass pipette over the surface of each layer in the stack.
4. The transfer tank is filled with transfer buffer and the sandwich is placed inside the tank with the membrane oriented to the anode and the gel to the cathode, so that proteins would migrate from the gel to the membrane, in the presence of an applied electric field.
5. An ice block and a stirring magnet are added into the transfer tank, which is placed on a magnetic stirrer at 4°C. The electrodes are then coupled and the electrophoretic transfer is performed at 400 mA for 2 h, with constant stirring.
6. When the transfer is finished, the apparatus is disassembled and the membrane is incubated with blocking solution containing no BSA on a rocking table, either for 1 h at room temperature or overnight at 4°C. In this manner, the non-specific binding of the antibody to the membrane is prevented.

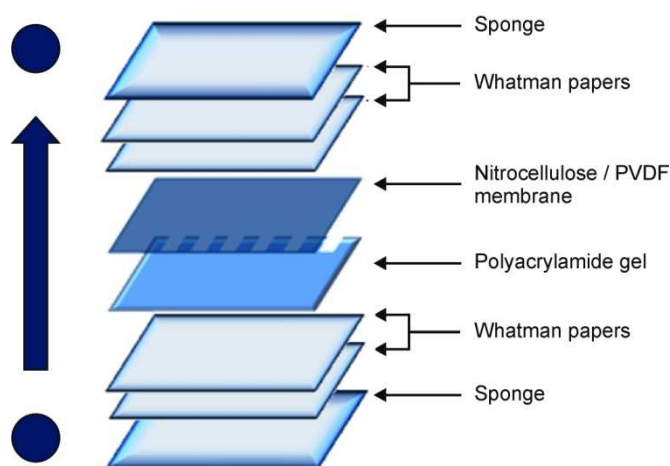


Figure 3.4 Schematic representation of the “sandwich” assembly for transferring proteins to a synthetic membrane. The polyacrylamide gel containing the proteins separated by SDS-PAGE is in contact with the nitrocellulose or PVDF membrane, which is located facing the anode. The membrane and gel are placed between two filter papers, and these in turn are located between two sponges. The whole system is immersed in a tank filled with Transfer Buffer (Appendix VII). Proteins, which are negatively charged because of the bound SDS, migrate towards the anode when an electric field is applied, being retained in the membrane.

7. The membrane is then incubated with the primary antibody for 1 h at room temperature on a rocking table.
 - For MyD88 detection, mouse anti-His monoclonal antibody (GE Healthcare) was diluted 1:3000 in blocking solution.
 - For recombinant IRAK-4 detection, mouse anti-FLAG® M2 monoclonal antibody (Sigma-Aldrich) was diluted 1:3000 in blocking solution.
 - For IRAK-M detection, mouse anti-MYC monoclonal antibody (Sigma-Aldrich) was diluted 1:5000 in blocking solution.
8. The blocking solution is removed and the membrane is washed six times (about 5 min each) with Tris-buffered saline solution (TBS).
9. The membrane is incubated on a rocking table, for 1 h, with Polyclonal Rabbit Anti-Mouse Immunoglobulin/HRP (Dako), at room temperature. The antibody was diluted 1:10000 in blocking solution.
10. The antibody-containing solution is removed and the membrane is washed six times with TBS (about 5 min each).

To develop the WB, a chemiluminescence reaction is carried out using the Immobilon Western Chemiluminescent HRP Substrate (Millipore), following the manufacturer's instructions. During the chemiluminescence reaction, horseradish peroxidase covalently coupled to the secondary antibody, and therefore indirectly to the membrane-bound target proteins, catalyzes the oxidation of luminol, a light-emitting reaction. Emitted photons are usually captured on a Curix RP 2 Plus photographic film (AGFA) placed over the membrane, in a dark room, and using G334 and G139 (AGFA) as fixating and developing reagents, respectively. Different films were exposed to the membrane for increasing periods of time. Alternatively, the emitted light was detected using the KODAK Image Station 4000MM Pro (Carestream Molecular Imaging), equipped with a CCD camera, to capture digital images of the Western blot.

3.8 Monocyte Isolation and Culture

Peripheral blood mononuclear cells were isolated from blood of healthy donors by centrifugation on Ficoll-Hypaque Plus (Amersham Biosciences), as previously reported [125, 132]. Cells were initially cultured for 2 h to a density of 10^6 cells/mL in Dulbecco's Modified Eagle Medium (D-MEM, Gibco/Invitrogen) supplemented with antibiotics (100 IU/mL penicillin and 100 μ g/mL streptomycin). The supernatant was then removed and adherent cells (2×10^6 per well) were cultured in the same medium supplemented with 10% of heat-inactivated fetal bovine serum. Purity of all cultures was verified by CD14 staining.

To prepare monocyte lysates, cells were resuspended in cold phosphate-buffered saline (PBS) at a concentration of about 10^6 cells/mL, washed, and finally incubated at 4°C for 30 min with ice-cold cell lysis buffer (see Appendix VII for buffers compositions) with gentle rotation. Cellular debris was then removed by centrifugation at 15,000g for 30 min, and the supernatant was aliquoted and stored at -20°C until further use.

3.9 Heterocomplex Formation of MyD88 and IRAK Proteins in Solution

To evaluate MyD88 affinity for the different IRAK proteins, several experiments were performed. In some cases, proteins were directly incubated in binding buffer and then purified with Ni-NTA agarose. In other cases, protein were first denatured in 8 M urea and then incubated in a proper renaturing solution, prior to Ni-NTA agarose purification. The specific procedures followed in each case are described below (see Appendix VII for the composition of buffers used).

3.9.1 Binding Assays Performed with Soluble MyD88/IRAK-4 Recombinant Fragments

To qualitatively assess IRAK-4 affinity for death domain-containing fragments of MyD88, equimolar amounts of the purified recombinant proteins of interest were mixed in binding buffer at 37°C for 2 h. After this time, the mixtures were incubated for 15 min with excess Ni-NTA agarose matrix previously equilibrated in the same buffer, and then centrifuged at 800g. The matrix was then thoroughly washed with wash buffer and specifically bound proteins were finally eluted with the same buffer supplemented with up to 500 mM imidazole (see section 3.5.1). The same binding assays and purification procedures were performed simultaneously with IRAK-4 recombinant fragments alone to exclude non-specific binding of IRAK-4 fragments to the Ni-NTA agarose matrix. To verify complex formation, samples of IRAK-4 only and MyD88+IRAK-4 were subjected to SDS-PAGE and analyzed either by protein staining or WB methods (sections 3.7.2 and 3.7.3). In some experiments, samples were alternatively separated using anti-His tag monoclonal antibody coupled to magnetic microbeds (Miltenyi Biotec), following the manufacturer's instructions.

Alternatively, various amounts of IRAK-4(L) were incubated in binding buffer with 1 μ g of purified MyD88(L) for 2 h, at 37°C. Equal volumes of Ni-NTA agarose matrix were then added to these mixtures and further incubated for 15 min. Mixtures were centrifuged to recover the affinity matrix, which was thoroughly washed with wash buffer, containing 10 mM imidazole, before eluting specifically bound proteins with reducing sample buffer. Protein fractions were analyzed by WB using anti-FLAG or anti-6xHis monoclonal antibodies.

3.9.2 Demonstration of Recombinant MyD88 Interaction with Natural Full-Length IRAK-4 Kinase

Fixed amounts (2 μg) of purified MyD88(S) or MyD88(L) were incubated with increasing quantities of cytosolic extracts from cultured human monocytes (from 1 to 100 μg of total monocyte proteins). After incubation at room temperature for 30 min, Ni-NTA agarose matrix was added to the mixtures, and samples were centrifuged at 800g for 2 min. The supernatants were precipitated with 5 volumes of cold acetone, and specifically bound proteins were recovered with reducing sample buffer after thoroughly washing the affinity matrix with cell lysis buffer. Samples were subjected to SDS-PAGE and analyzed by WB, using a human IRAK-4 affinity-purified polyclonal antibody (R&D Systems).

3.9.3 Detergent Screening to Enhance MyD88(L)-IRAK-4(L) Complex Formation

Clusters of hydrophobic residues on the protein surface can promote non-specific aggregation and interfere with complex formation with physiologically relevant partners, even if they are present in molar excess. The addition of mild, biological detergents can enhance protein solubility and promote complex formation by disturbing these non-specific hydrophobic interactions. To explore whether non-ionic detergents could enhance MyD88•IRAK-4 complex formation *in vitro*, 24 different detergents from Detergent Screen 1 (Hampton Research) were added to equimolar mixtures of recombinant MyD88(L) and IRAK-4(L) variants (see Appendix IX for a detailed formulation of the used detergents). Ten μL of each detergent were used per 100- μL aliquot of the MyD88(L)/IRAK-4(L) mixture. Each sample was incubated for 3-4 h with equal amounts of Ni-NTA matrix on a rotary shaker, at 37°C, and treated as described above (section 3.5.1).

3.9.4 Co-renaturation of MyD88 and IRAK Recombinant Domains

As another approach for demonstrating complex formation, equimolar amounts of MyD88 and IRAK variants were separately denatured in 8 M urea, mixed in various proportions, and subjected to the fractional factorial folding screen, essentially as described in section 3.4.2. After overnight incubation at 4°C, the pH was adjusted to 7.0 with concentrated sodium phosphate and excess Ni-NTA matrix equilibrated in the appropriate renaturing condition was added. Samples were incubated for 30 min at room temperature, and then the affinity matrix was treated as described in section 3.5.1 to recover specifically bound proteins. For larger-scale experiments, protein mixtures were added drop-wise to the most suitable renaturing condition

found in the factorial screen, and treated as above. Samples of all eluted fractions were analyzed by WB (see section 3.7.3).

Alternatively, a fixed amount of MyD88(S) (10 μg) was incubated with increasing quantities of IRAK-4(L) (from 1 to 20 μg) in 8 M urea, and mixtures were co-renatured by rapid dilution in FoldIt condition 5 (with sodium phosphate pH 7.0 instead of MES). Soluble proteins were pulled down with Ni-NTA matrix, and treated as described above. A similar experiment was conducted with approximately molar equivalent amounts of IRAK-4(S) (from 0.58 to 11.63 μg). Samples of all eluted fractions were analyzed by Western blot.

3.10 Protein Characterization

3.10.1 Dynamic Light Scattering

Dynamic light scattering (DLS) is a non-invasive technique for measuring the size of macromolecules and small particles typically in the submicron size range. Particles and molecules in suspension undergo Brownian motion, which is caused by the large number of solvent molecules continuously colliding with the much larger particles, which consequently move in a random manner. If the particles or molecules are illuminated with a laser, the intensity of the scattered light fluctuates at a rate that is dependent upon the size of the particles (smaller particles move faster). The particle diameter that is measured in DLS experiments is called the hydrodynamic diameter, and refers to how a particle diffuses within a fluid. The diameter obtained by this technique is that of a sphere that has the same translational diffusion coefficient as the particle being measured. The translational diffusion coefficient depends not only on the size of the particle core, but also on any surface structure, as well as on the concentration and nature of ions in the solution [219].

In this work, purified proteins to be analyzed were first centrifuged and filtered to remove dust particles from the solution, and then subjected to DLS. Twenty μL of each protein at 0.1 mg/mL were measured in a 100- μl quartz micro cuvette using a Zetasizer Nano S instrument (Malvern Instruments Ltd), equipped with a He-Ne ion laser (633 nm). The results were evaluated with built-in software.

3.10.2 Limited Proteolysis

Purified recombinant proteins or their complexes were incubated at 25°C with endoproteinases Glu-C or chymotrypsin at a 1:100 enzyme to protein ratio. Additionally, free

MyD88(L) was digested at 37°C with endoproteinase Arg-C at a 1:200 enzyme to protein ratio. The procedures followed for each enzyme digestion are described below.

a) **Glu-C digestion**

Approximately 50 µg of the proteins of interest were buffer-exchanged into 100 mM ammonium bicarbonate, pH 7.9, and concentrated to a final volume of 350 µL using ultrafiltration devices (see section 3.6.2). A 40-µL aliquot was taken from each sample before adding endoproteinase Glu-C, and incubated with 8 µL of reducing sample buffer (see Appendix VII) at 95°C for 10 min. Five hundred ng of sequencing grade endoproteinase Glu-C (Roche) were added to the remaining protein samples, and mixtures were incubated at 25°C in a heating block for up to 8 h. Forty-µL aliquots were taken during the digestion process, usually from 5 min to 8 h. The reactions were stopped by immediately adding 8 µL of 6X reducing sample buffer to each aliquot and heating the tubes at 95°C for 10 min. All samples were subjected to SDS-PAGE and WB analysis, using appropriate antibodies (see section 3.7.3). The same protocol was followed for MyD88(S)•IRAK-4(L) Glu-C digestion. Prior to the experiment, the complex was prepared using 50 µg of IRAK-4(L) and an equimolar amount of MyD88(S), and purified with Ni-NTA agarose (see section 3.5.1).

b) **Chymotrypsin digestion**

Fifty µg of the proteins to be digested were buffer-exchanged into chymotrypsin digestion buffer (100 mM ammonium bicarbonate, pH 7.9, 10 mM CaCl₂) and concentrated to a final volume of 350 µL, using ultrafiltration devices (see section 3.6.2). Aliquots were taken from each sample before adding the protease, and incubated for 10 min with 8 µL of 6X reducing sample buffer, at 95°C. Five-hundred ng of chymotrypsin sequencing-grade (Roche) were then added to the remaining samples and incubated for up to 8 h in a heating block, at 25°C. Forty-µL aliquots were taken during the digestion process at various times (from 5 min to 8 h). The reactions were stopped by immediately adding 8 µL of reducing sample buffer to each aliquot and heating the tubes at 95°C for 10 min. All samples were subjected to SDS-PAGE and WB analysis, using appropriate antibodies (see section 3.7.3).

c) **Arg-C digestion**

Proteins of interest were buffer-exchanged into Arg-C digestion buffer (100 mM Tris-HCl pH 7.6, 10 mM CaCl₂) and concentrated to a final volume of 260 µL, using ultrafiltration devices (see section 3.6.2). Thirty µL activation solution (50 mM DTT, 5 mM EDTA) were added to the concentrated sample, and a 30-µL aliquot was taken from this mixture and mixed with 3 µL of 0.5 M EDTA. Sequencing-grade endoproteinase Arg-C (Roche) was resuspended in a solution

containing 50 mM Tris-HCl pH 8.0, 10 mM CaCl₂, 5 mM EDTA, at a final concentration of 0.1 µg/mL. Eight µL of this Arg-C aliquot were added to the protein sample at a final enzyme to protein ratio of 1:200. Arg-C digestion was allowed to proceed at 37°C for up to 8 h in a heating block, and 30-µL aliquots were taken at various times (from 5 min to 8 h). All aliquots were immediately mixed with 3 µL of 0.5 M EDTA, in order to stop proteolysis. Alternatively, the digestion was stopped by adding 6 µL of 6X reducing sample buffer to all aliquots, instead of EDTA, and the mixtures were heated for 10 min in a heating block, at 95°C. All samples were subjected to SDS-PAGE (see section 3.7.1) and the gels were stained with Coomassie Brilliant Blue (see section 3.7.2).

3.10.3 Surface Plasmon Resonance Studies

For surface plasmon resonance (SPR) studies, one interacting partner (the ligand) is attached to the surface of a sensor chip, and then a solution containing the other interaction partners (the analytes) is allowed to pass over the coated surface. Binding of molecules to the sensor surface generates a response that is proportional to the bound mass, and changes in the amount of bound protein can be detected on the sensor surface. The response is measured in resonance units (RU) and is directly proportional to the concentration of biomolecules bound to the surface.

One approach for attaching biomolecules to the surface of the sensor chip is the high affinity capture, where the molecule of interest is attached by non-covalent interaction with another molecule, which is in turn covalently immobilized to the chip surface. In this work, all SPR studies were performed at 25°C, using Sensor Chip NTA (GE Healthcare).

a) Sensor Chip NTA

This sensor chip has a glass surface covered with a uniform thin layer of gold, and a covalently bound layer of carboxymethylated dextran molecules to protect samples from contact with the metal layer. This dextran surface also contains immobilized NTA (manufactured by

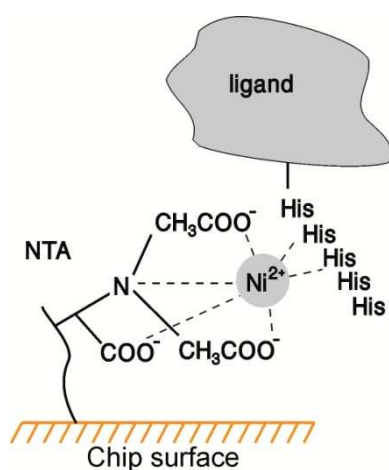


Figure 3.5 Ni²⁺-NTA interaction with polyhistidine-tagged ligands. Nickel ions form a chelation bond between NTA immobilized on the surface and polyhistidine tags on the ligand. (From [220]).

Qiagen), which chelates metal ions such as Ni^{2+} , creating coordination sites that bind to polyhistidine-tagged ligands (Figure 3.5).

b) Protein immobilization procedure

All SPR studies were carried out at the Institut de Biologie Structurale (Grenoble, France), under the supervision of Dr. Nicole Thielens. All experiments were performed on a Biacore® X system (GE Healthcare), which contains two flow cells (Fc1 and Fc2), using the built-in BIAevaluation software. First, before immobilization, proteins of interest were diluted in SPR running buffer (see Appendix VII), previously filtered through a 0.45 μm pore-size membrane, and all protein solutions were centrifuged at 13,000 rpm for 10 min. The chip was washed by passing 20 μL of 350 mM EDTA through Fc1 and Fc2, at a flow of 20 $\mu\text{L}/\text{min}$. Then, to allow capture of histidine-tagged proteins, the surface of the sensor chip NTA was activated with Ni^{2+} by passing 20 μL of 500 μM NiCl_2 through both flow cells. Then, 40 μL His-tagged protein solution were passed over the surface of the chip (through Fc2 only) in SPR running buffer, at a constant flow of 20 $\mu\text{L}/\text{min}$. After stabilization of the signal, 40 μL of analytes were injected through both flow cells, in SPR running buffer, at a constant flow of 20 $\mu\text{L}/\text{min}$. Binding was detected and registered during the experimental procedure and sensorgrams were analyzed with the provided software. To remove any nickel ions and bound proteins remaining on the NTA surface, the chip was regenerated after each analysis cycle with 60 μL of 350 mM EDTA along with other different solutions. See Table 4.3 (Results) for a summary of all experimental set-up steps used for SPR analysis.

3.10.4 Analytical Ultracentrifugation

Analytical ultracentrifugation (AUC) is a technique used to analyze biological molecules in solution, in specially designed centrifuges, which can, for instance, separate the different multimeric states of a given biological molecule. The sedimentation rate of the molecule is monitored continuously to obtain the molecular weight profile of the species observed, from which the multimeric state(s) of this molecule can be determined. This technique is also very helpful for studying protein-protein interactions in solution. In AUC analysis, sedimentation velocity is much more frequently used than sedimentation equilibrium, since it can be applied to a wider range of biological systems. Sedimentation velocity is a method that measures the rate at which molecules move towards the bottom of the cell in response to a high speed centrifugal force generated in a centrifuge. This sedimentation rate provides information about both the molecular mass and shape of the molecule(s) under study.

Sedimentation velocity experiments were performed on a ProteomeLab™ XL-I Analytical Ultracentrifuge, equipped with an 8-place An-50 Ti Rotor and cells with double-sector

centerpieces of 12 mm optical path length and sapphire windows (Beckman-Coulter Instruments). For the first measurements, a wavelength and radial scan at 280 nm was acquired at 20°C at a rotor speed of 3000 rpm. Afterwards, sedimentation velocity was performed at 20°C at a rotor speed of 42000 rpm, overnight, at 280 nm. The duration of the scan was ~1.5 min per radial scan at a given wavelength per cell, and samples were analyzed with SEDFIT [221]. Each sample was dissolved in a different solution, which was used as optical reference for that sample (see Appendix VII for the composition of each buffer used). The loading volume (~450 µL) was identical for the reference and sample chambers of the double-sector centerpiece, and a counterbalance was used in one cell to provide a reference for calibrating radial distances and to balance the opposing cell. Major sample and buffer characteristics are summarized in Table 4.4 (Results). The density and viscosity of the ultracentrifugation buffers were calculated from their respective compositions, and the partial specific volume and molecular weights of the proteins were calculated based on the amino acid composition, using the software SEDNTERP [222].

3.11 Crystallization of MyD88 DD Recombinant Fragments and Their Complexes with IRAK-4(L)

3.11.1 Protein and Complex Preparation for Crystallization

Crystallization tests were performed with protein samples that were previously dialyzed against HEPES or Tris-based buffers (see Appendix X) using Amicon Ultra-15 ultrafiltration devices (Millipore), and concentrated to final concentrations of 1-10 mg/mL using these and Microcon ultrafiltration devices (Millipore), for further concentration (section 3.6.2). Samples were either dialyzed directly after Ni-NTA purification (section 3.5.1), or separated into monomers, dimers and multimers by FPLC procedures (section 3.5.3), prior to dialysis.

3.11.2 Finding Optimal Crystallization Conditions for Crystal Growth

Screenings to find optimal crystallization conditions for crystal growth were performed by hanging-drop and sitting-drop vapor-diffusion methods (see Figure 3.6). Hanging-drop vapor-diffusion trials were set up in 24-well ComboPlates™ (Greiner), using siliconized glass coverslips (18 mm diameter) to cover each well, and silicone grease (Bayer) to seal the plates. Alternatively, EasyXtal 15-Well (formerly 24-Well) Tool plates with standard X-Seal crystallization supports (both from Qiagen), which minimize evaporation and prolongs the reuse of reservoir solutions, were used for hanging-drop experiments. Sitting-drop vapor-diffusion trials were set up in 24-well Linbro Plates (Hampton Research), using Crystal Clear sealing tape (Hampton Research) to seal the plates.

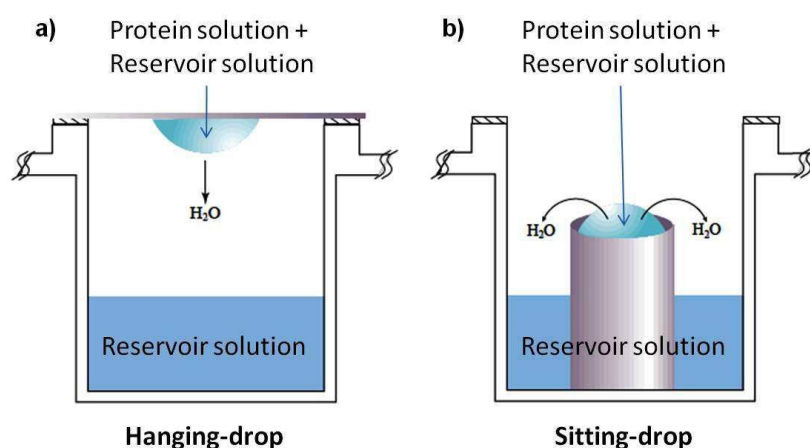


Figure 3.6 Hanging- and sitting-drop vapor diffusion crystallization methods. Hanging- and sitting-drop vapor diffusion methods entail a droplet containing purified protein, buffer and precipitants, which is allowed to equilibrate against a larger reservoir containing the same buffer and precipitants. Initially, the droplet of protein solution contains an insufficient concentration of precipitant for crystallization, but as water vaporizes from the drop and transfers to the reservoir, the precipitant concentration increases to a level optimal for crystallization. Both methods require a closed system, and differ in the vertical orientation of the protein solution drop within the system. **a)** Diagram of the hanging-drop method, in which the drop hangs from a cover slice placed on top of the reservoir. **b)** Diagram of the sitting-drop method, in which the protein drop sits on a pedestal above the reservoir solution. Drop volumes varied from 1 to 3 μL and could have different volume ratios between the protein and crystallization solutions. (Modified from [223]).

Initial screenings were performed using reagents from Crystal Screens 1 and 2 (Hampton Research) and Morpheus™ MD1-46 (Molecular Dimensions). Crystallization reagents from ProPlex™ MD1-38 were also used for some crystallization assays (see Appendix X for a detailed list of used crystallization solutions). Protein solutions were centrifuged at 13,000g for 2-5 min to remove all suspended particles before setting up the crystallization experiments. Regardless of the used system, one drop of concentrated protein solution (1-2 μl) was mixed with one drop of crystallization solution, of equal volume. Manipulation of the drop volume ratio is one of the commonly used strategies for optimizing the crystallization conditions. In this study, initial screenings were performed using 1 μL of protein solution and 1 μL of crystallization solution for a final drop volume of 2 μL . In all cases, this final drop was allowed to equilibrate over a reservoir containing 0.5-1 mL crystallization solution in a Rumed 3201 incubator (Rumed), at a constant temperature of 20°C. Drops were periodically observed under a Nikon SMZ800 zoom stereomicroscope equipped with a digital camera.

3.11.3 Crystal-quality Optimization Methods

Crystallization is a phase transition phenomenon that can be illustrated by a phase diagram showing which state (soluble, crystalline or amorphous) is stable under a variety of

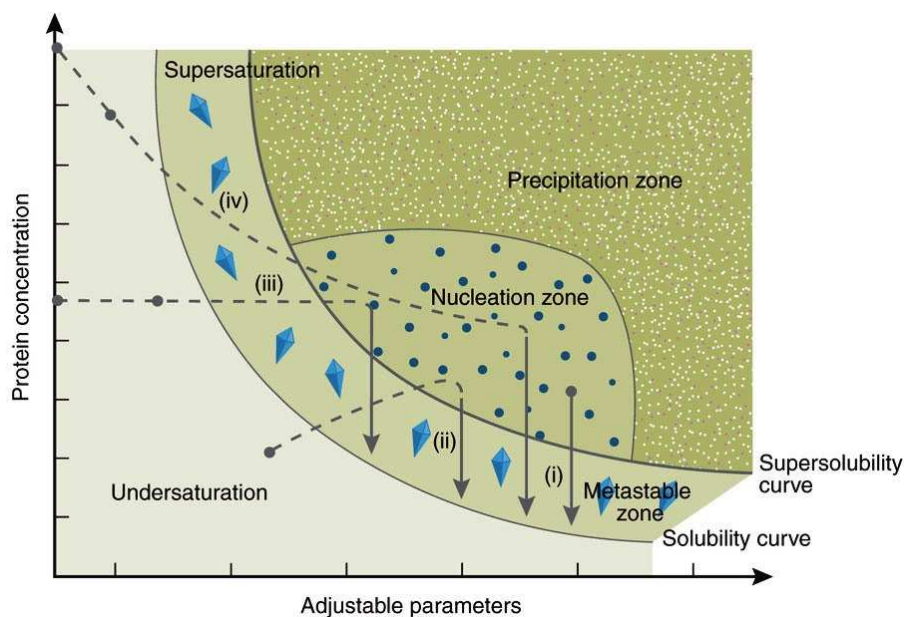


Figure 3.7 Schematic illustration of a protein solubility phase diagram. Adjustable parameters include precipitant or additive concentration, pH and temperature. The four most commonly used crystallization methods are represented: (i) microbatch, (ii) vapor diffusion, (iii) dialysis and (iv) free interface diffusion. Each involves a different route to reach the nucleation and metastable zones, assuming the adjustable parameter is precipitant concentration. The filled black circles represent the starting conditions. Two alternative starting points are shown for (iii) and (iv) because the undersaturated protein solution can contain either protein alone or protein mixed with a low concentration of the precipitating agents. The solubility curve is defined by the concentration of protein in the solution that is in equilibrium with that in crystals. The supersolubility curve separates conditions under which the crystallization solution remains clear from those under which spontaneous nucleation, phase separation or amorphous precipitation occurs. (From [224]).

physico-chemical parameters. The phase diagram is obtained experimentally by varying two parameters at a time. In a typical crystallization phase diagram (Figure 3.7), four regions can be distinguished: an area of very high supersaturation, where the protein will precipitate; an zone of moderate supersaturation, where spontaneous nucleation will take place; an region of lower supersaturation just below the nucleation zone, where crystals are stable and may grow, but no further nucleation will take place (referred to as the metastable zone, this region is usually best for growth of large, well-ordered crystals); and an undersaturated area, where the protein is fully stable in solution and will never crystallize [225-227].

Crystallization proceeds in two phases: nucleation (a prerequisite) and growth. The optimal conditions for nucleation may not be the same as for crystal growth: nucleation occurs when the solution is supersaturated, whereas ordered growth of crystals is optimal in a state of lower supersaturation, corresponding to the metastable zone (Figure 3.7). Once a critical nucleus has formed, growth follows spontaneously [227-229]. By examining the crystallization phase diagram and solubility properties of a protein, an understanding may be gained to optimize the

process of crystal growth. The four commonly used crystallization methods (microbatch, vapor diffusion, dialysis and free interface diffusion) proceed through the phase diagram following different routes. In the vapor diffusion method, the protein solution is initially undersaturated and gradually reaches supersaturation by equilibration with a solution containing the crystallization agents (see Figure 3.7).

a) Pre-growth optimization techniques

Sometimes in a crystallization test, the system is far from the nucleation zone and no crystals are allowed to form. However, very often, excess nucleation occurs, resulting in the formation of numerous low-quality crystals [230]. Excess nucleation can be bypassed by inserting formed nuclei directly into the metastable zone, which ensures the presence of only one or a limited number of nuclei that can then grow into large single crystals. The best way to achieve this is by seeding the metastable zone with already-grown small crystals (macro-seeding), microcrystals or an ordered precipitate (micro-seeding), of the same protein [229, 231, 232].

In this study both macro- and micro-seeding techniques were employed. For macro-seeding procedures, which involve seeding with visible single crystals, a loop was used to move the crystal from the drop it grew in, to a new metastable drop. For micro-seeding, in which the seeds are too small to be viewed directly, a hair or fiber was used to touch a crystal and pick some microcrystals from the contact. The hair was then streaked through the new drops, dispensing the seeds as a dilution series (see Figure 3.8).

Other parameters that can be varied to influence the crystallization process are the concentration of the precipitant agent, the volume of the reservoir, the ratio between the volumes of protein and crystallization solutions in the drop, the pH of the crystallization solution, the use of additives such as detergents, and the size of the crystallization drop. In this study, 1:2, 1:1, 1.5:1, 2:1 and 3:1 protein to crystallization solution ratios were tested, in final drop volumes of 1-3 μL , and the reservoir volume was varied from 0.5 to 1 mL.

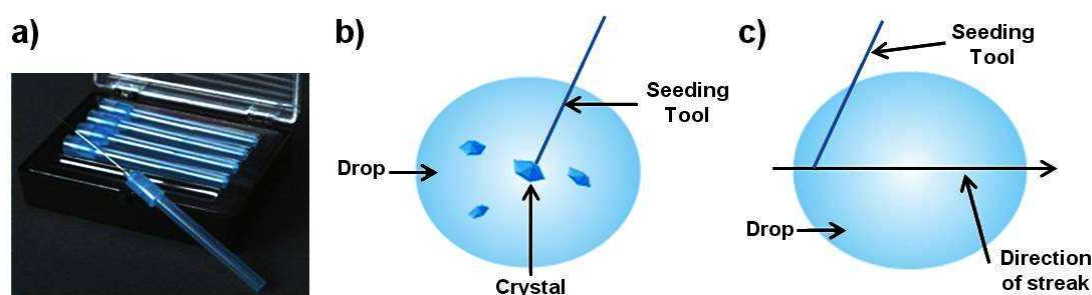


Figure 3.8 Micro-seeding technique for growing protein crystals. A hair or fiber is used to pick some microseeds from a drop, and dispense them through a new drop. **a)** Seeding tool used to pick up the seeds. **b)** Microseeds are first collected from the original drop by contact. **c)** Microseeds are spread on a new drop by passing the fiber through it. (From [233]).

b) Post-growth optimization techniques

The crystal harvesting and data collection techniques described in sections 3.11.4 and 3.11.5 below can distort the crystal lattice and increase the mosaicity of the crystal, ultimately resulting in a lower data resolution. To overcome this problem, frequently associated with an incorrect manipulation of the crystal and ice formation on its surface, the crystal can be submitted to an annealing procedure before data collection. In this study, crystals were sometimes annealed by the flash-annealing technique [234], in which the cold nitrogen stream that is directed to the crystal during data collection (Figure 3.9, section 3.11.5) is blocked for a few seconds. In this manner, the cryoprotectant is allowed to homogeneously distribute through the crystal before cooling it down again to the temperature of liquid nitrogen.

3.11.4 Crystal Harvesting and Cryopreservation

To overcome the radiation damage associated with room-temperature data collection, cryogenic conditions are nowadays almost always used. In this method, crystals are flash-cooled to cryogenic temperatures, usually near 110 K [235], and maintained at this temperature during data collection. It is essential to cool the crystal while preventing ice formation on its surface, which may produce high backgrounds due to water scattering, and without distorting the crystal lattice or increasing its mosaic spread. This is achieved by modifying the liquid layer with reagents known as cryoprotectants, which effectively prevent ice formation when added at an appropriate concentration. The most frequently used cryoprotectants are 10-30% (v/v) glycerol, 10-30% (v/v) ethylene glycol, and 25-35% (v/v) polyethylene glycol (PEG) 400. The use of glucose, 2-methyl-2,4-pentanediol (MPD), or xylitol has also been reported [236]. In this study, cryoprotectants were selected by comparing the condition in which a particular crystal was grown to the conditions of the Crystal Screen Cryo kit (Hampton Research); the selected cryoprotectant was the one used in the most similar condition of this kit. Crystals were collected directly from the drop with either nylon loops (Hampton Research) or LithoLoopsTM (Molecular Dimensions) of the appropriate size. After a brief immersion in the cryoprotectant solution, the crystal was quickly placed in liquid N₂, where the loop containing the crystal was inserted into a magnetic vial. Crystals grown in MorpheusTM crystallization conditions (Molecular Dimensions) were directly frozen in liquid N₂, since their formulations include cryoprotectant agents. All crystals were maintained in liquid N₂ until data collection.

3.11.5 X-Ray Diffraction Data Collection

To obtain the diffraction patterns, the loop containing the crystal was mounted on a goniometer head under a steady stream of liquid N₂ to prevent crystal decay during data

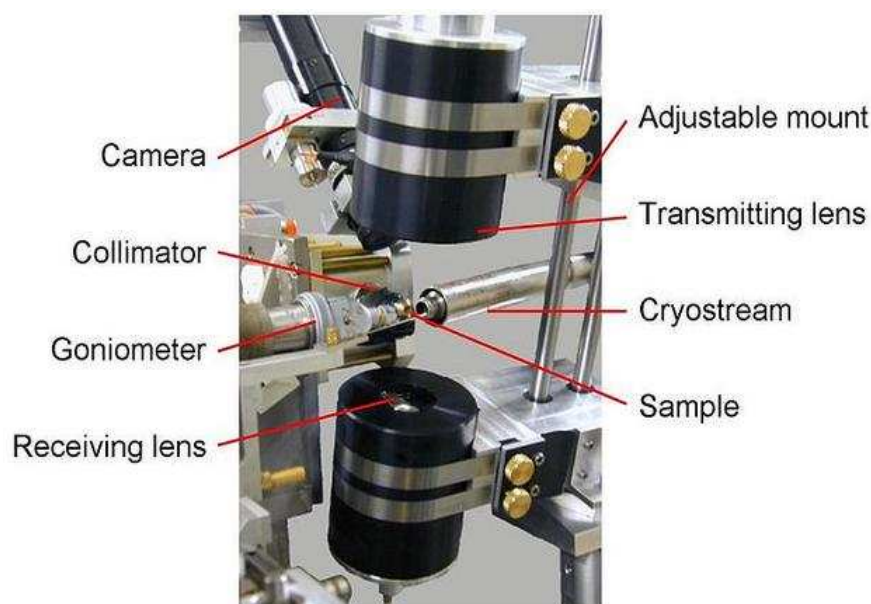


Figure 3.9 Typical X-ray diffraction unit. Example taken from ID14-4 (ESRF). The X-ray source consists of a tube having a filament, which acts as a cathode opposite to a water cooled anode. A high voltage is passed through the filament and high energy electrons are produced. The sample holder is a needle that holds the crystal in place while the X-ray diffractometer takes readings. The detector is a transducer that counts the number of photons that collide into it. This photon counter gives a digital readout in number of photons per unit time. The crystal can be rotated during measurements, and a liquid N₂ stream is directed to it at all times to keep it cold.

collection. The crystal was aligned in a beam of X-rays and diffraction data was collected with a coupled X-ray detector as the crystal was rotated with the goniometer (see Fig. 3.9). An image was taken at each angle of rotation, usually between 0.5-1 degrees, depending on the cell constants and crystal quality (mosaicity), as discussed below.

In this study, all diffraction measurements were performed at the European Synchrotron Radiation Facility (ESRF), in Grenoble (France), using the ID-29, ID-23, BM-16 or ID-14 beamlines, equipped with different detectors (see details in Table 3.2).

Table 3.2 Main characteristics of the ESRF beamlines used for X-ray diffraction analysis of protein crystals.

Beamline	Energy (keV)	Minimum beam size (μm^2)	Maximum beam size (μm^2)	Detector
ID14-1	13.27 (fixed)	50x50	300x300	ADSC Q210 CCD
ID14-2	13.294 (fixed)	50x50	200x200	ADSC Q4 CCD
ID23-1	5-20 (tunable)	10x10	30x45	ADSC Q315R CCD
ID23-2	14.2 (fixed)	8x5	8x5	MarMosaic225 CCD
ID29	6-20 (tunable)	10x10	75x30	Pilatus 6M
BM16	6.5-17 (tunable)	100x100	200x200	ADSC Q210r CCD

Collecting a full data set from a single crystal requires previous knowledge of its space group, unit cell parameters, and its orientation with respect to the X-ray beam. With this information, an adequate strategy for data collection can be established, determining the optimal rotation angle(s) for data collection (the lower the symmetry, the greater the rotation angle). In this study, a small number of diffraction data was initially collected for each crystal (usually two images, at perpendicular angles). These initial images were useful for evaluating the crystal quality and anisotropy, in the first place, and determining basic crystallographic information (possible space group and cell constants) for a full data collection. Data collection was controlled with the beam-line control computer using the MxCuBe software [237].

3.11.6 Diffraction Data Processing: Integration and Data Reduction

For the mathematic analysis of crystal diffraction data, it is useful to consider the diffracted beams as resulting from reflections on crystal planes. Each reflection can be labeled with a value (hkl) corresponding to the Miller indices of the lattice planes [238]. In this work, the intensities corresponding to each reflection were determined with MOSFLM [239], following the steps briefly summarized below.

First, the space group, crystal orientation and unit cell dimensions were determined with the autoindexing option and initial data (usually one or two images). This unit cell was then refined with data from at least two images or groups of images separated by 90°, and all frames were integrated to obtain the whole set of I(hkl) intensities. Finally, these intensities were reduced to the corresponding structure factor modules F(hkl), which contain information from all atoms within the asymmetric unit of the crystal. The structure factor F(hkl) is a mathematical function describing the amplitude and phase of a wave diffracted from crystal lattice planes, characterized by Miller indices (hkl). This function is defined by Equation 3.3, where (x,y,z) are the coordinates of the individual atoms of the unit cell, f_j is the scattering factor of the atom j, and N is the total number of atoms contained in the crystal unit cell. In this study, structure factors were calculated using the CCP4i program suite [240] and, in particular, the SCALA program [241].

$$F(hkl) = \sum_{j=1}^N f_j e^{2\pi i(hx_j + ky_j + lz_j)} \quad \text{Equation 3.3}$$

The three-dimensional electron density map determined from an X-ray diffraction experiment, is the Fourier transform of the structure factors. This function is defined by Equation 3.4, where $p(xyz)$ is the electron density function in a point of the unit cell given by the coordinates (x,y,z), corresponding to a diffracted beam with Miller indices (hkl), and $\Phi(hkl)$ represent the phases of the structure factors F(hkl).

$$\rho(xyz) = \frac{1}{V} \sum_h \sum_k \sum_l |F(hkl)| \cos 2\pi(hx + ky + lz - \Phi(hkl)) \quad \text{Equation 3.4}$$

The electron density map describes the contents of the unit cells averaged over the whole crystal. However, to calculate an electron density map, both amplitudes and phases of the diffracted X-rays are needed, and the phases cannot be experimentally measured. This is known as the phase problem, and the resolution of a crystal structure necessarily starts with the calculation of an appropriate set of phases $\Phi(hkl)$.

3.11.7 Crystal Structure Determination

As mentioned above, solving the phase problem is a crucial step for crystal structure determination. In this study, we attempted to solve the phase problem by molecular replacement, a method in which a similar known structure is used to derive initial phase values (Φ_{calc}). This method is also known as Patterson search. The Patterson function $P(u,v,w)$ is essentially the Fourier transform of the intensities rather than the structure factors, and it is defined by Equation 3.5, where coordinates (u,v,w) represent the differences between the coordinates (x,y,z) of each pair of atoms in the crystal: $u=x_1-x_2$, $v=y_1-y_2$, $w=z_1-z_2$.

$$P(u,v,w) = \sum_h \sum_k \sum_l |F(hkl)|^2 e^{-2\pi i(hu+kv+lw)} \quad \text{Equation 3.5}$$

The Patterson function simplifies the information contained in the electron density function (Equation 3.4), since the term containing the phases is removed and the amplitudes of the structure factors are replaced by their squares. The Patterson function can be calculated immediately from the available experimental data (intensities), and the information provided by the maxima of this function corresponds to the relative positions between each pair of atoms in the structure. If Patterson maps are generated for the data derived from both the unknown and the similar, known structures, the correct orientation and position of the unknown molecule within its unit cell can be inferred, since both maps should be closely correlated. Fortunately, the molecular replacement search in a six-dimensional space can be usually divided into two independent three-dimensional searches: a rotation and a translation search.

In the rotation function, the unknown Patterson map is compared to Patterson maps derived from the known similar structure in different orientations. The R-factor (R) is a measure of the agreement between the crystallographic model (F_{calc}) and the experimental X-ray diffraction data (F_{obs}), and it is used to score the rotation function. The R-factor can be calculated from Equation 3.6, where F is the structure factor, and the sums extend over all the reflections measured and their calculated counterparts. The highest correlation is obtained when the two structures (known and unknown) are in similar orientations.

$$R = \frac{\sum |F_{\text{obs}} - F_{\text{calc}}|}{\sum |F_{\text{obs}}|} \quad \text{Equation 3.6}$$

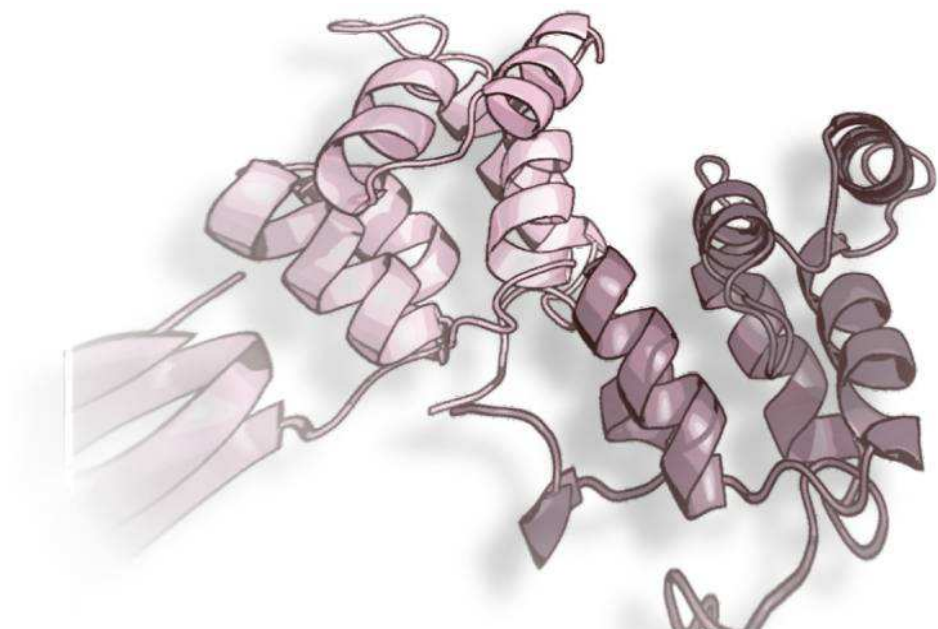
The second step of the molecular replacement search is the translation function, in which the oriented model is correctly positioned by translating it to the correct coordinates within the asymmetric unit. This is accomplished by moving the model, calculating a new Patterson map, and comparing it to the unknown-derived Patterson map.

Once the phasing models are correctly oriented and translated, the phases derived from them can be used to calculate electron density maps, used to build and refine an atomic model of the unknown structure. The quality of an electron density map depends on the quality of the diffraction data collected, especially on the obtained resolution.

3.12 Three-Dimensional Modeling of MyD88 and IRAK-4 Death Domains

Three-dimensional models were generated with SWISS-MODEL server [242] and depicted with the MIFit 8 program (<http://code.google.com/p/mifit>). Model quality was assessed with PROCHECK [243], and structure figures were generated with PyMOL [244].

4. Results



4.1 Preliminary Studies on MyD88 and IRAK Recombinant Proteins

4.1.1 Sequence Comparisons Indicate the Presence of a Seventh C-Terminal Helix in the Death Domain of MyD88, in Addition to the Conserved Six-Helix Bundle

Despite notable similarities in immune responses in insects and mammals, there also exist important differences. To study complex formation between human MyD88 and IRAK proteins, and to analyze the contributions of the corresponding globular/unstructured regions to this process, we cloned and overexpressed the death domains of these proteins, both alone and extended by the full-length linkers to their C-terminal TIR or kinase domains (see Figure 4.1 for a schematic representation of domain organization and structure of generated variants). To determine the boundaries of the globular domains, the amino acid sequences of MyD88 and IRAK-4 from different vertebrate species were aligned with the help of available structural information on murine IRAK-4 death domain [111] and the Tube•Pelle complex [174]. The results of the combined analysis are summarized in Appendix II. Of particular note, residues Ile¹⁰⁹ to Lys¹¹⁹

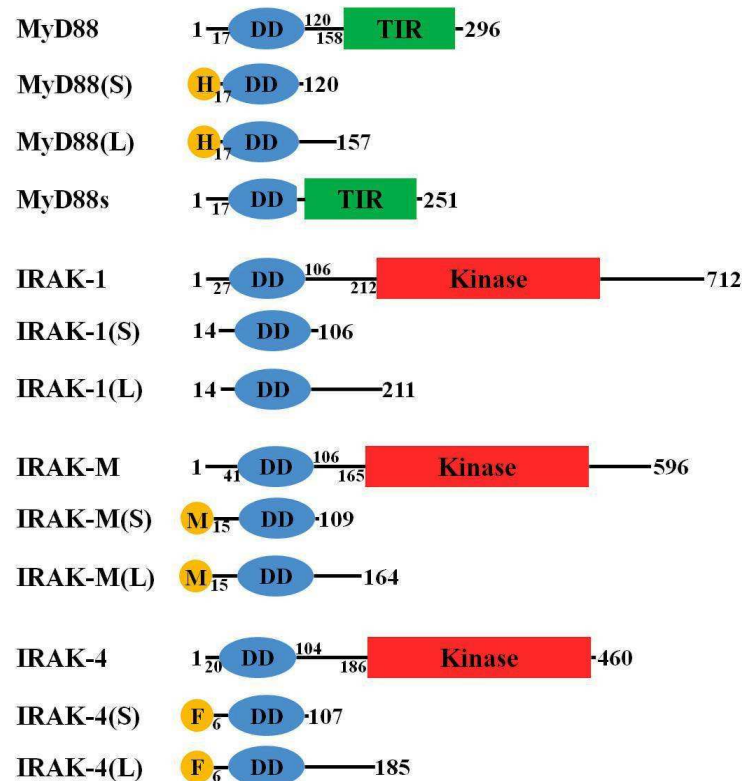


Figure 4.1 Schematic representation of domain organization in human MyD88 and IRAK proteins. Numbers indicate approximate domain boundaries; those of MyD88 death domain correspond to the structure-based alignment given in Appendix II. The structure of truncated variants generated in the current study is shown below their corresponding native proteins; encircled letters H, M and F point to the N-terminal tags attached to these recombinant forms (6xHis, c-MYC and FLAG, respectively). Also represented is the natural truncated variant MyD88s, which lacks the last helix of the death domain from the adaptor along with most of the DD-TIR linker (see text for details).

in human MyD88 are highly similar to those of *Drosophila* Pelle, in striking contrast to the rather low sequence conservation throughout the DD superfamily. This observation and the results of secondary structure predictions allow us to predict with high confidence that MyD88 possesses a seventh, C-terminal helix, in addition to the conserved framework of six antiparallel helices observed in Pelle [174], as well as in death domains from murine IRAK-4 [111], *Drosophila* Tube [174], Fas [103] and FADD [109, 245].

4.1.2 Expression and Characterization of MyD88 and IRAK Death Domains

“Short” and “long” variants of MyD88 and IRAK-death domains were expressed in *E. coli* cells and purified as described in Materials and Methods. A summary of protein expression, renaturation and purification conditions is given in Table 4.1, and an SDS-polyacrylamide gel of the eight purified recombinant proteins is shown in Figure 4.2 (see also Table 4.2 for the main physicochemical parameters of these recombinant fragments).

In our preliminary expression experiments we noticed that preparations of the linker-extended forms of the studied proteins underwent limited proteolysis upon longer incubation at 4 °C. Analysis of these fractions revealed molecular masses ranging between those of the “L” and

Table 4.1 Summary of expression, renaturation and purification conditions for MyD88 and IRAK recombinant fragments generated in the current investigation. The most frequently used *E. coli* strains and conditions for the expression of MyD88 and IRAK recombinant fragments are indicated, as well as the preferred renaturation and purification conditions for each variant (see text for further details). IB, inclusion bodies.

Construct	Host	Localization	Renaturation and purification conditions
MyD88(S)	BL21(DE3) or BL21 Star TM (DE3)pLysS	Insoluble (IB)	FoldIt condition 13 ^(a) /Affinity chromatography on Ni-NTA
MyD88(L)	BL21 Star TM (DE3)pLysS	Soluble (cytosol)	- /Affinity chromatography on Ni-NTA
IRAK-1(S)	BL21 Star TM (DE3)pLysS	Soluble (cytosol)	-/Anion-exchange chromatography on Q-Sepharose
IRAK-1(L)	BL21 Star TM (DE3)pLysS	Insoluble (IB)	FoldIt condition 8 ^(b) /Anion-exchange chromatography on Q-Sepharose
IRAK-M(S)	BL21(DE3)	Soluble (cytosol)	-/Anion-exchange chromatography on Q-Sepharose
IRAK-M(L)	BL21(DE3)	Insoluble (IB)	FoldIt condition 8 ^(c) /Anion-exchange chromatography on Q-Sepharose
IRAK-4(S)	BL21(DE3)	Insoluble (IB)	Dialysis against low-salt buffer*/Anion-exchange chromatography on Q-Sepharose
IRAK-4(L)	BL21(DE3)	Insoluble (IB)	FoldIt condition 8 ^(d) /Anion-exchange chromatography on Q-Sepharose

^(a)Similar results were obtained in FoldIt condition 6. ^(b)Similar results were obtained in FoldIt condition 16. ^(c)Similar results were obtained in FoldIt conditions 3, 7, 9, 13 and 14. ^(d)Similar results were obtained in FoldIt conditions 3, 6, 9, 10, 11 and 12. *Dialysis buffer: 20 mM Tris-HCl, pH 8.0, 100 mM NaCl, 5 mM 2-ME, 1 mM LDAO.

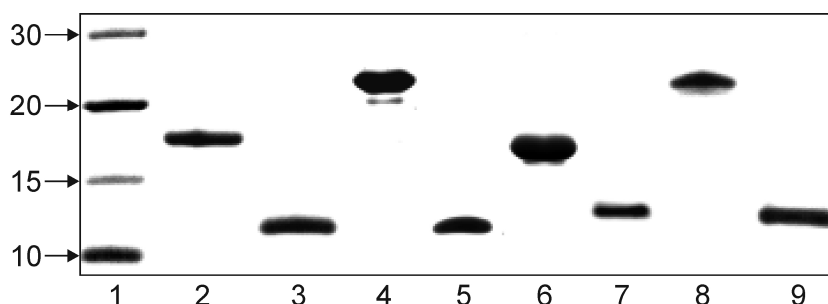


Figure 4.2 Overexpression of human death domains from MyD88 and IRAK proteins. Approximately 5 μ g of each of the recombinant proteins used in this investigation were resolved in a 12% SDS-Tris-Tricine polyacrylamide gel and stained with Coomassie Brilliant Blue. Samples were applied as follows: lane 2, MyD88(L); lane 3, MyD88(S); lane 4, IRAK-1(L); lane 5, IRAK-1(S); lane 5, IRAK-M(L), lane 6, IRAK-M(S), lane 7, IRAK-4(L), lane 8, IRAK-4(S). All samples were incubated with reducing Laemmli buffer. Lane 1 contains the Novex® Sharp Pre-stained Protein Molecular Weight Standard (Invitrogen); the corresponding molecular masses are given in kDa. Notice that all proteins migrate approximately as expected from their theoretical masses (see Table 4.2).

“S” variants, and degraded forms of MyD88(L) and IRAK-4(L) were recognized by the corresponding anti-tag monoclonal antibody (data not shown). These findings suggested that the linker regions are notably more accessible to proteolytic attack than the N-terminal globular domains, and indirectly confirm correct folding of the recombinant proteins.

Table 4.2 Major physicochemical parameters of recombinant proteins generated for the current study. Protein parameters were calculated using the ProtParam tool from the proteomic server ExPASy [246]. All MyD88 and IRAK proteins were recombinantly expressed in *E. coli*. M_r (Da), calculated relative mass expressed in Daltons. pI, theoretical isoelectric point. ϵ , extinction coefficient at 280 nm, measured in water and expressed in g/mol/cm . A_{280} (0.1%), theoretical absorbance of a 1-g/L solution of pure protein at 280 nm.

Construct	N-residue	C-residue	Tag	M_r (Da)	pI	ϵ (g/mol/cm)	A_{280} (0.1%)
MyD88(S) ¹	Thr ¹⁷	Gln ¹²⁰	6xHis	12,621	6.05	13,980	1.108
MyD88(L)	Thr ¹⁷	Met ¹⁵⁷	6xHis	16,521	5.29	13,980	0.846
IRAK-1(S)	Gly ¹⁴	Ala ¹⁰⁶	None	10,894	7.98	30,480	2.798
IRAK-1(L)	Gly ¹⁴	Asn ²¹¹	None	21,661	8.40	46,980	2.169
IRAK-4(S)	Thr ⁶	Lys ¹⁰⁷	FLAG	12,446	5.03	15,470	1.243
IRAK-4(L)	Thr ⁶	Ile ¹⁸⁵	FLAG	21,429	4.98	18,450	0.861
IRAK-M(S)	Thr ¹⁵	Leu ¹⁰⁹	c-MYC	11,701	5.26	24,980	2.135
IRAK-M(L)	Thr ¹⁵	Asn ¹⁶⁴	c-MYC	17,788	5.21	26,470	1.488
MyD88 R81E	Thr ¹⁷	Met ¹⁵⁷	6xHis	16,495	5.05	13,980	0.848
MyD88 I109X	Thr ¹⁷	Ser ¹⁰⁸	6xHis	11,130	6.30	12,490	1.122
MyD88 Y116C	Thr ¹⁷	Met ¹⁵⁷	6xHis	16,462	5.29	12,490	0.759
MyD88 E143X	Thr ¹⁷	Ala ¹⁴²	6xHis	14,957	5.65	13,980	0.935
IRAK-4 E92R	Thr ⁶	Ile ¹⁸⁵	FLAG	21,456	5.25	18,450	0.860
IRAK-4 V105X	Thr ⁶	Ala ¹⁰⁴	FLAG	12,122	4.83	15,470	1.276
IRAK-4 N110X	Thr ⁶	Ala ¹⁰⁹	FLAG	12,618	5.03	15,470	1.226
IRAK-4 K115X	Thr ⁶	Ser ¹¹⁴	FLAG	13,131	5.03	15,470	1.178

¹The C-terminus of MyD88(S) differs from the previously reported form, MyD88s, which lacks residues 110 to 157.

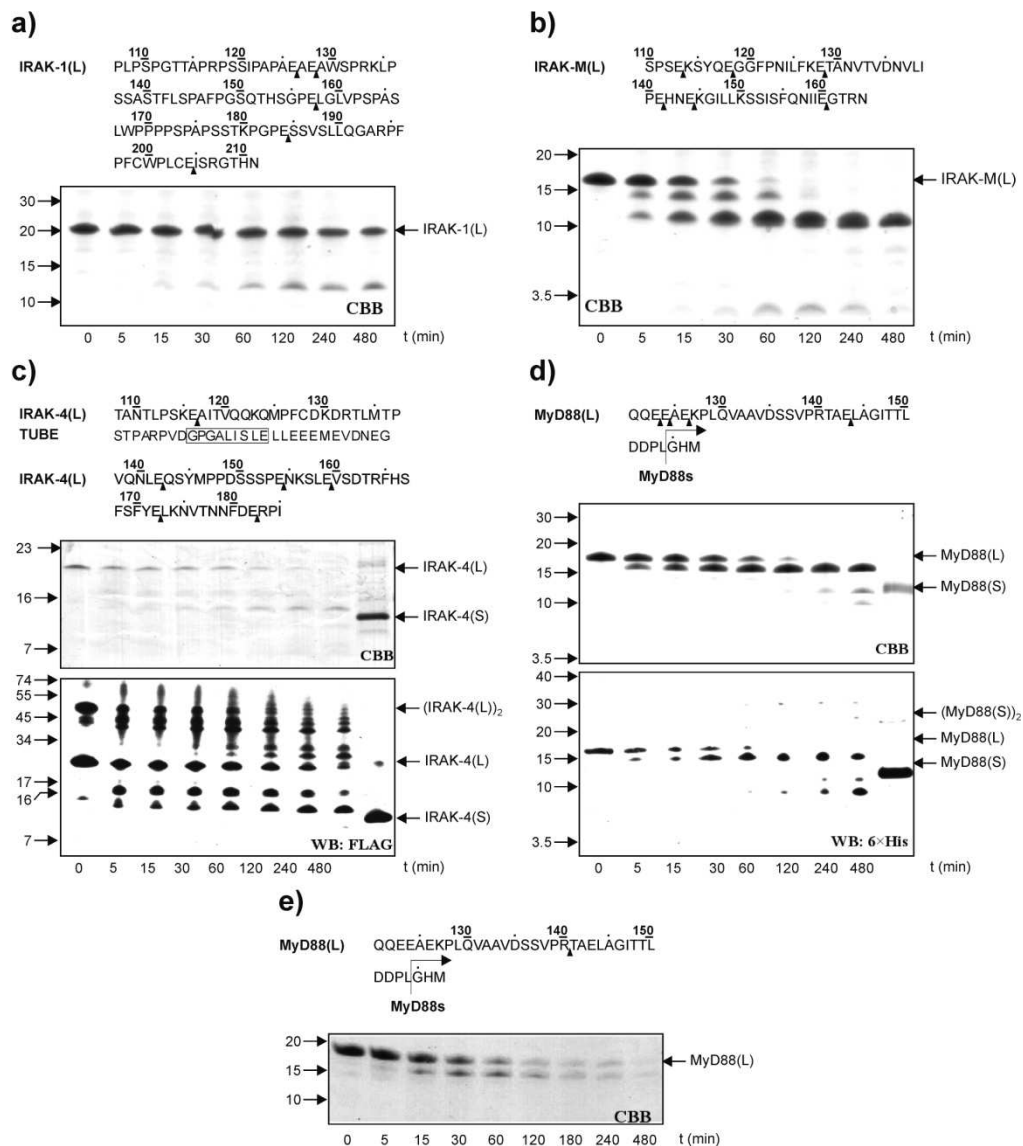


Figure 4.3 Preferential cleavage of interdomain linkers in recombinant proteins suggests correct folding of MyD88 and IRAK variants. Approximately 50 μ g of IRAK-1(L) (a), IRAK-M(L) (b), IRAK-4(L) (c) and MyD88(L) (d), were digested with 500 ng endoproteinase Glu-C in 100 mM ammonium bicarbonate buffer, pH 7.9. Purified samples of IRAK-4(S) and MyD88(S) were loaded along samples of panels c and d, respectively. Additionally, the same amount of MyD88(L) was digested with endoproteinase Arg-C at a 1:200 enzyme to protein ratio (e), as described in Materials and Methods. Samples were taken at the indicated times and subjected to SDS-PAGE for Coomassie Blue Staining (CBB). MyD88(L) and IRAK-4(L) samples were also immunoblotted with anti-FLAG (c, lower panel) or anti-His (d, lower panel) antibodies, respectively. The sequences of C-terminal linkers to the TIR (MyD88) and kinase domains (IRAK variants) are given on top of each panel; putative Glu-C (a-d) and Arg-C (e) cleavage sites are indicated with black arrowheads. The sequence of the Tube tail is also shown along with the linker residues of IRAK-4 (d), and the polypeptide stretch from Tube that engages in major contacts with the death domain of the kinase Pelle is boxed. Additionally, the C-terminal end of the sequence missing in MyD88s is indicated in panels d and e. Notice that, in all cases, a stable fragment of an apparent molecular mass slightly higher than the corresponding linker-less variant is generated. Based on the distances migrated by these stable proteolytic fragments, their most likely C-terminal residues are Glu¹²⁶ or Glu¹²⁸ (IRAK-1, panel a), Glu¹¹³ or Glu¹¹⁸ (IRAK-M, panel b), Glu¹¹⁶ (IRAK-4, panel c), Glu¹⁴³ (MyD88, panel d) and Arg¹⁴⁰ (MyD88, panel e). Notice that dimers of intact and proteolytically modified forms of IRAK-4(L), but not MyD88(L), are detected by immunoblotting (compare panels c and d).

To directly verify that residues from the C-terminal tails of the “long” variants are unstructured and thus more prone to proteolysis, we treated samples of MyD88(L), IRAK-4(L), IRAK-1(L) and IRAK-M(L) with endoproteinase Glu-C for several times. The results of this analysis confirmed preferential cleavage of Glu-Xxx scissile peptide bonds within the irregular linker peptides (Figure 4.3a-d; potential cleavage sites within the tails are marked with black arrowheads). According to the distances migrated by the cleavage products in SDS-polyacrylamide gels, the C-terminal residues of the stable fragments formed upon limited proteolysis appear to be Glu¹⁴³ (MyD88), Glu¹²⁶ and/or Glu¹²⁸ (IRAK-1), Glu¹¹³ and/or Glu¹¹⁸ (IRAK-M) and Glu¹¹⁶ (IRAK-4). We note, however, that upon prolonged incubation (> 6 h) a shorter form of MyD88 started to accumulate, indicating cleavage of the Glu¹¹⁰-Glu¹¹¹ and/or Glu¹¹¹-Asp¹¹² peptide bonds. Additionally, and in order to obtain a truncated variant of MyD88 containing only a few residues of the DD-TIR linker, free MyD88(L) was digested at 37°C with endoproteinase Arg-C at a 1:200 enzyme to protein ratio, as described in Materials and Methods (see Fig. 4.3e). Only the Arg¹⁴⁰-Thr¹⁴¹ peptide bond of the DD-TIR linker, but none of the Arg-Xxx linkages of MyD88(L) DD, was cleaved after 8 h of incubation, indirectly confirming correct folding of MyD88(L).

4.1.3 Purified Death Domains of MyD88 and IRAK-4 Form Large Aggregates in the Absence of Detergents

In preliminary experiments we noticed that preparations of MyD88 and IRAK-4 variants undergo unspecific aggregation even in the presence of reducing agents (Figure 4.4). To further assess the size and polydispersity properties of MyD88 and IRAK-4 recombinant fragments, dynamic light scattering (DLS) was performed on these purified samples. The results of this

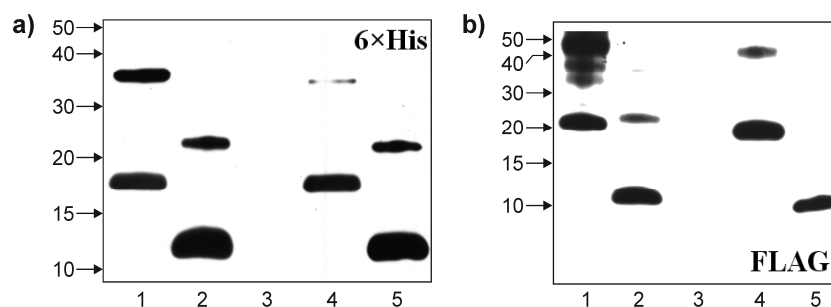


Figure 4.4 Human MyD88 and IRAK-4 death domains have a strong tendency to form aggregates. Fifty ng of the recombinant proteins were separated by SDS-PAGE and transferred to a PVDF membrane for WB analysis. Samples in lanes 1-2 of both panels were incubated with non-reducing Laemmli buffer, and samples in lanes 4-5 of both panels were incubated with reducing Laemmli buffer. Molecular masses are given on the left, in kDa. **a)** MyD88 samples probed with anti-6xHis antibody. Lanes 1 and 4, MyD88(L). Lanes 2 and 5, MyD88(S). **b)** IRAK-4 samples probed with anti-FLAG antibody. Lanes 1 and 4, IRAK-2(L). Lanes 2 and 5, IRAK-4(S). Notice that dimers are formed even in reduced samples, pointing to an exacerbated tendency to homodimerization.

analysis also revealed that these recombinant forms of death domains form large aggregates in solution (up to one-hundred monomers), even in the presence of relatively large urea concentrations (see Figure 4.5).

Gel filtration studies also showed that MyD88(L) has a strong tendency to form large aggregates in solution (see Figure 4.6). In these studies, the void volume (V_0) and elution volumes (V_e) of known globular proteins were used to plot a standard curve of V_e/V_0 against MW, as explained in Materials and Methods (section 3.5.3), and the theoretical V_e of an MyD88(L) monomer was estimated to be ~ 78.5 mL (see Figure 4.6a). When analyzing MyD88(L) samples, however, most of the protein was found to elute around 40 mL, corresponding to MW of ~ 330 kDa (19 to 20 monomers), even though the running buffer contained 0.1% β -OG. These results confirm that MyD88(L) is mostly found in aggregated forms (see upper panels in Figure 4.6b). This strong tendency of MyD88(L) to self-aggregate seems to be reduced only when using low protein concentrations (≤ 0.5 mg/mL, see lower panel in Fig. 4.6b).

When performing gel filtration analysis on the adaptor variant truncated at Glu¹⁴³, MyD88 E143X, (see Supplemental Figure 1, Appendix XI), a strong tendency to form large aggregates in solution was observed as well. As seen in Supplemental Figure 2 (Appendix XI), the V_e of MyD88 E143X monomers was estimated to be ~ 80.7 mL, and most of the protein eluted at around 44 mL (corresponding to a MW of ~ 240 kDa, about 17 protein monomers). MyD88 E143X was also found to form large aggregates at higher concentrations (3.3 mg/mL), since part of the protein was eluted at ~ 39 mL, corresponding to a MW of 350 kDa (~ 25 monomers). Generally, the poor solubility of these variants resulting from their tendency to form large aggregates in solution was overcome with the addition of mild detergents, as seen later on in Figure 4.8 for MyD88(L)•IRAK-4(L) complex studies.

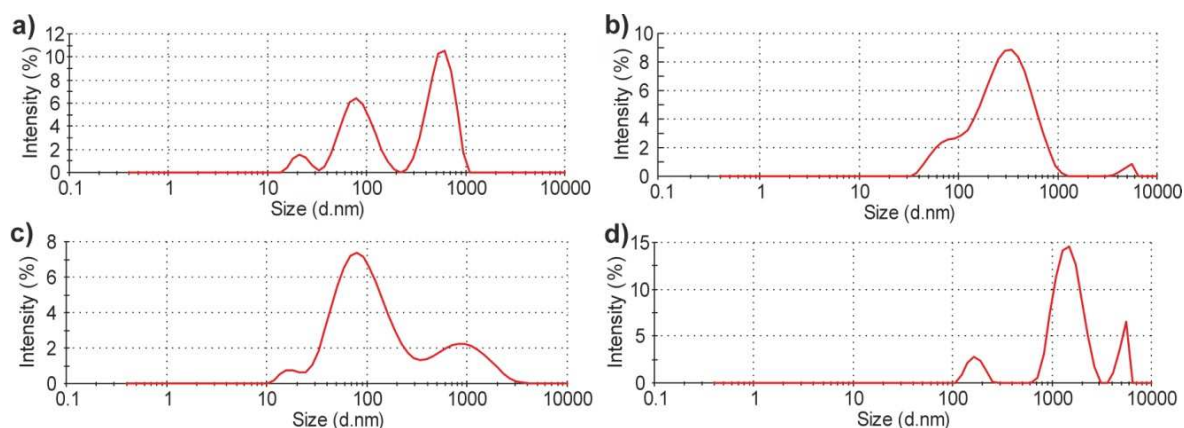


Figure 4.5 DLS analysis of purified recombinant proteins. The results of MyD88(L) (a), MyD88(S) (b), IRAK-4(L) (c) and IRAK-4(S) (d) DLS analysis are given as intensity (%) against particle size (diameter, given in nm). Notice that all four recombinant proteins form large aggregates of molecular diameter ranging between 100 and 700 nm, which would correspond to particles containing up to several hundred-thousand molecules each.

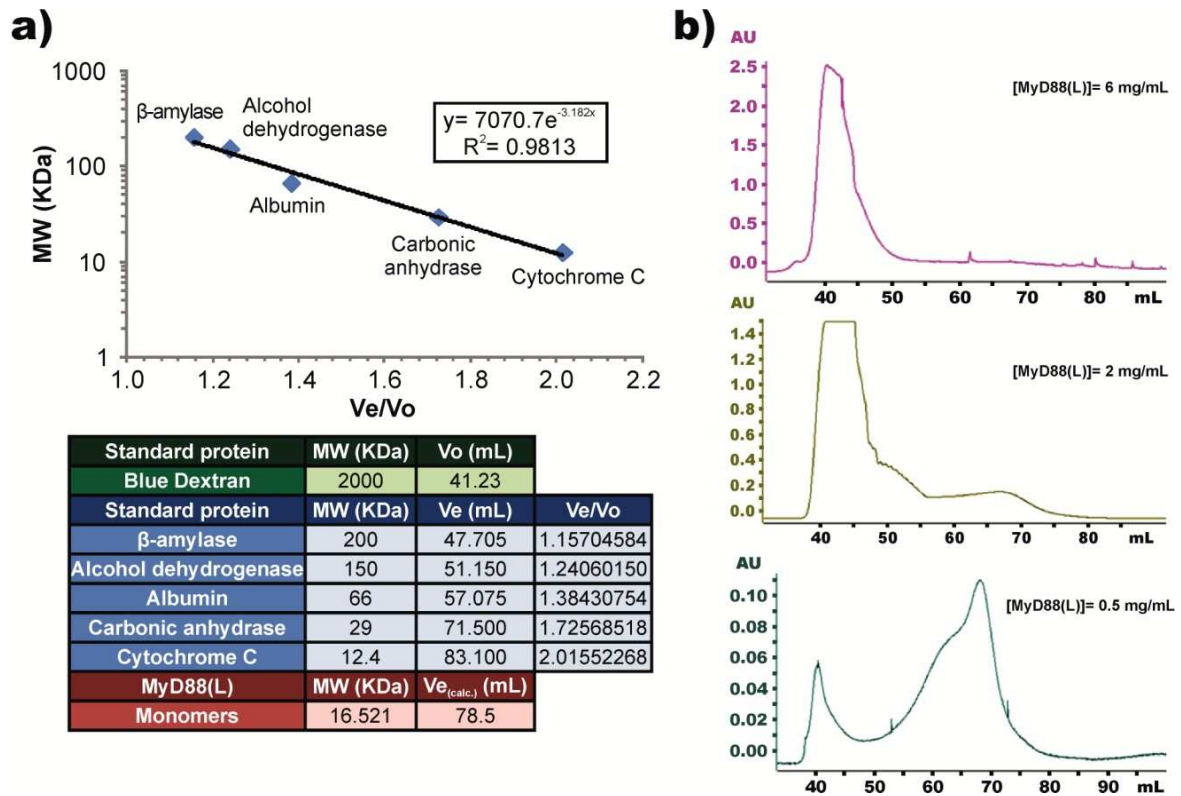


Figure 4.6 Gel filtration analysis of recombinant MyD88(L) samples. **a)** Standard curve for MW determination. The ratios of the elution volumes (V_e) of β -amylase, alcohol dehydrogenase, albumin, carbonic anhydrase and cytochrome C over the V_e of blue dextran (void volume, V_o) were plotted against their known MW, and the V_e of MyD88(L) was calculated from its MW (table cells in red). **b)** Different examples of MyD88(L) FPLC analysis run at a flow of 2 mL/min. MyD88(L) is normally eluted at ~ 40 mL corresponding to a MW of ~ 330 kDa (19 to 20 monomers) at concentrations of 2 and 6 mg/mL (upper and middle panels). As expected, MyD88(L) aggregates are reduced when using lower protein concentrations (≤ 0.5 mg/mL, lower panel), as indicated by a major elution peak at ~ 70 mL, corresponding to a MW of 31.86 kDa (MyD88(L) dimers).

4.2 Interactions Between MyD88 and IRAK-4 Recombinant Variants

4.2.1 The Isolated Death Domains of MyD88 and IRAK-4 Form a Stable Complex in Solution

Although the bipartite adaptor, MyD88, is known to recruit IRAK proteins *in vivo*, it has not been unambiguously established whether additional cofactors are necessary for kinase binding. To verify that the death domain of MyD88 suffices to recruit IRAK-4, we took advantage of the presence of an N-terminal polyhistidine tag in our recombinant constructs of the adaptor. MyD88(L) was incubated with an equimolar amount of purified IRAK-4(L), purified with Ni-NTA agarose matrix, and purification fractions were analyzed by SDS-PAGE and Western blotting, as explained in Materials and Methods. As a control, the same amount of

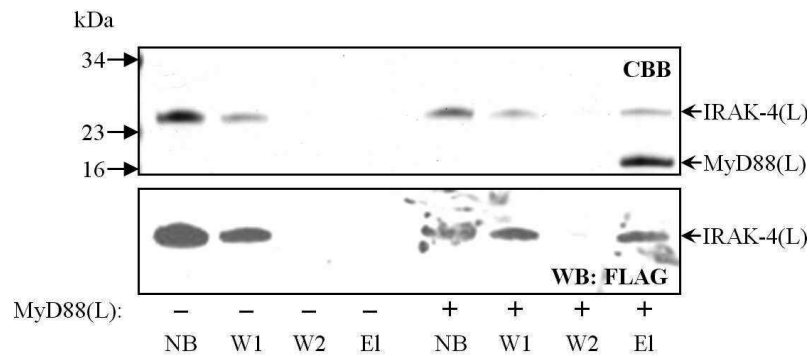


Figure 4.7 Formation of MyD88(L)•IRAK-4(L) heterodimer in solution. Equimolar amounts of purified MyD88(L) and IRAK-4(L) were incubated in binding buffer and purified with Ni-NTA agarose as explained in Materials and Methods. Non-bound (NB), wash (W) and elution (EI) fractions were collected and separated by SDS-PAGE. Proteins on the gel were either stained with Coomassie Brilliant Blue (CBB) (upper panel) or transferred onto a nitrocellulose membrane for Western blot analysis using anti-FLAG monoclonal antibody (lower panel).

IRAK-4(L) was treated in a similar manner. IRAK-4(L) was pulled down by the affinity matrix in the presence but not in the absence of MyD88(L), indicating death domain-mediated formation of the MyD88(L)•IRAK-4(L) complex (Figure 4.7). However, we observed only partial complex formation, apparently because forces holding together aggregates of individual components were strong enough to effectively interfere with heterodimer formation *in vitro*.

To identify conditions that could enhance complex formation *in vitro* we analyzed the influence of several experimental variables (e.g., incubation time and temperature, as well as ionic strength) on MyD88(L)-IRAK-4(L) complex formation. As expected, and in line with the negative effect of aggregation discussed above, low protein concentrations had the highest positive impact on heterodimer formation. We also studied the effects of 24 unique non-ionic detergents on MyD88(L) and IRAK-4(L) complexation, and the results of this screen showed that several detergents notably enhance complex formation (see Figure 4.8). Thus, combining low protein concentrations with the use of detergents β -OG and $C_{12}E_9$ in binding, wash and elution buffers resulted in quantitative formation and purification of a stable MyD88(L)•IRAK-4(L) complex in solution.

In other experiments, we incubated increasing amounts of IRAK-4(L) with a fixed quantity of MyD88(L), and fractions purified with Ni-NTA agarose were analyzed by Western blotting with anti-His and anti-FLAG antibodies (Figure 4.10a). The results of this experiment confirmed specific binding of the kinase death domain to the adaptor, MyD88. Interestingly, at low IRAK-4 concentrations no heterocomplex was detected, and the MyD88(L) DD-TIR linker was partially cleaved by a contaminating protease. Degradation was prevented at higher IRAK-4(L) concentrations that support complex formation, suggesting protection of the linkers in the heterodimer. These findings were verified with the help of an anti-His tag monoclonal antibody coupled to magnetic microbeads. Again, the death domain of the kinase was pulled down in the presence but not in the absence of MyD88(L) (data not shown).

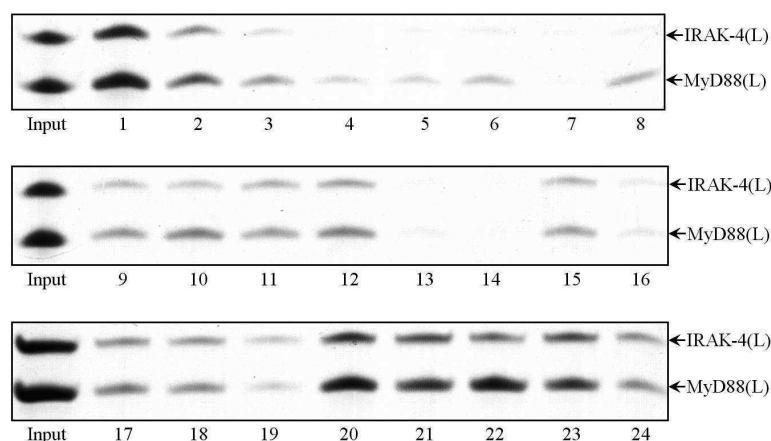


Figure 4.8 Several non-ionic detergents support formation of stoichiometric MyD88(L)•IRAK-4(L) complex. Aliquots containing equimolar amounts of purified MyD88(L) and IRAK-4(L) were incubated with detergents from Detergent Screen 1 (Hampton Research) and purified with Ni-NTA agarose, as described in Materials and Methods. Elution fractions were analyzed by SDS-PAGE and stained with Coomassie Brilliant Blue. The used detergents (see Appendix IX) and their critical micellar concentrations are as follows: Lane 1, C₁₂E₉ (0.08 mM); 2, C₁₂E₈ (0.11 mM); 3, n-dodecyl- β -D-maltoside (0.17 mM); 4, sucrose monolaurate (0.20 mM); 5, CYMAL-6 (0.56 mM); 6, TRITON X-100 (0.90 mM); 7, CTAB (1.00 mM); 8, deoxy BigChap (1.40 mM); 9, n-decyl- β -D-maltoside (1.80 mM); 10, LDAO (2.00 mM); 11, CYMAL-5 (2.40 mM); 12, ZWITTERGENT 3-12 (4.00 mM); 13, nonyl- β -D-glucoside (6.50 mM); 14, 1-s-octyl- β -D-thiogluconide (9.00 mM); 15, DDAO (10.4 mM); 16, HECAMEG (19.5 mM); 17, n-octylsucrose (24.4 mM); 18, Heptyl- β -D-thiogluconide (30.0 mM); 19, n-octyl- β -D-glucoside (24.5 mM); 20, CYMAL-3 (34.5 mM); 21, CHEGA- 10 (35.0 mM); 22, ZWITTERGENT 3-10 (40.0 mM); 23, MEGA-8 (79.0 mM); 24, n-hexyl- β -D-glucoside (250.0 mM).

4.2.2 The Death-Domains of MyD88 and IRAK-4 Can Be Co-renatured to Form a Stoichiometric Complex

To confirm heterodimer formation while minimizing interference of aggregation effects, we subjected mixtures of MyD88(L) and IRAK-4(L) previously denatured in 8 M urea to renaturation trials by rapid dilution in refolding solutions of the FoldIt Screen shown in Appendix VIII. Following this procedure, we found several conditions in which apparently equimolar amounts of MyD88(L) and IRAK-4(L) remained in solution after removal of chaotropic agents, and which could be quantitatively recovered by metal affinity chromatography. Best results were obtained in FoldIt solution 5 (Figure 4.9, see Appendix VIII), which was employed for larger-scale experiments (using sodium phosphate pH 7.0 instead of MES). In these experiments, a protein mixture containing a slight molar excess of MyD88(L) was incubated in the presence of reduced and oxidized glutathione, and soluble material was recovered with Ni-NTA agarose, as detailed in Materials and Methods (Figure 4.10b). The results of this experiment demonstrated formation of MyD88(L)•IRAK-4(L) heterodimer by co-renaturation of its components, providing a simple means for analysis of death domain-mediated complex formation.

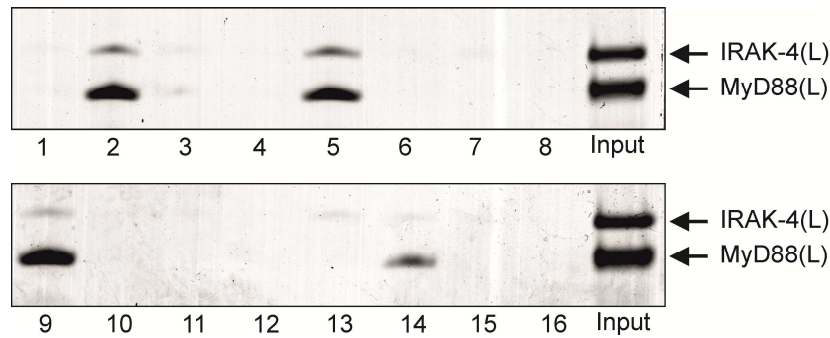


Figure 4.9 MyD88(L) and IRAK-4(L) co-renaturation trial by rapid dilution in refolding solutions. Aliquots containing equimolar amounts of purified MyD88(L) and IRAK-4(L), previously denatured in 8 M urea, were diluted in each of the 16 folding solutions of the FoldIt Screen and incubated overnight at 4 °C on a rocker. Samples were then centrifuged to remove precipitated material, supernatants were analyzed by SDS-PAGE and stained with Coomassie Brilliant Blue. Best results were obtained in solutions 2, 5 and 9, in which a significant fraction of IRAK-4(L) remained in solution after centrifugation, apparently complexed with MyD88(L). FoldIt solution 5 was chosen for larger-scale experiments. The composition of each renaturing condition tested can be found in Appendix VIII.

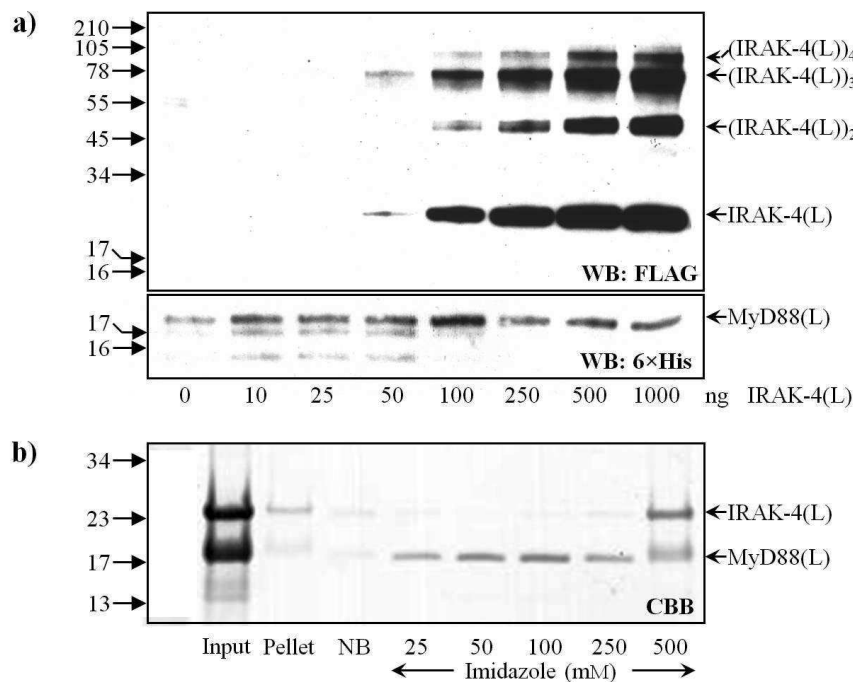


Figure 4.10 The isolated death domains of MyD88(L) and IRAK-4(L) form a stable complex in solution. **a)** Increasing amounts of IRAK-4(L) were incubated with 1 μ g purified MyD88(L) in binding buffer supplemented with 80 mM $C_{12}E_9$ and 0.7% β -OG, as explained in Materials and Methods. Equal volumes of Ni-NTA agarose matrix were added to these mixtures and specifically bound proteins were eluted with Laemmli sample buffer. Protein fractions were separated by SDS-PAGE, blotted onto PVDF membranes, and analyzed by Western blot using anti-FLAG (upper panel) or anti-6xHis (lower panel) monoclonal antibodies. Notice that increasing amounts of IRAK-4(L) are retained in the matrix, indicating formation of MyD88(L) \cdot IRAK-4(L) heterodimers. **b)** IRAK-4(L) and MyD88(L) were denatured in 8 M urea, mixed in an equimolar proportion, and refolded by rapid dilution in renaturation solution, as detailed in Materials and Methods. Insoluble material was removed and soluble proteins were purified with Ni-NTA agarose using increasing imidazole concentrations. Samples were analyzed by SDS-PAGE and stained with Coomassie Brilliant Blue (CBB).

4.2.3 The Unstructured Death Domain-TIR Linker of MyD88 Is Not Required for IRAK-4 Recruitment

After having demonstrated the formation of stable, death domain-mediated complexes of MyD88 and IRAK-4, we wished to determine whether the unstructured interdomain connectors of these proteins are required for complex formation. To this end, we performed experiments essentially as described above, but replacing the “long” forms of the recombinant proteins by their linker-less counterparts. First, we analyzed whether MyD88(S) was able to form a stable complex with IRAK-4(L). This was indeed the case, as IRAK-4(L) could be pulled down with Ni-NTA matrix in the presence of the death domain-only form of the bipartite adaptor (Figure 4.11a).

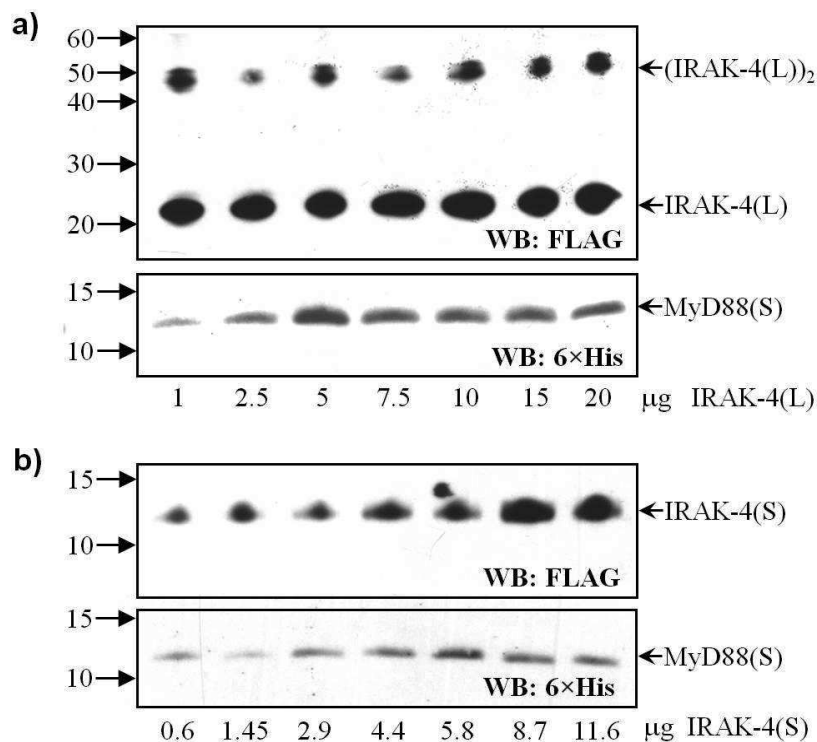


Figure 4.11 The death domain-TIR linker of MyD88 is not required for kinase recruitment, but the DD-kinase linker of IRAK-4 is important for heterodimer formation. **a)** A fixed amount of MyD88(S) (10 µg), was incubated with increasing quantities of IRAK-4(L) (from 1 to 20 µg) in 8 M urea, and mixtures were co-renatured by rapid dilution in the same solution used for MyD88(L) / IRAK-4(L) co-renaturation (see Figure 4.10b). After centrifugation to remove insoluble material, Ni-NTA agarose was added to the supernatant. The affinity matrix was thoroughly washed and specifically bound proteins were recovered with elution buffer. Samples of the eluted fractions were analyzed by SDS-PAGE and immunoblotted with anti-FLAG (upper panel) or anti-6xHis (lower panel) monoclonal antibodies. Notice saturable binding of IRAK-4(L) to the death domain-only variant of the adaptor, indicating that MyD88 linker residues Gln¹²¹-Met¹⁵⁷ do not contribute significantly to heterodimer formation. **b)** A similar experiment was conducted with approximately molar equivalent amounts of IRAK-4(S) (from 0.58 to 11.63 µg). Notice that, by contrast to the linker-containing form of the kinase, much lower quantities of IRAK-4(S) are pulled down by MyD88(S), indicating that residues from the DD-kinase linker of IRAK-4 are important for heterodimer formation.

4.2.3.1 The Isolated Death-Domain of MyD88 Interacts with Native IRAK-4

To verify the ability of recombinant death domain-only variants of MyD88 to pull down the natural full-length kinase, IRAK-4, we mixed purified MyD88(L) or MyD88(S) with increasing amounts of human monocyte extracts obtained as described in Materials and Methods (section 3.8). After incubation of these mixtures with Ni-NTA matrix, specifically bound proteins were separated on SDS-polyacrylamide gels, transferred to PDVF membranes, and subjected to immunoblotting with an anti-human IRAK-4 polyclonal antibody. The results of this experiment demonstrate quantitative, saturable binding of natural IRAK-4 by the recombinantly expressed death domain of the adaptor (Figure 4.12).

Of particular note, the fact that both recombinant variants of MyD88 death domain interact with natural IRAK-4, corroborates that the DD-TIR linker of the adaptor is not required for kinase recruitment. Incomplete pull-down of IRAK-4 by MyD88(S) (compare left panels in Fig. 4.12a and Fig. 4.12b) probably results from the higher tendency to self-aggregation of this recombinant variant. Further, the apparent contradiction with the reported inability of MyD88s to interact with IRAK-4 [79] suggests involvement of MyD88 helix $\alpha 7$ in kinase recruitment.

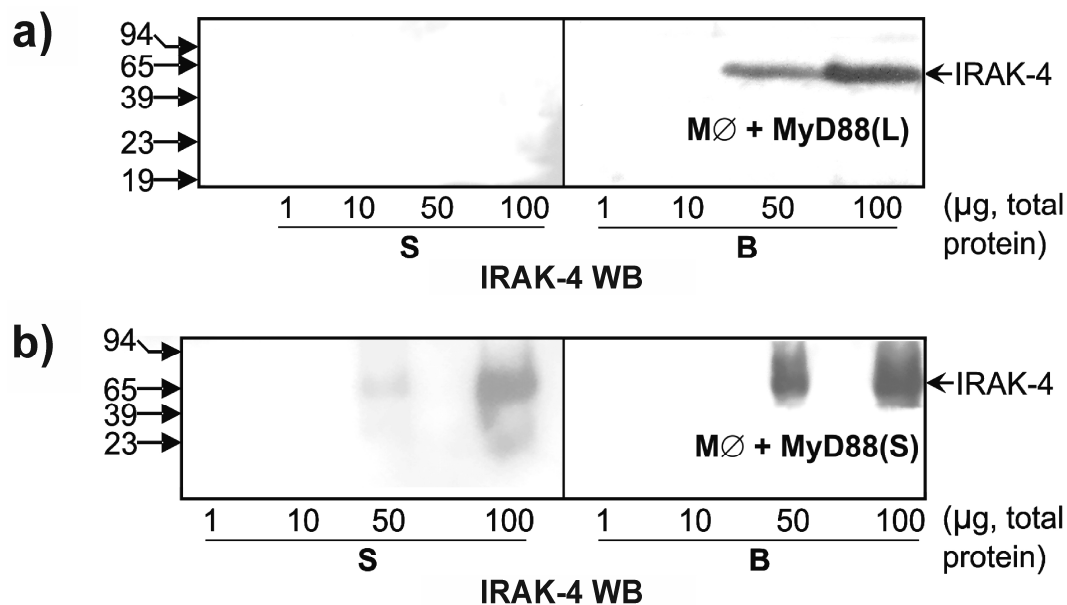


Figure 4.12 The death domain of MyD88 pulls down natural IRAK-4 from monocyte extracts. Human monocytes were cultured in DMEM, and cytosolic proteins were extracted by incubation in ice-cold Cell Lysis Buffer with gentle rotation at 4°C for 30 min. Fixed amounts (2 µg) of MyD88(L) (a) or MyD88(S) (b) were added to increasing quantities of these extracts (from 1 to 100 µg total monocyte proteins). After incubation at room temperature for 30 min, Ni-NTA agarose matrix was added to this mixture and samples were centrifuged. The supernatants (labeled “S”) were precipitated with 5 volumes of cold acetone, while specifically bound proteins (labeled “B”) were recovered with Laemmli buffer after thoroughly washing the affinity matrix with Cell Lysis Buffer. Samples were resolved on 12% Tris-Glycine-SDS polyacrylamide gels, electroblotted into PVDF membranes, and analyzed by Western blotting with an anti-IRAK-4 polyclonal antibody. Notice that left and right panels are derived from separately loaded SDS-polyacrylamide gels to avoid running-over of samples.

4.2.3.2 SPR Analysis of DD-Mediated MyD88–IRAK-4 Interactions

In an attempt to quantitate the strength of DD-mediated IRAK-4–MyD88 interactions, we performed a surface plasmon resonance (SPR) analysis, using Sensor Chip NTA and the recombinant variants expressed and purified as described above. A total of four SPR tests were performed with MyD88(S) as the ligand, immobilized to the sensor chip surface via its N-terminal polyhistidine tag, and IRAK-4(L) as the analyte, as described in Materials and Methods (Section 3.10.3). Different concentrations of MyD88(S) and IRAK-4(L) were used, as seen in Table 4.3 (see also Figure 4.13a-d and legend for details). To exclude any responses due to non-specific interactions between IRAK-4(L) and the surface of the sensor chip, MyD88(S) was injected only to Fc2, at concentrations of either 187 nM (tests 1 to 3) or 837 nM (test 4), and IRAK-4(L) was then injected to both Fc1 and Fc2 at concentrations ranging from 1.33 μ M (Test 1) to 55.2 nM (Test 4). However, and as seen in Figure 4.13e, the relative responses obtained for MyD88(S) were not in agreement with the input protein concentrations, being equal in tests 1-3 (panels a-c) and higher in test 4 (panel d). Moreover, IRAK-4 (L) presented higher affinity for the reference channel, with no MyD88(S) attached to it (Fc1, shown in red in all panels of Figure 4.13), than

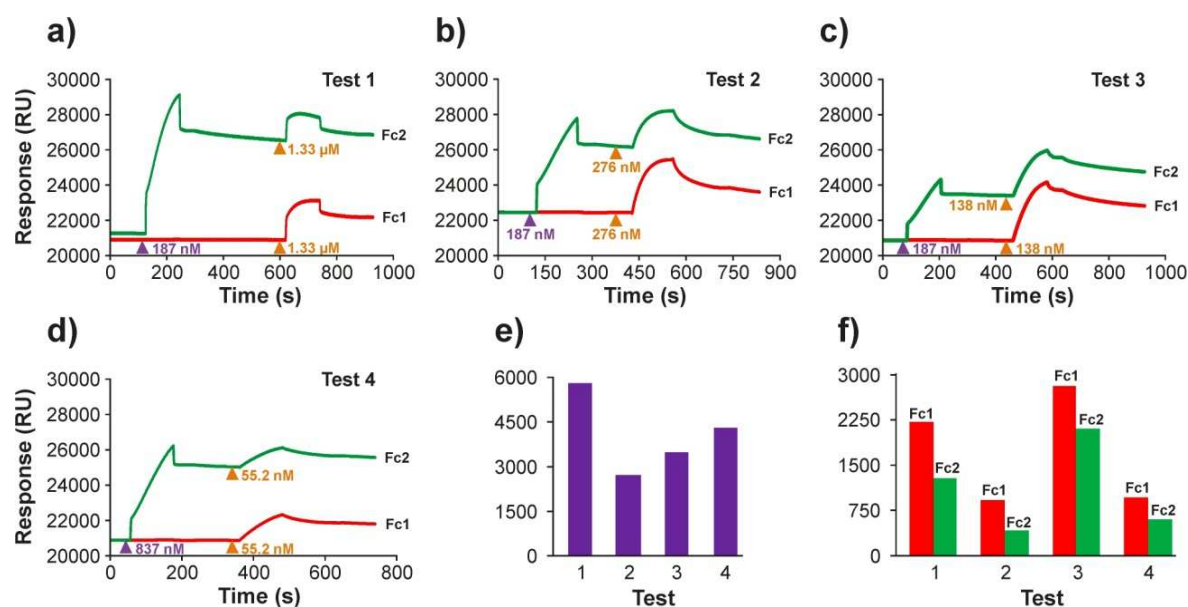


Figure 4.13 Surface plasmon resonance studies of MyD88(S)–IRAK-4(L) interactions. Four different SPR tests were performed, using Sensor Chip NTA (GE Healthcare), previously activated with Ni^{2+} . All experiments were performed at 25 °C in SPR running buffer (see Appendix VII), as described in Materials and Methods. **a-d**) Response over time plots, obtained for tests 1- 4, respectively. MyD88(S) injections (purple triangles) proceeded only through Fc2 at the following concentrations: 187 nM (**a-c**), 837 nM (**d**). IRAK-4(L) injections (yellow triangles) proceeded through both Fc1 and Fc2, at the following concentrations: 1.33 μ M (**a**), 276 nM (**b**), 138 nm (**c**), 55.2 nM (**d**). **e**) Comparison of the responses obtained with MyD88(S) in tests 1- 4 (only Fc2 shown). Note that the obtained responses were not in agreement to the used MyD88(S) concentrations. **f**) Comparison of the responses obtained with IRAK-4(L) in both flow cells of each test. Note that higher responses were obtained through Fc1 (without MyD88) than through Fc2 (containing the adaptor). Y-axes in all panels indicate the obtained response, in Resonance Units (RU), as shown in (**a**) and (**d**).

Table 4.3 Summary of experimental set-up and solutions used for SPR analysis of MyD88(S)–IRAK-4(L) interactions. A total of four tests were performed using MyD88(S) and IRAK-4(L), in running buffer (see text). All proteins and solutions were passed at a flow rate of 20 $\mu\text{L}/\text{min}$. MyD88(S) was passed through Fc2 only, while IRAK-4(L) was injected through both Fc1 and Fc2. The following reagents were used at the following concentrations: EDTA, 350 mM; NiCl_2 , 500 mM; MgCl_2 , 3 M; GdnHCl (Guanidine hydrochloride), 6 M.

Protocol steps	Test 1	Test 2	Test 3	Test 4
(1) Wash	20 μL EDTA	20 μL EDTA	20 μL EDTA	20 μL EDTA
(2) Surface activation	20 μL NiCl_2	20 μL NiCl_2	20 μL NiCl_2	20 μL NiCl_2
(3) Ligand immobilization	40 μL MyD88(S) (187 nM)	40 μL MyD88(S) (187 nM)	40 μL MyD88(S) (187 nM)	40 μL MyD88(S) (837 nM)
(4) Analyte injection	40 μL IRAK-4(L) (1.33 μM)	40 μL IRAK-4(L) (276 nM)	40 μL IRAK-4(L) (138 nM)	40 μL IRAK-4(L) (55.2 nM)
(5) Regeneration	60 μL EDTA, 40 μL MgCl_2 , 20 μL GdnHCl	60 μL EDTA, 20 μL GdnHCl	60 μL EDTA, 20 μL GdnHCl, 10 μL GdnHCl	60 μL EDTA, 20 μL GdnHCl

for the MyD88(S)-coated channel of the chip (Fc2, in green, in the same figure), even when extensively coating the sensor chip with high concentrations of MyD88(S), as in test 4. This lack of detectable MyD88–IRAK-4 interactions probably results from the high tendency of the proteins to self-aggregate, and the absence of reducing agents in the SPR running buffer (see Appendix VII for composition). Further, MyD88(S) residues important for interactions with IRAK-4(L) may not be accessible due to the adaptor orientation on the surface of the chip.

4.2.4 Residues up to Ser¹¹⁴ in IRAK-4 DD-Kinase Linker Are Required for MyD88 Binding

We have previously shown that IRAK-4(S) bound only weakly to the DD-only form of MyD88 (compare intensity of bands in the anti-FLAG panels of Fig. 4.11a and Fig. 4.11b), and similar results were obtained with MyD88(L) (data not shown), indicating that the DD-kinase connector of IRAK-4 is important for complex formation. To verify whether the DD-TIR linker of kinase IRAK-4 was required for complex formation with MyD88, and encouraged by our previous findings (Figure 4.10a), we compared accessibility of this polypeptide stretch to proteolytic attack in the presence or absence of MyD88(S). Similar to the experiments described above for protein characterization (Figure 4.3), we incubated Ni-NTA-bound MyD88(S)•IRAK-4(L) complex with Glu-C for various times. Presence of the adaptor completely abolished proteolysis of the Glu¹¹⁶-Ala¹¹⁷ peptide bond, while the more C-terminal Glu¹⁴³-Leu¹⁴⁴ site was hydrolyzed as in free IRAK-4(L), although with slower kinetics (Figure 4.14, compare with Figure 4.3c). In line with our previous observations, linker residues were in general protected to a greater extent in the complex, and substantial amounts of uncleaved IRAK-4(L) remained after 8 h incubation with the protease.

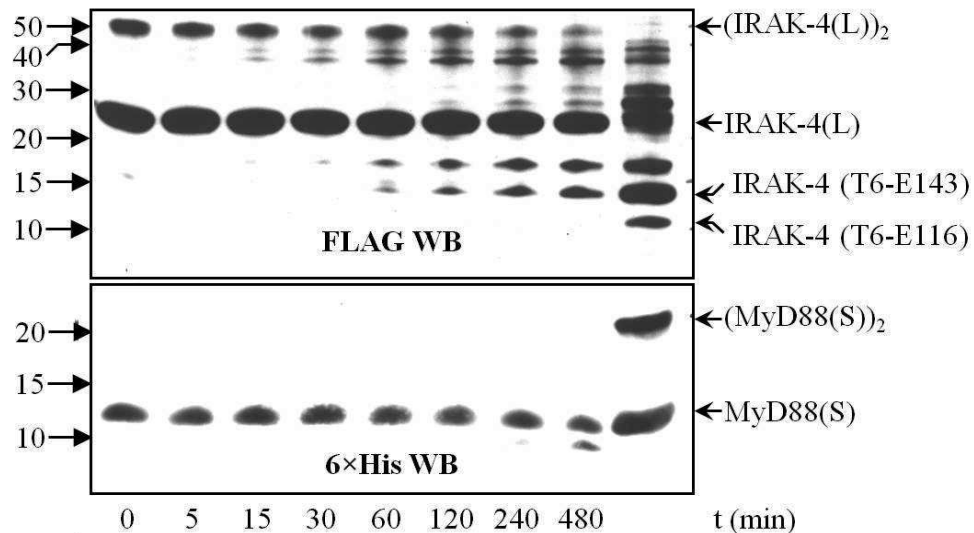


Figure 4.14 Residues up to Glu¹¹⁶ in IRAK-4 linker are protected from proteolytic attack in the complex with MyD88. The equimolar MyD88(S)•IRAK-4(L) complex, obtained as described in the legend for Figure 4.11, was immobilized in Ni-NTA agarose, buffer-exchanged into 100 mM ammonium bicarbonate buffer, pH 7.9, and incubated with endoproteinase Glu-C at 25 °C for the indicated times. Samples were centrifuged to separate soluble from matrix-bound material, and the latter was analyzed by SDS-PAGE and Western blotting with anti-FLAG (upper panel) or anti-His (lower panel) antibodies. Lane 9 in the upper panel contains free IRAK-4(L) treated with the same amount of Glu-C for up to 8 hours; the corresponding lane in the lower panel contains 0.8 µg free MyD88(S). Notice that the Glu¹¹⁶-Ala¹¹⁷ peptide bond is not cleaved in MyD88-bound IRAK-4(L), indicating protection of these residues in the complex.

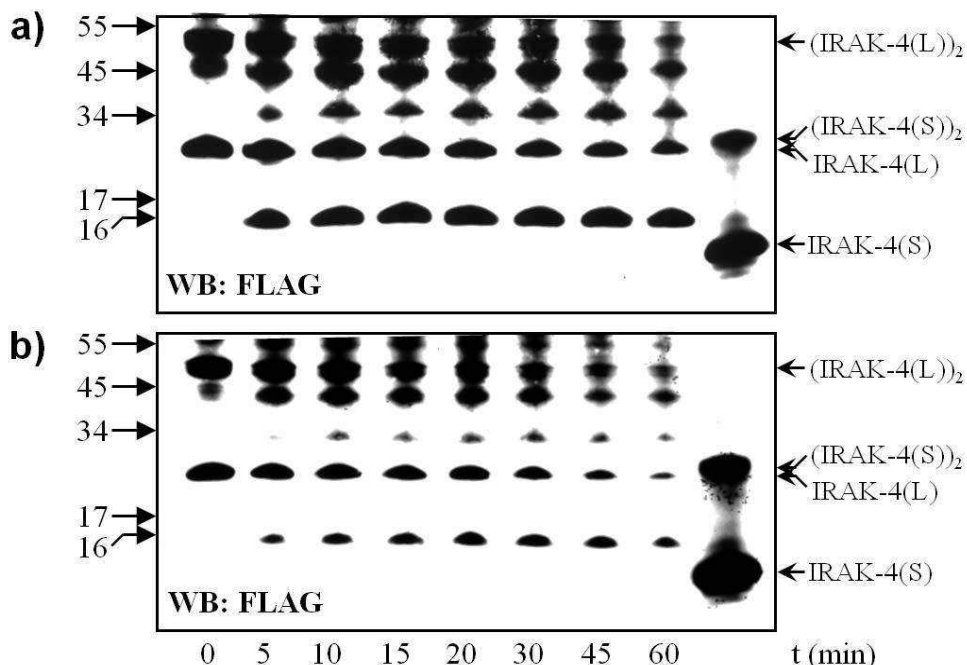


Figure 4.15 Similar kinetics of chymotrypsin cleavage of free and complexed IRAK-4(L). Samples of free IRAK-4(L) (a) and MyD88(S)•IRAK-4(L) complex (b) containing the same amount of the kinase domain were buffer-exchanged into 100 mM ammonium bicarbonate buffer, pH 7.9, with 10 mM CaCl₂, and incubated with sequencing-grade chymotrypsin at 25 °C (enzyme to protein ratio, 1:100) for the indicated times. Samples were analyzed by Western blotting with anti-FLAG antibody. Lane 10 in both panels contains untreated IRAK-4(S).

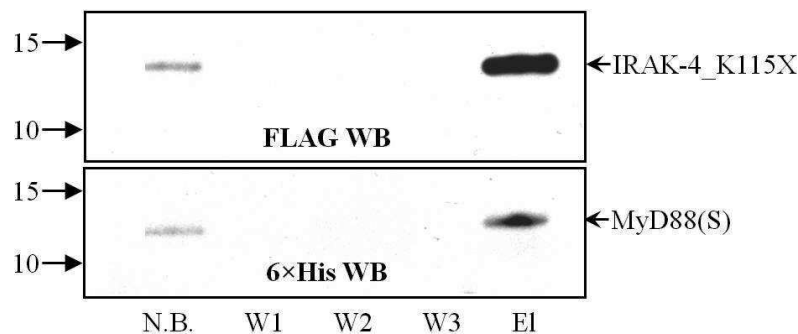


Figure 4.16 Residues beyond Ser¹¹⁴ in IRAK-4 linker do not contribute to complex formation with MyD88. Equimolar amounts of MyD88(S) and the kinase variant IRAK-4 K115X, were denatured in 8 M urea and co-renatured in FoldIt solution 5 (see Appendix VII). Ni-NTA matrix was added to the mixture and processed as described in Materials and Methods. Non-bound (NB), wash (W) and elution (E) fractions were analyzed by SDS-PAGE and immunoblotted with anti-FLAG (upper panel) or anti-His (lower panel) monoclonal antibodies. Unimpaired complex formation of these two proteins indicates that IRAK-4 residues C-terminally of Ser¹¹⁴ are dispensable for binding to the adaptor.

In other experiments, we incubated aliquots of IRAK-4(L) alone and of MyD88(S)•IRAK-4(L) complex with chymotrypsin. In this case, however, cleavage patterns of free and adaptor-bound IRAK-4(L) were essentially identical (Figure 4.15), indicating that the scissile peptide bond Phe¹²⁷-Glu¹²⁸ is not protected in the MyD88•IRAK-4 complex.

Next, with the aim of verifying the kinase residues involved in complex formation with MyD88, we expressed and purified the IRAK-4 K115X mutant, truncated at Lys¹¹⁵ (Supplemental Figure 1, Appendix XI), and studied its ability to complex with MyD88(S). Equimolar amounts of MyD88(S) and IRAK-4 K115X were denatured in 8 M urea and co-renatured in FoldIt solution 5 (see Materials and Methods and Appendix VII). Ni-NTA matrix was then added to the mixture and specifically bound proteins were eluted with increasing imidazole concentrations. All samples were analyzed by SDS-PAGE and immunoblotted with anti-FLAG (Figure 4.16, upper panel) or anti-His (lower panel) monoclonal antibodies. The obtained results showed that MyD88(S) and IRAK-4 K115X can form a stable complex in solution, indicating that IRAK-4 residues C-terminally of Ser¹¹⁴ are dispensable for binding to the adaptor.

4.2.5 MyD88•IRAK-4 Complexes Form Large Aggregates in Solution

In previous expression and characterization experiments, we have repeatedly noticed that recombinant MyD88 and IRAK-4 variants undergo unspecific aggregation even in the presence of reducing agents (see Figures 4.7 and 4.8). To assess the size and aggregation properties of these proteins and their complexes, AUC analysis was further employed. Different conditions and protein concentrations (with A_{280} values ranging from 0.1 to 1) were used for the study of MyD88(S), MyD88(L) and IRAK-4(L) individual proteins, as well as MyD88(S)•IRAK-4(L),

MyD88(L)•IRAK-4 K115X and MyD88(L)•IRAK-4(L) (Figure 4.17). A summary of the conditions used for each sample, as well as the obtained results can be seen in Table 4.4. Complexes were obtained by mixing individual components directly into the cell or by renaturation in FoldIt condition 5, and were previously verified by SDS-PAGE. In addition, the results of an electrophoretic analysis of MyD88(L)•IRAK-4(L) and MyD88(L)•IRAK-4 K115X samples under native conditions are shown in Supplemental Figure 3, Appendix XI. Interpretation of the results was complicated by very weak signals (in some cases, no data analysis could be performed), with typical signal-to-noise ratios of 2-3. (Notice that, for a proper analysis, signal-to-noise ratios above 20 are usually required). Probably also related to this issue, the results of these experiments were difficult to reproduce accurately (compare results obtained for identical samples in Figure 4.17b). In spite of these technical problems, which seem to be inherent to the nature of the analyzed samples, the obtained results showed that these MyD88 recombinant forms of death domains not only form large aggregates individually but also when in complex with IRAK-4.

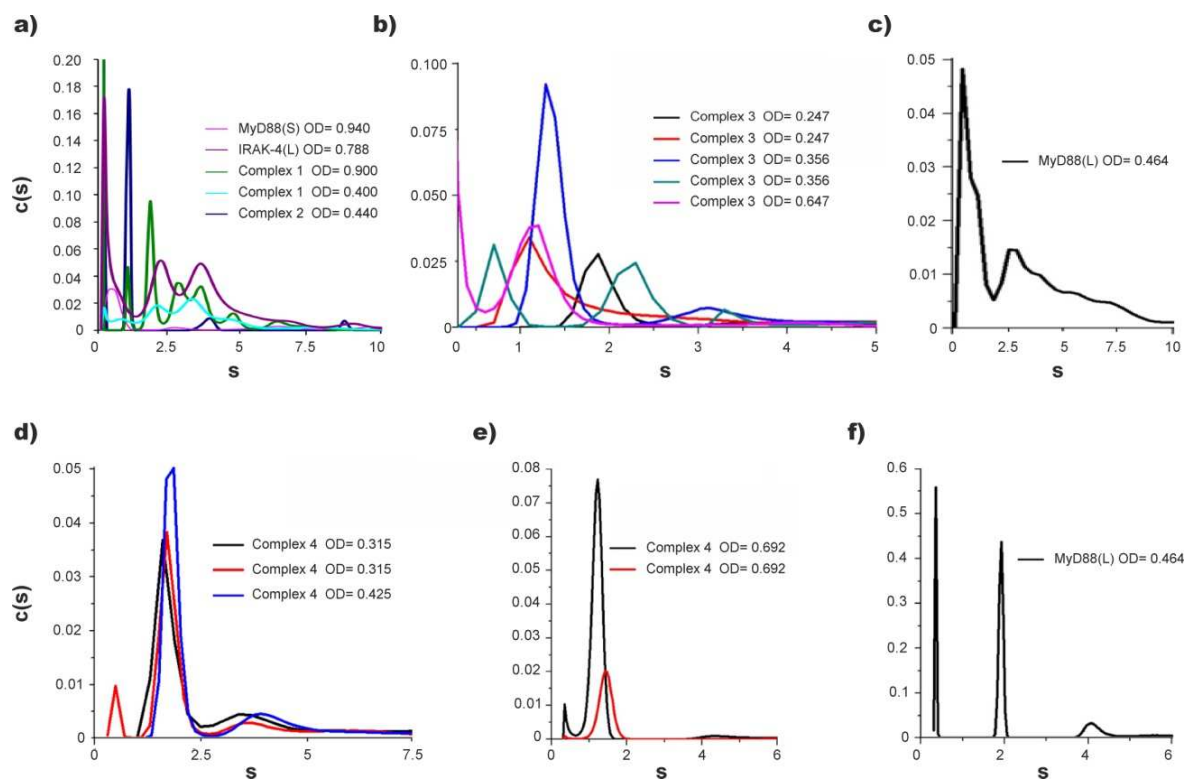


Figure 4.17 AUC analysis of MyD88 and IRAK-4 recombinant fragments and their complexes. AUC tests were performed using sedimentation velocity, as detailed in Materials and Methods. **a)** Analysis of MyD88(S)•IRAK-4(L) obtained either by mixing the individual components directly into the cell (Complex 1), or after previous co-renaturation in FoldIt condition 5 (Complex 2). The individual components of the complex were also analyzed. **b)** Analysis of MyD88(L)•IRAK-4 K115X (Complex 3) at different concentrations and including some replicates. **c)** and **f)** Identical aliquots of MyD88(L) analyzed in different runs. **d)** and **e)** MyD88(L)•IRAK-4(L) (Complex 4) analysis. **e)** Analysis of MyD88(L)•IRAK-4(L) (Complex 4) at different concentrations. All analyses were performed at 10°C except for (a), run at 20°C. See Table 4.4 for a list of all species found in each sample.

Table 4.4 Main characteristics of samples and buffers used for AUC analysis. Buffer density and viscosity were calculated from their respective compositions. Protein partial specific volumes were calculated using SEDNTERP [222] (see Table 4.2 for other protein parameters). Two identical aliquots (al.) of MyD88(L) and complexes 1 and 2 samples were used. C1, MyD88(S)•IRAK-4(L) Complex 1, obtained by mixing individual components; C2, MyD88(S)•IRAK-4(L) Complex 2, obtained by renaturation; C3, MyD88(L)•IRAK-4 K115X Complex 3; C4, MyD88(L)•IRAK-4(L) Complex 4; AUC buffer, buffer in which proteins to be analyzed are dissolved (see Appendix VII).

Sample	Sample A_{280}	V bar (mL/mg)	AUC buffer	Density (g/mL)	Viscosity (cp)	Results (found species)
MyD88 (S)	0.94	0.733	Buffer 1	1.0762	1.501	0.6 S (33%), 3.0 S (4%), 6.2 S (11%), 9.7 S (8%), 15.4 S (8%), 20.3 S (9%), 39.2 (27%) (Fig. 4.17a)
MyD88 (L)	0.464 (al. 1)	0.729	Buffer 2	1.0121	1.034	0.8 S (35%), 2.7 S (18%), 4.0 S (9%), 5.5 S (8%), 7.5 S (8%), 13.0 S (7%), 24.9 S (3%), 36.2 S (3%), 60.6 S (8%) (Fig. 4.17c)
	0.464 (al. 2)	0.729	Buffer 2	1.0121	1.034	0.3 S (23%), 1.9 S (48%), 4.1 S (13%), 9.9 S (5%) (Fig. 4.17f)
IRAK-4 (L)	0.788	0.726	Buffer 3	1.0407	1.44	0.5-S (25%), 2.2 S (24%), 3.7 S (33%), 8.7 S (18%) (Fig. 4.17a)
C1	0.9	0.729	Buffer 4	1.0762	1.501	0.1 S (67%), 1.1 S (2%), 1.9 S (10%), 2.9 S (7%), 3.6 S (8%), 4.7 S (3%), 6.7 S (3%) (Fig. 4.17a)
	0.4	0.729	Buffer 4	1.0762	1.501	0.7 S (13%), 2.1 S (24%), 3.4 S (37%), 4.8 S (13%), 7.7 S (7%), 14.9 S (4%) (Fig. 4.17a)
C2	0.22	0.729	Buffer 5	1.0723	2.064	Not analyzed
	0.354	0.729	Buffer 5	1.0723	2.064	0.6 S (24%), 11.7 S (27%), 27.7 S (7%), 39.4 S (8%), 83.1 S (34%)
	0.44	0.729	Buffer 5	1.0723	2.064	0.1 S (93%), 1.1 S (5%), 3.9 S (1%), 15.2 S (1%) (Fig. 4.17a)
C3	0.247 (al. 1)	0.729	Buffer 2	1.0120	1.034	Not processed (Fig. 4.17b)
	0.247 (al. 2)	0.729	Buffer 2	1.0120	1.034	1.2 S (35%), 2.7 S (10%), 5.2 S (8%), 9.0 S (8%), 15.8 S (8%), 22.0 S (5%), 30.0 S (5%), 53.5 S (19%) (Fig. 4.17b)
	0.356 (al. 1)	0.729	Buffer 2	1.0120	1.034	1.3 S (62%), 3.2 S (14%), 8.8 S (20%), 20.6 (3%) (Fig. 4.17b)
	0.356 (al. 2)	0.729	Buffer 2	1.0120	1.034	0.7 S (22%), 2.2 S (29%), 3.4 S (6%), 5.2 S (8%), 8.4 S (8%), 13.4 S (8%), 23.9 S (5%), 29.3 S (2%), 47.1 S (9%) (Fig. 4.17b)
	0.642 (al. 1)	0.729	Buffer 2	1.0120	1.034	0.2 S (50%), 1.2 S (43%), 3.6 S (6%) (Fig. 4.17b)
	0.642 (al. 2)	0.729	Buffer 2	1.0120	1.034	Not analyzed
C4	0.315 (al. 1)	0.729	Buffer 2	1.0121	1.034	1.7 S (41%), 3.6 S (14%), 7.2 S (13%), 11.7 S (4%), 16.4 S (7%), 28.3 S (6%), 52.6 S (11%) (Fig. 4.17d)
	0.315 (al. 2)	0.729	Buffer 2	1.0121	1.034	0.5 S (5%), 1.7 S (46%), 3.8 S (11%), 6.3 (9%), 10.1 S (8%), 17.2 (6%) (Fig. 4.17d)
	0.425 (al. 1)	0.729	Buffer 2	1.0121	1.034	1.8 S (55%), 4.2 S (18%), 8.2 S (11%) (Fig. 4.17d)
	0.425 (al. 2)	0.729	Buffer 2	1.0121	1.034	Not analyzed
	0.692 (al. 1)	0.729	Buffer 2	1.0121	1.034	0.4 S (4%), 1.2 S (87%), 4.5 S (4%) (Fig. 4.17e)
	0.692 (al. 2)	0.729	Buffer 2	1.0121	1.034	0.4 S (1%), 1.4 S (96%), 6.3 S (1%) (Fig. 4.17e)

Indeed, and in line with our previous results (see Figures 4.7-4.9), AUC analysis revealed a high tendency of the individual proteins to form large aggregates in solution. MyD88(S) analysis revealed several species, the most relevant ones at 39.2 S (indicating the presence of aggregates with up to 40 monomers), although the sample was very polydisperse (Figure 4.17a). Several oligomeric states were found as well when analyzing MyD88(L). Although they could not be analyzed individually due to the large number of species observed in aliquot 1 (Figure 4.17c), most protein in aliquot 2 was found as 1.9 S, corresponding to an 18-kDa globular protein, most likely the MyD88(L) monomer (Figure 4.17f). Finally, IRAK-4(L) analysis also revealed several different species, which could be interpreted as monomers (0.5 S), dimers (2.2 S), tetramers (3.7 S) and higher aggregates (8.7 S) (Figure 4.17a).

AUC analysis of MyD88(S)•IRAK-4(L) samples (complexes 1 and 2) revealed several different species (Figure 4.17a). Most protein, however, was found as large aggregates (11.7 S and 83.1 S). Aggregation was also detected in MyD88(L)•IRAK-4(L) (Complex 4). Although the majority of the protein sediments at ~ 1.7 S, corresponding to a 16-kDa globular protein (probably not complexed protein), other peaks are observed at ~ 3.8 S (53-kDa globular protein, probably corresponding to an elongated heterodimer) and higher sedimentation coefficients (Figure 4.17d and e). Importantly, diminished aggregation was detected when performing AUC analysis on MyD88(L)•IRAK-4 K115X (Complex 3), as seen in Figure 4.17b.

The strong tendency of MyD88 and IRAK-4 recombinant fragments to form large aggregates when in complex was also demonstrated by FPLC analysis of MyD88(L)•IRAK-4(L) and MyD88 E143X•IRAK-4(L) (MyD88 E143X•IRAK-4(L) complex formation had been previously demonstrated, as shown in Supplemental Figure 4, Appendix XI). Samples were injected at relatively low concentrations of 0.5 and 0.9 mg/mL, respectively, and analyzed as explained in Materials and Methods. Using the data obtained from the standard curve given in

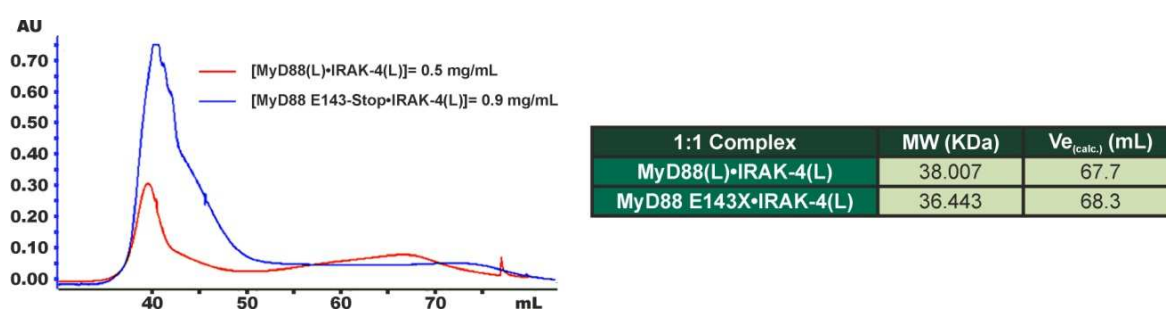


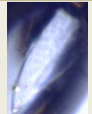


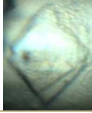
Figure 4.18 FPLC analysis on MyD88(L)•IRAK-4(L) and MyD88 E143X•IRAK-4(L) complexes. MyD88(L)•IRAK-4(L) (in red, injected at 0.5 mg/mL) and MyD88 E143X•IRAK-4(L) (in blue, injected at 0.9 mg/mL) eluted mostly at ~ 40 mL, corresponding to a MW of ~ 323 kDa (8 to 9 monomeric complexes). Expected elution volumes for 1:1 complexes were calculated from the standard curve given in Figure 4.6a.

Figure 4.6a, the elution volumes were estimated to be 67.7 mL for MyD88(L)•IRAK-4(L) and 68.3 mL for MyD88 E143X•IRAK-4(L) monomeric complexes. As seen in Figure 4.18, both complexes were found to elute at around 40 mL, corresponding to a MW of ~ 325 kDa (8 to 9 monomeric complexes, assuming a globular arrangement).

4.2.6 Recombinant Death Domain-Only Variants of MyD88 Can Be Crystallized

To unveil the structural basis of MyD88-IRAK complex formation, we performed crystallization trials on MyD88(L), MyD88 E143X and IRAK-4(L) recombinant fragments, as well as on their complexes, with the aim of growing crystals that are large and ordered enough for X-ray crystal analysis. Individual proteins were expressed, extracted and purified as described in sections 3.3-3.5, and their complexes were usually obtained by co-renaturation (section 3.9.3). Crystallization experiments were conducted manually using the hanging-drop method, as explained in Materials and Methods (see Appendix X for a detailed list of all used conditions). Drops were allowed to stand at 20°C in a Rumed 3201 incubator, and observed periodically under a Nikon SMZ800 zoom stereomicroscope. Although a large number of trials were performed, diffracting protein crystals were only obtained for uncomplexed MyD88(L) and MyD88 E143X. These crystals were grown in different conditions, shown in Table 4.5, although only the best hits are described here.

Table 4.5 Summary of crystallization conditions used on MyD88 recombinant fragments. All crystals were grown at 20°C using the hanging-drop method. Monomers, dimers and aggregates refer to gel-filtration samples (see Figure 4.6 and Supplemental Figure 2). Crystallization solutions are shown by the name of the used screen and tube number, using the following abbreviations: SS1, Structure Screen Box 1; SS2, Structure Screen Box 2; M1, MorpheusTM Box 1; M2, MorpheusTM Box 2. The detailed compositions of these solutions, as well as of HEPES and Tris-based buffers, can be found in Appendix X.

Protein	Crystallization solution	Protein concentration (mg/mL)	Protein/Solution Volume (μL)	Crystals
MyD88(L)	M2-2	5	0.75/0.75	
MyD88 E143X (Monomers)	SS2-28	4.3	1/0.5	
MyD88 E143X (Dimers)	SS1-36	4.2	0.5/1	
MyD88 E143X (Aggregates)	SS2-28	4.8	0.5/1	

Unfortunately, crystals were only poorly reproducible, and no clear common patterns were found in terms of preferred precipitant agents and pH values. Selected crystals were analyzed using synchrotron radiation at the ESRF facilities (Grenoble, France), using 20% glycerol as cryoprotectant, when necessary. Although crystals were generally small (0.05-0.1 mm) and, in most cases, diffracted X-rays only poorly, they were established to be protein crystals as they presented typical protein diffraction patterns (see Supplemental Figure 5, Appendix XI). No complete diffraction sets of these crystals could be collected due to their small sizes and/or their extreme anisotropy.

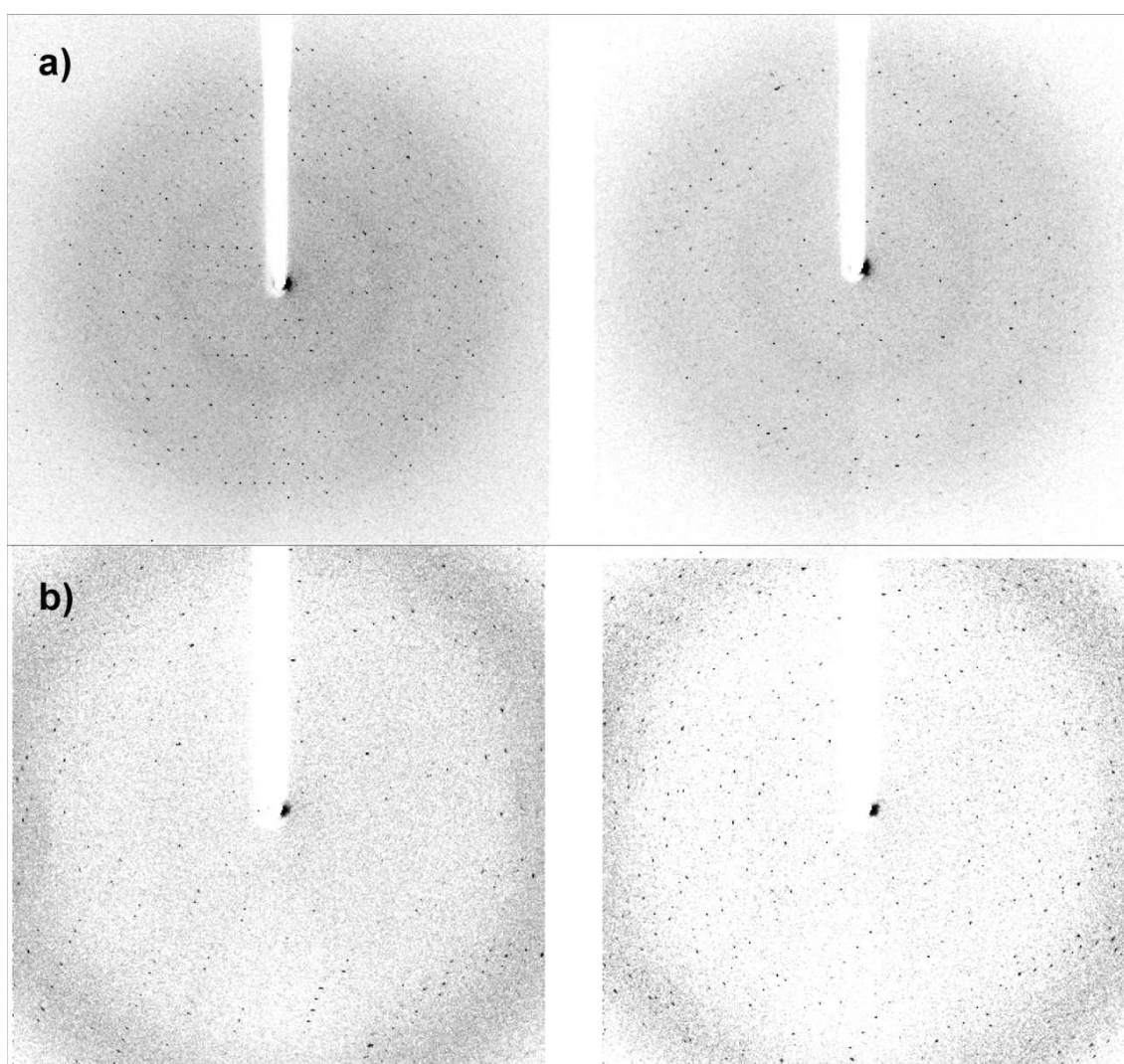


Figure 4.19 Orthogonal images of diffraction patterns obtained from MyD88 E143X crystals. All crystals were grown as described in text and Table 4.5. **a)** Diffraction patterns of MyD88 E143X (crystal 1), obtained at orthogonal positions. This crystal presents ordered diffraction patterns and a full data set at a resolution of 1.8 Å was collected. **b)** Diffraction patterns of MyD88 E143X (crystal 2), obtained at orthogonal positions. This crystal also presents ordered diffraction patterns and a full data set at a resolution of 2 Å was collected. Diffraction patterns were measured at the ESRF beamline ID23-2, equipped with a MarMosaic225 CCD detector.

MyD88 E143X crystals grown from apparently monomeric (crystal 1) or aggregated fractions (crystal 2), respectively, were obtained in solution 28 of the Structure Screen 2 crystallization kit. Since they presented ordered diffraction patterns (see Figure 4.19), a full data set of each crystal was collected at ESRF beamline ID23-2 (at resolutions of 1.8 and 2 Å, respectively) using the parameters given in Table 4.6.

Indexing of crystals 1 and 2 allowed us to establish that they are orthorhombic and both pertain to the C222 or related space groups. The determined cell constants (see Table 4.6) suggest that asymmetric units of these crystals contain, with about 80-90% probability, 3 protein molecules and 42% of solvent content. These structures were tried to be solved by molecular replacement, using the recently reported crystal structures of MyD88 DD in complex with the death domains of IRAK-4 and IRAK-2 [178], and also using truncated models derived from other reported DDs structures, such as the Fas/FADD death domain assembly [247] and the uncomplexed RAIDD DD [112] and Pelle DD [248] (PDB codes: 3OQ9, 3MOP, 2O71 and 1IK7, respectively). Unfortunately, no solution has been obtained so far, suggesting a major rearrangement of the six-helix bundle during the long time needed for crystallization, perhaps similar to the more compact Pelle structure previously reported by Xiao and co-workers [248].

Table 4.6 Summary of used and calculated parameters during data collection of MyD88 E143X crystals. Crystals obtained from monomeric (crystal 1) and aggregated (crystal 2) forms of MyD88 E143X, were analyzed using X-ray diffraction at ESRF beamline ID-23-2. Complete data sets were collected at maximum resolutions of 1.8 and 2 Å, respectively. The main parameters used for data collection are shown. Determined cell constants are defined by vectors a , b and c (forming the edges of the parallelepiped), and the angles between these vectors α , (between b and c), β (between a and c), and γ (between a and b).

Crystal 1		Crystal 2	
Wavelength	0.8726 Å	Wavelength	0.8726 Å
Transmission	100%	Transmission	100%
Exposure Time	10 s	Exposure Time	10 s
# Collected images	360	# Collected images	120
Oscillation range ($\Delta\phi$)	1°	Oscillation range ($\Delta\phi$)	1°
Sample to detector distance	210 cm	Sample to detector distance	238 cm
Space group	C222	Space group	C222
Unit cell constants	$a = 87.26 \text{ \AA}$ $b = 97.19 \text{ \AA}$ $c = 89.99 \text{ \AA}$ $\alpha = 90^\circ$ $\beta = 90^\circ$ $\gamma = 90^\circ$	Unit cell constants	$a = 87.23 \text{ \AA}$ $b = 96.99 \text{ \AA}$ $c = 90.27 \text{ \AA}$ $\alpha = 90^\circ$ $\beta = 90^\circ$ $\gamma = 90^\circ$

4.3 Interactions Between MyD88 and IRAK-M Recombinant Variants

4.3.1 The Linker-Extended Versions of MyD88 and IRAK-M Form a Stable Complex in Solution

To verify that MyD88 is able to recruit IRAK-M, similar to what we have previously shown for IRAK-4, we took advantage of the N-terminal 6xHis tag present in our MyD88 recombinant fragments. MyD88(L) was firstly incubated with an equimolar amount of purified IRAK-M(L). Excess Ni-NTA agarose matrix was then added to this mixture, and treated as described in Materials and Methods (section 3.5.1). All fractions of the purification procedure were recovered and analyzed by SDS-PAGE and Coomassie Brilliant Blue staining. As a control, the same amount of IRAK-M(L) was treated in a similar manner. IRAK-M(L) was pulled down by the affinity matrix in the presence but not in the absence of MyD88(L) (except for some unspecific interaction), indicating formation of the MyD88(L)•IRAK-M(L) complex (Figure 4.20). As with IRAK-4(L), we observed only partial complex formation, probably because a fraction of the individual components form aggregates that do not dissociate in the presence of the binding partner, thus effectively interfering with heterodimer formation *in vitro*.

In other experiments, to confirm heterodimer formation while minimizing interference of aggregation effects, we subjected mixtures of MyD88(L) and IRAK-M(L) previously denatured in 8 M urea to renaturation trials by rapid dilution in refolding solutions of the FoldIt Screen (see Appendix VIII). Following this procedure, we found several conditions in which apparently equimolar amounts of MyD88(L) and IRAK-M(L) remained in solution after removal of chaotropic agents, and which could be quantitatively recovered by metal affinity chromatography.

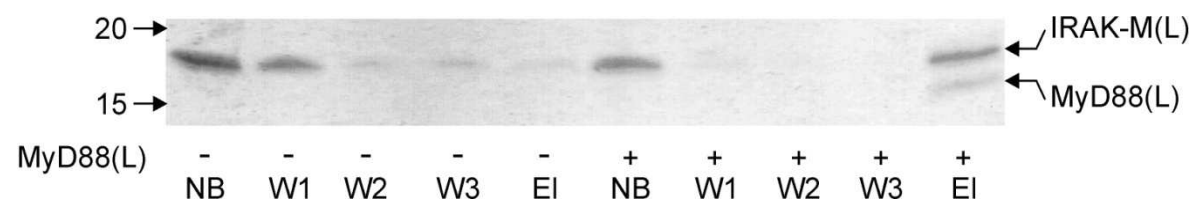


Figure 4.20 Formation of MyD88(L)•IRAK-M(L) heterodimer in solution. Equimolar amounts of purified MyD88(L) and IRAK-M(L) were incubated for 2 hours at room temperature in binding buffer (see Appendix VII) and then Ni-NTA agarose matrix was added to this mixture. After centrifugation to remove non-bound material (NB), the matrix was washed several times with binding buffer (W) and specifically bound proteins were finally recovered with elution buffer (EI). Samples were separated by SDS-PAGE and stained with Coomassie Brilliant Blue (MWs given in kDa, on the left). Notice that, despite some unspecific interaction between IRAK-M(L) and the Ni-NTA agarose matrix, much larger quantities of IRAK-M are bound to the matrix in the presence of MyD88(L) indicating MyD88(L)•IRAK-M(L) complex formation.

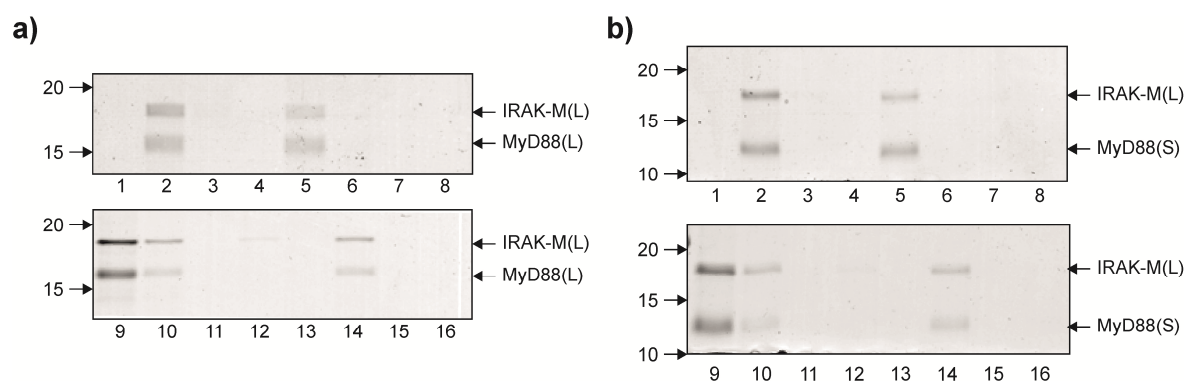


Figure 4.21 MyD88 and IRAK-M(L) co-renaturation trials by rapid dilution in refolding solutions. Aliquots containing equimolar amounts of purified IRAK-M(L) and either MyD88(L) or MyD88(S), previously denatured in 8 M urea, were incubated overnight at 4 °C on a rocker with each of the 16 folding solutions of the FoldIt Screen (Appendix VIII). Samples were then centrifuged to remove precipitated material, and supernatants were analyzed by SDS-PAGE and stained with Coomassie Brilliant Blue. **a)** MyD88(L) and IRAK-M(L) co-renaturation trials. **b)** MyD88(S) and IRAK-M(L) co-renaturation trials. Notice that, in both cases, best results were obtained in FoldIt solutions 2, 5, 9, 10 and 14, in which apparently equimolar amounts of MyD88(L)/(S) and IRAK-M(L) remained in solution after centrifugation. Molecular weights, determined with Novex® Sharp Pre-stained Protein Molecular Weight Standard, are given on the left of each gel, in kDa.

Best results were obtained with FoldIt solutions 2, 5, 9, 10 and 14 (see Appendix VIII), as seen in Figure 4.21a. When the same procedures were repeated using MyD88(S) instead of the linker-extended version of the adaptor, similar results were obtained (Figure 4.21b). Using a slightly modified FoldIt solution 9 (containing sodium phosphate pH 7.0 instead of MES), we performed a larger-scale refolding experiment by incubating a protein mixture containing a slight molar excess of MyD88(L) in the presence of reduced and oxidized glutathione (see Materials and Methods). The supernatant was incubated with excess Ni-NTA agarose and bound proteins were recovered with elution buffer. The results of this experiment (shown in Figure 4.22) demonstrate MyD88(L)•IRAK-M(L) heterodimer formation by co-renaturation of its components.

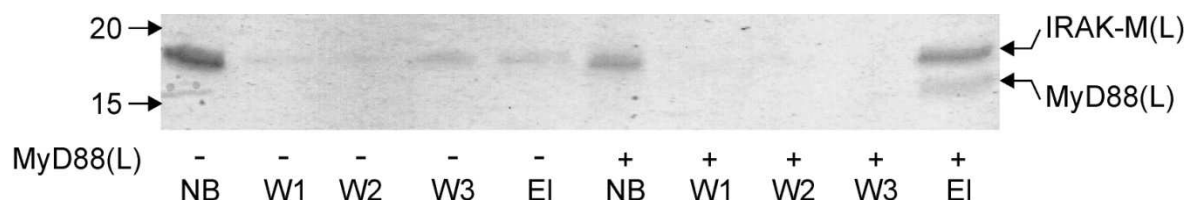


Figure 4.22 The linker-extended variants of MyD88 and IRAK-M form a stable complex. Equimolar amounts of IRAK-M(L) and MyD88(L) were denatured in 8 M urea, and refolded together by rapid dilution in FoldIt condition 9 (see Appendix VIII). After centrifugation to remove insoluble material, Ni-NTA agarose was added to the supernatant and specifically bound proteins were recovered with elution buffer (see Appendix VII), as explained in Materials and Methods. Non-bound (NB), wash (W), and elution (EI) fractions were analyzed by SDS-PAGE and stained with Coomassie Brilliant Blue (MWs given in kDa, on the left). As in Figure 4.20, much larger quantities of IRAK-M(L) are bound to the matrix in the presence of MyD88(L) indicating MyD88(L)•IRAK-M(L) complex formation.

4.3.2 Residues Beyond Glu¹⁴³ in the DD-TIR Linker of MyD88 Are Not Required for IRAK-M Recruitment

After having demonstrated the formation of a stable MyD88(L)•IRAK-M(L) complex, we wished to analyze the importance of the unstructured DD-TIR linker of the adaptor protein in complex formation. With this aim, we performed experiments essentially as described above, but replacing MyD88(L) by the variant with a shorter linker, MyD88 E143X, which had been previously shown to be fully functional in terms of IRAK-4 binding (see Supplemental Figure 4, Appendix XI). First, we analyzed whether MyD88 E143X was able to form a stable complex with IRAK-M(L) in binding buffer (see Appendix VII for composition). This was indeed the case, as IRAK-M(L) could be pulled down with Ni-NTA matrix in the presence of the truncated form of the bipartite adaptor (Figure 4.23a). The same results were obtained when repeating the same experiments in FoldIt condition 9 (see Appendix VIII for composition), indicating that residues beyond Glu¹⁴³ in the DD-TIR linker of MyD88 are not required for heterodimer formation (Figure 4.23b).

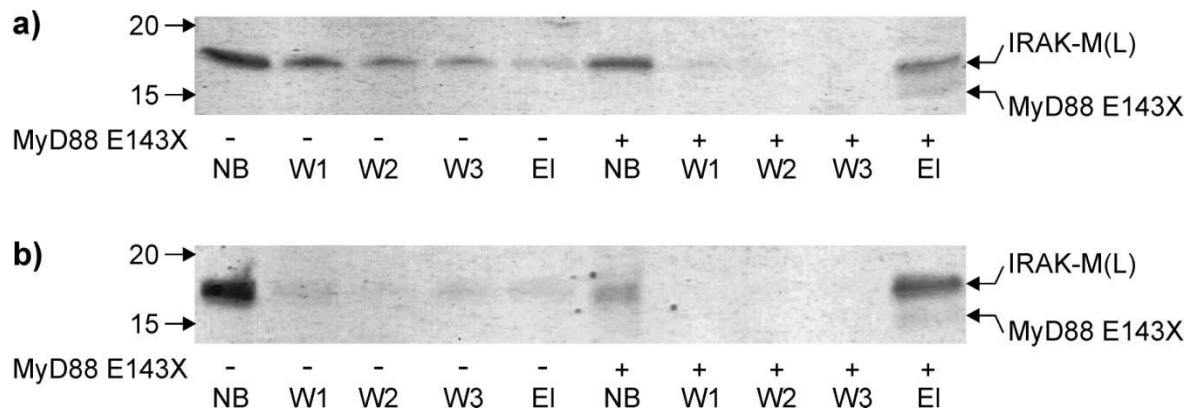
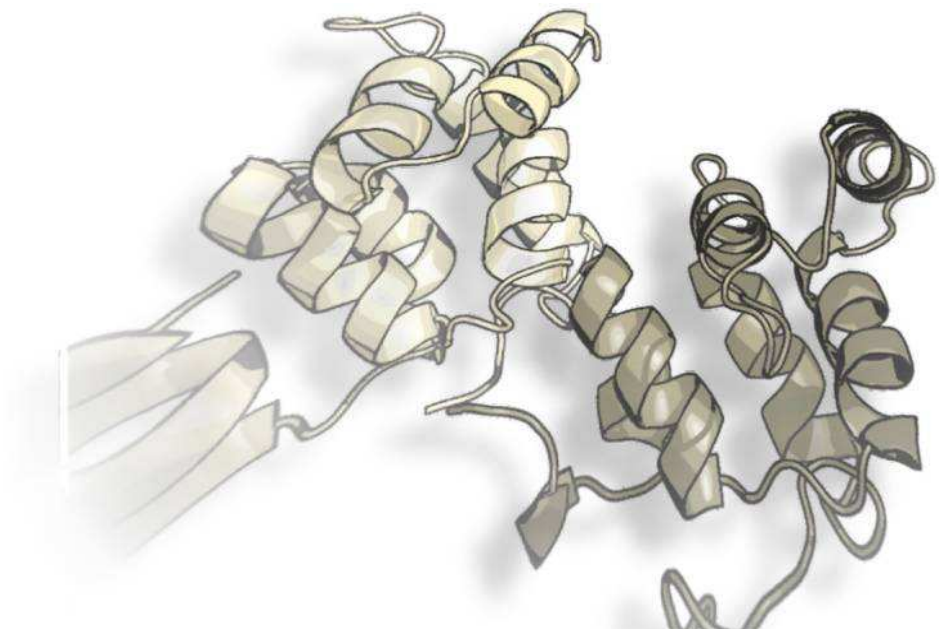


Figure 4.23 Residues beyond Glu¹⁴³ in the DD-TIR linker of MyD88 are not required for IRAK-M recruitment. Equimolar amounts of purified MyD88 E143X and IRAK-M(L) were incubated for 2 hours at room temperature in binding buffer (see Appendix VII) (**a**) or denatured in 8 M urea and refolded by rapid dilution in FoldIt condition 9 (see Appendix VIII) (**b**). Ni-NTA agarose matrix was added to both mixtures and non-bound (NB), wash (W) and elution (EI) fractions were analyzed by SDS-PAGE and stained with Coomassie Brilliant Blue (MWs given in kDa, on the left). Despite some unspecific interaction between IRAK-M(L) and the Ni-NTA agarose matrix, much more quantities of the kinase are bound to the matrix in the presence of MyD88 E143X, indicating MyD88 E143X•IRAK-M(L) complex formation. Notice that unspecific interactions are diminished when proteins are allowed to co-renature, as compared to simple mixing of the two components in binding buffer.

5. Discussion



5.1 Overexpression and Characterization of Death Domains of MyD88 and IRAK Proteins

Although the innate immune responses in insects and mammals share many similarities, and for instance the Toll-MyD88-Tube-Pelle cascade is functionally equivalent to that of TLRs-MyD88-IRAKs [184, 189], they also present important differences. Most notably, mammals on the one hand possess several relatives of the kinase Pelle, termed IRAK proteins, but on the other lack a true Tube ortholog. In fact, the role that this adaptor plays in insects appears to be assumed in mammals by one of the IRAK members, IRAK-4 (refs. [79, 138, 184, 190-192] and Figure 1.8).

Previous investigations on the interface between the death domains (DD) of *Drosophila* Pelle and its adaptor, Tube, indicated that two major regions of the latter are critical for complex formation: (i) exposed DD residues mostly donated by helices $\alpha 4$ and $\alpha 5$ and their connecting loop, and (ii) a short polypeptide stretch within the non-structured C-terminal extension to this globular domain, which inserts between helix $\alpha 5$ and the N-terminus of Pelle DD [174]. Similar interactions have been observed in other complexes between members of the death domain superfamily. For example, (i) both the α -helical DED module and the irregular C-terminal tail of PEA-15, an important modulator of the ERK/MAP kinase pathway, are required for ERK binding [96], and (ii) a short stretch preceding the Fas death domain is required for recruiting the bipartite adaptor of the extrinsic apoptotic pathway, FADD [249]. Altogether, these findings suggest that several members of the DD superfamily combine interactions mediated by globular domains and unstructured linkers for specific heterodimer formation.

In line with these findings, and in particular highlighting the connection between the death domains of the Toll and TLR pathways, we have observed a previously unrecognized similarity between mammalian MyD88 and *Drosophila* Pelle. Indeed, a detailed inspection of the sequence alignments of MyD88 and IRAK-4 death domains from various species (Appendix II), prepared considering the results of secondary structure prediction methods (see Appendices III-IV), revealed that MyD88 possesses a seventh, C-terminal 3_{10} helix, in addition to the conserved framework of six antiparallel helices previously observed in death domains from murine IRAK-4 [111] and *Drosophila* Tube [174], as well as in Fas [103] and in FADD [109, 245]. It is particularly striking that residues C-terminally of helix $\alpha 6$ in MyD88 (Ile¹⁰⁹ to Lys¹¹⁹ in the human adaptor) are highly similar to those of *Drosophila* Pelle, in contrast to the rather low sequence conservation throughout the DD superfamily.

In turn, this observation suggested an arrangement of the mammalian MyD88 DD•IRAK-4 DD heterodimer similar to that observed in the crystal structure of the Pelle•Tube complex [174], and prompted us to study complex formation between human MyD88 and IRAK proteins,

and to analyze the contributions of the corresponding globular and unstructured regions to this process. To this end, we cloned, overexpressed, and purified the death domains of MyD88 and of all known IRAK proteins (with the exception of IRAK-2), both alone and extended by the full-length linkers to their C-terminal TIR or kinase domains (see Figure 4.1 and Appendix XI).

Although all eight initial constructs used in this study had been similarly optimized, we observed significant differences in expression yields and solubility of recombinant proteins, even between “long” and “short” variants of the same protein. For instance, MyD88(L) but not MyD88(S) could be recovered from the cytosolic fraction of BL21(DE3)pLysS cells (see Table 4.1), most probably because of the stronger tendency of the DD-containing only recombinant variant to self-aggregate, as indicated by analytical ultracentrifugation, gel filtration and dynamic light scattering analyses of these MyD88 recombinant fragments (see Figures 4.4, 4.6 and 4.17, and Appendix XI). The higher solubility of MyD88(L) suggests that the DD-TIR linker is largely responsible for adaptor solubility in the cytosol, in the absence of activating stimuli and receptor engagement. How would inclusion of this unstructured interdomain/linker enhance solubility of the adaptor DD? It is tempting to speculate that this relatively long peptide covers, at least transiently, a hydrophobic patch on the globular death domain that mediates unspecific aggregation. Residues with aliphatic side chains within the MyD88 linker, and in particular the well-conserved Leu¹²⁹, Val¹³¹, Val¹³⁴ and Val¹³⁸, are likely candidates for interacting with an apolar surface on the N-terminal DD. It is particularly noteworthy that residue Leu¹²⁹ is strictly conserved in mammals, and conserved or conservatively replaced by Ile/Val in other vertebrates. Further, position 134 is always occupied by valine or isoleucine. This high degree of conservation within an otherwise flexibly disordered region points to an important functional role. In line with these observations, the designed recombinant variant MyD88 E143X, truncated at Glu¹⁴³ and thus containing the hydrophobic residues mentioned above, was recovered from the cytosolic fraction of BL21(DE3)pLysS cells, similar to the linker extended variant MyD88(L) (data not shown). In turn, interactions of the DD-TIR linker of the adaptor with the DD module would locate these two globular domains in close proximity, forming a somewhat “closed” structure and thus avoiding its untimely recruitment by the TIR domains of IL-1R / TLRs, and concomitant activation of downstream IRAK kinases (see below).

The strong tendency of the studied MyD88 recombinant variants to form large aggregates in solution is consistent with previous findings of massive aggregation observed in other overexpression experiments of the bipartite adaptor. Most notably, studies on the subcellular localization of MyD88 have shown that the protein is present as condensed forms in the cytoplasm, such as discrete foci, fibrillar aggregates, and inclusion bodies [119-122] (see Figure 5.1). Although most of the reported work suggests that aggregation of full-length MyD88 is essentially mediated by homotypic interactions between its death domains [73, 182], a recent work presents evidence indicating that the entire non-TIR region (i.e., DD and linker) is required

to form these aggregate structures [121]. Our *in vitro* results, however, support a more important role of the DD module in this regard.

Interestingly, the situation is exactly opposite in the case of IRAK proteins, as the DD-only recombinant variants IRAK-1(S) and IRAK-M(S), but not their linker-extended counterparts, were expressed as soluble proteins in *E. coli* (see Table 4.1). It would seem that the unstructured DD-(pseudo)kinase linkers are prone to aggregate formation *per se*. Along these lines, most reported aggregation-prone motifs are rich in β -branched aliphatic and aromatic residues as well as in hydroxyl-containing Ser/Thr residues, but show a lower-than-expected proportion of charged residues [250]. These features are observed in the DD-kinase linker of human IRAK-1. In particular, the Ser¹³⁸-Ser¹⁴⁴ stretch is predicted as an aggregation "hot spot" by Aggrescan [251] (<http://bioinf.uab.es/aggrescan/>), which almost exactly matches the region of maximum aggregation propensity within the linker identified by ProA (<http://www.abl.ku.edu/ProA/>), Ser¹³⁷-Phe¹⁴².

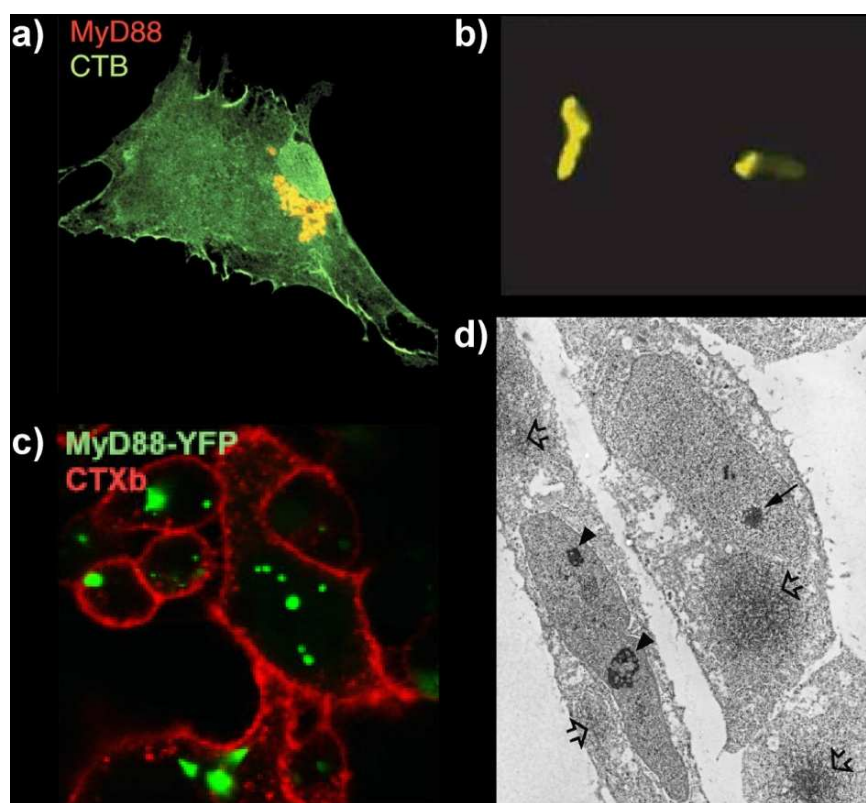


Figure 5.1 Overexpressed MyD88 is localized in the cytoplasm as large condensed forms. a) Micrographs of mouse embryonic fibroblasts expressing hemagglutinin-tagged MyD88. MyD88 was found in discrete foci scattered throughout the cytosol, as identified with FITC-cholera toxin B (CTB) (extracted from [119]). b) HEK293 cells were transfected with yellow fluorescent protein (YFP)-tagged MyD88 and visualized by inverted fluorescence microscopy. Notice that MyD88-YFP is expressed as a condensed form in the cytoplasm (extracted from [120]). c) Confocal image of HEK293T-MyD88-YFP cells stained with Alexa Fluor 594-conjugated CTXb (cholera toxin B subunit) (extracted from [121]). d) Ultrathin sections of HeLa cells transfected with Flag-tagged MyD88. Cytoplasmic aggregates (open arrows) and nuclear aggregates (closed arrows) were observed in transfected cells (extracted from [122]). Refer to cited publications for details.

In the case of the pseudo-kinase, the linker region is particularly rich in aliphatic / aromatic residues, and Aggrescan identifies stretches Asn¹²³-Ala¹³⁰, Thr¹³³-Val¹³⁷, and Leu¹⁴⁸-Ile¹⁵⁸ as potential hot spots for aggregation, while ProA maxima were predicted between residues 120-134 and 146-156. In the case of IRAK-4, however, the presence of the linker did not influence the solubility of the different recombinant variants, as both the DD-only and the linker-extended variants were repeatedly recovered from the insoluble fractions in overexpression experiments (see Table 4.1). The fact that our IRAK-4(S) recombinant fragment is expressed in inclusion bodies is in striking contrast with the recent work of Lasker and co-workers, in which IRAK-4 DD could be expressed as a soluble protein in *E. coli* [111]. A possible explanation for this contradiction comes from the fact that the recombinant form designed by Lasker and co-workers comprises residues 1-113, and thus includes a few extra polar residues C-terminally of the DD module (e.g. Thr¹⁰⁸ and Thr¹¹¹), compared to our designed variant IRAK-4(S). However, although the formation of IBs has been found to be affected by many factors (e.g. the amino acid sequence of the recombinant protein, the induction temperature, the culture condition, the rate of protein production and folding, and the availability of essential chaperones [252-256]), it has been recently proposed that other factors besides amino acid composition and high concentrations of overexpressed protein, play a major role in formation of such aggregated structures [257]. The lack of a thorough understanding of the formation of IBs in *E. coli* make it difficult to predict whether a recombinant protein will be soluble, partially or completely deposited into IBs.

For urea-extracted fractions of MyD88 and IRAK recombinant fragments, most of the sixteen refolding conditions routinely tested were successful and large quantities of properly folded recombinant proteins could be recovered in this manner. These findings suggest that these aggregates contain properly folded DDs and/or native-like folding intermediates that are easily forced into the correct 3D conformation in the presence of specific chaotropic agents and detergents. In this regard, of course, the fact that all these DDs are single-domain, all α -helical proteins with a rather simple topology, and which in addition lack disulfide bridges, greatly facilitates adoption of the proper 3D configuration. Correct folding of these fragments was directly demonstrated by the fact that only Glu-Xxx scissile peptide bonds within the irregular C-terminal tails of the linker-containing variants of MyD88 and IRAK proteins, but not those within their globular death domains, are susceptible to Glu-C cleavage (Figure 4.3). The ultimate proof of the native-like conformation of recombinantly expressed DD variants of MyD88 was the demonstration of specific interactions with natural IRAK-4 kinase from monocyte extracts (Figure 4.12).

In line with our current findings, aggregation has been also found in other members of the DD superfamily (see Figure 5.2): (i) DED-dependent filaments were detected in the cytoplasm of cells overexpressing caspase-8 or FADD, and these aggregates were almost completely insoluble in two commonly used non-ionic detergents, NP-40 and Triton X-100 [258]. Further, (ii)

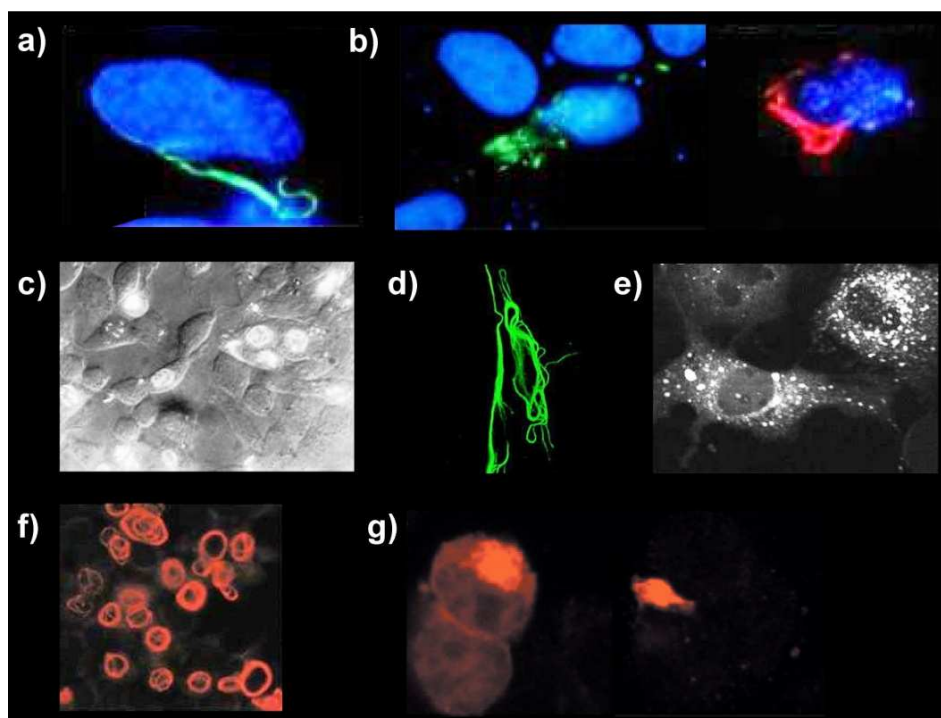


Figure 5.2 Aggregation is a common feature of members of the DD superfamily. **a)** HeLa cells transfected with the DED-containing prodomain of caspase-8, fused to GFP, and immunostained. A distinctive cytoplasmic filament network can be observed (from [258]). **b)** The same cells were transfected with the DED domain of FADD either fused to GFP (left panel) or without any epitope tag (right panel). Numerous filaments could also be detected by immunostaining (from [258]). **c)** NIH-3T3 cells were transfected with a GFP fusion protein consisting of the prodomain region of caspase-2, and photographed using a fluorescence microscope. The CARD-GFP fusion protein appeared as discrete filamentous structures inside the nucleus (from [259]). **d)** Fluorescence confocal micrographs of HeLa cells expressing a bcl10 truncated protein, containing only the CARD domain. Notice the clear pattern of discrete and interconnecting cytoplasmic filaments exhibited by this form, resembling the DED filaments shown in **(a)** (from [260]). **e)** COS cells were transfected with a GFP construct containing the CARD domain of caspase-2, directly fused to the caspase domain. Cells were fixed and analyzed by confocal microscopy. As it can be observed, the CARD-containing GFP fusion protein forms large aggregates in the cytoplasm (from [261]). **f)** HEK293T cells transfected with a FLAG-tagged RAIDD-CARD construct were fixed, immunostained, and observed by fluorescence microscopy. The RAIDD-CARD appears as an extensive filamentous network within the cytoplasm, sometimes appearing as lariat structures around the nucleus (from [262]). **g)** PC12 cells transfected with a pCDNA3 vector encoding RAIDD were fixed, stained and visualized by confocal microscopy. Overexpressed RAIDD is localized predominantly within a perinuclear cytoplasmic region, forming aggregates of a spherical shape (left panel). Of note, this RAIDD-induced aggregates are relatively insoluble, as the same cells transfected with rat RAIDD and briefly exposed to detergent still showed a perinuclear immunostaining pattern (right panel), indicating that these RAIDD aggregates are resistant to detergent extraction (from [263]).

overexpressed caspase-2 and its isolated CARD module form large aggregates that are visualized as discrete dot- or filament-like structures by fluorescence microscopy [259, 261]. Likewise, (iii), similar CARD-dependent filamentous or spherical aggregates have been reported for its adaptors, RAIDD [262, 263], and bcl10 [260]. Of particular note, the recently presented crystal structure of the oligomeric RAIDD-DD•PIDD-DD complex reveals an intricate asymmetric arrangement of

seven RAIDD and five PIDD death modules [264], as it will be discussed below. Finally, and highlighting the possibility of reverting multimerization with minimal structural changes, (iv) FADD aggregates at neutral pH in solution while the conservative point mutant F25Y remains monomeric even at high protein concentrations [100, 245].

Given that TLR engagement is followed by receptor oligomerization to form “receptosomes” that in turn recruit MyD88 [72], and that overexpressed MyD88 automatically induces death domain-dependent activation of downstream signaling pathways [30, 121, 123, 124], we consider that multimerization of our recombinant proteins reflects the *in vivo* signaling pathway.

5.2 Death Domain Interactions Between MyD88 and IRAK Proteins

Although it is generally accepted that MyD88 acts by recruiting protein kinases of the IRAK family through interactions between their respective DDs, it has not been unambiguously established whether additional cofactors are necessary for MyD88-mediated IRAK recruitment *in vivo*, and the specific residues involved in such interactions have been only partially characterized. Our current findings directly confirm that the DD alone, eventually extended by the more N-terminal portion of the linkers suffices for complex formation *in vitro*. These findings, in turn, strongly suggest that the bipartite adaptor alone can recruit IRAK-4 and IRAK-M to its membrane-proximal complexes with IL-1R / TLR *in vivo* (see Figures 4.10, 4.20 and 4.22). Further, our results unambiguously establish that the C-terminal TIR (MyD88) and kinase (IRAK) domains are dispensable for complex formation.

In the absence of added detergents, we have repeatedly observed only partial complex formation between MyD88(L) and IRAK-4(L) (Figure 4.7), probably because aggregation of individual DDs interferes with heterodimer formation *in vitro*. As previously discussed for the individual components, large aggregates of purified MyD88•IRAK-4 complexes were also observed by gel filtration and AUC analyses (see Figures 4.17 and 4.18). Notably, a decreased tendency for aggregation was observed when complexating the linker-extended recombinant variant of the adaptor with the truncated variant IRAK-4 K115X, and also the linker-extended variant of IRAK-4 with the truncated variant MyD88 E143X, suggesting that residues beyond Lys¹¹⁵, in the kinase linker, and Glu¹⁴³, in the adaptor, may play an important role in protein aggregation.

In order to limit formation of large aggregates, we combined the use of low protein concentrations and specific non-ionic detergents (Figure 4.8), which allowed quantitative formation of the MyD88(L)•IRAK-4(L) complex in solution (see Figure 4.10a). Interestingly, and as can be seen in this figure, no heterocomplex was detected at very low IRAK-4 concentrations, and the MyD88(L) linker was partially cleaved by a contaminating protease. Since degradation

was prevented at the higher IRAK-4(L) concentrations that support complex formation, our results suggest protection of the linkers in the MyD88(L)•IRAK-4(L) heterodimer (discussed below). In addition, we have established co-renaturation of MyD88 and either IRAK-4 or IRAK-M recombinant death domains as a novel method for complex formation, providing a simple means for analysis of DD-mediated interactions while minimizing the effects of aggregation (see Figures 4.10b and 4.22). Notably, the MyD88(L)•IRAK-4(L) complex bound more tightly to the metal affinity matrix than the free DD of the adaptor, pointing to formation of dimers or higher order aggregates of the heterodimer. In this regard, as previously mentioned, MyD88 is known to dimerize following receptor recruitment *in vivo* [73], and recent evidence indicates that enforced adaptor dimerization suffices to trigger signaling [124].

In our studies to determine whether the interdomain connector of MyD88 is required for complex formation with IRAK proteins, we have demonstrated not only that IRAK-M is able to associate with MyD88 (Figures 4.20 and 4.22), but also that residues beyond Glu¹⁴³ of the DD-TIR linker of the adaptor are not required for complex formation with IRAK-M (see Figure 4.22). IRAK-M interactions with MyD88 are of particular interest, as the pseudo-kinase has been shown to play an inhibitory role in the TLR/IL-1R signaling pathway [136]. However, the mechanism(s) underlying this inhibitory function of the pseudo-kinase are still speculative. In this regard, several studies suggest that IRAK-M does not prevent IRAK-1 or IRAK-4 recruitment to the TLR/IL-1R•MyD88 complexes, but inhibits dissociation of the activated kinases from the receptor complex and therefore blocks LPS-induced NF- κ B activation [85, 125, 127, 129, 130, 132, 136, 147, 200, 265]. IRAK-M has been recently speculated to bind to IRAK-2, which does not contact MyD88 in the reported crystal structure, to prevent IRAK-2 or IRAK-1 dissociation and signaling [178]. In fact, most IRAK-4 residues reported to interact with MyD88 by Lin and co-workers [178] are not conserved in IRAK-M, except perhaps for a limited similarity at the type II interface (see Figure 5.3), which would indirectly support this theory. On the other hand, our results unambiguously establish that IRAK-M is able to interact directly with MyD88, in line with

12	R	C	L	N	V	G	L	I	R	K	L	S	D	F	I	D	P	Q	E	G	W	K	K	L	A	V	A	I	K	K	P	S	G	D	45	IRAK-4		
					+																																	
21	P	P	A	L	L	G	E	L	C	A	V	L	D	S	C	D	G	A	L	G	W	R	G	L	A	E	R	L	S	S	W	L	D	54	IRAK-M			
46	D	R	Y	N	Q	F	H	I	R	F	E	A	L	L	Q	T	G	K	S	P	T	S	E	L	L	F	D	W	G	T	T	N	78	IRAK-4				
										+																												
55	-	-	-	-	-	-	-	V	R	H	I	E	K	Y	V	D	Q	G	K	S	G	T	R	E	L	L	W	S	W	A	Q	K	N	80	IRAK-M			

Figure 5.3 Partial sequence comparison between human IRAK-4 and IRAK-M. Notice that most IRAK-4 residues reported by Wu and co-workers to be involved in type I (in yellow), type II (in purple) and type III (in green) interactions with MyD88 [178] are not conserved in IRAK-M. This observation suggests that IRAK-M does not compete with IRAK-4 for MyD88 binding (see text). Conserved residues are written between both sequences. Similar residues are marked with +.

previous work showing specific MyD88–IRAK-M interactions [137]. Future studies are needed to clarify if IRAK-M down-regulates TLR signaling by competing with kinases IRAK-1 and IRAK-4 for MyD88 binding, or if all three kinases can be simultaneously attached to the adaptor.

Focusing more specifically on the analysis of MyD88–IRAK-4 interactions, we first demonstrated that the full DD-TIR linker of MyD88 is dispensable for IRAK-4 binding, as MyD88(S) forms a stable complex with IRAK-4(L) (Figure 4.11a), and pulls down the natural kinase from monocyte extracts (Figure 4.12). Previous results had indicated that residues 110 to 154 of MyD88 are strictly required for interactions between IRAK-4 and the adaptor. Indeed, the truncated variant MyD88, MyD88s, lacking residues Glu¹¹⁰-Leu¹⁵⁴, is unable to recruit the kinase to the IL-1R complex (see refs. [79, 169] and Figure 4.1). The missing stretch in MyD88s comprises the C-terminal extra α -helix of the adaptor death domain and almost the complete DD-TIR linker. One possible explanation for the inactivity of this linker-less variant is that juxtaposition of DD and TIR domains compromises IRAK-4 recruitment because the TIR domain covers an important binding site on the death domain of the adaptor, thus interfering with DD-mediated heterodimer formation. We note, however, that lack of the interdomain linker does not impair heterodimerization of MyD88 and MyD88s [169]. Further, our modeling experiments suggest that the two globular domains would remain fairly independent in MyD88s, and the TIR domain would not approach the putative IRAK-4-binding site on the adaptor moiety (see below). In light of current structural and functional evidence for the *Drosophila* Tube•Pelle complex [174], our observation of similar binding to IRAK-4 by both MyD88(S) and MyD88(L) strongly suggests an alternative explanation, namely, that the C-terminal helix of MyD88 death domain and surrounding residues (Glu¹¹⁰ to Gln¹²⁰) play a major role in IRAK-4 recruitment. In support of our hypothesis, the mutated variant Y116C in murine MyD88 results in reduced immune responses to several pathogen-associated ligands [266]. It is important to stress that the residue topologically equivalent to Tyr¹¹⁶ in Pelle, Tyr¹²⁸, engages in van-der-Waals interactions with the Tube tail [174]. Finally, we note that the aromatic Tyr¹¹⁶ and surrounding residues are conserved in MyD88 from different species (see Appendix II), also supporting a functional role of helix α 7.

Although the affinity of IRAK-4 death domain for MyD88 could not be assessed by SPR due to non-specific binding of IRAK-4(L) to the surface of the sensor chip (Figure 4.13), incubation of purified MyD88(L) or MyD88(S) with increasing amounts of human monocyte extracts demonstrated quantitative, saturable binding of natural IRAK-4 by the recombinant death-domain of the adaptor (Figure 4.12). As mentioned before, the fact that both recombinant forms of MyD88 interact with native IRAK-4 corroborates that the DD-TIR linker of the adaptor (residues 121-158) is not required for kinase binding. Incomplete pull-down of the downstream kinase by MyD88(S) probably results from the higher tendency to self-aggregation of this recombinant variant (see Figure 4.5), and/or from partial unfolding of helix α 7 in the absence of most of the DD-TIR linker.

On the other hand, the DD-only variant of the adaptor, MyD88(S), bound only weakly to IRAK-4(S), as compared to IRAK-4(L) (Figure 4.11), indicating that the DD-kinase connector of IRAK-4 is important for heterodimer formation. Tube residues of the linker that engage in important interactions with Pelle are located just 10 to 20 positions downstream of the globular death domain (see [174]; this stretch is boxed in Figure 4.3c). In a similar manner, residues of the PEA-15 tail involved in ERK binding are clustered about 30 to 40 positions from the end of the globular DED moiety [96]. Therefore, we speculated that IRAK-4 residues proximal to the helical death domain might also be critical for complex formation, while the more C-terminal region could be less relevant in this regard. Indeed, Glu-C digestions of the MyD88(S)•IRAK-4(L) complex showed that presence of the adaptor completely abolishes proteolysis of the Glu¹¹⁶-Ala¹¹⁷ peptide bond, while the more C-terminal Glu¹⁴³-Leu¹⁴⁴ site is hydrolyzed as in free IRAK-4(L), albeit with slower kinetics (compare Figures 4.3c and 4.14). On the other hand, chymotrypsinolysis of free and adaptor-bound IRAK-4(L) proceeded following essentially identical kinetics (see Figure 4.15), indicating that the Phe¹²⁷-Glu¹²⁸ site is not protected in the MyD88•IRAK-4 complex. Further, and since the truncated variant IRAK-4 K115X was able to form a stable complex with both MyD88(S) and MyD88(L) (see Figure 4.16 and Appendix XI), we conclude that residues up to Lys¹¹⁵ in the DD-kinase linker of IRAK-4, and not beyond, are critical for recruitment by MyD88.

With the aim of gaining more insight on the structure of MyD88 and IRAK death domains, as well as on their interactions, we performed crystallization trials of several of the expressed recombinant fragments. However, although protein crystals of MyD88(L) and MyD88 E143X have been obtained (Tables 4.5 and 4.6, Figure 4.19, and Appendix XI), only crystals of the truncated form showed diffraction patterns ordered enough for data collection, most probably because residues beyond Glu¹⁴³ in the DD-TIR linker of the adaptor are flexibly disordered and therefore interfere with regular lattice formation. Analysis of the obtained data suggested the presence of three protein molecules in the asymmetric unit of MyD88 E143X crystals, in line with our previous observations on MyD88 having a strong tendency for self-aggregation. However, we have not been yet able to solve these structures by molecular replacement, probably because of unfolding of the DD upon prolonged incubation at room temperature, as previously reported for the protein kinase Pelle [248]. Awaiting new, clarifying crystallographic results, we propose a docking model of the MyD88-IRAK-4 heterodimer, discussed below.

5.3 A Proposed Mechanism for MyD88•IRAK-4 Complex Assembly

Although our biochemical and biophysical observations on MyD88 interactions with IRAK proteins have not been yet supported by clear crystallographic results, we wondered whether available structural and functional information could be used to generate a docking model of the

MyD88•IRAK-4 heterodimer (see section 3.12 in Materials and Methods). The results discussed above strongly suggested a topological equivalence of MyD88-Pelle and IRAK-4-Tube pairs [174], and would in particular imply that IRAK-4 tail residues are “clamped” between helix $\alpha 7$ and the main globular death domain of the adaptor in a similar manner as Tube binding to Pelle [174] (see Appendix II and compare Figures 1.9 and 5.2a). Nevertheless, it must be stressed that several residues involved in important intermolecular contacts in the Tube•Pelle heterodimer are not conserved in IRAK-4•MyD88 (see Appendix II). For instance, Glu⁵⁰ (Tube) and Arg³⁵ (Pelle) form a salt bridge in the *Drosophila* complex, but are replaced by proline and alanine/valine in IRAK-4 and MyD88, respectively. Further, only two of the six basic residues that surround the tail-binding cleft in Pelle are conserved in MyD88. Finally, the tail sequences of Tube and IRAK-4 appear to be only marginally related (see Figure 4.3c). These differences, altogether, preclude a straightforward adoption of the Tube•Pelle structure as template for modeling the mammalian MyD88•IRAK-4 complex.

The Tube-Pelle interface belongs to type II of the three topologically distinct DD-DD interfaces [267]. The recently solved crystal structure of the heterocomplex between death domains of RAIDD and PIDD [264] demonstrated that these interfaces represent most, if not all, possible interaction modes within the death domain superfamily. Importantly, the structural analysis revealed different subtypes within each of these interaction forms. It is also noteworthy that the Pelle-Tube interface shows considerable plasticity, as revealed by significant differences between the two independent complex molecules found in the asymmetric unit [174]. Closer examination of the RAIDD-PIDD type II interface reveals that a basic arginine side chain at the C-terminal end of RAIDD helix $\alpha 4$ forms a strong salt bridge with an aspartate of the $\alpha 5$ - $\alpha 6$ linker in PIDD. Interestingly, these residues possess counterparts in MyD88 (Arg⁸¹) / IRAK-4 (Glu⁹²). However, residues that follow the latter glutamate are not polar/charged as in PIDD but aromatic/aliphatic (Phe-Phe-Ala in the human kinase). They closely resemble the topologically equivalent Tube triplet, Leu¹⁴¹-Phe¹⁴²-Ser¹⁴³, of which Phe¹⁴² and Ser¹⁴³ are critical for Pelle binding [174]. Thus, it is conceivable that the MyD88•IRAK-4 heterodimer combines elements from both RAIDD-PIDD and Pelle-Tube type II interfaces. Along these lines, we notice that the nature of type I contacts differs between the procaspase-9 CARD•Apaf-1 CARD complex, which is mediated by complementary electrostatic fields [268], and the network of hydrophobic and hydrogen bond interactions that stabilize the topologically equivalent RAIDD DD•PIDD DD interface [264].

Unbiased predictions of surface areas of MyD88 and IRAK-4 death domains that are important for protein-protein interactions also support our model. For MyD88, the PPI-Pred server identified the cluster of polar aromatic residues donated by helices $\alpha 2$, $\alpha 3$, and their connecting loop, as the most likely protein-protein binding site (see Appendix III). This region includes residue Phe⁵⁶, which has been shown to be implied in DD-mediated adaptor dimerization

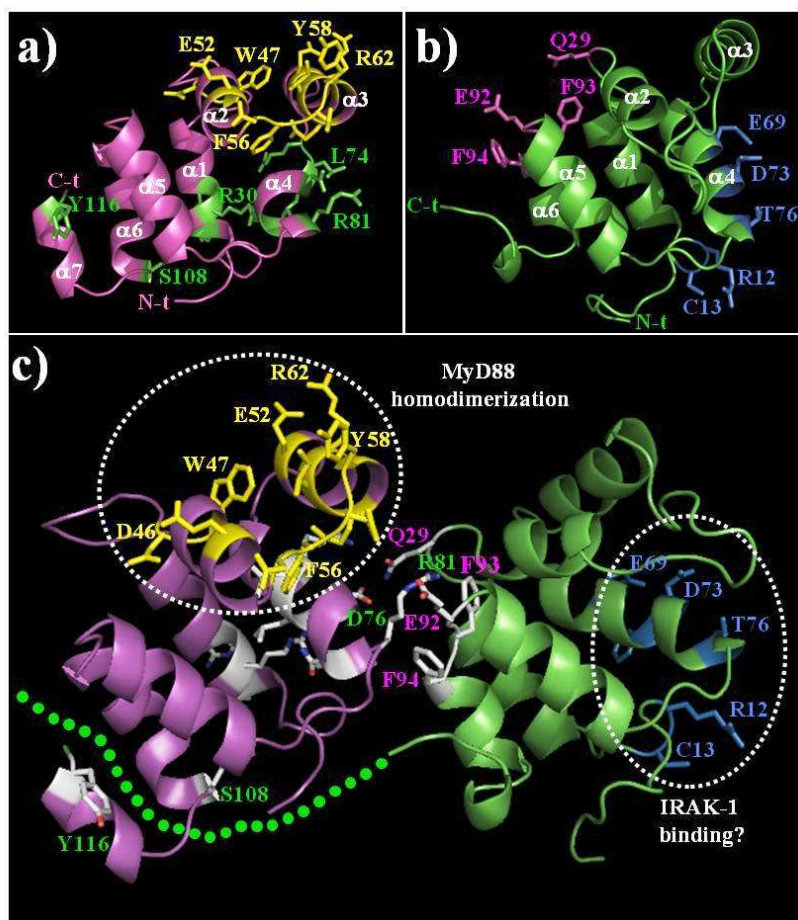


Figure 5.4 Hypothetical model of death domain-mediated heterocomplex formation between MyD88 and IRAK-4. **a** and **b**) Three-dimensional models of death domains from human MyD88 and IRAK-4. Major α -helices and the N- and C-termini of both modules are marked. The highest scoring patch in MyD88 appears to correspond to the MyD88–MyD88 interaction area, as replacement of Phe⁵⁶ by an asparagine is known to impair DD-mediated adaptor dimerization [73]. On the other hand, replacement of Tyr¹¹⁶ by a cysteine compromises immune responses against several pathogen-related molecules [266]; its close distance to the last residue included in the second highest patch (Ser¹⁰⁸) and the fact that the residue topologically equivalent in Pelle, Tyr¹²⁸, engages in van-der-Waals interactions with the Tube tail in the Tube•Pelle complex [174], suggests that it belongs to the IRAK-4 binding surface. **c**) Putative MyD88•IRAK-4 heterodimer, modeled on the basis of the type II interface observed in the RAIDD•PIDD structure [264]. The structures of Pelle DD free in solution [269] and bound to the adaptor, Tube [174], are essentially identical; similar observations have been made by comparing the structures of free [112] and PIDD-bound [264] RAIDD death domains. Therefore, death domain-mediated heterodimerization would appear to occur without major structural rearrangements, as an assemblage of rather rigid modules. In all panels, selected residues within the two highest scoring patches identified by PPI-Pred are indicated with their side chain atoms, colored and labeled yellow and green (MyD88) or blue and pink (IRAK-4), respectively.

[73] (these residues are clustered on "top" of the molecule in Figure 5.4a). In line with our hypothesis, Arg⁸¹ ranked on top of the second highest scoring patch, which also included nearby polar / aliphatic residues from helix α 4, but also a number of basic side chains from the neighboring helix α 1 (Arg²⁸, Arg³⁰, Arg³¹), as well as the more distant Ser¹⁰⁸. Importantly, the

close distance of Tyr¹¹⁶ to this serine residue, and the fact that the residue topologically equivalent in Pelle (Tyr¹²⁸) engages in van-der-Waals interactions with the Tube tail in the Tube•Pelle complex [174], suggests that it belongs to the IRAK-4 binding surface.

For IRAK-4 DD, the expected MyD88-interactive region was also identified as the second highest scoring area (see Appendix IV). This region includes Glu⁹² and neighboring exposed aromatic side chains (Phe⁹³, Phe⁹⁴), and several charged or aromatic exposed residues from helix α 1 (e.g., Lys²¹, Asp²⁴, Phe²⁵; see Figure 5.4b). Interestingly, the most likely protein-protein interaction site for this domain (to the right in Figure 5.4b) involves a distinct cluster of N-terminal (e.g., Arg¹², Cys¹³) and nearby residues from helix α 1 (e.g., Val¹⁶, Leu¹⁸) but in particular from α 4 (e.g., Glu⁶⁹, Phe⁷², Asp⁷³, and Thr⁷⁶). This patch is thus topologically equivalent to the IRAK-4 binding site on MyD88.

To verify that the MyD88-IRAK-4 interactive mode is compatible with a type II interface, we superimposed our models of MyD88 and IRAK-4 death domains on those of the corresponding RAIDD•PIDD heterodimer. Inspection of the generated structure after rigid-body refinement revealed that the predicted interactions can be simultaneously satisfied in the putative MyD88 DD•IRAK-4 DD complex (Figure 5.4c). In support of our model, we notice that adaptor dimerization would not interfere with IRAK-4 recruitment, in line with experimental observations. Given that the structures of Pelle DD free in solution [269] and bound to the adaptor, Tube [174], are essentially identical, and that similar observations have been made by comparing the structures of free [112] and PIDD-bound [264] RAIDD death domains, death domain-mediated heterodimerization appears to occur without major structural rearrangements, as an assemblage of rather rigid modules.

There is ample experimental supporting a scaffolding role for death domains of IRAK proteins, while the actual catalytic function is performed by the C-terminal kinase domain. Indeed, truncated IRAK-1 and 4 variants that consist of the death domain, eventually extended by the linker to the kinase domain have a potent negative-dominant effect in overexpression experiments [74, 138]. On the other hand, deletion of IRAK-1 DD abolishes all downstream signaling activities [270]. In this regard, the TLR-MyD88-IRAK system represents a counterpart to the Fas-FADD-procaspase-8/10 extrinsic apoptotic pathway, where the bipartite adaptor, FADD, regulates formation of the multimeric death-inducing signaling complex (DISC) by binding Fas via death domain-mediated interactions. Two markedly different crystal structures of the complex between DDs from Fas and FADD have been recently presented. In one of the structures, Scott and co-workers show a Fas•FADD DD complex with a tetrameric arrangement of four FADD DDs bound to four Fas DDs, in which Fas provides all contacts [271] (see Figure 5.5a). In striking contrast, Wang and co-workers reported later a Fas•FADD death domain complex composed of two layers, with five Fas DD molecules in the “upper” layer and five FADD DD molecules in the

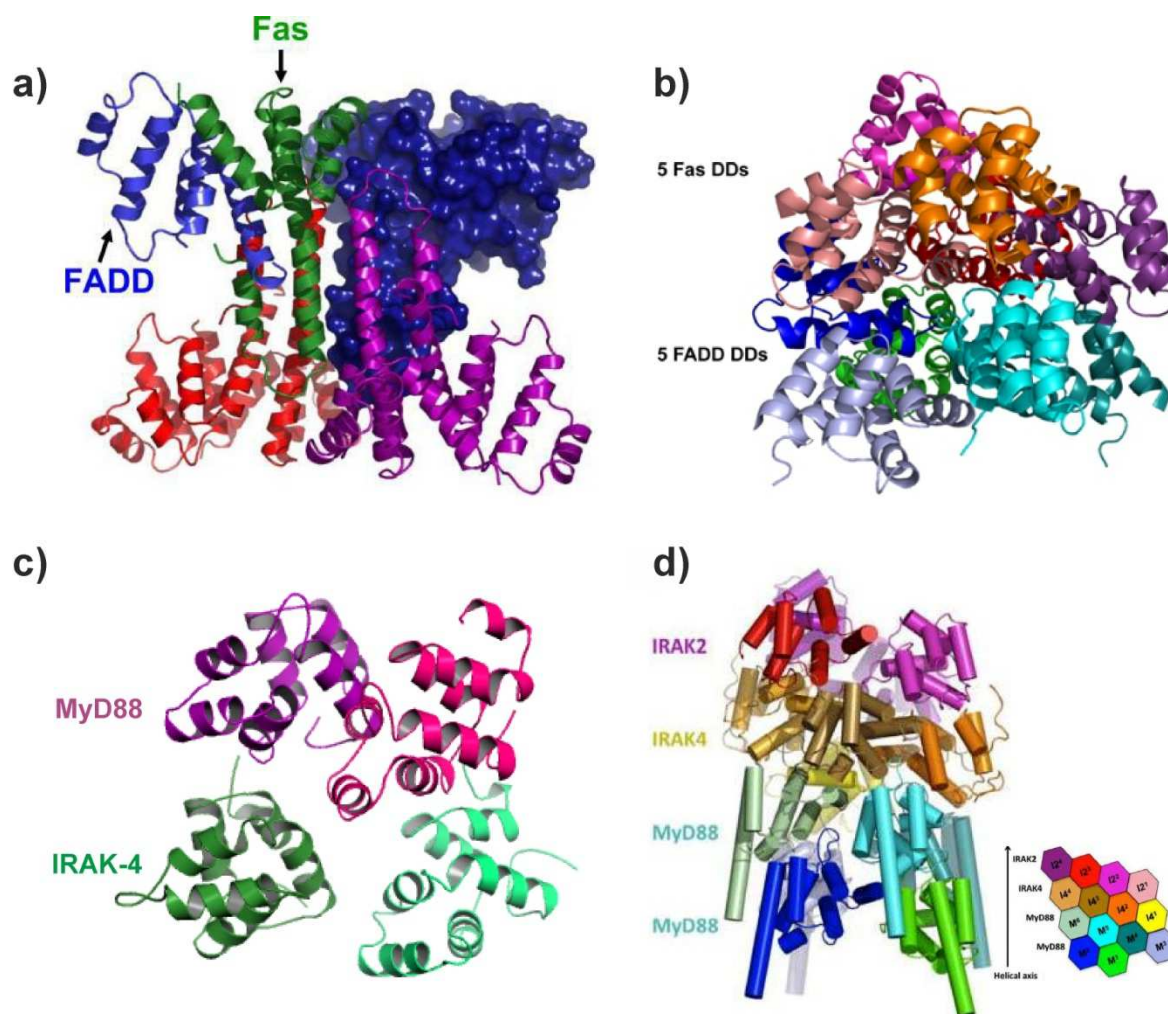
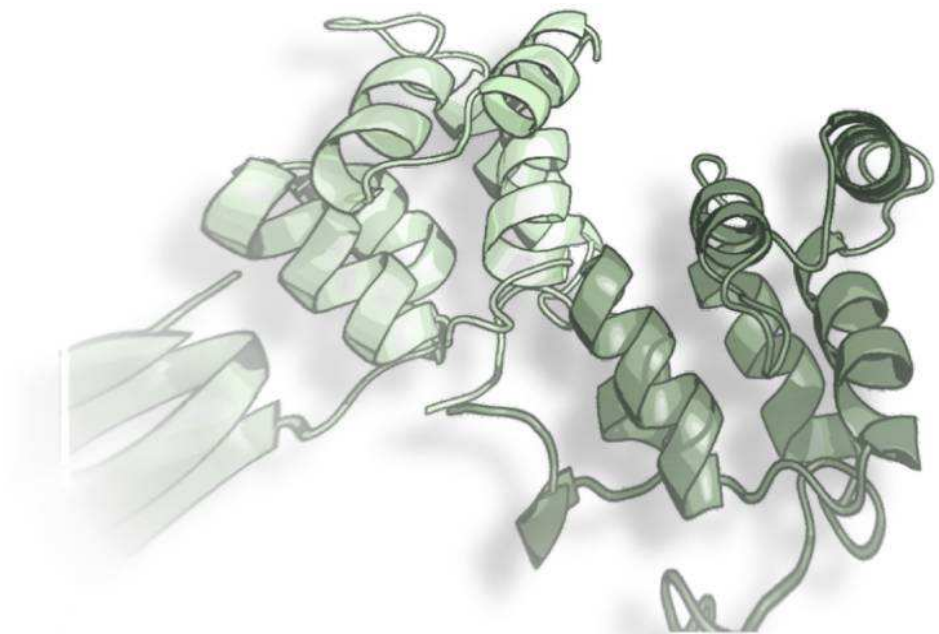


Figure 5.5 Different arrangements of death domain heterodimers. **a)** Tetrameric arrangement of the Fas/FADD DD complexes reported by Scott and co-workers [271]. Contacts between the complexes are solely mediated by Fas molecules. One Fas•FADD DD complex is displayed in green (Fas) and blue (FADD) ribbons, while the remaining three complexes are colored red, magenta and blue (the latter, in surface representation). **b)** Alternative Fas•FADD DD complex composed of two layers, with five Fas DD molecules in the “upper” layer and five FADD DD molecules in the “lower” one, reported by Wang and co-workers [247]. The Fas molecules are shown in warm, and the FADD DD molecules in cold colors. **c)** Model of the MyD88•IRAK-4 DD complex proposed in this work, in which only two MyD88•IRAK-4 heterodimers are sufficient to allow cross-phosphorylation and activation of the kinase moieties of adaptor-bound IRAK-4. MyD88 and IRAK-4 molecules are shown in purple and green, respectively. Notice the topological equivalence with the arrangement of Fas and FADD DD modules shown in **(a)**, as opposed to the Fas•FADD and MyD88•IRAK-4•IRAK-2 DD complexes shown in **(b)** and **(d)**, respectively. **d)** Ribbon diagram of the MyD88•IRAK-4•IRAK-2 DD complex reported by Lin and co-workers [178], composed of 6 MyD88 molecules (in cold colors), 4 IRAK-4 molecules (in earth-tone colors) and 4 IRAK-2 molecules (in warm colors), in a tower-shaped arrangement. The planar arrangement of the complex is also shown.

“lower” one [247] (see Figure 5.5b), similar to the layered structure of the oligomeric PIDD DD•RAIDD DD complex [264]. Similar to this second Fas•FADD DD complex, the recent structure of the MyD88•IRAK-4•IRAK-2 DD complex presented by Lin and co-workers reveals a tower-shaped structure composed of four layers [178] (see Figure 5.5d). In this arrangement, 6 MyD88 DD molecules form the two bottom layers, 4 IRAK-4 DD molecules comprise the middle layer, and 4 IRAK-2 DD molecules form the top layer. However, the existence of two very different experimental structures of Fas•FADD DD complexes suggests that the molecule arrangement of MyD88 and IRAK-4 DD molecules proposed by Lin and co-workers is only one possible solution, and not necessarily the most relevant from a physiological point of view, in particular in cases of low cytosolic concentrations of MyD88 and/or IRAK kinases. In fact, our proposed arrangement of MyD88 and IRAK-4 DD modules is more similar to the crystal structure of the Fas•FADD DD complex proposed by Scott and co-workers, since only two MyD88•IRAK-4 heterodimers are sufficient to allow cross-phosphorylation and activation of the kinase moieties of adaptor-bound IRAK-4 (see Figure 5.5c). This structure entails a much more simple arrangement of molecules, probably more suitable in the context of natural membrane association. Structural and functional investigations now in progress should refine this model and identify residues of both moieties involved in heterodimer formation, as well as in recruitment of the downstream kinase IRAK-1.

6. Conclusions



6.1 Conclusions

- 1) The death domains (DDs) of the human adaptor, MyD88, and of the (pseudo)kinases IRAK-1, IRAK-4 and IRAK-M can be expressed as heterologous proteins in *Escherichia coli*.
 - Both DD-only variants and forms C-terminally extended by different lengths of the linkers to the TIR or (pseudo)kinase modules, respectively, were overexpressed at high yields and purified to homogeneity.
- 2) Renaturation of urea-denatured inclusion bodies allows large quantities of recombinant DD variants of MyD88 and IRAK proteins to fold into their native-like conformations.
 - Only Glu-Xxx scissile peptide bonds within the irregular C-terminal tails of the linker-containing variants of MyD88 and IRAK proteins, but not those within their globular death domains, are susceptible to Glu-C cleavage.
 - Both the DD-only variant of the adaptor, MyD88(S), renatured from urea-solubilized inclusion bodies, and the linker-extended form MyD88(L) pull down natural, full-length IRAK-4 from human monocyte extracts.
- 3) The isolated death domains of MyD88 and IRAK proteins tend to form large aggregates in solution.
 - MyD88(S) has a stronger tendency for self-aggregation than the linker-containing variant of the adaptor, suggesting that the DD-TIR linker is important for adaptor solubility in the cell cytoplasm.
 - The linker-extended recombinant variants IRAK-1(L) and IRAK-M(L) have a stronger tendency for self-aggregation than the DD-only variants of the proteins, suggesting that the unstructured DD-(pseudo)kinase linkers are prone to aggregate formation *per se*.
 - The combined use of specific non-ionic detergents and low protein concentrations decreases formation of large aggregates between these DDs.
- 4) Co-renaturation of MyD88 and IRAK recombinant death domains results in correct protein folding, and could be established as a novel method for complex formation.

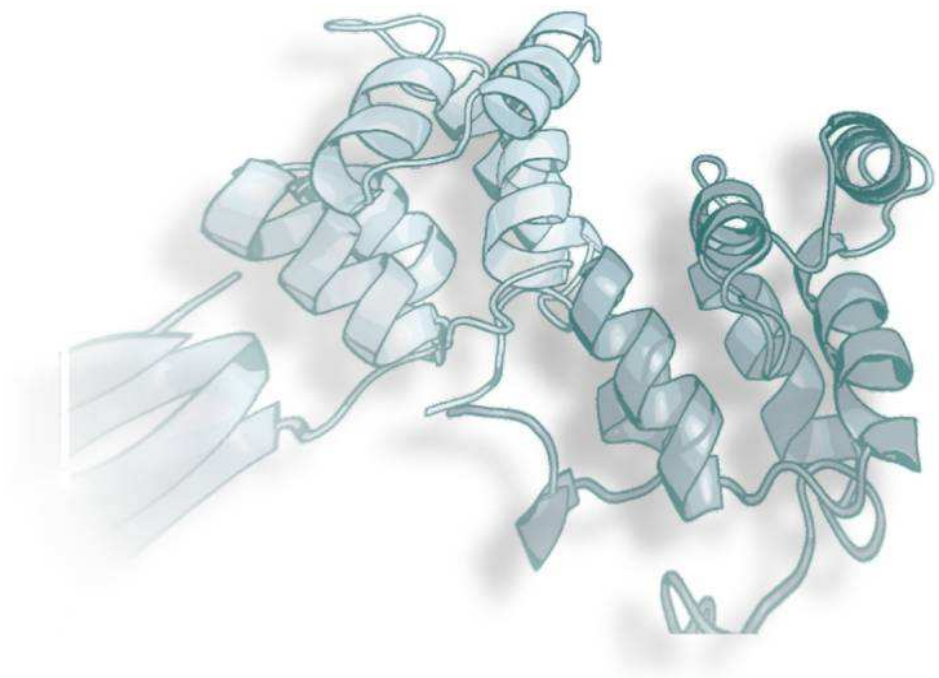
- 5) The isolated death domains of MyD88 and IRAK-4 strongly interact with each other.
- Both forms of recombinant MyD88 bind to the linker-extended variant of IRAK-4 death domain.
 - Residues Glu¹¹⁰-Gln¹²⁰, which include the C-terminal helix α 7 of MyD88, but not the irregular DD-TIR linker, are required for IRAK-4 recruitment, which explains the inability of naturally-occurring truncated variant MyD88s (lacking residues Glu¹¹⁰-Leu¹⁵⁴) to recruit the kinase to the IL-1R complex.
 - Residues up to Lys¹¹⁵ in the DD-kinase linker of IRAK-4, and not beyond, are needed for strong interactions with the adaptor, and therefore IRAK-4(S) (residues Thr⁶-Lys¹⁰⁷) does not form a stable complex with the adaptor.
- 6) Our experimental results and the topological equivalence of MyD88-Pelle and IRAK-4-Tube pairs suggest a possible MyD88•IRAK-4 complex in which the kinase tail residues are “clamped” between helix α 7 and the main globular death domain of the adaptor in a similar manner as Tube binding to Pelle.
- The MyD88•IRAK-4 heterodimer appears to combine elements from both RAIDD-PIDD and Pelle-Tube type II interfaces.
 - We propose an arrangement of MyD88 and IRAK-4 DD modules in which only two MyD88•IRAK-4 heterodimers are sufficient to allow cross-phosphorylation and activation of the kinase moieties of adaptor-bound IRAK-4.
- 7) IRAK-M is able to associate with MyD88 through interactions between their death domains.
- Residues beyond Glu¹⁴³ in the MyD88 DD-TIR linker, at least, are dispensable for IRAK-M recruitment by the adaptor.
 - The inhibitory role of IRAK-M on innate immune responses does not seem to result from competition with IRAK-4 for complex formation with MyD88, as IRAK-4 residues in contact with MyD88 are not conserved in IRAK-M.
 - Rather, IRAK-M might exert its inhibitory role by stabilizing the MyD88-IRAK-1 complex.

6.2 Conclusiones

- 1) Los dominios DD de la proteína adaptadora humana, MyD88, y de las (pseudo)quinasas IRAK-1, IRAK-4 e IRAK-M se pueden expresar como proteínas heterólogas en *Escherichia coli*.
 - Tanto las variantes compuestas únicamente por el dominio DD, como las formas extendidas en el extremo C-terminal por diferentes fragmentos del conector DD-TIR o DD-(pseudo)quinasa, respectivamente, se sobreexpresaron en grandes cantidades y se purificaron a homogeneidad.
- 2) La renaturalización de los cuerpos de inclusión desnaturalizados con urea permite el plegamiento de grandes cantidades de las variantes recombinantes de MyD88 e IRAK DDs, en sus conformaciones nativas.
 - Sólo los enlaces peptídicos Glu-Xxx que se encuentran en los conectores irregulares C-terminales de las variantes extendidas de MyD88 e IRAK, pero no aquellos que se encuentran en sus dominios globulares, son susceptibles de ser hidrolizados por la proteinasa Glu-C.
 - Tanto la variante compuesta únicamente por el DD del adaptador, MyD88(S), renaturalizada a partir de cuerpos de inclusión solubilizados en urea, como la forma extendida por el conector, MyD88(L), reclutan la quinasa IRAK-4 natural de extractos de monocitos humanos.
- 3) Los dominios globulares aislados de MyD88 y de las proteínas IRAK tienden a formar grandes agregados en disolución.
 - MyD88(S) tiene una mayor tendencia a la auto-agregación que la variante del adaptador extendida por el conector, lo que sugiere que el conector DD-TIR es importante para la solubilidad de MyD88 en el citoplasma celular.
 - Las variantes recombinantes IRAK-1(L) e IRAK-M (L), extendidas por el conector, tienen mayor tendencia a la auto-agregación que las variantes de estas proteínas que contienen únicamente el dominio DD, lo que sugiere que los conectores carentes de estructura secundaria DD-(pseudo)quinasa son propensos a la formación de agregados *per se*.
 - El uso combinado de detergentes no iónicos específicos y de bajas concentraciones de proteína, disminuye la formación de grandes agregados entre estos dominios DD.

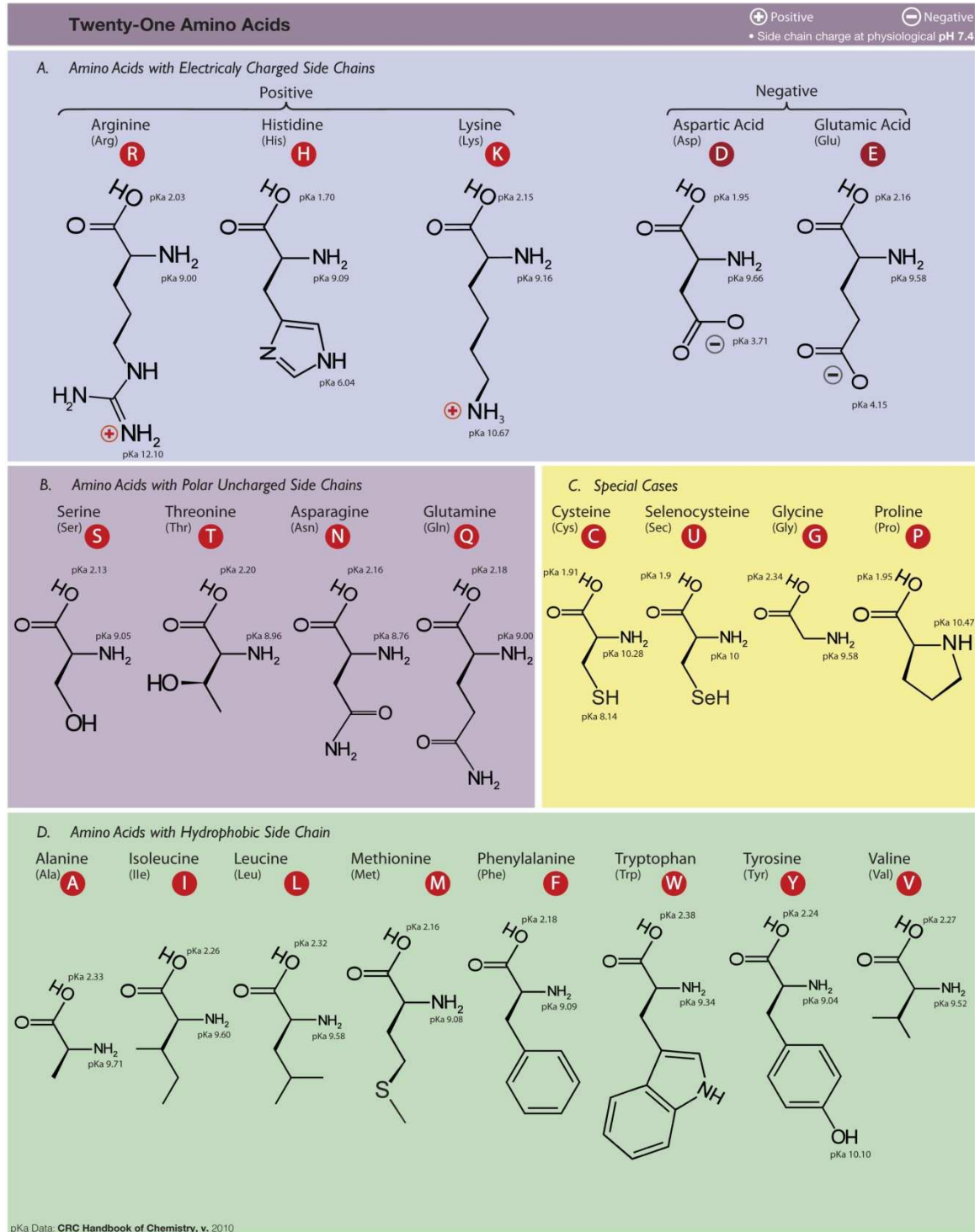
- 4) La co-renaturalización de los dominios DD recombinantes de MyD88 y las proteínas IRAK permite el plegamiento apropiado de las proteínas, y se ha podido establecer como un nuevo método para la formación de complejos.
- 5) Los dominios DD aislados de MyD88 e IRAK-4 interaccionan fuertemente entre sí.
- Las dos formas recombinantes de MyD88 se unen a la variante del dominio DD de IRAK-4 extendida por el conector.
 - Los residuos Glu¹¹⁰-Gln¹²⁰, que incluyen la hélice C-terminal $\alpha 7$ de MyD88 pero no el conector irregular DD-TIR, son necesarios para el reclutamiento de IRAK-4, lo que explica la incapacidad de la variante natural truncada MyD88s (que carece de los residuos Glu¹¹⁰-Leu¹⁵⁴) para reclutar la quinasa al complejo IL-1R
 - Los residuos hasta Lys¹¹⁵ en el conector DD-quinasa de IRAK-4, y no más allá, son necesarios para establecer interacciones fuertes con el adaptador y, por tanto, IRAK-4(S) (residuos Thr⁶-Lys¹⁰⁷) no forma un complejo estable con el adaptador
- 6) Nuestros resultados experimentales y la equivalencia topológica de los pares MyD88-Pelle e IRAK-4-Tube sugieren un posible complejo MyD88•IRAK-4, en el cual los residuos de la cola de la quinasa se insertan entre la hélice $\alpha 7$ y el dominio principal DD del adaptador, de manera similar a la unión de Tube con Pelle.
- El heterodímero MyD88•IRAK-4 parece combinar elementos de las superficies de contacto de tipo II de RAIDD-PIDD y de Pelle-Tube.
 - Proponemos una disposición de los dominios DD de MyD88 e IRAK-4 en la cual sólo dos heteodímeros MyD88•IRAK-4 son suficientes para permitir la fosforilación cruzada y activación de los dominios quinasa de la IRAK-4 unida al adaptador.
- 7) IRAK-M es capaz de asociarse a MyD88 a través de interacciones entre sus dominios DD.
- Los residuos más allá de Glu¹⁴³ en el conector DD-TIR de MyD88, como mínimo, son dispensables para el reclutamiento de IRAK-M por el adaptador.
 - El papel inhibitorio de IRAK-M en las respuestas inmunes innatas no parece deberse a la competición con IRAK-4 por la formación del complejo con MyD88, ya que los residuos de IRAK-4 en contacto con MyD88 no están conservados en IRAK-M.
 - En cambio, IRAK-M podría ejercer su papel inhibitorio estabilizando el complejo MyD88-IRAK-1.

7. Appendices



Appendix I

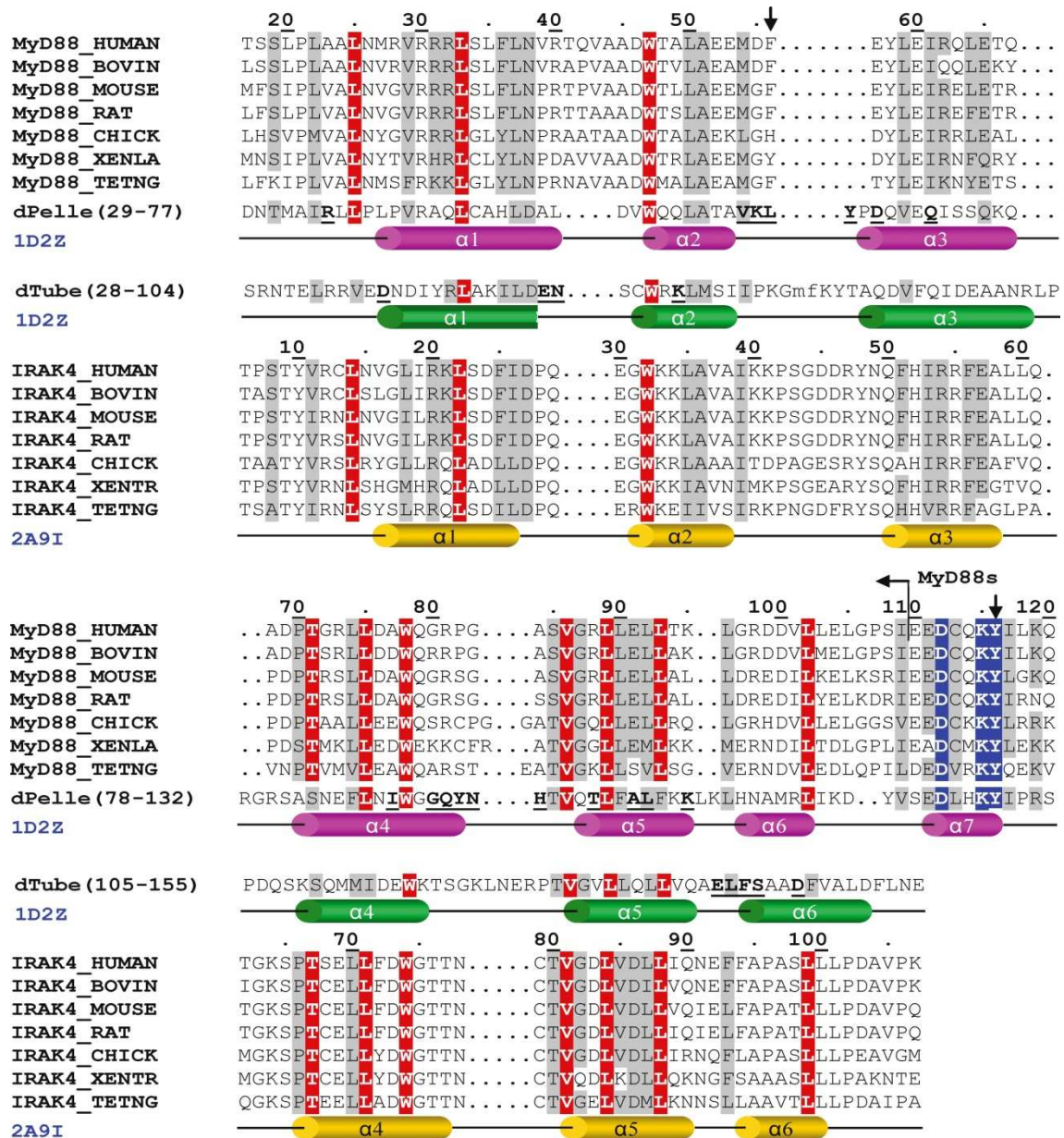
Structure and Classification of Amino Acids



Appendix II

Structure-Based Sequence Alignment of Death Domains from MyD88 and IRAK-4

Numberings on top of the alignments correspond to the human proteins. The inserted sequence in the $\alpha 2$ - $\alpha 3$ loop of Tube has been omitted for simplicity; the limits of this insertion are indicated by residues given in lower-case letters. The positions of major helices given below the sequences of Tube, Pelle and IRAK-4 follow DSSP analysis of reported structures (PDB codes 1D2Z and 2A9I, respectively). Residues conserved in all DDs from MyD88 and IRAK-4 are white with red shading; also marked in Tube and Pelle. Similar residues in helix $\alpha 7$ from Pelle and MyD88 are white with blue shading. Other conservative substitutions are shaded in grey. The C-terminal end of death domain in truncated variant MyD88s is indicated. Relevant mutants in MyD88 are marked with arrows: replacement of Phe⁵⁶ in the human cofactor to Asn (mutant MyD88-lpr) prevents adaptor dimerization, while mutation Tyr¹¹⁶→Cys in mouse MyD88 (mutant Lkd) results in reduced immune responses to various pathogen-associated ligands. Residues that engage in important intermolecular contacts in Tube and Pelle are bold and underlined. TETNG: *Tetraodon nigroviridis*. XENLA: *Xenopus laevis*. XENTR: *Xenopus tropicalis*.



Appendix III

Putative protein-protein interaction sites in MyD88 death domain

Interactions were predicted with PPI-Pred. Only the most probable binding site (left columns) and the second highest scoring patch (right columns) are given. The ten top-scoring residues in each region are shadowed.

Residue	Rank	Secondary structure	Predicted function	Residue	Rank	Secondary structure	Predicted function
Thr41	20	$\alpha 1-\alpha 2$	H O M O D I M E R I Z A T I O N	Leu20	13	N-term	I R A K 4 B I N D I N G
Ala45	19	$\alpha 1-\alpha 2$		Pro21	10	N-term	
Asp46	18	$\alpha 1-\alpha 2$		Ala23	8	N-term	
Thr48	12	$\alpha 2$		Ala24	12	N-term	
Trp47	9	$\alpha 2$		Leu25	17	N-term	
Ala49	15	$\alpha 2$		Asn26	19	N-term	
Ala51	8	$\alpha 2$		Met27	16	$\alpha 1$	
Glu52	7	$\alpha 2$		Arg28	18	$\alpha 1$	
Glu53	14	$\alpha 2$		Val29	20	$\alpha 1$	
Asp55	6	$\alpha 2-\alpha 3$		Arg30	11	$\alpha 1$	
Phe56	4	$\alpha 2-\alpha 3$		Arg31	15	$\alpha 1$	
Glu57	3	$\alpha 3$		Arg73	3	$\alpha 4$	
Tyr58	1	$\alpha 3$		Leu74	4	$\alpha 4$	
Glu60	11	$\alpha 3$		Leu75	5	$\alpha 4$	
Ile61	2	$\alpha 3$		Asp76	2	$\alpha 4$	
Arg62	5	$\alpha 3$		Gln79	9	$\alpha 4$	
Glu65	10	$\alpha 3$		Gly80	6	$\alpha 4$	
Asp69	16	$\alpha 3-\alpha 4$		Arg81	1	$\alpha 4$	
Trp78	13	$\alpha 4$		Gly83	7	$\alpha 4-\alpha 5$	
Leu96	17	$\alpha 5-\alpha 6$		Ser108	14	$\alpha 6-\alpha 7$	

Appendix IV

Putative protein-protein interaction sites in IRAK-4 death domain

Interactions were predicted with PPI-Pred. Only the most probable binding site (left columns) and the second highest scoring patch (right columns) are given. The ten top-scoring residues in each region are shadowed.

Residue	Rank	Secondary structure	Predicted function	Residue	Rank	Secondary structure	Predicted function	
Val11	10	N-term	I R A K 1	Lys21	2	$\alpha 1$	M y D 8 8	
Arg12	2	N-term		Asp24	5	$\alpha 1$		
Cys13	1	N-term		Phe25	6	$\alpha 1$		
Leu14	3	N-term		Pro28	11	$\alpha 1$ - $\alpha 2$		
Asn15	4	N-term		Gln29	15	$\alpha 1$ - $\alpha 2$		
Val16	6	$\alpha 1$		Gly31	16	$\alpha 2$		
Leu18	7	$\alpha 1$		Lys34	14	$\alpha 2$		
Ile19	11	$\alpha 1$		Asn91	10	$\alpha 5$ - $\alpha 6$		B I N D I N G
Arg20	12	$\alpha 1$		Glu92	9	$\alpha 5$ - $\alpha 6$		
Ser68	15	$\alpha 4$		Phe93	13	$\alpha 5$ - $\alpha 6$		
Glu69	16	$\alpha 4$	Phe94	8	$\alpha 6$			
Leu71	14	$\alpha 4$	Ala95	7	$\alpha 6$			
Phe72	9	$\alpha 4$	Pro96	12	$\alpha 6$			
Asp73	13	$\alpha 4$	Ser98	3	$\alpha 6$			
Thr76	5	$\alpha 4$	Leu99	1	$\alpha 6$			
Leu100	8	$\alpha 6$	Val105	4	DD-kinase			

Appendix V

pET-3a Restriction Map

pET-3a-d Vectors

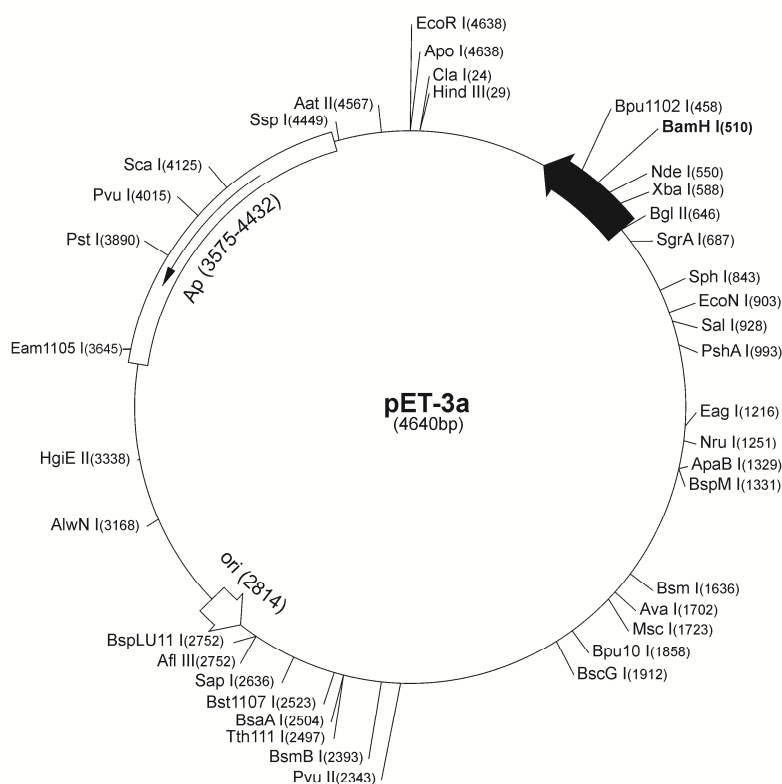
	Cat. No.
pET-3a DNA	69418-3
pET-3b DNA	69419-3
pET-3c DNA	69420-3
pET-3d DNA	69421-3

The pET-3a-d vectors carry an N-terminal T7•Tag® sequence and *Bam*H I cloning site. These vectors are the precursors to many pET family vectors; the pET-23a-d(+) series corresponds to pET-3a-d but incorporates several additional features. Unique sites are shown on the circle map. Note that the sequence is numbered by the pBR322 convention, so the T7 expression region is reversed on the circular map. The cloning/expression region of the coding strand transcribed by T7 RNA polymerase is shown below.

pET-3a sequence landmarks

T7 promoter	615-631
T7 transcription start	614
T7•Tag coding sequence	519-551
T7 terminator	404-450
pBR322 origin	2814
<i>bla</i> coding sequence	3575-4432

The maps for pET-3b, pET-3c and pET-3d are the same as pET-3a (shown) with the following exceptions: pET-3b is a 4639bp plasmid; subtract 1bp from each site beyond *Bam*H I at 510. pET-3c is a 4638bp plasmid; subtract 2bp from each site beyond *Bam*H I at 510. pET-3d is a 4637bp plasmid; the *Bam*H I site is in the same reading frame as in pET-3c. An *Nco* I site is substituted for the *Nde* I site with a net 1bp deletion at position 550 of pET-3c. As a result, *Nco* I cuts pET-3d at 546. For the rest of the sites, subtract 3bp from each site beyond position 551 in pET-3a. *Nde* I does not cut pET-3d.



Novagen (www.merck-chemicals.com)

Appendix VI

DNA Sequences of MyD88 and IRAK Recombinant Fragments

All inserts cloned at the *Nde* I and *Bam*H I sites of the T7 promoter region of the expression plasmid pET-3a

Synthetic gene	DNA sequence (5'-3')
MyD88(S)	catcaccaccatcaccacacctcttctgcccactggctgactgaaatgcgtgtacgtcgtcgtctgcctgttctgaacgtacgta cccagggtgctgcagactggactgactggctgaagagatggactcgaataacctgaaatccgtcagctcgaactcaggcagatc caactggctcgtcgtcgtatgcatggcagggtcgtccagggtcatctgttggctcgtcgtcgaactgctcaccaaactgggtcgtgac gatgtgctcctggaaactgggtccgtctatcgag
MyD88(L)	catcaccaccatcaccacacctcttctgcccactggctgactgaaatgcgtgtacgtcgtcgtctgcctgttctgaacgtacgta cccagggtgctgcagactggactgactggctgaagagatggactcgaataacctgaaatccgtcagctcgaactcaggcagatc caactggctcgtcgtcgtatgcatggcagggtcgtccagggtcatctgttggctcgtcgtcgaactgctcaccaaactgggtcgtgac gatgtgctcctggaaactgggtccgtctatcgaggaagactgccagaatacctgaaacagcagcaggaagaagccgagaacc actgcaggttgacgtgtgacagctctgtaccaggtacggctgaactggctggtatcaccactctcgtgacctgggtcagatg catg
IRAK-1(S)	catatggggccccagcacttctgtacgaggtccaccgtgggtaatgtgccgtttctacaaagtattggacgcgctggaaccggctg actgggtgactgttgcagccctcatcgttcgcagaccgaactgcgtctgtcgaactgttctgtcagcgcactgcgtctgttctgt ggccgtggatcaaccgcaacgctcgtgttcagacctgggtcacatcctgacgcactctgcagctgctcgtcgtgatatcatcac cgcatggcatccgcccggcgttaaggatcc
IRAK-1(L)	catatgggtgctgcagcacttctctacgaagtaccaccgtgggttatgtgccgtttctacaaagtattggacgcctggaaccggctg ttggtgccagttcgcagcgtgatcgttcgcgaccagaccgaactgcgtctgtcgaactgttctgtcagcgtaccgctcgtcgtct ggccgtggatcaaccgcaacgctcgttcgccgatctgggtcacatcctgactcacctgcagctcgtcgtcgtgatcatcatcac cgcttggcatccgcccaccactgcccgtctccgggtactaccgctccagctccagcattccggctccgagaaagcggaaag cgtggtctccggtaaactgcccctctctgcgagcacttctctcggcattccaggctctcagaccattctgttccggaactgg gtctcgttccgctccggcctctctgtggccgccaccatctccagctccgtccagcaccaaaccaggcccggagagctctgtaag cctgctcaggggtgcagctccgttcccgttttctgcccactgtgcgagatctctcgtggcagcacaactaaggatcc
IRAK-4(S)	gactacaaagacgacgacgataaaggcactcctctactacgtacgttgccctgaactgtaggtctcatccgcaactgagcgacttca tcgaccacaggaaggttgaaaaactggcagttgccatcaaaaaaccgtctggtgatgacctgacaaccagttccacattcgtc tttgaagctctgctgcagactggcaaatctcagactctgagctcctgtttgactgggtaccacgaactgtaccgtagggtgatctggt gatctgctcatccagaacgagttcttctcagactctctcctgctccagatgcagttccgaaaactgcgaactctgccgttaaag aggcgattactgtcagcagaacagatgccgttttgcgaaaagaccgtaccctgatgactccagttcagaacctcgaacagagcta catgccaccggttctctcagagaacaaagcctggaagtatccgataaccgtttccactcttctcctcttacgagctgaaaaac gtcaccacaactcgtatgaactccgac
IRAK-4(L)	gactacaaagacgacgacgataaaggcactcctctactacgtacgttgccctgaactgtaggtctcatccgcaactgagcgacttca tcgaccacaggaaggttgaaaaactggcagttgccatcaaaaaaccgtctggtgatgacctgacaaccagttccacattcgtc tttgaagctctgctgcagactggcaaatctcagactctgagctcctgtttgactgggtaccacgaactgtaccgtagggtgatctggt gatctgctcatccagaacgagttcttctcagactctctcctgctccagatgcagttccgaaaactgcgaactctgccgttaaag aggcgattactgtcagcagaacagatgccgttttgcgaaaagaccgtaccctgatgactccagttcagaacctcgaacagagcta catgccaccggttctctcagagaacaaagcctggaagtatccgataaccgtttccactcttctcctcttacgagctgaaaaac gtcaccacaactcgtatgaactccgac
IRAK-M (S)	catatggaacagaaactgatcagcgaagaagatctgacgtcgtgttccgatctccaccagcgtcgtggcgaaactgtgcgctgttc tggacagctgtgatggtcactgggtggcgtggtcgtgacgtcgtcctctcttggctcagctgctcgtatcgagaatac tcgatcagggcaaatccggtactcgtgactcgtctgttggcgcagaaaaacaaaccattggcgacctctcaggtactgca ggaaatgggtcaccgtcgtgcaatccactgatcacaactatggtgccgttctgtaaggatcc
IRAK-M (L)	catatggaacagaactgatctccgaagagatctgacgtcgtctttgatctcccagctcgtcgtgggtgaaactgtgcgactg gactctgtgatggtcactcgttggcgtggtcgtgacgtcgtcctctcttggctcagctgctcgtatcctcagctcagctcagct gaccagggcaaaagcgtactcgtgaactcgtgtgttggcccagaaaaacaaaccattcgtgacctcctcaggttctcag gaaatgggtcactcgtcgtatccactgatcacaactacggtcgtgttctgtcctcagagaaatcctaccaggaaggtggttc ccgaacatcctctcaagaaaccgtaactgactgtgacaactcgtgtatccggaaacacaacgagaagggcgtactgctcaat cctctatcagctccagaacatcattgaaggatccgtaactaaggatcc

Appendix VII

Buffers and Solutions

All solutions prepared in distilled water, unless specified otherwise.

Abbreviations:

2-ME: 2-mercaptoethanol. **EDTA:** Ethylenediaminetetraacetic acid. **PMSF:** Phenyl-methyl sulphoxide. **SDS:** Sodium dodecyl sulfate. **TEMED:** Tetramethylethylenediamine. **Tris:** 2-Amino-2-(hydroxymethyl)propane-1,3-diol. **β -OG:** n-octyl- β -D-glucopyranoside

BACTERIAL CULTURE MEDIA

LB (Luria Bertani) medium

1% (w/v) Tryptone
0.5% (w/v) Yeast extract
1% (w/v) NaCl
pH 7.0

SOB (Super Optimal broth) medium

2% (w/v) Tryptone
0.5% (w/v) Yeast extract
10 mM NaCl
2.5 mM KCl
10 mM MgCl₂
10 mM MgSO₄
pH 7.0

SOC (Super Optimal broth with Catabolite repression) medium

20 mM Glucose in SOB medium

LB/Agar

1.5% (w/v) Agar in LB medium

CELL CULTURE MEDIA

PBS (Phosphate Buffered Saline)

137 mM NaCl
22.7 mM KCl
10 mM Na₂HPO₄
2 mM KH₂PO₄
pH 7.4

Cell Lysis Buffer

10 mM Imidazole
500 mM NaCl
0.5% (v/v) Triton X-100
0.2 mM Sodium orthovanadate
0.2 mM PMSF
2 mM Sodium azide
pH 7.3

PROTEIN EXTRACTION**B-PER solution**

10 mM MgCl₂
20 mM 2-ME
1 mM EDTA
200 mM NaCl
10 mM Imidazole
B-PER® reagent (Thermo Scientific) up to final volume

Extraction buffer

25 mM Sodium phosphate
200 mM NaCl
10 mM 2-ME
500 μM EDTA
0.5% (w/v) β-OG
pH 7.8

Ni-NTA PURIFICATION OF RECOMBINANT FRAGMENTS**Binding buffer**

25 mM Sodium phosphate
300 mM NaCl
5 mM 2-ME
0.5% β-OG
pH 7.8

Wash buffer

25 mM Sodium phosphate
300 mM NaCl
5 mM 2-ME
0.5% β-OG
10 mM Imidazole
pH 7.8

Elution Buffer

25 mM Sodium phosphate
300 mM NaCl
5 mM 2-ME
0.5% β-OG
500 mM Imidazole
pH 7.8

FPLC PURIFICATION OF RECOMBINANT FRAGMENTS**Gel filtration buffer**

20 mM Tris pH 7.4
100 mM NaCl
0.1% β-OG

GEL ELECTROPHORESIS UNDER DENATURING CONDITIONS**Sample buffer**

50 mM Tris-Cl
2% (w/v) SDS
10% (v/v) Glycerol
0.01 % (v/v) Bromophenol blue
pH 6.8

Reducing sample buffer

50 mM Tris-Cl
2% (w/v) SDS
10% (v/v) Glycerol
200 mM DTT
0.01 % (v/v) Bromophenol blue
pH 6.8

Tris-tricine gels:**Separating**

12% (v/v) Bis-acrylamide
1 M Tris
0.1% (w/v) SDS
10% (v/v) Glycerol
0.15% (w/v) Ammonium persulfate
0.047% (v/v) TEMED
pH 8.45

Stacking

4.5% (v/v) Bis-acrylamide
0.75 M Tris
0.07% SDS
0.06% (w/v) Ammonium persulfate
0.12% (v/v) TEMED
pH 8.45

Cathode buffer

0.1 M Tris
0.1 M Tricine
0.1% (w/v) SDS

Anode buffer

0.2 M Tris-Cl
pH 8.9

Tris-glycine gels:**Separating**

12 % (w/v) Bis-acrylamide
0.375 M Tris
0.2% (w/v) SDS
0.05% (w/v) Ammonium persulfate
0.05% (v/v) TEMED
pH 8.8

Stacking

9.36 % Bis-acrylamide
0.2 M Tris
0.16 % (w/v) SDS
0.04% (w/v) Ammonium persulfate
0.08% (v/v) TEMED
pH 7.0

Running buffer

25 mM Tris
192 mM Glycine
0.1% (w/v) SDS

GEL ELECTROPHORESIS UNDER NATIVE CONDITIONS**Native sample buffer**

50 mM Tris-Cl
10% (v/v) Glycerol
0.01% (v/v) Bromophenol blue
pH 6.8

Separating

11% Bis-acrylamide
0.5 M Tris
0.022% (w/v) Ammonium persulfate
0.055% TEMED
pH 8.8

Stacking

4.5% (v/v) Bis-acrylamide
375 mM Tris
0.06% (w/v) Ammonium persulfate
0.12% (v/v) TEMED
pH 8.8

Running buffer

25 mM Tris
192 mM Glycine
0.1% (w/v) SDS

PROTEIN GEL STAINING

Coomassie Blue Staining:

Coomassie stain solution

10% (v/v) Acetic acid
50% (v/v) Methanol
0.25% (w/v) Coomassie dye R-250

Destaining solution I

10% (v/v) Acetic acid
50% (v/v) Methanol

Destaining solution II

10% (v/v) Acetic acid
7% (v/v) Methanol

Silver staining:

Fixative solution

30% (v/v) Ethanol
10% (v/v) Acetic acid

Silver staining solution

0.2% (w/v) Silver nitrate
0.02% (v/v) Formaldehyde

Developer solution

6% (w/v) Sodium carbonate
0.05 % (v/v) Formaldehyde
0.0004% (w/v) Sodium thiosulfate

WESTERN BLOT

Transfer buffer

0.05 M Tris
0.4 M Glycine
0.5% SDS
20% Methanol

Blocking solution

5% (w/v) Non-fat dry milk in TBS

TBS (Tris-buffered saline)

10 mM Tris
100 mM NaCl
pH 7.0

SURFACE PLASMON RESONANCE

SPR running buffer

25 mM Sodium phosphate
200 mM NaCl
0.0005% (v/v) Surfactant P20
50 μ M EDTA
pH 7.8

ANALYTICAL ULTRACENTRIFUGATION

Buffer 1

25 mM Sodium phosphate
300 mM NaCl
0.5% β -OG
1 M Imidazole
pH 7.8

Buffer 2

25 mM Sodium phosphate
300 mM NaCl
5 mM 2-ME
0.5% β -OG
500 mM Imidazole
pH 7.8

Buffer 3

20 mM Tris
1 M NaCl
pH 8.0

Buffer 4

9.69 mM Sodium phosphate
12.248 mM Tris pH 8.0
728.68 mM NaCl
0.1938% β -OG
387.6 mM Imidazole
pH 7.8

Buffer 5

25 mM Sodium phosphate
264 mM NaCl
11 mM KCl
2.2 mM MgCl₂
2.2 mM CaCl₂
440 mM Sucrose
pH 7.0

Appendix VIII

FoldIt Screen

Abbreviations:

DTT: Dithiothreitol. **EDTA:** Ethylenediaminetetraacetic acid. **GSH:** Reduced glutathione. **GSSG:** Oxidized glutathione. **MES:** 2-(N-morpholino)ethanesulfonic acid. **PEG3350:** Polyethylene glycol (molecular weight: 3350 Da). **Tris:** 2-Amino-2-(hydroxymethyl)propane-1,3-diol.

FoldIt #	Formulations					
	Buffer	Salt	PEG3350 (% w/v)	Guanidine HCl	Cation/ Chelator	Polar & Nonpolar Additives
1	55mMTris pH8.2	264mMNaCl, 11mMKCl	0.055%	0 mM	1.1 mM EDTA	none
2	55mMMESpH6.5	1056mMNaCl, 044mMKCl	none	550 mM	22mMMgCl ₂ ,22mMCACl ₂	none
3	55mMMESpH6.5	1056mMNaCl, 044mMKCl	0.055%	550 mM	1.1 mM EDTA	440 mM Sucrose 550 mL-Arginine
4	55mMTris pH8.2	264mMNaCl, 11mMKCl	none	0 mM	22mMMgCl ₂ ,22mMCACl ₂	440 mM Sucrose 550 mL-Arginine
5	55mMMESpH6.5	264mMNaCl, 11mMKCl	none	0 mM	22mMMgCl ₂ ,22mMCACl ₂	440 mM Sucrose
6	55mMTris pH8.2	1056mMNaCl, 044mMKCl	0.055%	550 mM	1.1 mM EDTA	440 mM Sucrose
7	55mMTris pH8.2	1056mMNaCl, 044mMKCl	none	550 mM	22mMMgCl ₂ ,22mMCACl ₂	550 mL-Arginine
8	55mMMESpH6.5	264mMNaCl, 11mMKCl	0.055%	0 mM	1.1 mM EDTA	550 mL-Arginine
9	55mMMESpH6.5	264mMNaCl, 11mMKCl	0.055%	550 mM	22mMMgCl ₂ ,22mMCACl ₂	440 mM Sucrose
10	55mMTris pH8.2	1056mMNaCl, 044mMKCl	none	0 mM	1.1 mM EDTA	440 mM Sucrose
11	55mMTris pH8.2	1056mMNaCl, 044mMKCl	0.055%	0 mM	22mMMgCl ₂ ,22mMCACl ₂	550 mL-Arginine
12	55mMMESpH6.5	264mMNaCl, 11mMKCl	none	550 mM	1.1 mM EDTA	550 mL-Arginine
13	55mMTris pH8.2	264mMNaCl, 11mMKCl	none	550 mM	1.1 mM EDTA	none
14	55mMMESpH6.5	1056mMNaCl, 044mMKCl	0.055%	0 mM	22mMMgCl ₂ ,22mMCACl ₂	none
15	55mMMESpH6.5	1056mMNaCl, 044mMKCl	none	0 mM	1.1 mM EDTA	440 mM Sucrose 550 mL-Arginine
16	55mMTris pH8.2	264mMNaCl, 11mMKCl	0.055%	550 mM	22mMMgCl ₂ ,22mMCACl ₂	440 mM Sucrose 550 mL-Arginine

FoldIt Additions - Pipetting and Dilution Table for FoldIt

FoldIt #	FoldIt Volume	0.1 M DTT	30 mM Lauryl Maltoside	100 mM GSH	10 mM GSSG	Ligand	Protein
1	950 µL	10 µL	-	-	-	up to 10 mM	~50 µL
2	950 µL	-	10 µL	10 µL	10 µL	-	~50 µL
3	950 µL	-	-	10 µL	10 µL	up to 10 mM	~50 µL
4	950 µL	10 µL	10 µL	-	-	-	~50 µL
5	950 µL	-	-	10 µL	10 µL	up to 10 mM	~50 µL
6	950 µL	10 µL	10 µL	-	-	-	~50 µL
7	950 µL	10 µL	-	-	-	up to 10 mM	~50 µL
8	950 µL	-	10 µL	10 µL	10 µL	-	~50 µL
9	950 µL	10 µL	-	-	-	-	~50 µL
10	950 µL	-	10 µL	10 µL	10 µL	up to 10 mM	~50 µL
11	950 µL	-	-	10 µL	10 µL	-	~50 µL
12	950 µL	10 µL	10 µL	-	-	up to 10 mM	~50 µL
13	950 µL	-	-	10 µL	10 µL	-	~50 µL
14	950 µL	10 µL	10 µL	-	-	up to 10 mM	~50 µL
15	950 µL	110 µL	-	-	-	-	~50 µL
16	950 µL	-	10 µL	10 µL	10 µL	up to 10 mM	~50 µL

(modified from the work of N. Armstrong and co-workers [214])

Appendix IX

Detergent Screen 1 Formulation (Hampton Research)

Abbreviations:

CMC, Critical micelle concentration. MW, Molecular Weight in Da.

Reagent #	Detergent	Description	MW (Da)	CMC (mM)
1	C ₁₂ E ₉	nonaethylene glycol monododecyl ether	~583	0.05
2	C ₁₂ E ₈	octaethylene glycol monododecyl ether	538.8	0.11
3	n-Dodecyl-β-D-maltoside	dodecyl-β-D-maltopyranoside	510.6	0.17
4	Sucrose monolaurate	lauric acid sucrose ester	524.6	0.30
5	CYMAL-6	cyclohexyl-hexyl-β-D-maltoside	508.5	0.56
6	TRITON X-100	nonaethylene glycol octylphenol ether	650	0.90
7	CTAB	cethyltrimethylammonium bromide	364.46	1.00
8	Deoxy BigChap	<i>N,N</i> -bis-(3-D-glucoamidopropyl)-deoxycholamine	862.1	1.40
9	n-Decyl-β-D-maltoside	decyl-β-D-maltopyranoside	482.6	1.80
10	LDAO	lauryldimethylamine oxide	229.41	2.0
11	CYMAL-5	cyclohexyl-pentyl-β-D-maltoside	494.5	5.0
12	ZWITTERGENT® 3-12	3-(dodecyldimethylammonio)propane-1-sulfonate	335.6	4.0
13	Nonyl-β-D-glucoside	β-D-glucopyranoside	306.4	6.50
14	1-s-Octyl-β-D-thioglucoside	octyl-β-D-thioglucopyranoside / OSG	308.4	9.00
15	DDAO	<i>N,N</i> -dimethyldecylamine-β-oxide	201.35	10.40
16	HECAMEG	methyl-6- <i>O</i> -(<i>N</i> -heptylcarbamoyl)-α-D-glucopyranoside	335.4	19.50
17	n-Octanoylsucrose	n-octanoyl-β-D-fructofuranosyl-α-D-glucopyranoside	468.5	24.40
18	n-Heptyl-β-D-thioglucoside	n-heptyl-β-D-thioglucopyranoside	294.4	30
19	n-Octyl-β-D-glucoside	octyl-β-D-glucopyranoside / BOG	292.4	20
20	CYMAL-3	cyclohexyl-propyl-β-D-maltoside	466.5	34.5
21	CHEGA- 10	cyclohexylbutanoyl- <i>N</i> -hydroxyethylglucamide	377.5	35
22	ZWITTERGENT® 3-10	3-(decyldimethylammonio)propane-1-sulfonate	307.5	40
23	MEGA-8	(octanoyl- <i>N</i> -methylglucamide	321.4	79
24	n-Hexyl-β-D-glucoside	hexyl-β-D-glucopyranoside	264.3	250

Hampton Research Corp. (www.hamptonresearch.com)

Appendix X

Crystallization Conditions

Abbreviations:

Alcohols: 1,6-Hexanediol; 1-Butanol; 1,2-Propanediol (racemic); 2-Propanol; 1,4-Butanediol; 1,3-Propanediol. Ethylene glycols, Diethyleneglycol; Triethyleneglycol; Tetraethyleneglycol; Pentaethyleneglycol. Monosaccharides, D-Glucose; D-Mannose; D-Galactose; L-Fructose; D-Xylose; N-acetyl-D-glucosamine. **Amino acids:** L-Na-glutamate; Alanine (racemic); Glycine; Lysine HCl (racemic); Serine (racemic). **Bicine:** N,N-Bis(2-hydroxyethyl)glycine. **Buffer 1** (1.0 M, pH 6.5): Imidazole; Sodium cacodylate; MES (acid); Bis-Tris. **Buffer 2** (1.0 M, pH 7.5): Sodium HEPES; MOPS (acid). **Buffer 3** (1.0 M, pH 8.5): Tris (base); Bicine. **Carboxylic acids:** Na-formate; NH₄-acetate; Na₃-Citrate; NaK-Tartrate (racemic); Na-oxamate. **CTAB:** Cetyltrimethylammonium bromide. **Divalents:** MgCl₂; CaCl₂. **EDO_P8K** (60 %): Ethylene glycol; PEG 8K. **GOL_P4K** (60%), Glycerol; PEG 4K. **Halogens:** NaF; NaBr; NaI. **HEPES:** 2-(4-(2-Hydroxyethyl)-1-piperazinyl)ethanesulfonic Acid. **MES:** 2-(N-morpholino)ethanesulfonic acid. **MME:** Monomethylether. **MOPS:** 3-(N-Morpholino)-propanesulfonic acid. **MPD:** 2,4-Methyl pentanediol. **MPD_P1K_P3350** (75%), MPD (racemic); PEG 1K; PEG 3350. **NPS** (Nitrate Phosphate Sulfate): NaN₃; Na₂HPO₄; (NH₄)₂SO₄. **P550MME_P20K** (60%): PEGMME 550; PEG 20K. **PEG:** Polyethylene glycol (molecular weight in Da. 1.5K, 4K and 8K, in KDa). **Tris:** 2-Amino-2-(hydroxymethyl)propane-1,3-diol. **β-OG:** n-octyl-β-D-glucopyranoside

PROTEIN SOLUTIONS		
Buffer	Formulation	pH
Tris-based buffer	20 mM Tris	7.4
	100 mM NaCl	
	0.1% β-OG	
HEPES-based buffer	10 mM HEPES	7.2
	100 mM NaCl	
	0.1% β-OG	
	0.1 mM DTT	

STRUCTURE SCREEN 1 (MOLECULAR DIMENSIONS)				
Tube #	Salt	Buffer	pH	Precipitant
1	0.02 M Calcium chloride	0.1 M Sodium acetate	4.6	30 % v/v MPD
2	0.2 M Ammonium acetate	0.1 M Sodium acetate	4.6	30 % w/v PEG 4K
3	0.2 M Ammonium sulfate	0.1 M Sodium acetate	4.6	25 % w/v PEG 4K
4	None	0.1 M Sodium acetate	4.6	2.0 M Sodium formate
5	None	0.1 M Sodium acetate	4.6	2.0 M Ammonium sulfate
6	None	0.1 M Sodium acetate	4.6	8 % w/v PEG 4K
7	0.2 M Ammonium acetate	0.1 M Tri-sodium citrate	5.6	30 % w/v PEG 4K
8	0.2 M Ammonium acetate	0.1 M Tri-sodium citrate	5.6	30 % v/v MPD
9	None	0.1 M Tri-sodium citrate	5.6	20 % v/v 2-Propanol, 20% w/v PEG 4K
10	None	0.1 M Tri-sodium citrate	5.6	1.0 M Ammonium dihydrogen phosphate
11	0.2 M Calcium chloride	0.1 M Sodium acetate	4.6	20 % v/v 2-Propanol
12	None	0.1 M Sodium cacodylate	6.5	1.4 M Sodium acetate
13	0.2 M Tri-sodium citrate	0.1 M Sodium cacodylate	6.5	30 % v/v 2-Propanol
14	0.2 M Ammonium sulfate	0.1 M Sodium cacodylate	6.5	30 % w/v PEG 8K
15	0.2 M Magnesium acetate	0.1 M Sodium cacodylate	6.5	20 % w/v PEG 8K
16	0.2 M Magnesium acetate	0.1 M Sodium cacodylate	6.5	30 % v/v MPD
17	None	0.1 M Imidazole	6.5	1.0 M Sodium acetate
18	0.2 M Sodium acetate	0.1 M Sodium cacodylate	6.5	30 % w/v PEG 8K
19	0.2 M Zinc acetate	0.1 M Sodium cacodylate	6.5	18 % w/v PEG 8K
20	0.2 M Calcium acetate	0.1 M Sodium cacodylate	6.5	18 % w/v PEG 8K
21	0.2 M Tri-sodium citrate	0.1 M Na HEPES	7.5	30 % v/v MPD
22	0.2 M Magnesium chloride	0.1 M Na HEPES	7.5	30 % v/v 2-Propanol
23	0.2 M Calcium chloride	0.1 M Na HEPES	7.5	28 % v/v PEG 400
24	0.2 M Magnesium chloride	0.1 M Na HEPES	7.5	30 % v/v PEG 400
25	0.2 M Tri-sodium citrate	0.1 M Na HEPES	7.5	20 % v/v 2-Propanol
26	None	0.1 M Na HEPES	7.5	0.8 M K/Na tartrate
27	None	0.1 M Na HEPES	7.5	1.5 M Lithium sulfate
28	None	0.1 M Na HEPES	7.5	0.8 M Na dihydrogen phosphate/ 0.8 M K dihydrogen phosphate
29	None	0.1 M Na HEPES	7.5	1.4 M Tri-sodium citrate
30	None	0.1 M Na HEPES	7.5	2 % v/v PEG 400, 2.0 M Ammonium sulfate
31	None	0.1 M Na HEPES	7.5	10 % v/v 2-Propanol, 20% w/v PEG 4K
32	None	0.1 M Tris	8.5	2.0 M Ammonium sulfate
33	0.2 M Magnesium chloride	0.1 M Tris	8.5	30 % w/v PEG 4K
34	0.2 M Tri-sodium citrate	0.1 M Tris	8.5	30 % v/v PEG 400
35	0.2 M Lithium sulfate	0.1 M Tris	8.5	30 % w/v PEG 4K
36	0.2 M Ammonium acetate	0.1 M Tris	8.5	30 % v/v 2-Propanol
37	0.2 M Sodium acetate	0.1 M Tris	8.5	30 % w/v PEG 4K
38	None	0.1 M Tris	8.5	8 % w/v PEG 8K
39	None	0.1 M Tris	8.5	2.0 M Ammonium dihydrogen phosphate
40	None	None	-	0.4 M K/Na Tartrate
41	None	None	-	0.4 M Ammonium dihydrogen phosphate
42	0.2 M Ammonium sulfate	None	-	30 % w/v PEG 8K
43	0.2 M Ammonium sulfate	None	-	30 % w/v PEG 4K
44	None	None	-	2.0 M Ammonium sulfate
45	None	None	-	4.0 M Sodium formate
46	0.05 M Potassium dihydrogen phosphate	None	-	20 % w/v PEG 8K
47	None	None	-	30 % w/v PEG 1.5K
48	None	None	-	0.2 M Magnesium formate
49	1.0 M Lithium sulfate	None	-	2 % w/v PEG 8K
50	0.5 M Lithium sulfate	None	-	15 % w/v PEG 8K

Molecular Dimensions (www.moleculardimensions.com)

STRUCTURE SCREEN 2 (MOLECULAR DIMENSIONS)				
Tube #	Salt	Buffer	pH	Precipitant
1	0.1 M Sodium chloride	0.1 M Bicine	9.0	30 % v/v PEG 550 MME
2	None	0.1 M Bicine	9.0	2.0 M Magnesium chloride
3	None	0.1 M Bicine	9.0	2 % v/v 1,4-Dioxane/10 % w/v PEG 20,000
4	0.2 M Magnesium chloride	0.1 M Tris	8.5	3.4 M 1,6-Hexanediol
5	None	0.1 M Tris	8.5	25 % v/v Tert-butanol
6	0.01 M Nickel chloride	0.1 M Tris	8.5	1.0 M Lithium sulfate
7	1.5 M Ammonium sulfate	0.1 M Tris	8.5	12 % v/v Glycerol
8	0.2 M Ammonium dihydrogen phosphate	0.1 M Tris	8.5	50 % v/v MPD
9	None	0.1 M Tris	8.5	20 % v/v Ethanol
10	0.01 M Nickel chloride	0.1 M Tris	8.5	20 % w/v PEG 2000 MME
11	0.5 M Ammonium sulfate	0.1 M Na HEPES	7.5	30 % v/v MPD
12	None	0.1 M Na HEPES	7.5	10 % w/v PEG 6000, 5% v/v MPD
13	None	0.1 M Na HEPES	7.5	20 % v/v Jeffamine M-600
14	0.1 M Sodium chloride	0.1 M Na HEPES	7.5	1.6 M Ammonium sulfate
15	None	0.1 M Na HEPES	7.5	2.0 M Ammonium formate
16	0.05 M Cadmium sulfate	0.1 M Na HEPES	7.5	1.0 M Sodium acetate
17	None	0.1 M Na HEPES	7.5	70 % v/v MPD
18	None	0.1 M Na HEPES	7.5	4.3 M NaCl
19	None	0.1 M Na HEPES	7.5	10 % w/v PEG 8000, 8 % v/v Ethylene glycol
20	None	0.1 M MES	6.5	1.6 M Magnesium sulfate
21	0.1 M Potassium phosphate + 0.1 M Sodium phosphate	0.1 M MES	6.5	2.0 M NaCl
22	None	0.1 M MES	6.5	12 % w/v PEG 20,000
23	1.6 M Ammonium sulfate	0.1 M MES	6.5	10 % v/v Dioxane
24	0.05 M Caesium chloride	0.1 M MES	6.5	30 % v/v Jeffamine M-600
25	0.01 M Cobalt chloride	0.1 M MES	6.5	1.8 M Ammonium sulfate
26	0.2 M Ammonium sulfate	0.1 M MES	6.5	30 % w/v PEG 5000 MME
27	0.01 M Zinc sulfate	0.1 M MES	6.5	25 % v/v PEG 550 MME
28	None	0.1 M Na HEPES	7.5	20 % w/v PEG 10,000
29	0.2 M Potassium sodium tartrate	0.1 M Na citrate	5.6	2.0 M Ammonium sulfate
30	0.5 M Ammonium sulfate	0.1 M Na citrate	5.6	1.0 M Lithium sulfate
31	0.5 M Sodium chloride	0.1 M Na citrate	5.6	4 % v/v Polyethyleneimine
32	None	0.1 M Na citrate	5.6	35 % v/v Tert-butanol
33	0.01 M Ferric chloride	0.1 M Na citrate	5.6	10 % v/v Jeffamine M-600
34	0.01 M Manganese chloride	0.1 M Na citrate	5.6	2.5 M 1,6-Hexanediol
35	None	0.1 M Na acetate	4.6	2.0 M NaCl
36	0.2 M Sodium chloride	0.1 M Na acetate	4.6	30 % v/v MPD
37	0.01 M Cobalt chloride	0.1 M Na acetate	4.6	1.0 M 1,6-cl
38	0.1 M Cadmium chloride	0.1 M Na acetate	4.6	30 % v/v PEG 400
39	0.2 M Ammonium sulfate	0.1 M Na acetate	4.6	30 % w/v PEG 2000 MME
40	2.0 M Sodium chloride	None	None	10 % w/v PEG 6000
41	0.01 M CTAB	None	None	0.5 M NaCl, 0.1 M MgCl ₂
42	None	None	None	25 % v/v Ethylene glycol
43	None	None	None	35 % v/v Dioxane
44	2.0 M Ammonium sulfate	None	None	5 % v/v 2-Propanol
45	None	None	None	1.0 M Imidazole pH 7.0
46	None	None	None	10 % w/v PEG 1000, 10 % w/v PEG 8000
47	1.5 M Sodium chloride	None	None	10 % v/v Ethanol
48	None	None	None	1.6 M Sodium citrate pH 6.5
49	15 % w/v Polyvinylpyrrolidone	None	None	None
50	2.0 M Urea	None	None	None

Molecular Dimensions (www.moleculardimensions.com)

MORPHEUS™ BOX 1 (MOLECULAR DIMENSIONS)				
Tube #	Ligand	Buffer	pH	Precipitant
1	0.06 M Divalents	0.1 M Buffer 1	6.5	30.0% P550MME_P20K
2	0.06 M Divalents	0.1 M Buffer 1	6.5	30.0% EDO_P8K
3	0.06 M Divalents	0.1 M Buffer 1	6.5	30.0% GOL_P4K
4	0.06 M Divalents	0.1 M Buffer 1	6.5	37.5% MPD_P1K_P3350
5	0.06 M Divalents	0.1 M Buffer 2	7.5	30.0% P550MME_P20K
6	0.06 M Divalents	0.1 M Buffer 2	7.5	30.0% EDO_P8K
7	0.06 M Divalents	0.1 M Buffer 2	7.5	30.0% GOL_P4K
8	0.06 M Divalents	0.1 M Buffer 2	7.5	37.5% MPD_P1K_P3350
9	0.06 M Divalents	0.1 M Buffer 3	8.5	30.0% P550MME_P20K
10	0.06 M Divalents	0.1 M Buffer 3	8.5	30.0% EDO_P8K
11	0.06 M Divalents	0.1 M Buffer 3	8.5	30.0% GOL_P4K
12	0.06 M Divalents	0.1 M Buffer 3	8.5	37.5% MPD_P1K_P3350
13	0.09 M Halogens	0.1 M Buffer 1	6.5	30.0% P550MME_P20K
14	0.09 M Halogens	0.1 M Buffer 1	6.5	30.0% EDO_P8K
15	0.09 M Halogens	0.1 M Buffer 1	6.5	30.0% GOL_P4K
16	0.09 M Halogens	0.1 M Buffer 1	6.5	37.5% MPD_P1K_P3350
17	0.09 M Halogens	0.1 M Buffer 2	7.5	30.0% P550MME_P20K
18	0.09 M Halogens	0.1 M Buffer 2	7.5	30.0% EDO_P8K
19	0.09 M Halogens	0.1 M Buffer 2	7.5	30.0% GOL_P4K
20	0.09 M Halogens	0.1 M Buffer 2	7.5	37.5% MPD_P1K_P3350
21	0.09 M Halogens	0.1 M Buffer 3	8.5	30.0% P550MME_P20K
22	0.09 M Halogens	0.1 M Buffer 3	8.5	30.0% EDO_P8K
23	0.09 M Halogens	0.1 M Buffer 3	8.5	30.0% GOL_P4K
24	0.09 M Halogens	0.1 M Buffer 3	8.5	37.5% MPD_P1K_P3350
25	0.09 M NPS	0.1 M Buffer 1	6.5	30.0% P550MME_P20K
26	0.09 M NPS	0.1 M Buffer 1	6.5	30.0% EDO_P8K
27	0.09 M NPS	0.1 M Buffer 1	6.5	30.0% GOL_P4K
28	0.09 M NPS	0.1 M Buffer 1	6.5	37.5% MPD_P1K_P3350
29	0.09 M NPS	0.1 M Buffer 2	7.5	30.0% P550MME_P20K
30	0.09 M NPS	0.1 M Buffer 2	7.5	30.0% EDO_P8K
31	0.09 M NPS	0.1 M Buffer 2	7.5	30.0% GOL_P4K
32	0.09 M NPS	0.1 M Buffer 2	7.5	37.5% MPD_P1K_P3350
33	0.09 M NPS	0.1 M Buffer 3	8.5	30.0% P550MME_P20K
34	0.09 M NPS	0.1 M Buffer 3	8.5	30.0% EDO_P8K
35	0.09 M NPS	0.1 M Buffer 3	8.5	30.0% GOL_P4K
36	0.09 M NPS	0.1 M Buffer 3	8.5	37.5% MPD_P1K_P3350
37	0.12 M Alcohols	0.1 M Buffer 1	6.5	30.0% P550MME_P20K
38	0.12 M Alcohols	0.1 M Buffer 1	6.5	30.0% EDO_P8K
39	0.12 M Alcohols	0.1 M Buffer 1	6.5	30.0% GOL_P4K
40	0.12 M Alcohols	0.1 M Buffer 1	6.5	37.5% MPD_P1K_P3350
41	0.12 M Alcohols	0.1 M Buffer 2	7.5	30.0% P550MME_P20K
42	0.12 M Alcohols	0.1 M Buffer 2	7.5	30.0% EDO_P8K
43	0.12 M Alcohols	0.1 M Buffer 2	7.5	30.0% GOL_P4K
44	0.12 M Alcohols	0.1 M Buffer 2	7.5	37.5 % MPD_P1K_P3350
45	0.12 M Alcohols	0.1 M Buffer 3	8.5	30.0% P550MME_P20K
46	0.12 M Alcohols	0.1 M Buffer 3	8.5	30.0% EDO_P8K
47	0.12 M Alcohols	0.1 M Buffer 3	8.5	30.0% GOL_P4K
48	0.12 M Alcohols	0.1 M Buffer 3	8.5	37.5% MPD_P1K_P3350

Molecular Dimensions (www.moleculardimensions.com)

MORPHEUS™ BOX 2 (MOLECULAR DIMENSIONS)				
Tube #	Ligand	Buffer	pH	Precipitant
1	0.12 M Ethylene Glycols	0.1 M Buffer 1	6.5	30.0% P550MME_P20K
2	0.12 M Ethylene Glycols	0.1 M Buffer 1	6.5	30.0% EDO_P8K
3	0.12 M Ethylene Glycols	0.1 M Buffer 1	6.5	30.0% GOL_P4K
4	0.12 M Ethylene Glycols	0.1 M Buffer 1	6.5	37.5% MPD_P1K_P3350
5	0.12 M Ethylene Glycols	0.1 M Buffer 2	7.5	30.0% P550MME_P20K
6	0.12 M Ethylene Glycols	0.1 M Buffer 2	7.5	30.0% EDO_P8K
7	0.12 M Ethylene Glycols	0.1 M Buffer 2	7.5	30.0% GOL_P4K
8	0.12 M Ethylene Glycols	0.1 M Buffer 2	7.5	37.5% MPD_P1K_P3350
9	0.12 M Ethylene Glycols	0.1 M Buffer 3	8.5	30.0% P550MME_P20K
10	0.12 M Ethylene Glycols	0.1 M Buffer 3	8.5	30.0% EDO_P8K
11	0.12 M Ethylene Glycols	0.1 M Buffer 3	8.5	30.0% GOL_P4K
12	0.12 M Ethylene Glycols	0.1 M Buffer 3	8.5	37.5% MPD_P1K_P3350
13	0.12 M Monosaccharides	0.1 M Buffer 1	6.5	30.0% P550MME_P20K
14	0.12 M Monosaccharides	0.1 M Buffer 1	6.5	30.0% EDO_P8K
15	0.12 M Monosaccharides	0.1 M Buffer 1	6.5	30.0% GOL_P4K
16	0.12 M Monosaccharides	0.1 M Buffer 1	6.5	37.5% MPD_P1K_P3350
17	0.12 M Monosaccharides	0.1 M Buffer 2	7.5	30.0% P550MME_P20K
18	0.12 M Monosaccharides	0.1 M Buffer 2	7.5	30.0% EDO_P8K
19	0.12 M Monosaccharides	0.1 M Buffer 2	7.5	30.0% GOL_P4K
20	0.12 M Monosaccharides	0.1 M Buffer 2	7.5	37.5% MPD_P1K_P3350
21	0.12 M Monosaccharides	0.1 M Buffer 3	8.5	30.0% P550MME_P20K
22	0.12 M Monosaccharides	0.1 M Buffer 3	8.5	30.0% EDO_P8K
23	0.12 M Monosaccharides	0.1 M Buffer 3	8.5	30.0% GOL_P4K
24	0.12 M Monosaccharides	0.1 M Buffer 3	8.5	37.5% MPD_P1K_P3350
25	0.10 M Carboxylic acids	0.1 M Buffer 1	6.5	30.0% P550MME_P20K
26	0.10 M Carboxylic acids	0.1 M Buffer 1	6.5	30.0% EDO_P8K
27	0.10 M Carboxylic acids	0.1 M Buffer 1	6.5	30.0% GOL_P4K
28	0.10 M Carboxylic acids	0.1 M Buffer 1	6.5	37.5% MPD_P1K_P3350
29	0.10 M Carboxylic acids	0.1 M Buffer 2	7.5	30.0% P550MME_P20K
30	0.10 M Carboxylic acids	0.1 M Buffer 2	7.5	30.0% EDO_P8K
31	0.10 M Carboxylic acids	0.1 M Buffer 2	7.5	30.0% GOL_P4K
32	0.10 M Carboxylic acids	0.1 M Buffer 2	7.5	37.5% MPD_P1K_P3350
33	0.10 M Carboxylic acids	0.1 M Buffer 3	8.5	30.0% P550MME_P20K
34	0.10 M Carboxylic acids	0.1 M Buffer 3	8.5	30.0% EDO_P8K
35	0.10 M Carboxylic acids	0.1 M Buffer 3	8.5	30.0% GOL_P4K
36	0.10 M Carboxylic acids	0.1 M Buffer 3	8.5	37.5% MPD_P1K_P3350
37	0.10 M Amino acids	0.1 M Buffer 1	6.5	30.0% P550MME_P20K
38	0.10 M Amino acids	0.1 M Buffer 1	6.5	30.0% EDO_P8K
39	0.10 M Amino acids	0.1 M Buffer 1	6.5	30.0% GOL_P4K
40	0.10 M Amino acids	0.1 M Buffer 1	6.5	37.5% MPD_P1K_P3350
41	0.10 M Amino acids	0.1 M Buffer 2	7.5	30.0% P550MME_P20K
42	0.10 M Amino acids	0.1 M Buffer 2	7.5	30.0% EDO_P8K
43	0.10 M Amino acids	0.1 M Buffer 2	7.5	30.0% GOL_P4K
44	0.10 M Amino acids	0.1 M Buffer 2	7.5	37.5% MPD_P1K_P3350
45	0.10 M Amino acids	0.1 M Buffer 3	8.5	30.0% P550MME_P20K
46	0.10 M Amino acids	0.1 M Buffer 3	8.5	30.0% EDO_P8K
47	0.10 M Amino acids	0.1 M Buffer 3	8.5	30.0% GOL_P4K
48	0.10 M Amino acids	0.1 M Buffer 3	8.5	37.5% MPD_P1K_P3350

Molecular Dimensions (www.moleculardimensions.com)

PROPLEX BOX 1 (MOLECULAR DIMENSIONS)				
Tube #	Salt	Buffer	pH	Precipitant
1	None	0.1 M Tris	8.0	25% v/v PEG 350 MME
2	0.1 M Calcium acetate	0.1 M MES	6.0	15% v/v PEG 400
3	0.1 M Lithium chloride	0.1 M Na HEPES	7.5	20% v/v PEG 400
4	None	0.1 M Tris	8.0	25% v/v PEG 400
5	None	0.1 M MES	6.5	15% v/v PEG 550 MME
6	0.2 M Sodium chloride	0.1 M Na/K phosphate	6.5	25% w/v PEG 1000
7	0.1 M Ammonium sulfate	0.1 M Tris	7.5	20% w/v PEG 1500
8	0.2 M Ammonium sulfate	0.1 M Sodium acetate	5.5	10% w/v PEG 2000 MME
9	0.2 M Sodium chloride	0.1 M MES	6.0	20% w/v PEG 2000 MME
10	0.1 M Potassium chloride	0.1 M Tris	8.0	15% w/v PEG 2000 MME
11	None	0.1 M Na HEPES	7.5	25% w/v PEG 2000 MME
12	0.2 M Sodium acetate	0.1 M Sodium citrate	5.5	5% w/v PEG 4000
13	0.2 M Lithium sulfate	0.1 M Tris	7.5	5% w/v PEG 4000
14	0.1 M Calcium acetate	0.1 M Sodium acetate	4.5	10% w/v PEG 4000
15	0.2 M Sodium acetate	0.1 M Sodium citrate	5.5	10% w/v PEG 4000
16	0.2 M Sodium chloride	0.1 M MES	6.5	10% w/v PEG 4000
17	0.1 M Magnesium chloride	0.1 M Na HEPES	7.5	10% w/v PEG 4000
18	None	0.1 M Na HEPES	7.0	10% w/v PEG 4000/10% v/v 2-Propanol
19	0.2 M Ammonium acetate	0.1 M Sodium acetate	4.0	15% w/v PEG 4000
20	0.1 M Magnesium chloride	0.1 M Sodium citrate	5.0	15% w/v PEG 4000
21	None	0.1 M Sodium cacodylate	6.0	15% w/v PEG 4000
22	0.15 M Ammonium sulfate	0.1 M MES	6.0	15% w/v PEG 4000
23	None	0.1 M Na HEPES	7.0	15% w/v PEG 4000
24	0.1 M Magnesium chloride	0.1 M Na HEPES	7.0	15% w/v PEG 4000
25	0.15 M Ammonium sulfate	0.1 M Tris	8.0	15% w/v PEG 4000
26	None	0.1 M Sodium citrate	4.5	20% w/v PEG 4000
27	0.2 M Ammonium acetate	0.1 M Sodium acetate	5.0	20% w/v PEG 4000
28	0.2 M Lithium sulfate	0.1 M MES	6.0	20% w/v PEG 4000
29	None	0.1 M Tris	8.0	20% w/v PEG 4000
30	0.15 M Ammonium sulfate	0.1 M Na HEPES	7.0	20% w/v PEG 4000
31	None	0.1 M Sodium citrate	5.6	20% w/v PEG 4000/20% v/v 2-Propanol
32	0.2 M Sodium chloride	0.1 M Tris	8.0	20% w/v PEG 4000
33	None	0.1 M Sodium cacodylate	5.5	25% w/v PEG 4000
34	0.15 M Ammonium sulfate	0.1 M MES	5.5	25% w/v PEG 4000
35	None	0.1 M Sodium cacodylate	6.5	25% w/v PEG 4000
36	0.2 M Potassium iodide	0.1 M MES	6.5	25% w/v PEG 4000
37	0.2 M Sodium chloride	0.1 M Na HEPES	7.5	25% w/v PEG 4000
38	None	0.1 M MES	6.5	10% w/v PEG 5000 MME/12% v/v 1-Propanol
39	0.1 M Potassium chloride	0.1 M Na HEPES	7.0	15% w/v PEG 5000 MME
40	0.2 M Ammonium sulfate	0.1 M Tris	7.5	20% w/v PEG 5000 MME
41	0.1 M Magnesium chloride	0.1 M MES	6.0	8% w/v PEG 6000
42	0.15 M Sodium chloride	0.1 M Tris	8.0	8% w/v PEG 6000
43	None	0.1 M Sodium citrate	5.5	15% w/v PEG 6000
44	0.1 M Magnesium acetate	0.1 M Sodium cacodylate	6.5	15% w/v PEG 6000
45	None	0.1 M MES	6.5	15% w/v PEG 6000/5% w/v MPD
46	0.1 M Potassium chloride	0.1 M Na HEPES	7.5	15% w/v PEG 6000
47	None	0.1 M Tris	8.5	15% w/v PEG 6000
48	None	0.1 M Tris	8.5	20% w/v PEG 6000

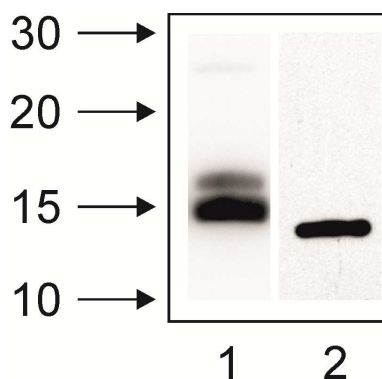
Molecular Dimensions (www.moleculardimensions.com)

PROPLEX BOX 2 (MOLECULAR DIMENSIONS)				
Tube #	Salt	Buffer	pH	Precipitant
1	0.1 M Magnesium acetate	0.1 M Sodium acetate	4.5	8% w/v PEG 8000
2	None	0.1 M Sodium citrate	5.0	8% w/v PEG 8000
3	0.2 M Sodium chloride	0.1 M Sodium cacodylate	6.0	8% w/v PEG 8000
4	None	0.1 M Na HEPES	7.0	8% w/v PEG 8000
5	None	0.1 M Tris	8.0	8% w/v PEG 8000
6	0.1 M Calcium acetate	0.1 M Sodium cacodylate	5.5	12% w/v PEG 8000
7	None	0.1 M Sodium phosphate	6.5	12% w/v PEG 8000
8	0.1 M Magnesium acetate	0.1 M MOPS	7.5	12% w/v PEG 8000
9	0.2 M Sodium chloride	0.1 M Na HEPES	7.5	12% w/v PEG 8000
10	0.2 M Ammonium sulfate	0.1 M Tris	8.5	12% w/v PEG 8000
11	None	0.1 M Sodium citrate	5.0	20% w/v PEG 8000
12	0.2 M Ammonium sulfate	0.1 M MES	6.5	20% w/v PEG 8000
13	None	0.1 M Na HEPES	7.0	20% w/v PEG 8000
14	0.2 M Lithium chloride	0.1 M Tris	8.0	20% w/v PEG 8000
15	0.1 M Magnesium acetate	0.1 M MES	6.5	10% w/v PEG 10000
16	None	0.1 M Na HEPES	7.0	18% w/v PEG 12000
17	0.1 M Sodium chloride	0.1 M Tris	8.0	8% w/v PEG 20000
18	None	0.1 M Na HEPES	7.0	15% w/v PEG 20000
19	None	0.1 M MES	6.5	0.5 M Ammonium sulfate
20	None	0.1 M Sodium acetate	5.0	1 M Ammonium sulfate
21	None	0.1 M MES	6.5	1 M Ammonium sulfate
22	None	0.1 M Tris	8.0	1 M Ammonium sulfate
23	None	0.1 M Sodium acetate	5.0	1.5 M Ammonium sulfate
24	None	0.1 M Na HEPES	7.0	1.5 M Ammonium sulfate
25	None	0.1 M Tris	8.0	1.5 M Ammonium sulfate
26	None	0.1 M Sodium acetate	5.0	2 M Ammonium sulfate
27	None	0.1 M Na HEPES	7.0	2 M Ammonium sulfate
28	None	0.1 M Tris	8.0	2 M Ammonium sulfate
29	1 M Potassium chloride	0.1 M Na HEPES	7.0	1 M Ammonium sulfate
30	None	0.1 M Sodium acetate	5.0	2 M Sodium formate
31	None	0.1 M Tris	7.5	3 M Sodium Formate
32	None	None	7.5	0.8 M Na/K hydrogen phosphate
33	None	None	7.0	1.3 M Na/K hydrogen phosphate
34	None	None	6.5	1.6 M Na/K hydrogen phosphate
35	None	0.1 M Na HEPES	7.5	1 M Sodium acetate
36	None	0.1 M Na HEPES	7.0	1 M Sodium citrate
37	None	0.1 M Sodium citrate	6.0	2 M Sodium chloride
38	None	0.1 M MES	6.5	1 M Lithium sulfate
39	None	0.1 M Tris	8.0	1.6 M Lithium sulfate
40	None	None	6.0	1.4 M Sodium malonate
41	None	0.1 M Tris	8.0	1.2 M Na/K tartrate
42	None	0.1 M MES	6.5	1.6 M Magnesium sulfate
43	None	0.1 M Sodium acetate	5.0	2% w/v PEG 4000/15% v/v MPD
44	50 mM Calcium acetate	0.1 M Sodium cacodylate	6.0	25% v/v MPD
45	None	0.1 M Imidazole	7.0	50% v/v MPD
46	50 mM Magnesium chloride	0.1 M MES	6.5	5% w/v PEG 4000/10% v/v 2-Propanol
47	0.2 M Ammonium acetate	0.1 M Na HEPES	7.5	25% v/v 2-Propanol
48	0.1 M Sodium chloride	0.1 M Tris	8.0	5% v/v MPD/15% v/v Ethanol

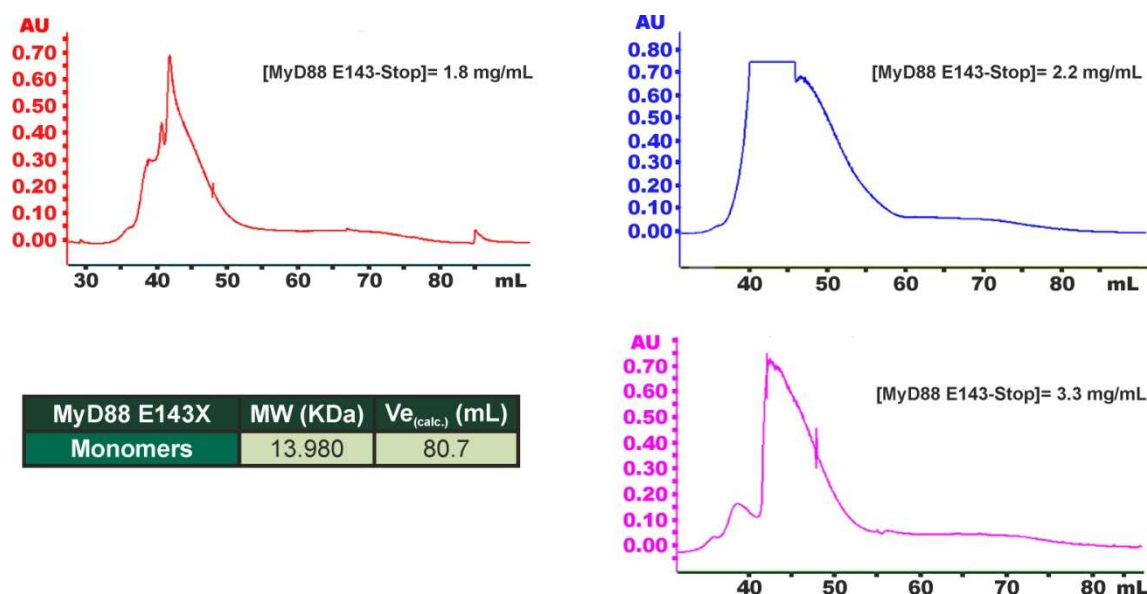
Molecular Dimensions (www.moleculardimensions.com)

Appendix XI

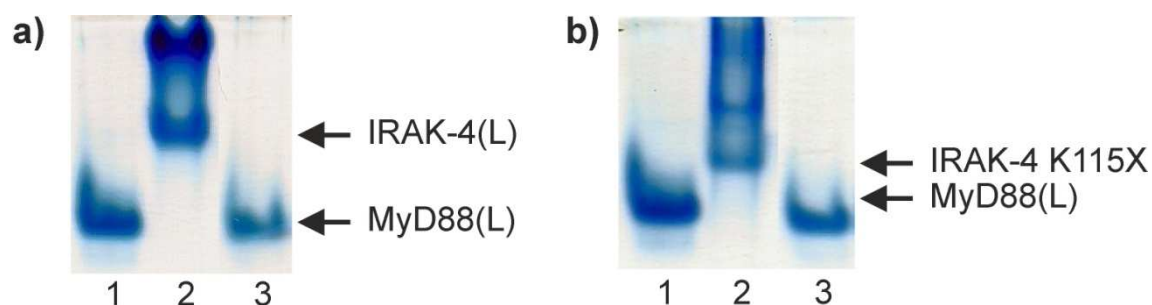
Supplemental Figures



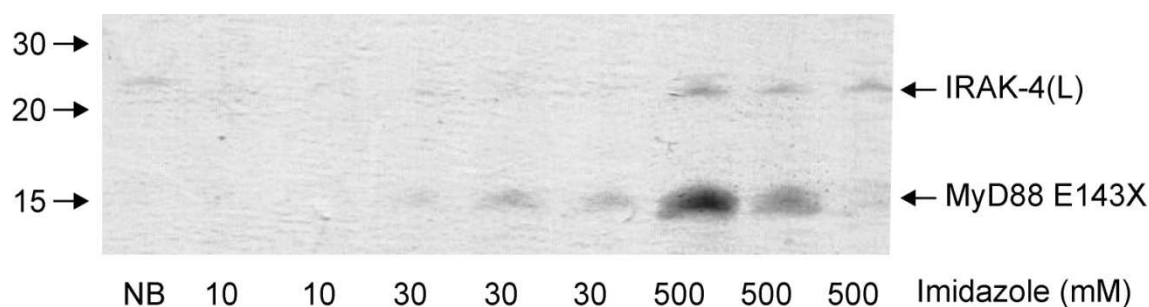
Supplemental Figure 1 Overexpression of MyD88 E143X and IRAK-4 K115X truncated variants. ~500 ng of each protein were analyzed by SDS-PAGE and transferred to a PVDF membrane for WB analysis. Novex® Sharp Pre-stained Protein Molecular Weight Standard was used to determine the molecular masses, given in kDa. Lane 1, MyD88 E143X variant probed with anti-6xHis antibody. Lane 2, IRAK-4 K115X variant probed with anti-FLAG antibody. Notice that both proteins migrate approximately as expected from their theoretical masses (see Table 4.2).



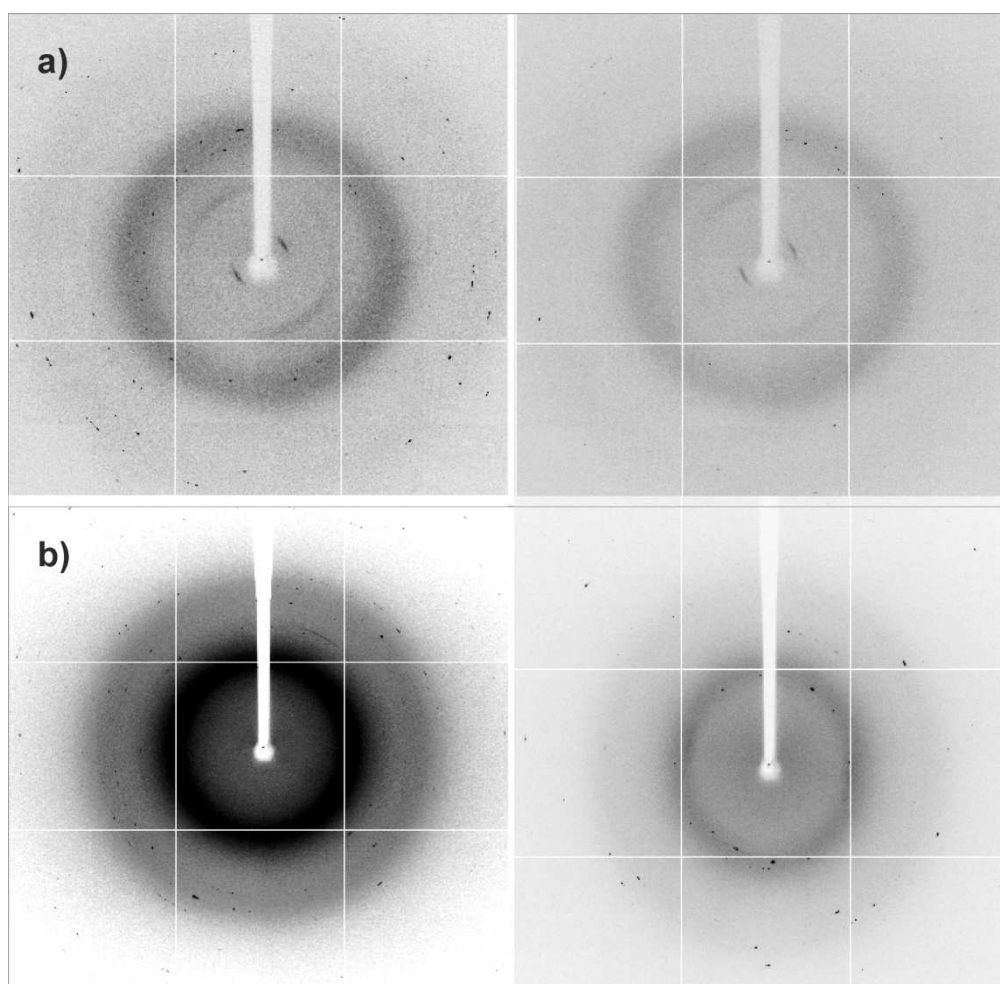
Supplemental Figure 2 Gel filtration analysis of MyD88 E143X variant. FPLC analyses were performed on MyD88 E143X at a flow of 2 mL/min. MyD88 E143X monomers were calculated to elute at ~ 80.7 mL, using the standard curve given in Figure 4.4a. In all cases, MyD88 E143X was eluted at ~ 44 mL, corresponding to a MW of 240 kDa (~ 17 protein monomers). At higher concentrations (bottom-right panel), an elution peak appeared at ~ 39 mL, corresponding to a MW of ~ 350 kDa (~ 25 monomers).



Supplemental Figure 3 Electrophoretic analysis of MyD88(L)•IRAK-4(L) and MyD88(L)•IRAK-4 K115X complexes under native conditions. MyD88(L)•IRAK-4(L) (a) and MyD88(L)•IRAK-4 K115X (b) complexes were obtained by co-renaturation in Fold-it condition 5, as explained in Materials and Methods (see Appendix VIII for composition). Samples were run in a Tris-glycine gel, pH 8.8, 11% acrylamide, as detailed in Appendix VII. Samples were applied as follows: **a)** lane 1, MyD88(L); lane 2, IRAK-4(L); lane 3, MyD88(L)•IRAK-4(L) complex. **b)** lane 1, MyD88(L); lane 2, IRAK-4 K115X; lane 3, MyD88(L)•IRAK-4 K115X complex.



Supplemental Figure 4 Formation of MyD88 E143X•IRAK-4(L) complex in solution. Equimolar amounts of MyD88 E143X and IRAK-4(L) were incubated for 2 hours at room temperature in binding buffer (see Appendix VII) and then Ni-NTA agarose was added to this mixture. After centrifugation to remove non-bound material (NB), proteins were washed and recovered from the matrix using increasing imidazole concentrations. Samples were separated by SDS-PAGE and stained with Coomassie Blue Staining. Notice that IRAK-4(L) is pulled down by MyD88 E143X, indicating MyD88 E143X•IRAK-4(L) complex formation.

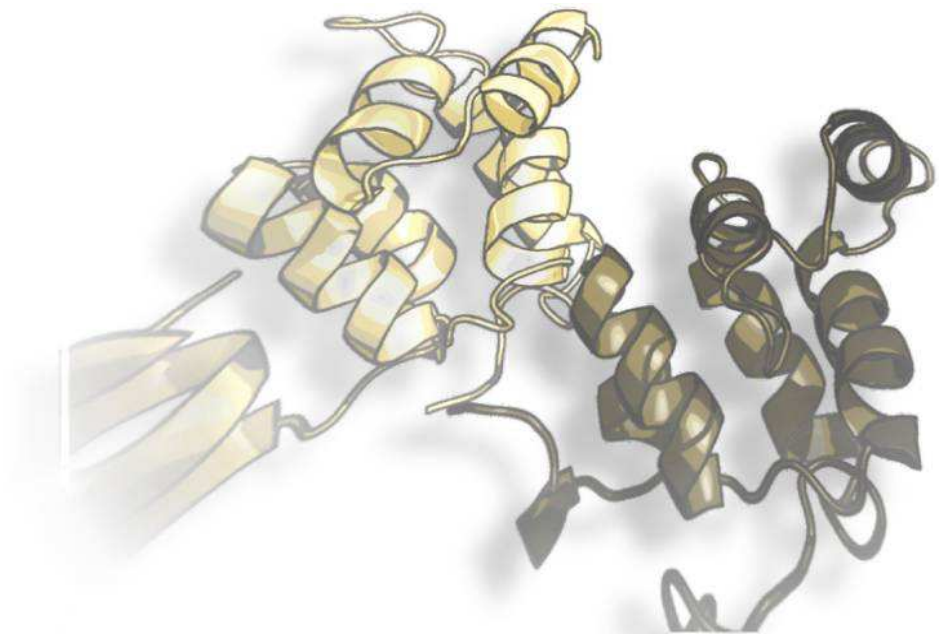


Supplemental Figure 5 Orthogonal images of diffraction patterns obtained for MyD88(L) and MyD88 E143X crystals. All crystals were obtained as described in Results (see Table 4.5). **a)** Diffraction patterns of an MyD88(L) crystal, obtained at orthogonal positions. Although poor diffraction is observed for this crystal, it presents typical protein diffraction patterns. **b)** Diffraction patterns of an MyD88 E143X crystal, obtained at orthogonal positions. Although this crystal yields poor diffraction results, it also presents typical protein diffraction patterns. Diffraction patterns were obtained at the ESRF beamline ID23-1, equipped with an ADSC Q315R CCD detector.

Appendix XII**Articles Published During the PhD Period**

1. **Mendoza-Barberá, E.**, Corral-Rodríguez, M.A., Soares-Schanoski, A., Velarde, M., Macieira, S., Messerschmidt, A., López-Collazo, E. and Fuentes-Prior, P. 2009. Contribution of globular death domains and unstructured linkers to MyD88-IRAK-4 heterodimer formation: an explanation for the antagonistic activity of MyD88s. *Biochem. Biophys. Res. Commun.*, 380(1):183-7.
2. **Mendoza-Barberá, E.**, Julve, J., Nilsson, S.K., Lookene, A., Martín-Campos, J.M., Roig, R., Lechuga-Sancho, A.M., Sloan, J.J., Fuentes-Prior, P. and Blanco-Vaca, F. Structural and functional analysis of *APOA5* mutations identified in patients with severe hypertriglyceridemia. *J. Lipid Res.* (under revision).
3. del Fresno, C., Soler-Rangel, L., Soares-Schanoski, A., Gómez-Piña, V., González-León, M. C., Gómez-García, L., **Mendoza-Barberá, E.**, Rodríguez-Rojas, A., García, F., Fuentes-Prior, P., Arnalich, F. and López-Collazo, E. 2007. Inflammatory responses associated with acute coronary syndrome up-regulate IRAK-M and induce endotoxin tolerance in circulating monocytes. *J Endotoxin Res.* 13(1):39-52.
4. González-León, M. C., Soares-Schanoski, A., del Fresno, C., Cimadevila, A., Gómez-Piña, V., **Mendoza-Barberá, E.**, García, F., Marin, E., Arnalich, F., Fuentes-Prior, P. and López-Collazo, E. 2006. Nitric oxide induces SOCS-1 expression in human monocytes in a TNF-alpha-dependent manner. *J Endotoxin Res.* 12(5):296-306.
5. Colletier, J.P., Aleksandrov, A., Coquelle, N., Mraihi, S., **Mendoza-Barberá, E.**, Field, M. and Madern, D. 2012. Sampling the conformational energy landscape of a hyperthermophilic protein by engineering key substitutions. *Mol. Biol. Evol.* 29(6):1683-94.

8. References



1. Charles A. Janeway, P.T., Mark Walport, Mark Shlomchik, *Immunobiology*. 5 ed. 2001, New York.: Garland Publishing.
2. Abreu, M.T., and M. Arditi, *Innate immunity and toll-like receptors: clinical implications of basic science research*. J Pediatr, 2004. **144**: p. 421-429.
3. Anderson, K.V. and Nusslein-Volhard, C., *Information for the dorsal--ventral pattern of the Drosophila embryo is stored as maternal mRNA*. Nature, 1984. **311**(5983): p. 223-7.
4. Anderson, K.V., Bokla, L., and Nusslein-Volhard, C., *Establishment of dorsal-ventral polarity in the Drosophila embryo: the induction of polarity by the Toll gene product*. Cell, 1985. **42**(3): p. 791-8.
5. Gay, N.J. and Keith, F.J., *Drosophila Toll and IL-1 receptor*. Nature, 1991. **351**(6325): p. 355-6.
6. Hashimoto, C., Hudson, K.L., and Anderson, K.V., *The Toll gene of Drosophila, required for dorsal-ventral embryonic polarity, appears to encode a transmembrane protein*. Cell, 1988. **52**(2): p. 269-79.
7. Lemaitre, B., E. Nicolas, L. Michaut, J. M. Reichhart, and J. A. Hoffmann, *The dorsoventral regulatory gene cassette spatzle/Toll/cactus controls the potent antifungal response in Drosophila adults*. Cell, 1996. **86**: p. 973-983.
8. Rock, F.L., G. Hardiman, J. C. Timans, R. A. Kastelein, and J. F. Bazan, *A family of human receptors structurally related to Drosophila Toll*. Proc Natl Acad Sci U S A, 1998. **95**: p. 588-593.
9. Sherwood, E.R., and T. Toliver-Kinsky, *Mechanisms of the inflammatory response*. Best Pract Res Clin Anaesthesiol, 2004. **18**: p. 385-405.
10. Dunn, G.P., A. T. Bruce, H. Ikeda, L. J. Old, and R. D. Schreiber, *Cancer immunoediting: from immunosurveillance to tumor escape*. Nat Immunol, 2002. **3**: p. 991- 998.
11. West, A.P., A. A. Koblansky, and S. Ghosh, *Recognition and signaling by toll-like receptors*. Annu Rev Cell Dev Biol, 2006. **22**: p. 409-437.
12. Chen, K., J. Huang, W. Gong, P. Iribarren, N. M. Dunlop, and J. M. Wang, *Toll-like receptors in inflammation, infection and cancer*. Int Immunopharmacol, 2007. **7**: p. 1271-1285.
13. Watters, T.M., Kenny, E.F., and O'Neill, L.A., *Structure, function and regulation of the Toll/IL-1 receptor adaptor proteins*. Immunol Cell Biol, 2007. **85**(6): p. 411-9.
14. Akira, S., Uematsu, S., and Takeuchi, O., *Pathogen recognition and innate immunity*. Cell, 2006. **124**(4): p. 783-801.
15. Medzhitov, R., Preston-Hurlburt, P., and Janeway, C.A., Jr., *A human homologue of the Drosophila Toll protein signals activation of adaptive immunity*. Nature, 1997. **388**(6640): p. 394-7.
16. Beutler, B., *Inferences, questions and possibilities in Toll-like receptor signalling*. Nature, 2004. **430**(6996): p. 257-63.
17. Chen, R., et al., *Inflammation, cancer and chemoresistance: taking advantage of the toll-like receptor signaling pathway*. Am J Reprod Immunol, 2007. **57**(2): p. 93-107.

18. Beutler, B., Hoebe, K., and Shamel, L., *Forward genetic dissection of afferent immunity: the role of TIR adapter proteins in innate and adaptive immune responses*. *C R Biol*, 2004. **327**(6): p. 571-80.
19. Takeuchi, O., et al., *Cutting edge: role of Toll-like receptor 1 in mediating immune response to microbial lipoproteins*. *J Immunol*, 2002. **169**(1): p. 10-4.
20. Wetzler, L.M., *The role of Toll-like receptor 2 in microbial disease and immunity*. *Vaccine*, 2003. **21 Suppl 2**: p. S55-60.
21. Takeuchi, O., Hoshino, K., and Akira, S., *Cutting edge: TLR2-deficient and MyD88-deficient mice are highly susceptible to Staphylococcus aureus infection*. *J Immunol*, 2000. **165**(10): p. 5392-6.
22. Vabulas, R.M., et al., *Endocytosed HSP60s use toll-like receptor 2 (TLR2) and TLR4 to activate the toll/interleukin-1 receptor signaling pathway in innate immune cells*. *J Biol Chem*, 2001. **276**(33): p. 31332-9.
23. Asea, A., et al., *Novel signal transduction pathway utilized by extracellular HSP70: role of toll-like receptor (TLR) 2 and TLR4*. *J Biol Chem*, 2002. **277**(17): p. 15028-34.
24. Dybdahl, B., et al., *Inflammatory response after open heart surgery: release of heat-shock protein 70 and signaling through toll-like receptor-4*. *Circulation*, 2002. **105**(6): p. 685-90.
25. Vabulas, R.M., et al., *HSP70 as endogenous stimulus of the Toll/interleukin-1 receptor signal pathway*. *J Biol Chem*, 2002. **277**(17): p. 15107-12.
26. Vabulas, R.M., et al., *The endoplasmic reticulum-resident heat shock protein Gp96 activates dendritic cells via the Toll-like receptor 2/4 pathway*. *J Biol Chem*, 2002. **277**(23): p. 20847-53.
27. Kataoka, K., et al., *Activation of macrophages by linear (1right-arrow3)-beta-D-glucans. Implications for the recognition of fungi by innate immunity*. *J Biol Chem*, 2002. **277**(39): p. 36825-31.
28. Underhill, D.M., et al., *The Toll-like receptor 2 is recruited to macrophage phagosomes and discriminates between pathogens*. *Nature*, 1999. **401**(6755): p. 811-5.
29. Yang, R.B., et al., *Toll-like receptor-2 mediates lipopolysaccharide-induced cellular signalling*. *Nature*, 1998. **395**(6699): p. 284-8.
30. Medzhitov, R., et al., *MyD88 is an adaptor protein in the hToll/IL-1 receptor family signaling pathways*. *Mol Cell*, 1998. **2**(2): p. 253-8.
31. Chow, J.C., et al., *Toll-like receptor-4 mediates lipopolysaccharide-induced signal transduction*. *J Biol Chem*, 1999. **274**(16): p. 10689-92.
32. Yang, H., et al., *Cellular events mediated by lipopolysaccharide-stimulated toll-like receptor 4. MD-2 is required for activation of mitogen-activated protein kinases and Elk-1*. *J Biol Chem*, 2000. **275**(27): p. 20861-6.
33. Poltorak, A., et al., *Defective LPS signaling in C3H/HeJ and C57BL/10ScCr mice: mutations in Tlr4 gene*. *Science*, 1998. **282**(5396): p. 2085-8.
34. Lien, E., et al., *Toll-like receptor 4 imparts ligand-specific recognition of bacterial lipopolysaccharide*. *J Clin Invest*, 2000. **105**(4): p. 497-504.

35. Okamura, Y., et al., *The extra domain A of fibronectin activates Toll-like receptor 4*. J Biol Chem, 2001. **276**(13): p. 10229-33.
36. Roelofs, M.F., et al., *Identification of small heat shock protein B8 (HSP22) as a novel TLR4 ligand and potential involvement in the pathogenesis of rheumatoid arthritis*. J Immunol, 2006. **176**(11): p. 7021-7.
37. Ohashi, K., et al., *Cutting edge: heat shock protein 60 is a putative endogenous ligand of the toll-like receptor-4 complex*. J Immunol, 2000. **164**(2): p. 558-61.
38. Bulut, Y., et al., *Chlamydial heat shock protein 60 activates macrophages and endothelial cells through Toll-like receptor 4 and MD2 in a MyD88-dependent pathway*. J Immunol, 2002. **168**(3): p. 1435-40.
39. Hayashi, F., et al., *The innate immune response to bacterial flagellin is mediated by Toll-like receptor 5*. Nature, 2001. **410**(6832): p. 1099-103.
40. Bauer, S., et al., *Human TLR9 confers responsiveness to bacterial DNA via species-specific CpG motif recognition*. Proc Natl Acad Sci U S A, 2001. **98**(16): p. 9237-42.
41. Hemmi, H., et al., *A Toll-like receptor recognizes bacterial DNA*. Nature, 2000. **408**(6813): p. 740-5.
42. Leadbetter, E.A., et al., *Chromatin-IgG complexes activate B cells by dual engagement of IgM and Toll-like receptors*. Nature, 2002. **416**(6881): p. 603-7.
43. Viglianti, G.A., et al., *Activation of autoreactive B cells by CpG dsDNA*. Immunity, 2003. **19**(6): p. 837-47.
44. Bieback, K., et al., *Hemagglutinin protein of wild-type measles virus activates toll-like receptor 2 signaling*. J Virol, 2002. **76**(17): p. 8729-36.
45. Kurt-Jones, E.A., et al., *Pattern recognition receptors TLR4 and CD14 mediate response to respiratory syncytial virus*. Nat Immunol, 2000. **1**(5): p. 398-401.
46. Alexopoulou, L., et al., *Recognition of double-stranded RNA and activation of NF-kappaB by Toll-like receptor 3*. Nature, 2001. **413**(6857): p. 732-8.
47. Kariko, K., et al., *mRNA is an endogenous ligand for Toll-like receptor 3*. J Biol Chem, 2004. **279**(13): p. 12542-50.
48. Diebold, S.S., et al., *Innate antiviral responses by means of TLR7-mediated recognition of single-stranded RNA*. Science, 2004. **303**(5663): p. 1529-31.
49. Heil, F., et al., *The Toll-like receptor 7 (TLR7)-specific stimulus loxoribine uncovers a strong relationship within the TLR7, 8 and 9 subfamily*. Eur J Immunol, 2003. **33**(11): p. 2987-97.
50. Lund, J.M., et al., *Recognition of single-stranded RNA viruses by Toll-like receptor 7*. Proc Natl Acad Sci U S A, 2004. **101**(15): p. 5598-603.
51. Vollmer, J., et al., *Immune stimulation mediated by autoantigen binding sites within small nuclear RNAs involves Toll-like receptors 7 and 8*. J Exp Med, 2005. **202**(11): p. 1575-85.
52. Lau, C.M., et al., *RNA-associated autoantigens activate B cells by combined B cell antigen receptor/Toll-like receptor 7 engagement*. J Exp Med, 2005. **202**(9): p. 1171-7.

53. Tabeta, K., et al., *Toll-like receptors 9 and 3 as essential components of innate immune defense against mouse cytomegalovirus infection*. Proc Natl Acad Sci U S A, 2004. **101**(10): p. 3516-21.
54. Krug, A., et al., *Herpes simplex virus type 1 activates murine natural interferon-producing cells through toll-like receptor 9*. Blood, 2004. **103**(4): p. 1433-7.
55. Lund, J., et al., *Toll-like receptor 9-mediated recognition of Herpes simplex virus-2 by plasmacytoid dendritic cells*. J Exp Med, 2003. **198**(3): p. 513-20.
56. Takeshita, F., et al., *Cutting edge: Role of Toll-like receptor 9 in CpG DNA-induced activation of human cells*. J Immunol, 2001. **167**(7): p. 3555-8.
57. Ishii, K.J., et al., *A Toll-like receptor-independent antiviral response induced by double-stranded B-form DNA*. Nat Immunol, 2006. **7**(1): p. 40-8.
58. Stetson, D.B. and Medzhitov, R., *Recognition of cytosolic DNA activates an IRF3-dependent innate immune response*. Immunity, 2006. **24**(1): p. 93-103.
59. Chen, K., et al., *Toll-like receptors in inflammation, infection and cancer*. Int Immunopharmacol, 2007. **7**(10): p. 1271-85.
60. Killeen, S.D., et al., *Exploitation of the Toll-like receptor system in cancer: a double-edged sword?* Br J Cancer, 2006. **95**(3): p. 247-52.
61. Youn, H.S., et al., *Specific inhibition of MyD88-independent signaling pathways of TLR3 and TLR4 by resveratrol: molecular targets are TBK1 and RIP1 in TRIF complex*. J Immunol, 2005. **175**(5): p. 3339-46.
62. Akira, S., Takeda, K., and Kaisho, T., *Toll-like receptors: critical proteins linking innate and acquired immunity*. Nat Immunol, 2001. **2**(8): p. 675-80.
63. Kawai, T. and Akira, S., *The role of pattern-recognition receptors in innate immunity: update on Toll-like receptors*. Nat Immunol, 2010. **11**(5): p. 373-84.
64. Kawai, T. and Akira, S., *Toll-like receptor downstream signaling*. Arthritis Res Ther, 2004. **7**(1): p. 12-9.
65. Oshiumi, H., et al., *TIR-containing adapter molecule (TICAM)-2, a bridging adapter recruiting to toll-like receptor 4 TICAM-1 that induces interferon-beta*. J Biol Chem, 2003. **278**(50): p. 49751-62.
66. Yamamoto, M., et al., *Role of adaptor TRIF in the MyD88-independent toll-like receptor signaling pathway*. Science, 2003. **301**(5633): p. 640-3.
67. Covert, M.W., et al., *Achieving stability of lipopolysaccharide-induced NF-kappaB activation*. Science, 2005. **309**(5742): p. 1854-7.
68. Honda, K. and Taniguchi, T., *IRFs: master regulators of signalling by Toll-like receptors and cytosolic pattern-recognition receptors*. Nat Rev Immunol, 2006. **6**(9): p. 644-58.
69. Moynagh, P.N., *TLR signalling and activation of IRFs: revisiting old friends from the NF-kappaB pathway*. Trends Immunol, 2005. **26**(9): p. 469-76.
70. Bowie, A.G. and Haga, I.R., *The role of Toll-like receptors in the host response to viruses*. Mol Immunol, 2005. **42**(8): p. 859-67.
71. Perry, A.K., et al., *The host type I interferon response to viral and bacterial infections*. Cell Res, 2005. **15**(6): p. 407-22.

72. Visintin, A., et al., *Lysines 128 and 132 enable lipopolysaccharide binding to MD-2, leading to Toll-like receptor-4 aggregation and signal transduction.* J Biol Chem, 2003. **278**(48): p. 48313-20.
73. Burns, K., et al., *MyD88, an adapter protein involved in interleukin-1 signaling.* J Biol Chem, 1998. **273**(20): p. 12203-9.
74. Muzio, M., et al., *IRAK (Pelle) family member IRAK-2 and MyD88 as proximal mediators of IL-1 signaling.* Science, 1997. **278**(5343): p. 1612-5.
75. Suzuki, N., et al., *Severe impairment of interleukin-1 and Toll-like receptor signalling in mice lacking IRAK-4.* Nature, 2002. **416**(6882): p. 750-6.
76. Fuentes-Prior, P. and Salvesen, G.S., *The protein structures that shape caspase activity, specificity, activation and inhibition.* Biochem J, 2004. **384**(Pt 2): p. 201-32.
77. Martinon, F. and Tschopp, J., *Inflammatory caspases: linking an intracellular innate immune system to autoinflammatory diseases.* Cell, 2004. **117**(5): p. 561-74.
78. Kollwe, C., et al., *Sequential autophosphorylation steps in the interleukin-1 receptor-associated kinase-1 regulate its availability as an adapter in interleukin-1 signaling.* J Biol Chem, 2004. **279**(7): p. 5227-36.
79. Burns, K., et al., *Inhibition of interleukin 1 receptor/Toll-like receptor signaling through the alternatively spliced, short form of MyD88 is due to its failure to recruit IRAK-4.* J Exp Med, 2003. **197**(2): p. 263-8.
80. Cao, Z., Henzel, W.J., and Gao, X., *IRAK: a kinase associated with the interleukin-1 receptor.* Science, 1996. **271**(5252): p. 1128-31.
81. Jiang, Z., et al., *Interleukin-1 (IL-1) receptor-associated kinase-dependent IL-1-induced signaling complexes phosphorylate TAK1 and TAB2 at the plasma membrane and activate TAK1 in the cytosol.* Mol Cell Biol, 2002. **22**(20): p. 7158-67.
82. Cao, Z., et al., *TRAF6 is a signal transducer for interleukin-1.* Nature, 1996. **383**(6599): p. 443-6.
83. Ishida, T., et al., *Identification of TRAF6, a novel tumor necrosis factor receptor-associated factor protein that mediates signaling from an amino-terminal domain of the CD40 cytoplasmic region.* J Biol Chem, 1996. **271**(46): p. 28745-8.
84. Lu, Y.C., Yeh, W.C., and Ohashi, P.S., *LPS/TLR4 signal transduction pathway.* Cytokine, 2008. **42**(2): p. 145-51.
85. Dauphinee, S.M. and Karsan, A., *Lipopolysaccharide signaling in endothelial cells.* Lab Invest, 2006. **86**(1): p. 9-22.
86. Lee, M.S. and Kim, Y.J., *Signaling pathways downstream of pattern-recognition receptors and their cross talk.* Annu Rev Biochem, 2007. **76**: p. 447-80.
87. Silverman, N. and Maniatis, T., *NF-kappaB signaling pathways in mammalian and insect innate immunity.* Genes Dev, 2001. **15**(18): p. 2321-42.
88. Yamin, T.T. and Miller, D.K., *The interleukin-1 receptor-associated kinase is degraded by proteasomes following its phosphorylation.* J Biol Chem, 1997. **272**(34): p. 21540-7.
89. Li, X., et al., *Mutant cells that do not respond to interleukin-1 (IL-1) reveal a novel role for IL-1 receptor-associated kinase.* Mol Cell Biol, 1999. **19**(7): p. 4643-52.

90. Jensen, L.E. and Whitehead, A.S., *IRAK1b, a novel alternative splice variant of interleukin-1 receptor-associated kinase (IRAK), mediates interleukin-1 signaling and has prolonged stability.* J Biol Chem, 2001. **276**(31): p. 29037-44.
91. Beinke, S. and Ley, S.C., *Functions of NF-kappaB1 and NF-kappaB2 in immune cell biology.* Biochem J, 2004. **382**(Pt 2): p. 393-409.
92. Hull, C., et al., *Lipopolysaccharide signals an endothelial apoptosis pathway through TNF receptor-associated factor 6-mediated activation of c-Jun NH2-terminal kinase.* J Immunol, 2002. **169**(5): p. 2611-8.
93. Patriotis, C., et al., *Tumor progression locus 2 (Tpl-2) encodes a protein kinase involved in the progression of rodent T-cell lymphomas and in T-cell activation.* Proc Natl Acad Sci U S A, 1993. **90**(6): p. 2251-5.
94. Ward, S.G. and Finan, P., *Isoform-specific phosphoinositide 3-kinase inhibitors as therapeutic agents.* Curr Opin Pharmacol, 2003. **3**(4): p. 426-34.
95. McEntyre, J.R. and Gibson, T.J., *Patterns and clusters within the PSM column in TiBS, 1992-2004.* Trends Biochem Sci, 2004. **29**(12): p. 627-33.
96. Hill, J.M., et al., *Recognition of ERK MAP kinase by PEA-15 reveals a common docking site within the death domain and death effector domain.* EMBO J, 2002. **21**(23): p. 6494-504.
97. Vaughn, D.E., et al., *Crystal structure of Apaf-1 caspase recruitment domain: an alpha-helical Greek key fold for apoptotic signaling.* J Mol Biol, 1999. **293**(3): p. 439-47.
98. Reed, J.C., Doctor, K.S., and Godzik, A., *The domains of apoptosis: a genomics perspective.* Sci STKE, 2004. **2004**(239): p. re9.
99. Natarajan, A., Ghose, R., and Hill, J.M., *Structure and dynamics of ASC2, a pyrin domain-only protein that regulates inflammatory signaling.* J Biol Chem, 2006. **281**(42): p. 31863-75.
100. Eberstadt, M., et al., *NMR structure and mutagenesis of the FADD (Mort1) death-effector domain.* Nature, 1998. **392**(6679): p. 941-5.
101. Chou, J.J., et al., *Solution structure of the RAIDD CARD and model for CARD/CARD interaction in caspase-2 and caspase-9 recruitment.* Cell, 1998. **94**(2): p. 171-80.
102. Hiller, S., et al., *NMR structure of the apoptosis- and inflammation-related NALP1 pyrin domain.* Structure, 2003. **11**(10): p. 1199-205.
103. Huang, B., et al., *NMR structure and mutagenesis of the Fas (APO-1/CD95) death domain.* Nature, 1996. **384**(6610): p. 638-41.
104. Park, H.H., et al., *The death domain superfamily in intracellular signaling of apoptosis and inflammation.* Annu Rev Immunol, 2007. **25**: p. 561-86.
105. Garvey, T.L., et al., *Binding of FADD and caspase-8 to molluscum contagiosum virus MC159 v-FLIP is not sufficient for its antiapoptotic function.* J Virol, 2002. **76**(2): p. 697-706.
106. Yang, J.K., et al., *Crystal structure of MC159 reveals molecular mechanism of DISC assembly and FLIP inhibition.* Mol Cell, 2005. **20**(6): p. 939-49.
107. Weber, C.H. and Vincenz, C., *The death domain superfamily: a tale of two interfaces?* Trends Biochem Sci, 2001. **26**(8): p. 475-81.

108. Kaufmann, M., et al., *Identification of a basic surface area of the FADD death effector domain critical for apoptotic signaling*. FEBS Lett, 2002. **527**(1-3): p. 250-4.
109. Jeong, E.J., et al., *The solution structure of FADD death domain. Structural basis of death domain interactions of Fas and FADD*. J Biol Chem, 1999. **274**(23): p. 16337-42.
110. Berglund, H., et al., *The three-dimensional solution structure and dynamic properties of the human FADD death domain*. J Mol Biol, 2000. **302**(1): p. 171-88.
111. Lasker, M.V., Gajjar, M.M., and Nair, S.K., *Cutting edge: molecular structure of the IL-1R-associated kinase-4 death domain and its implications for TLR signaling*. J Immunol, 2005. **175**(7): p. 4175-4179.
112. Park, H.H. and Wu, H., *Crystal structure of RAIDD death domain implicates potential mechanism of PIDDosome assembly*. J Mol Biol, 2006. **357**(2): p. 358-364.
113. Lord, K.A., Hoffman-Liebermann, B., and Liebermann, D.A., *Complexity of the immediate early response of myeloid cells to terminal differentiation and growth arrest includes ICAM-1, Jun-B and histone variants*. Oncogene, 1990. **5**(3): p. 387-96.
114. Wesche, H., et al., *MyD88: an adapter that recruits IRAK to the IL-1 receptor complex*. Immunity, 1997. **7**(6): p. 837-47.
115. Janssens, S. and Beyaert, R., *A universal role for MyD88 in TLR/IL-1R-mediated signaling*. Trends Biochem Sci, 2002. **27**(9): p. 474-82.
116. von Bernuth, H., et al., *Pyogenic bacterial infections in humans with MyD88 deficiency*. Science, 2008. **321**(5889): p. 691-6.
117. Loiarro, M., et al., *Identification of critical residues of the MyD88 death domain involved in the recruitment of downstream kinases*. J Biol Chem, 2009. **284**(41): p. 28093-103.
118. George, J., et al., *Two human MYD88 variants, S34Y and R98C, interfere with MyD88-IRAK4-myddosome assembly*. J Biol Chem, 2011. **286**(2): p. 1341-53.
119. Kagan, J.C. and Medzhitov, R., *Phosphoinositide-mediated adaptor recruitment controls Toll-like receptor signaling*. Cell, 2006. **125**(5): p. 943-55.
120. Kawai, T., et al., *Interferon-alpha induction through Toll-like receptors involves a direct interaction of IRF7 with MyD88 and TRAF6*. Nat Immunol, 2004. **5**(10): p. 1061-8.
121. Nishiya, T., et al., *Distinct roles of TIR and non-TIR regions in the subcellular localization and signaling properties of MyD88*. FEBS Lett, 2007. **581**(17): p. 3223-9.
122. Jaunin, F., et al., *Ultrastructural distribution of the death-domain-containing MyD88 protein in HeLa cells*. Exp Cell Res, 1998. **243**(1): p. 67-75.
123. Aliprantis, A.O., et al., *The apoptotic signaling pathway activated by Toll-like receptor-2*. EMBO J, 2000. **19**(13): p. 3325-36.
124. Hacker, H., et al., *Specificity in Toll-like receptor signalling through distinct effector functions of TRAF3 and TRAF6*. Nature, 2006. **439**(7073): p. 204-7.
125. del Fresno, C., et al., *Tumor cells deactivate human monocytes by up-regulating IL-1 receptor associated kinase-M expression via CD44 and TLR4*. J Immunol, 2005. **174**(5): p. 3032-3040.
126. Biswas, S.K., et al., *Role for MyD88-independent, TRIF pathway in lipid A/TLR4-induced endotoxin tolerance*. J Immunol, 2007. **179**(6): p. 4083-92.

127. del Fresno, C., et al., *Inflammatory responses associated with acute coronary syndrome up-regulate IRAK-M and induce endotoxin tolerance in circulating monocytes.* J Endotoxin Res, 2007. **13**(1): p. 39-52.
128. Gomez-Pina, V., et al., *Metalloproteinases shed TREM-1 ectodomain from lipopolysaccharide-stimulated human monocytes.* J Immunol, 2007. **179**(6): p. 4065-73.
129. Gonzalez-Leon, M.C., et al., *Nitric oxide induces SOCS-1 expression in human monocytes in a TNF-alpha-dependent manner.* J Endotoxin Res, 2006. **12**(5): p. 296-306.
130. Lopez-Collazo, E., et al., *Pathophysiology of interleukin-1 receptor-associated kinase-M: implications in refractory state.* Curr Opin Infect Dis, 2006. **19**(3): p. 237-44.
131. Soares-Schanoski, A., et al., *6-Methylprednisolone down-regulates IRAK-M in human and murine osteoclasts and boosts bone-resorbing activity: a putative mechanism for corticoid-induced osteoporosis.* J Leukoc Biol, 2007. **82**(3): p. 700-9.
132. Escoll, P., et al., *Rapid up-regulation of IRAK-M expression following a second endotoxin challenge in human monocytes and in monocytes isolated from septic patients.* Biochem Biophys Res Commun, 2003. **311**(2): p. 465-472.
133. Martin, M., et al., *Interleukin-1-induced activation of a protein kinase co-precipitating with the type I interleukin-1 receptor in T cells.* Eur J Immunol, 1994. **24**(7): p. 1566-71.
134. Croston, G.E., Cao, Z., and Goeddel, D.V., *NF-kappa B activation by interleukin-1 (IL-1) requires an IL-1 receptor-associated protein kinase activity.* J Biol Chem, 1995. **270**(28): p. 16514-7.
135. Thomas, J.A., et al., *Impaired cytokine signaling in mice lacking the IL-1 receptor-associated kinase.* J Immunol, 1999. **163**(2): p. 978-84.
136. Kobayashi, K., et al., *IRAK-M is a negative regulator of Toll-like receptor signaling.* Cell, 2002. **110**(2): p. 191-202.
137. Wesche, H., et al., *IRAK-M is a novel member of the Pelle/interleukin-1 receptor-associated kinase (IRAK) family.* J Biol Chem, 1999. **274**(27): p. 19403-10.
138. Li, S., et al., *IRAK-4: a novel member of the IRAK family with the properties of an IRAK-kinase.* Proc Natl Acad Sci U S A, 2002. **99**(8): p. 5567-72.
139. Rosati, O. and Martin, M.U., *Identification and characterization of murine IRAK-M.* Biochem Biophys Res Commun, 2002. **293**(5): p. 1472-7.
140. Feinstein, E., et al., *The death domain: a module shared by proteins with diverse cellular functions.* Trends Biochem Sci, 1995. **20**(9): p. 342-4.
141. Ye, H., et al., *Distinct molecular mechanism for initiating TRAF6 signalling.* Nature, 2002. **418**(6896): p. 443-7.
142. Flannery, S. and Bowie, A.G., *The interleukin-1 receptor-associated kinases: critical regulators of innate immune signalling.* Biochem Pharmacol, 2010. **80**(12): p. 1981-91.
143. Martin, M.U. and Kollwe, C., *Interleukin-1 receptor-associated kinase-1 (IRAK-1): A self-regulatory adapter molecule in the signaling cascade of the Toll/IL-1 receptor family.* Signal Transduction, 2001. **1**(2): p. 37-50.
144. Meylan, E. and Tschopp, J., *IRAK2 takes its place in TLR signaling.* Nat Immunol, 2008. **9**(6): p. 581-2.

145. Wang, Z., et al., *Crystal structures of IRAK-4 kinase in complex with inhibitors: a serine/threonine kinase with tyrosine as a gatekeeper*. *Structure*, 2006. **14**(12): p. 1835-44.
146. Kuglstatter, A., et al., *Cutting Edge: IL-1 receptor-associated kinase 4 structures reveal novel features and multiple conformations*. *J Immunol*, 2007. **178**(5): p. 2641-5.
147. Li, H., et al., *IL-1 receptor-associated kinase M is a central regulator of osteoclast differentiation and activation*. *J Exp Med*, 2005. **201**(7): p. 1169-77.
148. Kawagoe, T., et al., *Sequential control of Toll-like receptor-dependent responses by IRAK1 and IRAK2*. *Nat Immunol*, 2008. **9**(6): p. 684-91.
149. Horng, T., et al., *The adaptor molecule TIRAP provides signalling specificity for Toll-like receptors*. *Nature*, 2002. **420**(6913): p. 329-33.
150. Oshiumi, H., et al., *TICAM-1, an adaptor molecule that participates in Toll-like receptor 3-mediated interferon-beta induction*. *Nat Immunol*, 2003. **4**(2): p. 161-7.
151. Fitzgerald, K.A., et al., *Mal (MyD88-adaptor-like) is required for Toll-like receptor-4 signal transduction*. *Nature*, 2001. **413**(6851): p. 78-83.
152. Harte, M.T., et al., *The poxvirus protein A52R targets Toll-like receptor signaling complexes to suppress host defense*. *J Exp Med*, 2003. **197**(3): p. 343-51.
153. Maloney, G., Schroder, M., and Bowie, A.G., *Vaccinia virus protein A52R activates p38 mitogen-activated protein kinase and potentiates lipopolysaccharide-induced interleukin-10*. *J Biol Chem*, 2005. **280**(35): p. 30838-44.
154. Seki, M., et al., *Critical role of IL-1 receptor-associated kinase-M in regulating chemokine-dependent deleterious inflammation in murine influenza pneumonia*. *J Immunol*, 2010. **184**(3): p. 1410-8.
155. Gillespie, S.K. and Wasserman, S.A., *Dorsal, a Drosophila Rel-like protein, is phosphorylated upon activation of the transmembrane protein Toll*. *Mol Cell Biol*, 1994. **14**(6): p. 3559-68.
156. Kubo-Murai, M., et al., *IRAK-4-dependent degradation of IRAK-1 is a negative feedback signal for TLR-mediated NF-kappaB activation*. *J Biochem*, 2008. **143**(3): p. 295-302.
157. Ku, C.L., et al., *Selective predisposition to bacterial infections in IRAK-4-deficient children: IRAK-4-dependent TLRs are otherwise redundant in protective immunity*. *J Exp Med*, 2007. **204**(10): p. 2407-22.
158. Picard, C., et al., *Pyogenic bacterial infections in humans with IRAK-4 deficiency*. *Science*, 2003. **299**(5615): p. 2076-9.
159. Puel, A., et al., *Inherited disorders of NF-kappaB-mediated immunity in man*. *Curr Opin Immunol*, 2004. **16**(1): p. 34-41.
160. Medvedev, A.E., et al., *Distinct mutations in IRAK-4 confer hyporesponsiveness to lipopolysaccharide and interleukin-1 in a patient with recurrent bacterial infections*. *J Exp Med*, 2003. **198**(4): p. 521-31.
161. Liew, F.Y., et al., *Negative regulation of toll-like receptor-mediated immune responses*. *Nat Rev Immunol*, 2005. **5**(6): p. 446-58.
162. Su, J., et al., *Differential regulation and role of interleukin-1 receptor associated kinase-M in innate immunity signaling*. *Cell Signal*, 2007. **19**(7): p. 1596-601.

163. Yasukawa, H., Sasaki, A., and Yoshimura, A., *Negative regulation of cytokine signaling pathways*. *Annu Rev Immunol*, 2000. **18**: p. 143-64.
164. Mansell, A., et al., *Suppressor of cytokine signaling 1 negatively regulates Toll-like receptor signaling by mediating Mal degradation*. *Nat Immunol*, 2006. **7**(2): p. 148-55.
165. Baetz, A., et al., *Suppressor of cytokine signaling (SOCS) proteins indirectly regulate toll-like receptor signaling in innate immune cells*. *J Biol Chem*, 2004. **279**(52): p. 54708-15.
166. Gingras, S., et al., *Re-examination of the role of suppressor of cytokine signaling 1 (SOCS1) in the regulation of toll-like receptor signaling*. *J Biol Chem*, 2004. **279**(52): p. 54702-7.
167. Bulut, Y., et al., *Cooperation of Toll-like receptor 2 and 6 for cellular activation by soluble tuberculosis factor and Borrelia burgdorferi outer surface protein A lipoprotein: role of Toll-interacting protein and IL-1 receptor signaling molecules in Toll-like receptor 2 signaling*. *J Immunol*, 2001. **167**(2): p. 987-94.
168. Zhang, G. and Ghosh, S., *Negative regulation of toll-like receptor-mediated signaling by Tollip*. *J Biol Chem*, 2002. **277**(9): p. 7059-65.
169. Janssens, S., et al., *Regulation of interleukin-1- and lipopolysaccharide-induced NF-kappaB activation by alternative splicing of MyD88*. *Curr Biol*, 2002. **12**(6): p. 467-71.
170. Thomassen, E., Renshaw, B.R., and Sims, J.E., *Identification and characterization of SIGIRR, a molecule representing a novel subtype of the IL-1R superfamily*. *Cytokine*, 1999. **11**(6): p. 389-99.
171. Wald, D., et al., *SIGIRR, a negative regulator of Toll-like receptor-interleukin 1 receptor signaling*. *Nat Immunol*, 2003. **4**(9): p. 920-7.
172. Garlanda, C., et al., *Intestinal inflammation in mice deficient in Tir8, an inhibitory member of the IL-1 receptor family*. *Proc Natl Acad Sci U S A*, 2004. **101**(10): p. 3522-6.
173. Brint, E.K., et al., *ST2 is an inhibitor of interleukin 1 receptor and Toll-like receptor 4 signaling and maintains endotoxin tolerance*. *Nat Immunol*, 2004. **5**(4): p. 373-9.
174. Xiao, T., et al., *Three-dimensional structure of a complex between the death domains of Pelle and Tube*. *Cell*, 1999. **99**(5): p. 545-555.
175. Ohnishi, H., et al., *Structural basis for the multiple interactions of the MyD88 TIR domain in TLR4 signaling*. *Proc Natl Acad Sci U S A*, 2009. **106**(25): p. 10260-5.
176. Rossi, P., et al., *Solution NMR Structure of Human Myeloid Differentiation Primary Response (MyD88)*. *Protein Data Base*, 2009. **ID: 2JS7**.
177. Motshwene, P.G., et al., *An oligomeric signaling platform formed by the Toll-like receptor signal transducers MyD88 and IRAK-4*. *J Biol Chem*, 2009. **284**(37): p. 25404-11.
178. Lin, S.C., Lo, Y.C., and Wu, H., *Helical assembly in the MyD88-IRAK4-IRAK2 complex in TLR/IL-1R signalling*. *Nature*, 2010. **465**(7300): p. 885-890.
179. Khan, J.A., et al., *Crystal structure of the Toll/interleukin-1 receptor domain of human IL-1RAPL*. *J Biol Chem*, 2004. **279**(30): p. 31664-70.
180. Nyman, T., et al., *The crystal structure of the human toll-like receptor 10 cytoplasmic domain reveals a putative signaling dimer*. *J Biol Chem*, 2008. **283**(18): p. 11861-5.

181. Xu, Y., et al., *Structural basis for signal transduction by the Toll/interleukin-1 receptor domains*. Nature, 2000. **408**(6808): p. 111-5.
182. Mendoza-Barbera, E., et al., *Contribution of globular death domains and unstructured linkers to MyD88-IRAK-4 heterodimer formation: an explanation for the antagonistic activity of MyD88s*. Biochem Biophys Res Commun, 2009. **380**(1): p. 183-7.
183. Slack, J.L., et al., *Identification of two major sites in the type I interleukin-1 receptor cytoplasmic region responsible for coupling to pro-inflammatory signaling pathways*. J Biol Chem, 2000. **275**(7): p. 4670-8.
184. Sun, H., et al., *A heterotrimeric death domain complex in Toll signaling*. Proc Natl Acad Sci U S A, 2002. **99**(20): p. 12871-6.
185. Letsou, A., et al., *Genetic and molecular characterization of tube, a Drosophila gene maternally required for embryonic dorsoventral polarity*. Proc Natl Acad Sci U S A, 1991. **88**(3): p. 810-4.
186. Drier, E.A. and Steward, R., *The dorsoventral signal transduction pathway and the Rel-like transcription factors in Drosophila*. Semin Cancer Biol, 1997. **8**(2): p. 83-92.
187. Shen, B. and Manley, J.L., *Phosphorylation modulates direct interactions between the Toll receptor, Pelle kinase and Tube*. Development, 1998. **125**(23): p. 4719-28.
188. Zapata, J.M., et al., *The Drosophila tumor necrosis factor receptor-associated factor-1 (DTRAF1) interacts with Pelle and regulates NFkappaB activity*. J Biol Chem, 2000. **275**(16): p. 12102-7.
189. Horng, T. and Medzhitov, R., *Drosophila MyD88 is an adapter in the Toll signaling pathway*. Proc Natl Acad Sci U S A, 2001. **98**(22): p. 12654-8.
190. Lye, E., et al., *The role of interleukin 1 receptor-associated kinase-4 (IRAK-4) kinase activity in IRAK-4-mediated signaling*. J Biol Chem, 2004. **279**(39): p. 40653-8.
191. Kawagoe, T., et al., *Essential role of IRAK-4 protein and its kinase activity in Toll-like receptor-mediated immune responses but not in TCR signaling*. J Exp Med, 2007. **204**(5): p. 1013-24.
192. Kim, T.W., et al., *A critical role for IRAK4 kinase activity in Toll-like receptor-mediated innate immunity*. J Exp Med, 2007. **204**(5): p. 1025-36.
193. Moncrieffe, M.C., Grossmann, J.G., and Gay, N.J., *Assembly of oligomeric death domain complexes during Toll receptor signaling*. J Biol Chem, 2008. **283**(48): p. 33447-54.
194. Akira, S. and Takeda, K., *Toll-like receptor signalling*. Nat Rev Immunol, 2004. **4**(7): p. 499-511.
195. Bjorkbacka, H., et al., *Reduced atherosclerosis in MyD88-null mice links elevated serum cholesterol levels to activation of innate immunity signaling pathways*. Nat Med, 2004. **10**(4): p. 416-21.
196. Michelsen, K.S., et al., *Lack of Toll-like receptor 4 or myeloid differentiation factor 88 reduces atherosclerosis and alters plaque phenotype in mice deficient in apolipoprotein E*. Proc Natl Acad Sci U S A, 2004. **101**(29): p. 10679-84.
197. Goldstein, D.R., et al., *Critical role of the Toll-like receptor signal adaptor protein MyD88 in acute allograft rejection*. J Clin Invest, 2003. **111**(10): p. 1571-8.

198. Hosoi, T., et al., *Myeloid differentiation factor 88 (MyD88)-deficiency increases risk of diabetes in mice*. PLoS One, 2010. **5**(9).
199. Schuster, J.M. and Nelson, P.S., *Toll receptors: an expanding role in our understanding of human disease*. J Leukoc Biol, 2000. **67**(6): p. 767-73.
200. del Fresno, C., et al., *Nitric oxide activates the expression of IRAK-M via the release of TNF-alpha in human monocytes*. Nitric Oxide, 2004. **10**(4): p. 213-20.
201. Mytar, B., et al., *Tumor cell-induced deactivation of human monocytes*. J Leukoc Biol, 2003. **74**(6): p. 1094-101.
202. O'Neill, L.A., *Therapeutic targeting of Toll-like receptors for inflammatory and infectious diseases*. Curr Opin Pharmacol, 2003. **3**(4): p. 396-403.
203. Fischer, M. and Ehlers, M., *Toll-like receptors in autoimmunity*. Ann N Y Acad Sci, 2008. **1143**: p. 21-34.
204. Hong-Geller, E., Chaudhary, A., and Lauer, S., *Targeting toll-like receptor signaling pathways for design of novel immune therapeutics*. Curr Drug Discov Technol, 2008. **5**(1): p. 29-38.
205. Gearing, A.J., *Targeting toll-like receptors for drug development: a summary of commercial approaches*. Immunol Cell Biol, 2007. **85**(6): p. 490-4.
206. Boeckmann, B., et al., *The SWISS-PROT protein knowledgebase and its supplement TrEMBL in 2003*. Nucleic Acids Res, 2003. **31**(1): p. 365-370.
207. Linding, R., et al., *GlobPlot: Exploring protein sequences for globularity and disorder*. Nucleic Acids Res, 2003. **31**(13): p. 3701-3708.
208. Ward, J.J., et al., *The DISOPRED server for the prediction of protein disorder*. Bioinformatics, 2004. **20**(13): p. 2138-2139.
209. Dosztanyi, Z., et al., *IUPred: web server for the prediction of intrinsically unstructured regions of proteins based on estimated energy content*. Bioinformatics, 2005. **21**(16): p. 3433-3434.
210. Larkin, M.A., et al., *Clustal W and Clustal X version 2.0*. Bioinformatics, 2007. **23**(21): p. 2947-2948.
211. Cuff, J.A., et al., *JPred: a consensus secondary structure prediction server*. Bioinformatics, 1998. **14**(10): p. 892-893.
212. McGuffin, L.J., Bryson, K., and Jones, D.T., *The PSIPRED protein structure prediction server*. Bioinformatics, 2000. **16**(4): p. 404-405.
213. Rudolph, R. and Lilie, H., *In vitro folding of inclusion body proteins*. FASEB J, 1996. **10**(1): p. 49-56.
214. Armstrong, N., de Lencastre, A., and Gouaux, E., *A new protein folding screen: application to the ligand binding domains of a glutamate and kainate receptor and to lysozyme and carbonic anhydrase*. Protein Sci, 1999. **8**(7): p. 1475-83.
215. Qiagen, *The QIAexpressionist*. 5 ed. 2003.
216. Millipore, *Centrifugal Filter Devices for the Concentration and Purification of Biological Samples*. Millipore Corporation. Cited January 30, 2012. Available from: http://teachline.ls.huji.ac.il/72682/Booklets/AMICON_ultracentrifuge_devices.pdf.

217. Merril, C.R. and Washart, K.M., *Protein detection methods*, in *Gel Electrophoresis of Proteins: A Practical Approach*, 3rd edition. (B.D. Hames, Ed.). 1998, Oxford University Press: Oxford, United Kingdom. p. 53-92.
218. Switzer, R.C., Merril, C.R., and Shifrin, S., *A highly sensitive silver stain for detecting proteins and peptides in polyacrylamide gels*. *Anal Biochem*, 1979. **98**: p. 231-237.
219. Berne, B.J. and Pecora, R., *Dynamic light scattering : with applications to chemistry, biology and physics*. 1976, New York ; London: Wiley-Interscience. vii,376p.
220. Biacore, *Biacore Sensor Surface Handbook*. Biacore AB Corporation. 2003, Uppsala, Sweden.
221. Schuck, P., *Size-distribution analysis of macromolecules by sedimentation velocity ultracentrifugation and lamm equation modeling*. *Biophys J*, 2000. **78**(3): p. 1606-1619.
222. Laue, T.M., et al., *Computer-aided interpretation of analytical sedimentation data for proteins*, in *Analytical Ultracentrifugation in Biochemistry and Polymer Science*. (S.E. Harding, A.J. Rowe, J.C. Horton, Ed.). 1992, The Royal Society of Chemistry: Cambridge. p. 90-125.
223. Hampton_Research, *Crystal Growth Techniques*. Hampton Research Corporation. Cited January 30, 2012. Available from: http://hamptonresearch.com/documents/growth_101/2.pdf.
224. Chayen, N.E. and Saridakis, E., *Protein crystallization: from purified protein to diffraction-quality crystal*. *Nat Methods*, 2008. **5**(2): p. 147-153.
225. Giege, R. and Ducruix, A., *Crystallization of nucleic acids and proteins : a practical approach*. 2nd ed. ed. 1999, Oxford: Oxford University Press. xxii,435p.
226. Chayen, N.E., *Methods for separating nucleation and growth in protein crystallization*. *Prog. Biophys. Mol. Biol.*, 2005. **88**: p. 329-337.
227. Chayen, N.E., et al., *Trends and challenges in experimental macromolecular crystallography*. *Q Rev Biophys*, 1996. **29**(3): p. 227-278.
228. Ataka, M., *Protein crystal growth: An approach based on phase diagram determination*. *Phase Transitions*, 1993. **45**(2-3): p. 205-219.
229. Stura, E.A. and Wilson, I.A., *Applications of the streak seeding technique in protein crystallization*. *Journal of Crystal Growth*, 1991. **110**(1-2): p. 270-282.
230. Chayen, N.E., *Macromolecular Crystallography: Conventional and High-Throughput Methods*, in *Automation of non-conventional crystallization techniques for screening and optimization*. 2007, Oxford University Press: Oxford. p. 45-58.
231. Chayen, N.E., *Protein crystallization for genomics: throughput versus output*. *J. Struct. Funct. Genomics*, 2003. **4**: p. 115-120.
232. Bergfors, T., *Seeds to crystals*. *J Struct Biol*, 2003. **142**(1): p. 66-76.
233. Hampton_Research, *Seeding Tools*. Hampton Research Corporation. Cited January 30, 2012. Available from: http://hamptonresearch.com/documents/product/hr001084_8-133_-_user_guide.pdf.
234. Yeh, J.I. and Hol, W.G., *A flash-annealing technique to improve diffraction limits and lower mosaicity in crystals of glycerol kinase*. *Acta Crystallogr D Biol Crystallogr*, 1998. **54**(Pt 3): p. 479-480.

235. Hope, H., *Cryocrystallography of biological macromolecules: a generally applicable method*. Acta Crystallogr B, 1988. **44** (Pt 1): p. 22-26.
236. Rodgers, D.W., *Cryocrystallography*. Structure, 1994. **2**(12): p. 1135-1140.
237. Gabadinho, J., et al., *MxCuBE: a synchrotron beamline control environment customized for macromolecular crystallography experiments*. J Synchrotron Radiat, 2010. **17**(5): p. 700-707.
238. Rhodes, G., *Crystallography made crystal clear : a guide for users of macromolecular models*. 3rd ed. ed. 2006, Amsterdam ; Oxford: Elsevier Academic Press.
239. Leslie, A.G.W., *Recent changes to the MOSFLM package for processing film and image plate data*, in *Joint CCP4+ESF-EAMCB Newsletter on Protein Crystallography*. 1992, Daresbury Laboratory: Warrington, UK.
240. Collaborative Computational Project, N., *The CCP4 suite: programs for protein crystallography*. Acta Crystallogr D Biol Crystallogr, 1994. **50**(Pt 5): p. 760-763.
241. Evans, P.R., *Data reduction*. Proceedings of CCP4 Study Weekend On DataCollection & Processing, 1993: p. 114-122.
242. Schwede, T., et al., *SWISS-MODEL: an automated protein homology-modeling server*. Nucl. Acids Res., 2003. **31**(13): p. 3381-3385.
243. Laskowski, R.A., et al., *{PROCHECK}: a program to check the stereochemical quality of protein structures*. J. Appl. Cryst., 1993. **26**: p. 283-291.
244. DeLano, W.L., *The PyMOL Molecular Graphics System*. DeLano Scientific. Cited January 30, 2012. Available from: <http://www.pymol.org>.
245. Carrington, P.E., et al., *The structure of FADD and its mode of interaction with procaspase-8*. Mol Cell, 2006. **22**(5): p. 599-610.
246. Gasteiger, E., et al., *ExpASY: The proteomics server for in-depth protein knowledge and analysis*. Nucleic Acids Res, 2003. **31**(13): p. 3784-3788.
247. Wang, L., et al., *The Fas-FADD death domain complex structure reveals the basis of DISC assembly and disease mutations*. Nat Struct Mol Biol, 2010. **17**(11): p. 1324-1329.
248. Xiao, T., Gardner, K.H., and Sprang, S.R., *Cosolvent-induced transformation of a death domain tertiary structure*. Proc Natl Acad Sci U S A, 2002. **99**(17): p. 11151-11156.
249. Chang, H.Y., Yang, X., and Baltimore, D., *Dissecting Fas signaling with an altered-specificity death-domain mutant: requirement of FADD binding for apoptosis but not Jun N-terminal kinase activation*. Proc Natl Acad Sci U S A, 1999. **96**(4): p. 1252-6.
250. Wang, X., et al., *Potential aggregation prone regions in biotherapeutics: A survey of commercial monoclonal antibodies*. MAbs, 2009. **1**(3): p. 254-67.
251. Conchillo-Sole, O., et al., *AGGRESCAN: a server for the prediction and evaluation of "hot spots" of aggregation in polypeptides*. BMC Bioinformatics, 2007. **8**: p. 65.
252. Carrio, M.M. and Villaverde, A., *Protein aggregation as bacterial inclusion bodies is reversible*. FEBS Lett, 2001. **489**(1): p. 29-33.
253. Strandberg, L. and Enfors, S.O., *Factors influencing inclusion body formation in the production of a fused protein in Escherichia coli*. Appl Environ Microbiol, 1991. **57**(6): p. 1669-74.

254. Wilkinson, D.L. and Harrison, R.G., *Predicting the solubility of recombinant proteins in Escherichia coli*. Biotechnology (N Y), 1991. **9**(5): p. 443-8.
255. Garcia-Fruitos, E., et al., *Folding of a misfolding-prone beta-galactosidase in absence of DnaK*. Biotechnol Bioeng, 2005. **90**(7): p. 869-75.
256. Garcia-Fruitos, E., et al., *Divergent genetic control of protein solubility and conformational quality in Escherichia coli*. J Mol Biol, 2007. **374**(1): p. 195-205.
257. Zhao, Y., et al., *Two distinct states of Escherichia coli cells that overexpress recombinant heterogeneous beta-galactosidase*. J Biol Chem, 2012. **287**(12): p. 9259-68.
258. Siegel, R.M., et al., *Death-effector filaments: novel cytoplasmic structures that recruit caspases and trigger apoptosis*. J Cell Biol, 1998. **141**(5): p. 1243-53.
259. Colussi, P.A., Harvey, N.L., and Kumar, S., *Prodomain-dependent nuclear localization of the caspase-2 (Nedd2) precursor. A novel function for a caspase prodomain*. J Biol Chem, 1998. **273**(38): p. 24535-42.
260. Guiet, C. and Vito, P., *Caspase recruitment domain (CARD)-dependent cytoplasmic filaments mediate bcl10-induced NF-kappaB activation*. J Cell Biol, 2000. **148**(6): p. 1131-40.
261. Baliga, B.C., et al., *Role of prodomain in importin-mediated nuclear localization and activation of caspase-2*. J Biol Chem, 2003. **278**(7): p. 4899-905.
262. Shearwin-Whyatt, L.M., Harvey, N.L., and Kumar, S., *Subcellular localization and CARD-dependent oligomerization of the death adaptor RAIDD*. Cell Death Differ, 2000. **7**(2): p. 155-65.
263. Jabado, O., et al., *RAIDD aggregation facilitates apoptotic death of PC12 cells and sympathetic neurons*. Cell Death Differ, 2004. **11**(6): p. 618-30.
264. Park, H.H., et al., *Death domain assembly mechanism revealed by crystal structure of the oligomeric PIDDosome core complex*. Cell, 2007. **128**(3): p. 533-46.
265. Janssens, S. and Beyaert, R., *Functional diversity and regulation of different interleukin-1 receptor-associated kinase (IRAK) family members*. Mol Cell, 2003. **11**(2): p. 293-302.
266. Jiang, Z., et al., *Details of Toll-like receptor:adapter interaction revealed by germ-line mutagenesis*. Proc Natl Acad Sci U S A, 2006. **103**(29): p. 10961-6.
267. Weber, C.H. and Vincenz, C., *A docking model of key components of the DISC complex: death domain superfamily interactions redefined*. FEBS Lett, 2001. **492**(3): p. 171-6.
268. Qin, H., et al., *Structural basis of procaspase-9 recruitment by the apoptotic protease-activating factor 1*. Nature, 1999. **399**(6736): p. 549-57.
269. Moncrieffe, M.C., Stott, K.M., and Gay, N.J., *Solution structure of the isolated Pelle death domain*. FEBS Lett, 2005. **579**(18): p. 3920-6.
270. Li, X., et al., *IL-1-induced NFkappa B and c-Jun N-terminal kinase (JNK) activation diverge at IL-1 receptor-associated kinase (IRAK)*. Proc. Natl. Acad. Sci. U. S. A., 2001. **98**(8): p. 4461-4465.
271. Scott, F.L., et al., *The Fas-FADD death domain complex structure unravels signalling by receptor clustering*. Nature, 2009. **457**(7232): p. 1019-22.